Measurement of beauty quark production from dimuon events with the ZEUS detector at HERA II

Dissertation
zur Erlangung des Doktorgrades
des Departments Physik
der Universität Hamburg

vorgelegt von Danny Bot
aus Norderstedt

Hamburg, 2011

Wir müssen wissen,
wir werden wissen.

We must know,
we will know.

David Hilbert,
German mathematician
(*1862, †1943)

Understanding is a three edged sword: your side, their side, and the truth.

J. Michael Straczynski

Abstract

In this thesis, a measurement of beauty quark production via the process

$$ep \rightarrow e'b\bar{b}X \rightarrow e'\mu\mu X$$

in electron-proton collisions at HERA using a data sample recorded by the ZEUS detector in the years 2003-2007, corresponding to an integrated luminosity of 376 pb^{-1}, is presented. A low transverse momentum threshold for muon identification in combination with the large rapidity coverage of the ZEUS muon-detection sytem gives access to essentially the full phase space for beauty quark production. Dimuon charge correlations as well as hadronic isolation and the mass of the dimuon system were used to separate the beauty signal from backgrounds. Visible, differential and total cross sections for beauty quark production were measured and compared to next-to-leading order QCD calculations and previous measurements.

In addition, a first search for QCD instanton-induced processes containing both a charm- and beauty-quark pair in dimuon events was performed. In order to differentiate between beauty and instanton events, discriminating observables sensitive to the hadronic final state, so-called *event shape* variables, were used in combination with the dimuon requirement.

As technical part of this thesis, the reconstruction algorithm for so-called energy flow objects (EFOs) was modified. EFOs contain the combined information of primary and secondary vertex-fitted tracks as well as CAL energy measurements. The modification considers additional tracks close to but not fitted to the primary vertex and which fulfill reasonable track and impact parameter requirements. As a result, the efficiency to reconstruct muon candidates with high impact parameter values as energy flow objects was increased.

Kurzfassung

In dieser Arbeit wird eine Messung der Beauty-Quark-Produktion mittels des Prozesses

$$ep \rightarrow e'b\bar{b}X \rightarrow e'\mu\mu X$$

präsentiert. Dabei wurde ein vom ZEUS-Detektor aufgenommener Datensatz von Elektron-Proton Kollisionen bei HERA von den Jahren 2003 bis 2007, entsprechend einer integrierten Luminosität von 376 pb^{-1}, verwendet. Eine niedrige Transversalimpuls-Schwelle für die Myonidentifizierung kombiniert mit Abdeckung eines großen Rapiditätsbereiches durch das ZEUS Myondetektierungsystems ermöglicht den Zugriff auf den gesamten Phasenraum für die Beauty-Quark-Produktion. Ladungskorrelationen sowie die hadronische Isolation und invariante Masse des Zwei-Myon Systems wurden zur Trennung von Beauty-Signal und Untergründen verwendet. Sichtbare, differentielle und totale Wirkungsquerschnitte wurden gemessen und mit QCD-Berechnungen in nächsthöherer Ordnung sowie vorangegangen Messungen verglichen.

Desweiteren wurde eine erste Suche nach QCD instanton-induzierten Ereignissen, die zusätzlich ein Charm- und Beauty-Quark Paar beinhalten durchgeführt. Um Beauty-Ereignisse von instanton-induzierten zu unterscheiden, wurden auf den hadronischen Endzustand empfindliche Observablen, sogenannte *Eventshape*-Variablen, in Kombination mit der Forderung nach zwei Myonen im Endzustand verwendet.

Als technischer Teil dieser Arbeit wurde der Rekonstruktionsalgorithmus sogenannter Energy-flow-objects (EFOs) modifiziert. EFOs entstehen aus der kombinierten Information von vertex-assoziierten Spuren und Energiemessungen im Kalorimeter. Die Modifikation betrachtet zusätzlich nicht-vertex-assoziierte Spuren nahe dem Primärvertex, die passende Anforderungen am Impakt-Parameter und Spureigenschaften erfüllen. Das Resultat ist eine erhöhte Effizienz der Rekonstruktion von Myon-Kandidaten als EFOs bei hohem Impakt-Parameter.

Contents

Chapter 1

Introduction

Acccording to the Standard Model (SM) of particle physics [1], matter is made of twelve fundamental particles with spin $\frac{1}{2}$, so-called fermions, which are divided into three generations of leptons and quarks, as summarised in Tab. 1.1.

	Leptons			Quarks		
	Lepton	Charge	Mass [MeV]	Flavour	Charge	Mass [MeV]
1st Generation	$e^{\pm}$	± 1	0,511	$u, \bar{u}$	$\pm 2/3$	1,5 - 3,3
	$\nu_e, \bar{\nu}_e$	0	< 0,003	$d, \bar{d}$	$\mp 1/3$	3,5 - 6
2nd Generation	$\mu^{\pm}$	± 1	105,9	$c, \bar{c}$	$\pm 2/3$	1160 - 1340
	$\nu_\mu, \bar{\nu}_\mu$	0	< 0,19	$s, \bar{s}$	$\mp 1/3$	70 - 130
3rd Generation	$\tau^{\pm}$	± 1	1777	$t, \bar{t}$	$\pm 2/3$	171300 ± 1200
	$\nu_\tau, \bar{\nu}_\tau$	0	< 18,2	$b, \bar{b}$	$\mp 1/3$	4130 - 4370

Table 1.1: The fundamental fermions of the Standard Model [2]. The charge is given in units of the proton charge.

These fermions can interact by the exchange of gauge bosons, leading to four fundamental forces as summarised in Tab. 1.2:

Force	Gauge Boson	Mass [GeV]	Spin	Range
Gravitation	Graviton	0	2	∞
Electromagnetic	Photon γ	0	1	∞
Weak	Z^0	91,19	1	$\sim 10^{-18}$
	$W^{\pm}$	80,43	1	
Strong	8 gluons g	0	1	$\sim 10^{-15}$

Table 1.2: The four fundamental interactions as well as their gauge bosons [2]. The electromagnetic, weak and strong interaction are embedded into the Standard Model. It has not yet been achieved to incorporate the gravitation with its (hypotheical) gauge boson, the graviton, into the SM.

The weak interaction, mediated by the exchange of massive $W^{\pm}$ and Z^0 bosons, affects all

leptons and quarks. All electrically charged particles interact by the exchange of (virtual) photons, mediators of the electromagnetic force. Protons and neutrons, so-called hadrons, consist of quarks, which interact by the exchange of gluons, mediators of the strong interaction.

With the exception of gravitation, which is not incorporated into the Standard Model, the remaining three forces are described by quantum field theories: Electromagnetic interactions can be described by quantum electrodynamics (QED), an Abelian gauge theory (i.e. the symmetry group is commutative). The combination of the electromagnetic and weak force into the electroweak theory [3] as well as the theory of the strong interactions, quantum chromodynamics (QCD), are non-Abelian gauge theories. As a result, the exchange bosons do not only interact with fermions but also with themselves. The combination of the electroweak theory and QCD is referred to as the Standard Model with the group structure

$$SU(3)_C \times SU(2)_L \times U(1)_Y,$$

The last particle within the Standard Model, which has not been observed up to now, is the so-called Higgs boson, based on a scalar field with non-vanishing vacuum expectation value. The coupling of the Higgs field with the $W^\pm$ and Z^0 bosons generates the masses of the exchange bosons of the weak interaction.

In contrast to leptons, which exist as free particles, colour charged particles such as quarks are only observed within colourless bound states (hadrons). This is referred to as *confinement*, an important feature of QCD. At high energies (higher than about 1 GeV), the coupling strength of gluons becomes small and perturbative QCD methods (pQCD) are applicable. Theoretical calculations are expected to provide reliable predictions in all processes with a sufficiently high energy scale. The masses of the charm and beauty quark, referred to as heavy quarks, provide such a hard scale. Therefore, processes involving heavy quarks provide a rich testing ground for perturbative QCD.

The aim of the analysis presented in this thesis is the measurement of beauty quark production using decays into two muons. For this purpose, $e^\pm p$-collision data at HERA recorded by the ZEUS detector during the years 2003 till 2007 were used. Compared to the used data sample of a previous beauty production measurement with a dimuon tag [4, 64], the data sample used in this analysis offers two signifcant advantages: On the one hand, the statistics is three times higher than in the previous measurement. On the other hand, the micro vertex detector (MVD), which has been installed during the HERA upgrade in the year 2001, enables the exploitation of the lifetime information of the heavy hadrons. Thus, these two advantages allow a more precise measurement.

Furthermore, the Standard Model predicts processes which cannot be described by perturbation theory, e.g. the non-conservation of baryon and lepton number in case of the electroweak interaction and chirality in case of the strong interaction. Such processes are induced by instantons [5, 6]. While in electroweak interactions instantons might play a role at high energies of $\mathcal{O} \gtrsim 10$ TeV, instanton effects in QCD can become sizeable at present collider energies since the strong coupling constant α_s is much larger than the electroweak parameter α_w. However, an experimental verification is lacking until now. While previous searches for instanton-induced events at HERA [7–14] considered only instantons with the three light-flavour quark pairs $u\bar{u}, d\bar{d}$

and $s\bar{s}$ in deep inelastic scattering, the analysis presented in this thesis focusses on instanton-induced photoproduction events, which contain besides the light flavours both, a charm and a beauty quark pair (so-called heavy-flavour instantons). The heavy flavour quark pairs can be identified by their semileptonic decay into muons. Thus, the dimuon tag combined with discriminating observables will be used in this analysis to separate potential instanton events from beauty events. An experimental discovery of QCD instantons would be of fundamental significance for particle physics since such events would be an indirect evidence of baryon- and lepton-number violating sphalerons [16], which give an explanation for the asymmetry between matter and anti-matter [17].

This thesis is structured as follows: **Chapter 2** gives an overview of the theoretical background of high energy electron-proton scattering with emphasis on beauty quark production and their decay into muons. **Chapter 3** presents different measurements of beauty quark production in high energy collisions whereas in **chapter 4** the HERA collider and the ZEUS detector with particular emphasis on the detector components relevant for this analysis are described. **Chapter 5** is dedicated to the event reconstruction and muon finding algorithms. In addition, different methods to reconstruct the event kinematics as well as identification methods for beauty and instanton-induced events are presented. An overview of the Data and Monte Carlo samples followed by different cuts for the event and muon candidate selection used in this analysis is given in **chapter 6**. The determination of the beauty signal as well as a search for instantons in dimuon events is presented in **chapter 7** followed by the measurement of the cross sections and their systematic uncertainties in **chapter 8**. The last **chapter 9** contains a summary and outlook of this analysis.

Chapter 2

Theoretical Overview

This chapter describes the theoretical framework for this analysis. Beginning with a brief introduction into the kinematics of $e^{\pm}p$ collisions as well as their cross sections, an explanation of the quark-parton model is given followed by an overview of the theory of the strong interactions (QCD). In addition, the production and decay of heavy flavours is described. Finally, a summary of sources of dimuon events in $e^{\pm}p$ collisions and an overview of Monte Carlo simulations are given.

2.1   Kinematics of electron-proton scattering at HERA

In the Standard Model, lepton-nucleon scattering (at HERA electrons or positrons[1] and protons) occurs by exchange of vector bosons as shown in Fig. 2.1. The exchange of a $W^{\pm}$ is referred to as charged current (CC), where the lepton in the final state is a neutrino or antineutrino:

$$e^{\pm}p \to \overset{(-)}{\nu} X$$

The exchange of a photon or of a Z^0 is referred to as neutral current (NC), the dominating process at HERA. In these events the charge of the scattered lepton does not change:

$$e^{\pm}p \to e'^{\pm} X$$

Letting k and k' be the four-momenta of the incoming and scattered electron as well as P the four-momentum of the proton, one can define the following Lorentz-invariant variables in order to describe the kinematics of ep collisions:

The squared four-momentum of the exchanged photon[2] Q^2, also called virtuality, is given by

$$Q^2 = -q^2 = (k - k')^2 \tag{2.1}$$

---

[1]In the following, both electrons and positrons will be referred to as electrons

[2]For values of $Q^2 < m_{Z,W}^2$, the exchange of a $W^{\pm}$ or Z^0 is strongly suppressed, therefore the exchanged boson will be in the following referred to as photon
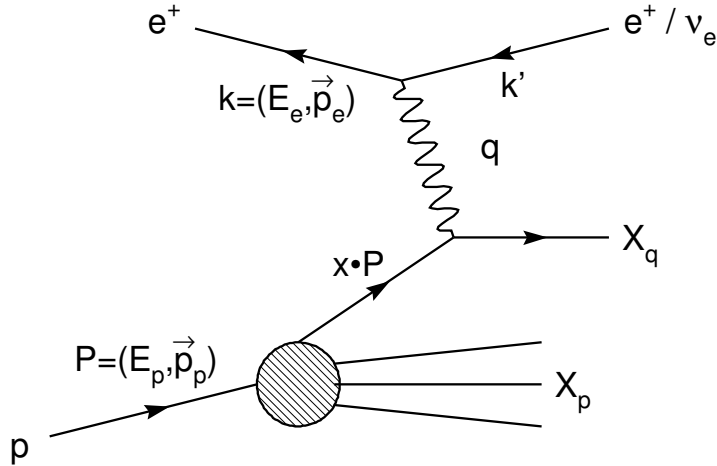
Figure 2.1: Feynman diagrams of the $e^{\pm}p$ collision at HERA. The exchanged boson q can be either a photon γ, a Z^0 or $W^{\pm}$.

In the simple quark-parton model picture, the fraction of the proton four-momentum carried by the struck quark is described by the Bjorken scaling variable x:

$$x = \frac{Q^2}{2P \cdot q}, \quad 0 \leq x \leq 1 \tag{2.2}$$

and the fraction of the electron energy transferred to the photon in the proton rest-frame by the inelasticity y:

$$y = \frac{P \cdot q}{P \cdot k}, \quad 0 \leq y \leq 1. \tag{2.3}$$

The squared centre-of-mass energy s of the electron-proton system is given by

$$s = (k + P)^2 \tag{2.4}$$

Assuming that the masses of the interacting electron and proton can be neglected, one gets:

$$s = (k + P)^2 = m_e^2 + m_P^2 + 2eP \approx 2ep \approx 4E_P E_e \tag{2.5}$$

Therefore, s depends only on the beam energies of the electron and proton. Furthermore, one can define the invariant mass W of the photon-proton system:

$$W = \sqrt{(P + q)^2} = \sqrt{ys - Q^2}. \tag{2.6}$$

At last the photon virtuality Q^2 can now be described by the three Lorentz-invariant variables

x, y and s:

$$Q^2 = xys. \tag{2.7}$$

Since s is constant, the kinematics can be described by only two of them, usually Q^2 and x.

The photon virtuality Q^2 defines two kinematic regimes. Events with values of $Q^2 \gtrsim 1$ GeV^2 and large hadronic centre-of-mass energy (i.e. $W^2 = (P + q)^2 \gg m_P^2$) classify the regime of *Deep Inelastic Scattering* (D.I.S.). There, the incoming electron is deflected and can be observed in the detector. For values of $Q^2 \ll 1$ GeV^2 the exchanged photon becomes quasi-real and the incoming electron is hardly deflected, so it is not detectable in the main detector. This is referred to as the *Photoproduction* regime (PHP).

2.2 Quark Parton Model, DIS Cross Sections and Proton Structure Function

In the DIS regime, the electron-proton scattering can be described as an incoherent sum of elastic scattering processes of the electron off a set of point-like partons. A simple illustration is the quark parton model (QPM) [18, 19], where the proton is assumed to be composed of point-like free objects called *partons*, which were later identified as *quarks*. In this picture, the Bjorken scaling variable x can be considered as the proton momentum fraction carried by the struck massless parton.

The general form of the electron-proton cross-section can be written as:

$$\frac{d^2\sigma}{dxdy} \sim L_{\mu\nu}W^{\mu\nu}, \tag{2.8}$$

where $L_{\mu\nu}$ is the leptonic tensor, describing the leptonic part of the interaction, and $W^{\mu\nu}$ represents the hadronic tensor [1]. The leptonic part is calculable via QED. The hadronic tensor includes the non-perturbative structure of the proton which can be expressed in the QPM as *structure functions* $F_1(x)$ and $F_2(x)$ [20], which are independent of the scale of the photon virtuality Q^2 (referred to as *scale invariance* [21]). For unpolarised beams, the neutral current cross section in terms of these structure functions is given by

$$\frac{d\sigma^2}{dQ^2dx} = \frac{4\pi\alpha_{em}^2}{xQ^4} \left[(1-y)F_2(x) \mp y^2 x F_1(x) \right], \tag{2.9}$$

where α_{em} is the fine structure constant. The structure functions are related to the *parton density functions* (PDFs) $f_q(x)$, describing the probability of finding a parton i with momentum fraction x in the proton. In the case that the parton i has a charge e_i, one obtains for the structure functions:

$$F_1(x) = \frac{1}{2} \sum_i e_i^2 f_i(x), \tag{2.10}$$

$$F_2(x) = x \sum_i e_i^2 f_i(x). \tag{2.11}$$

Comparing both expressions yields the Callan-Gross relation [22]:

$$F_2(x) = 2x F_1(x), \tag{2.12}$$

which is a consequence of the charged point-like constituents carrying spin 1/2 [23]. The structure functions can not be calculated from first principles but have to be extracted from experimental measurements. Although the QPM predicts the independence of the structure functions from the virtuality Q^2 of the photon, a deviation of the cross section with decreasing Q^2 from the prediction of the model (so-called *scaling violation*) was observed. This behaviour can be explained by means of quantum chromodynamics (QCD, cf. section 2.3). For the scattering via longitudinally polarised bosons, one complements equation 2.9 by the *longitudinal structure function F_L*, which is given by:

$$F_L(x) = F_2(x) - 2x F_1(x). \tag{2.13}$$

The structure function F_L is zero in the QPM since the quarks have zero transverse momentum. In QCD, gluon bremsstrahlung develops a non-zero transverse momentum, leading to non-zero values of F_L [24]. Another structure function $F_3(x, Q^2)$ [20] is introduced in order to include the parity violation which arises from γ/Z^0 interference. Therefore, the unpolarised neutral current (NC) DIS cross section is given by

$$\frac{d^2\sigma_{NC}}{dx dQ^2} = \frac{4\pi\alpha_{em}^2}{xQ^4} \cdot \left[Y_+(y) F_2^{NC}(x, Q^2) - y^2 F_L^{NC}(x, Q^2) \mp Y_-(y) x F_3^{NC}(x, Q^2) \right], \tag{2.14}$$

where $Y_\pm = 1 \pm (1 - y)^2$. In the case of charged current (CC) DIS scattering, the differential cross section can be written similarly to the NC differential cross section, but in terms of the CC structure functions F_1^{CC}, F_2^{CC} and F_3^{CC}:

$$\frac{d^2\sigma_{CC}}{dx dQ^2} = \frac{G_F^2}{4\pi x} \left(\frac{M_W^2}{Q^2 + M_W^2} \right)^2 \cdot \left[Y_+(y) F_2^{CC}(x, Q^2) - y^2 F_L^{CC}(x, Q^2) \mp Y_-(y) x F_3^{CC}(x, Q^2) \right], \tag{2.15}$$

where G_F is the Fermi constant. The NC structure functions are determined by the photon and Z^0 exchanges and by their interference while the CC structure funtions are the result of the $W^\pm$ exchange.

At lower values of Q^2, the Z^0 and $W^\pm$ exchanges are suppressed with respect to the photon exchange due to the masses $M_{Z^0, W^\pm}$ of the exchanged bosons:

$$\frac{\sigma(Z^0, W^\pm)}{\sigma(\gamma)} \sim \frac{Q^4}{(Q^2 + M_{Z^0, W^\pm}^2)^2}. \tag{2.16}$$

Hence, in the low Q^2 regime, the photon mediated NC DIS process is dominating (cf. Fig. 2.2).
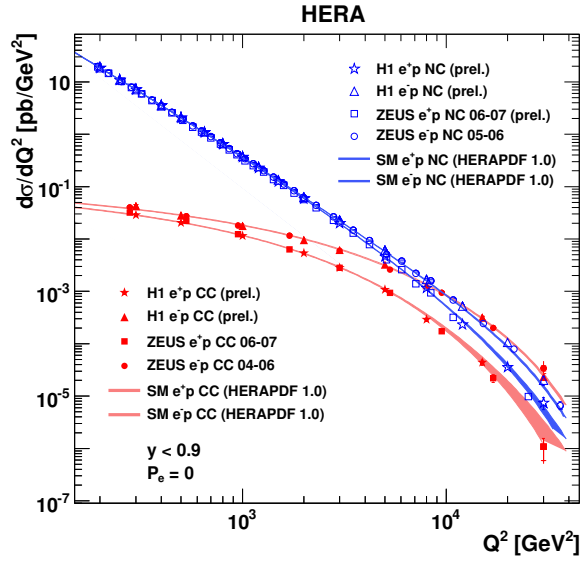
Figure 2.2: The NC and CC differential cross sections of ep scattering measured by the H1 and ZEUS experiments [28].

2.3   Quantum Chromodynamics

In quantum chromodynamics (QCD) [29], quarks can not be treated as free particles but they exchange gluons. QCD is a renormalizable non-Abelian gauge theory which describes the strong interaction as exchange of gluons. Gluons and quarks couple via colour charges. Each quark holds one of the three colours respectively anticolours in the case of antiquarks, therefore the symmetry of QCD is $SU(3)$. Eight independent linear combinations of colour-anticolour exist, represented by eight different gluons. Perturbative QCD (pQCD) provides a technique to calculate cross sections as power series in the strong coupling constant α_s. The lowest order process, which can be described by QCD, is the *leading order* (LO). Higher orders include gluon and quark loops (*virtual corrections*, cf. Fig. 2.3).
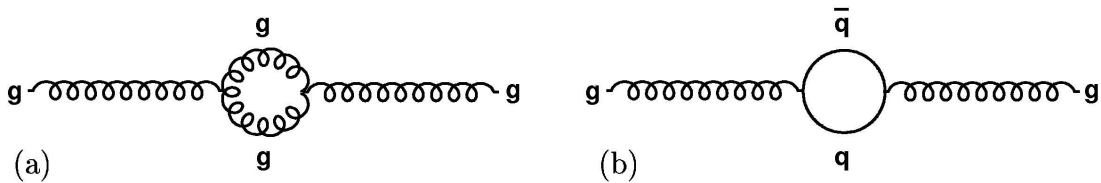
Figure 2.3: One loop virtual correction to the gluon propagator. Gluon (left) and quark (right) loops.

In order to calculate cross sections, integration over the full phase space of virtual and real quarks and gluons has to be performed. This integration introduces divergencies caused by infinite momenta of the virtual particle loop, referred to as *ultaviolet divergencies*. The soft or almost collinear emission of massless gluons leads to *infrared divergencies*. These divergencies

can be replaced by finite expressions by means of a procedure referred to as *regularisation* and *renormalisation* [25]. This procedure introduces an arbitary, unphysical parameter referred to as *renormalisation scale* μ_R. Any physical observable A has in general to be independent of μ_R, given by the *renormalisation group equation*:

$$\mu_R^2 \frac{dA}{d\mu_R^2} = 0. \tag{2.17}$$

Changes in μ_R have to be compensated by changes in the renormalisd coupling constant $\alpha_s(\mu_R^2)$ to ensure the independence of A on the choise of μ_R. The renormalisation group equation for α_s is then given by:

$$\mu_R^2 \frac{d\alpha_s}{d\mu_R^2} = \beta(\alpha_s), \tag{2.18}$$

where the β function is a power series in $\alpha_s(\mu)$ describing the depence of α_s on the renormalisation scale (running coupling), illustrated in Fig. 2.4.
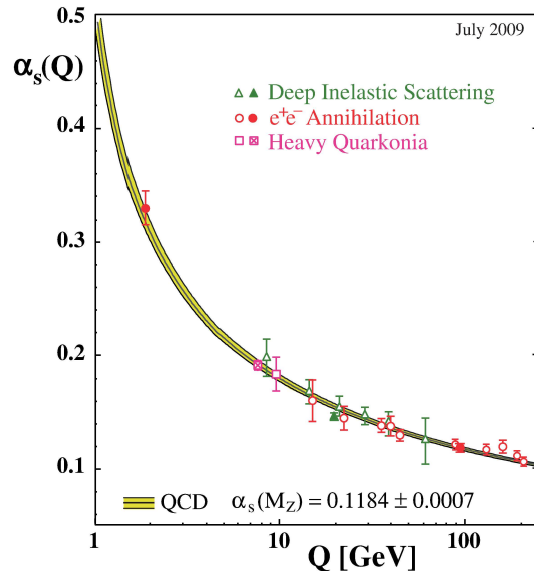
Figure 2.4: Running of the strong coupling constant α_s with the photon virtuality Q as the scale parameter μ (taken from [26]).

The leading order solution of Eq. 2.18 is given by:

$$\alpha_s(\mu) = \frac{12\pi}{(33 - 2n_f)\ln(\mu/\Lambda_{QCD}^2)}. \tag{2.19}$$

n_f stands for the number of active quark flavours with quark mass lighter than μ_R and Λ_{QCD} is the scale parameter of QCD which depends on the number of active quark flavours. Λ_{QCD} represents the energy scale at which α_s becomes large and perturbative QCD is not longer valid.

Divergencies arising from the emission of collinear gluons from the partons are absorbed in the definition of the parton density functions (PDFs) by means of the *factorisation scale* μ_f which separates the *ep* scattering process into two parts. The first part is the hard process,

the interaction of high energy particles, which is calculable by pQCD. The second part is the long range part of the low energy interactions in the initial state (soft process), which is not covered by pQCD. For example, the structure function F_2 can be therefore expressed as a convolution of the perturbative part, the *coefficient functions* C_2^a, and the non-perturbative PDFs $(f_a(\xi, \mu_f, \mu))$ for a given parton a:

$$F_2 = \sum_a \int_x^1 C_2^a \left(\frac{x}{\xi}, \frac{Q^2}{\mu^2}, \frac{\mu_f^2}{\mu^2}, \alpha_s(\mu) \right) f_a(\xi, \mu_f^2, \mu^2) d\xi \qquad (2.20)$$

This is referred to as *factorisation* [27]. The evolution of the PDFs with the scale μ is described by the DGLAP-equations[3] [30] given by:

$$\frac{dq_i(x, Q^2)}{d \ln Q^2} = \frac{\alpha_s(Q^2)}{2\pi} \int_x^1 \frac{d\xi}{\xi} \left[q_i(\xi, Q^2) P_{qq} \left(\frac{x}{\xi} \right) + g(\xi, Q^2) P_{qg} \left(\frac{x}{\xi} \right) \right], \qquad (2.21)$$

$$\frac{dg(x, Q^2)}{d \ln Q^2} = \frac{\alpha_s(Q^2)}{2\pi} \int_x^1 \frac{d\xi}{\xi} \left[\sum_i q_i(\xi, Q^2) P_{gq} \left(\frac{x}{\xi} \right) + g(\xi, Q^2) P_{gg} \left(\frac{x}{\xi} \right) \right], \qquad (2.22)$$

where $q_{i(}\xi, Q^2)$ is the PDF for a given quark flavour and $g_i(\xi, Q^2)$ the gluon density function. The DGLAP *splitting functions* $P_{ab} \left(\frac{x}{\xi} \right)$ represent the probability of a parton a to emit a parton b (gluon or quark) carrying a fraction of the momentum of parton a and can be expressed by:

$$P_{qq}(z) = \frac{4}{3} \left[\frac{1 + z^2}{1 - z} \right], \qquad (2.23)$$

$$P_{qg}(z) = \frac{1}{2} \left[z^2 + (1 - z)^2 \right], \qquad (2.24)$$

$$P_{gq}(z) = \frac{4}{3} \left[\frac{1 + (1 - z)^2}{z} \right], \qquad (2.25)$$

$$P_{gg}(z) = 6 \left[\frac{z}{1 - z} + \frac{1 - z}{z} + z(1 - z) \right]. \qquad (2.26)$$

In order to calculate the PDFs at a scale μ, the measurement of the PDFs at a particular scale μ_0, which is used to derive values at the scale μ, is required. As a consequence of the factorisation, the PDFs are process independent. Once they are measured, the PDFs can be exploited further in other measurements. In Fig. 2.5, the PDFs for the valence u and d quark, the gluons g and the sea quarks S determined from a combined next-to-leading order (NLO) QCD analysis of H1 and ZEUS is illustrated.

---

[3]Dokshitzer-Gribov-Lipatov-Altarelli-Parisi
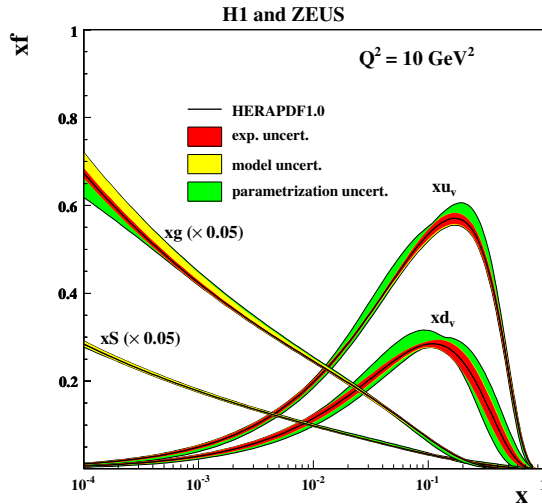
Figure 2.5: Parton density function for the valence quarks u and d, the sea quarks S as well as for the gluons g extracted from NLO QCD analyses on DIS data by the ZEUS and H1 collaboration at $Q^2 = 10$ GeV^2 [31]. Note that the PDFs for the gluons and sea quarks are scaled down by a factor 20.

2.4   Photoproduction and photon structure

The $e^{\pm}p$ DIS cross section in Eq. 2.14 shows a $1/Q^4$ dependence due to the photon propagator, therefore the dominant cross section contribution will originate from the photon exchange with very low virtuality. The average lifetime of the exchanged photons is $\sim E_\gamma/Q^2$, thus, for very low virtuality, this time appears long with respect to the characteristic time of the hard subprocess. At HERA, an electron scattered at very low angles can produce an almost real photon, therefore this kind of ep reaction can be regarded as γp collision.

The total cross section σ_{tot}^{ep} can be factorized as the total photon-proton cross section contribution $\sigma_{tot}^{\gamma p}$ times a flux factor $f_{e\to\gamma}(y)$, which represents the probability to produce a photon with energy $E_\gamma = yE_e$. For $Q^2 \to 0$ GeV^2, the photon longitudinal polarisation vanishes, thus, the photoproduction (PHP) cross section can be written to a good approximation as:

$$\frac{d^2\sigma^{ep}}{dydQ^2} \sim f_{e\to\gamma_T}(y, Q^2)\sigma_{tot}^{\gamma P}(y, Q^2), \tag{2.27}$$

where the transverse photon flux $f_{e\to\gamma_T}(y, Q^2)$ is given by [32]:

$$f_{e\to\gamma_T}(y, Q^2) = \frac{\alpha}{2\pi Q^2}\left[\frac{1+(1-y)^2}{y} - 2\frac{1-y}{y}\frac{Q_{min}^2}{Q^2}\right]. \tag{2.28}$$

Q_{min}^2 represents the lower kinematic limit, which is given by

$$Q_{min}^2 = \frac{m_e^2 y^2}{1-y}. \tag{2.29}$$

In general, this is known as the *equivalent photon approximation* (EPA). If the Q^2 dependence of the γp cross section is neglected, integration over the photon virtuality from Q^2_{min} up to an upper kinematic limit Q^2_{max} delivers

$$f^{WWA}_{e \to \gamma_T} = \frac{\alpha}{2\pi} \left[\frac{1 + (1-y)^2}{y} - 2\frac{1-y}{y} \ln \frac{Q^2_{max}}{Q^2_{min}} - 2\frac{1-y}{y} \left(1 - \frac{Q^2_{max}}{Q^2_{min}} \right) \right], \qquad (2.30)$$

which is known as the Weizsäcker-Williams approximation [33].

Although being classified as colour-neutral particle in the Standard Model, the photon is able to fluctuate into quark-antiquark pairs. The lifetime of these fluctuations increases with decreasing Q^2, hence, the photon can behave as a source of partons. In analogy to the proton structure functions, the factorisation principle also holds for the photon and *photon structure functions* can be determined. The main experimental input to the photon structure functions is derived from $\gamma\gamma$ processes in e^+e^- scattering. In the case of one quasi-real and one virtual photon, the interaction can be treated as deep inelastic $e\gamma$ scattering. The virtual photon then probes the hadronic structure of the quasi-real photon. Structure functions are defined in analogy to ep deep inelastic scattering, relating the $e\gamma$ cross section to the parton content of the photon. Like in the proton case, parton density functions f^γ_i can be extracted from experimental data using parton evolution equations.

Direct and resolved Photoproduction

In direct photoproduction, the photon acts like a point-like object which interacts with the partons in the proton, i.e. it participates <u>directly</u> in the hard subprocess. In contrast to hadron-hadron scattering, all the photon energy is available in the interaction with the parton. Therefore, the final state of the process is expected to have a higher transverse momentum in direct photoproduction than in reactions in which only part of the photon momentum is involved.
The dominant LO direct processes at HERA are QCD Compton scattering and boson-gluon-fusion (BGF), shown in Fig. 2.6. The processes look similar to those fore DIS at $O(\alpha_s)$, but the hard scale can not be set by Q^2 because the photon is quasi-real. Instead, a hard scale can be set by the internal propagator producing e.g. jets with high transverse energy.

In resolved photoproduction processes, the photon behaves like a source of partons with one of them interacting with a parton in the proton. In Fig. 2.7, examples of resolved PHP leading-order processes are illustrated. A gluon from the photon interacts with a gluon from the proton (referred to as gluon-gluon fusion), another possibility is a quark from the photon which interacts with a gluon from the proton (referred to as photon excitation). The resolved PHP final state differs from the direct one since the fragmentation products of the photon are also present in the event.
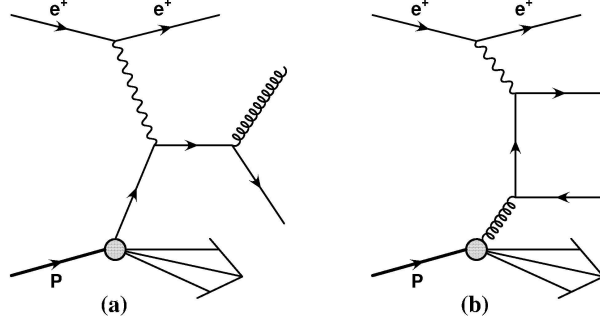
Figure 2.6: Examples for leading order direct photoproduction **a)** QCD Compton scattering, **b)** boson-gluon fusion.
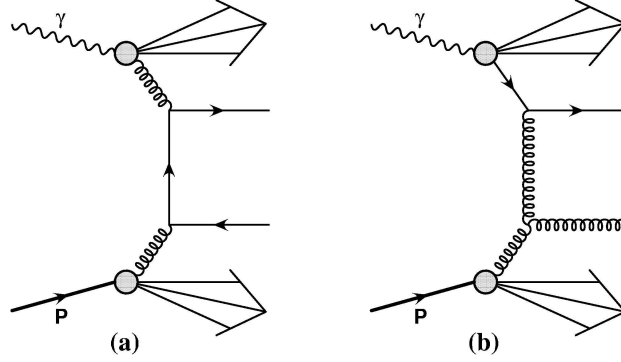
Figure 2.7: Examples for leading order resolved photoproduction.

Photoproduction generalized model

In leading order, the differential hard PHP cross section can be written as the sum of the direct and resolved components:

$$d\sigma_{\gamma P}(p_\gamma, p_P) = d\sigma_{\gamma P}^{dir}(p_\gamma, p_P) + d\sigma_{\gamma P}^{res}(p_\gamma, p_P), \tag{2.31}$$

where the two components are

$$d\sigma_{\gamma P}^{dir}(p_\gamma, p_P) = \sum_i \int dx f_{i/P}(x, \mu_F) d\sigma_\gamma(p_\gamma, x p_P, \alpha_s(\mu_R), \mu_R, \mu_F, \mu_\gamma), \tag{2.32}$$

$$d\sigma_{\gamma P}^{res}(p_\gamma, p_P) = \sum_{ij} \int dx dx_\gamma f_{j/\gamma}(x_\gamma, \mu_\gamma) f_{i/P}(x, \mu_F') d\sigma_{ij}(x_\gamma p_\gamma, x p_P, \alpha_s(\mu_R'), \mu_R', \mu_F', \mu_\gamma). \tag{2.33}$$

$d\sigma_\gamma$ and $d\sigma_{ij}$ represent the elementary 2→2 cross sections of the hard subprocess, $f_{i/P}$ as well as $f_{j/\gamma}$ give the probability to find a parton i and j with momentum fraction x and x_γ of the proton and the photon in the scattering process. The renormalisation scales μ_R and μ_R' of the strong coupling constant α_s can e.g. be set proportional to the transverse momentum $\hat{p}_T$ of

the final-state partons. Since α_s has to be small for reliable predictions, the parton transverse momentum has to be above some minimum value (~ 2 GeV). The factorisation scales μ_F, μ'_F as well as μ_γ separate the hard scatter from the soft long-range interactions in the photon and proton. They are in general set equal to the renormalisation scale.
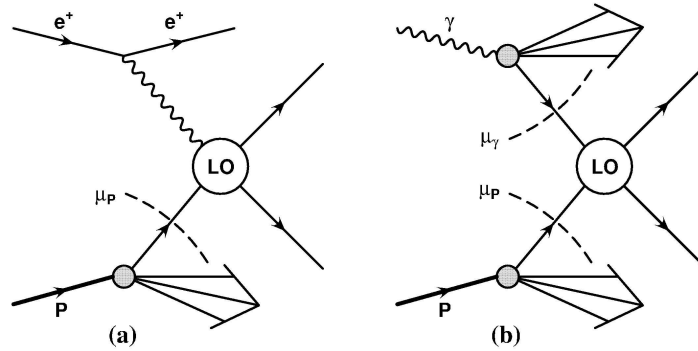
Figure 2.8: LO processes for direct and resolved photoproduction, the dashed lines represent the border between the hard subprocess (perturbative part) and non-perturbative part.

Direct and resolved processes can only be distinguished at LO, depending on the factorisation scale μ_γ of the photon, shown in Fig. 2.8. Beyond LO, there is an interplay between the direct and resolved component. Divergencies arising from collinear emission of quarks from the incoming direct photon are re-absorbed into the parton densities in the photon appearing in the resolved component. As a consequence, only the sum of direct and resolved components has a physical meaning.

2.5 Heavy Quark Production

The production of heavy quarks like the charm or beauty quark can not be easily explained by the quark parton model due to the lower mass of the proton compared to the masses of the heavy quarks ($m_c \approx 1.35$ GeV and $m_b \approx 4.75$ GeV), thus, no heavy quarks on their mass shell can be constituents of the proton. The dominant contribution to heavy quark production in ep collisions at HERA comes from the boson-gluon-fusion (BGF) process (cf. Fig. 2.6b), the lowest order heavy quark production. In such a process, a heavy $q\bar{q}$ pair can be produced if the squared centre-of-mass energy $\hat{s}$ of the photon-gluon system exceeds the squared mass of the $q\bar{q}$-pair:

$$\hat{s} = (\gamma^* + g)^2 = (g + \xi P)^2 > (2m_{q,\text{heavy}})^2. \tag{2.34}$$

The high quark mass provides a hard scale for the process allowing to obtain reliable predictions from pQCD since the value of the running coupling constant α_s is low at a scale corresponding to the heavy flavour masses (cf. Fig. 2.4). Measurements of heavy quark production allow insights into the gluon contribution in the proton due to the dominance of the BGF process. Two kinematic regions exist for heavy quark production: For $Q^2 \leq (2m_{q,\text{heavy}})^2$, boson-gluon-fusion is the lowest-order production process of a $q\bar{q}$ pair of mass $2m_{q,\text{heavy}}$, whereas

for $Q^2 \gg (2m_{q,\text{heavy}})^2$, the gluon splitting into a virtual $q\bar{q}$ pair can be considered to occur inside the proton. The QPM can be therefore applied for the production mechanism.

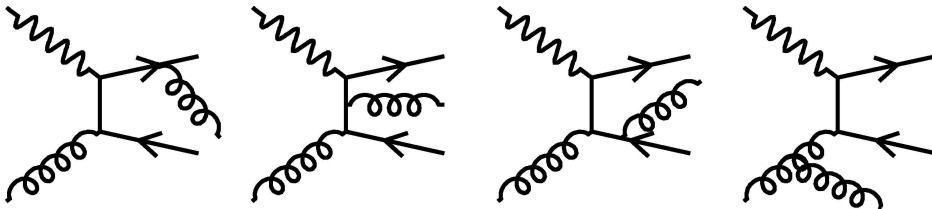The cross section of the production of a heavy $q\bar{q}$-pair in BGF can be calculated as [34]:

$$\sigma_{BGF} = \frac{\pi e_q^2 \alpha_{em} \alpha_s}{\hat{s}} \left[(2 + 2\omega - \omega^2) \ln \frac{1+\chi}{1-\chi} - 2\chi(1+\chi) \right], \tag{2.35}$$

where e_q represents the electromagnetic charge of a heavy quark q produced in the hard process and ω as well as χ are defined by:

$$\omega = \frac{4m_q^2}{\hat{s}}, \quad \chi = \sqrt{1-\omega}. \tag{2.36}$$

From Eq. 2.35 one can see that the production of charm-quark pairs is favored with respect to beauty quark production due to the different charge and mass of both heavy quarks. At the energy of the HERA collider, the beauty quark is mainly produced near the mass threshold. In this kinematic region, the cross section of beauty quark production is roughly about two orders of magnitude lower than the charm cross section.

Next-to-leading order (NLO) calculations of heavy quark production have been performed as well, and the NLO contributions to the cross section were found to be significant. Compared to leading-order calculations, the main difference is the additional radiation of hard gluons and the interference with virtual corrections. Some examples of these processes are illustrated in Fig. 2.9 and Fig. 2.10.

Figure 2.9: Examples of NLO contributions to the beauty cross section from additional gluon radiation.

2.6   Parton Hadronisation

Due to the confinement of the QCD, free quarks do not exist. Thus, directly after the production of quark pairs in the scattering process, colourless hadrons like mesons or baryons have to be formed from these partons. This process can be described as a series of different steps. In a first perturbative step, additional partons are emitted from an initial-state parton or from the heavy quark (referred to as *parton shower*). In a second non-perturbative step, referred to as *hadronisation* or *fragmentation*, phenomenological methods are used to form hadrons from these partons. Both steps are described in the following:
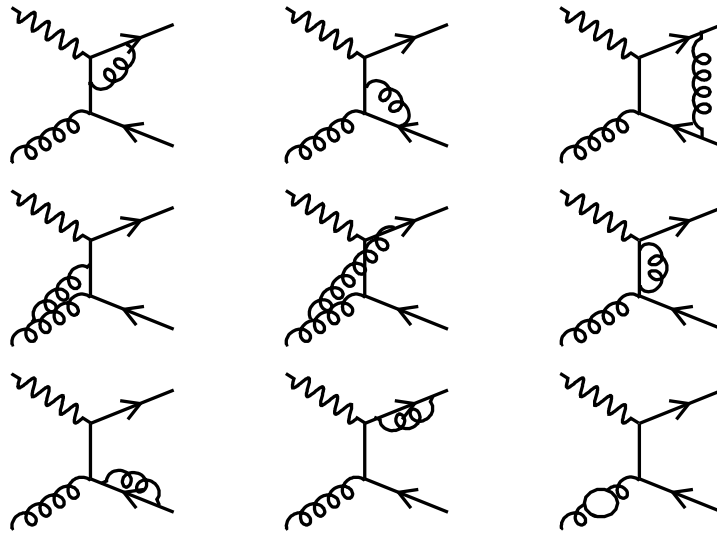
Figure 2.10: Examples of NLO contributions to the beauty cross section from virtual corrections.

Parton Showers

In the parton showering process, partons from the partonic structure of the incoming particles and partons originating from the hard subprocess can emit gluons ($q \rightarrow qg$ etc.) or split into $q\bar{q}$ pairs ($g \rightarrow q\bar{q}$), also referred to as inital- and final-state radiation. The model of parton shower approximates multiple parton emissions by a series of successive parton splittings. The probability that a parton is emitted from a parent parton with a given virtuality is taken from splitting functions [30], which are part of the evolution equations. Initial- and final-state parton showers have to be considered in different ways. Both are started at a scale Q^2_{max}, which defines the transition between the initial- and final-state radiation and the hard subprocess. The initial-state parton shower starts from a parton coming from the proton which continues to emit space-like parton showers until it reaches the hard subprocess. The simulation of this process is carried out in the so-called *backward evolution scheme* starting from the scale Q^2_{max} and then tracing the showers backward in time in a sequence of decreasing space-like virtualities Q^2 down until a minimal cut-off value of $Q^2_0 \approx 1$ GeV^2 is reached. The final-state radiation splits the final-state partons into time-like showers starting at Q^2_{max}. The evolution continues until the cut-off value Q^2_0.

Hadronisation

The transformation of final-state partons into hadrons can not be calculated by means of perturbative methods, therefore phenomenological models have to be used instead. The model applied in the Monte-Carlo generators used for this analysis is the *string fragmentation* [35], as illustrated in Fig. 2.11. There, the $q\bar{q}$ pairs are connected by colour flux tubes, referred to as *strings*. The string has a uniform energy per unit length, corresponding to a linear quark confining potential. Therefore, the potential rises with increasing distance between the quarks.
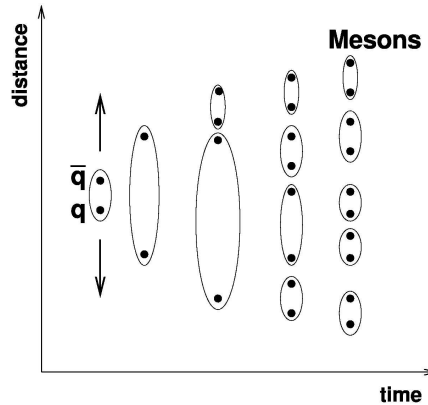
Figure 2.11: Illustration of the string fragmentation model.

If the potential energy is sufficient to produce a new $q\bar{q}$ pair, the string is broken up into two. This process continues until the invariant mass of the string pieces exceeds the on-shell mass of a hadron. Heavy hadrons from a produced string fragment are formed by means of *fragmentation functions*. These describe the probability that a hadron h is produced from a parton q with the longitudinal momentum fraction z of the parton. A commonly used fragmentation function for heavy-flavour production is the *Peterson fragmentation function* [36]:

$$D_q^h(z) = \frac{1}{z \left[1 - \frac{1}{z} - \frac{\epsilon_q}{1-z} \right]^2}, \qquad (2.37)$$

where the free Peterson parameter ϵ_q is expected to scale with the quark mass ($\epsilon_q \sim 1/m_q$). Fig. 2.12 shows the shape of the Peterson fragmentation function in an arbitary scale for typical values of ϵ_q for charm ($\epsilon_c \approx 0.035$) and beauty quarks ($\epsilon_b \approx 0.0035$) [37]. The fragmentation of beauty quarks to beauty hadrons shows a harder spectrum than in the case of charm due to the larger beauty mass.
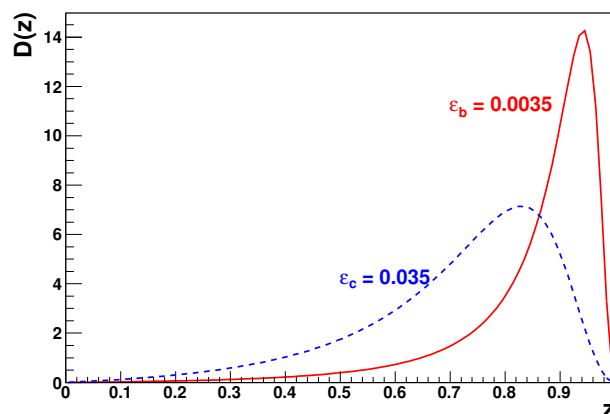
Figure 2.12: Comparison of the shape of the Peterson fragmentation function for charm and beauty.

2.7 Beauty hadrons and decays

Since beauty quarks produced in the hard interaction fragment to beauty hadrons, the properties of these hadrons are outlined in this section. This analysis is restricted in the first stage to the semileptonic decay of open beauty hadrons[4], decaying with a lifetime of $\sim 10^{-12}$s. This lifetime is rather long for a decay via the weak force given the high quark mass and a factor of 3 higher than the lifetimes of charm hadrons. The following Tab. 2.1 lists the properties of the most frequently produced beauty (b) and charm (c)hadrons at HERA.

Hadron	Quark content	Mass [MeV]	Decay length $c\tau[\mu m]$
B^+/B^-	$ub/\bar{u}b$	5279.17±0.29	492.0
$B^0/\bar{B}^0$	$d\bar{b}/\bar{d}b$	5279.50±0.30	455.4
$B_s^0/\bar{B}_s^0$	$s\bar{b}/\bar{s}b$	5366.30±0.60	441.0
$\Lambda_b^0/\bar{\Lambda}_b^0$	$udb/\bar{u}d\bar{b}$	5620.20±1.60	427.0
D^+/D^-	$cd/\bar{c}d$	1869.62±0.20	311.8
$D^0/\bar{D}^0$	$c\bar{u}/\bar{c}u$	1864.84±0.17	122.9
$D_s^+/\bar{D}_s^-$	$c\bar{s}/\bar{c}s$	1968.49±0.34	149.9
Λ_c^+/Λ_c^-	$udc/\bar{u}d\bar{c}$	2286.46±0.14	59.9

Table 2.1: Beauty and charm hadrons [2].

In order to understand the longer lifetime of the beauty hadrons, one introduces the CKM (*Cabibbo-Kobayashi-Maskawa*) matrix:

$$V_{CKM} = \begin{pmatrix} V_{ud} & V_{us} & V_{ub} \\ V_{cd} & V_{cs} & V_{cb} \\ V_{td} & V_{ts} & V_{tb} \end{pmatrix} = \begin{pmatrix} 0.97419 & 0.2257 & 0.00359 \\ 0.2256 & 0.97334 & 0.0415 \\ 0.00874 & 0.0407 & 0.999133 \end{pmatrix} \qquad (2.38)$$

It can be observed that decays within the same generation are favoured over decays between generations. The transition probability $b \to c$, given by the matrix element V_{cb}, is much smaller than the matrix element V_{cs} of the process $c \to s$, resulting in a longer life time for B-hadrons. Therefore, any lifetime-related quantities (e.g. impact parameters or decay length measurements) are useful for separating b and c hadrons.

Semileptonic beauty quark decay

Due to their short lifetime, B-hadrons can not be detected directly but have to be identified by their decay products. The simplest model to describe hadron decays is given by the spectator model, as shown in Fig. 2.13. The beauty quark decays weakly into a charm quark and a W-boson, which subsequently decays into a muon and a muon-neutrino. The high mass of the beauty quark leads to a suppression of higher order QCD effects. Beauty quarks decay predominantly via an intermediate charm quark rather than directly to an up quark, as the transition probability $b \to c$, given by $\Gamma \sim |V_{cb}|^2$, is two order of magnitude larger than
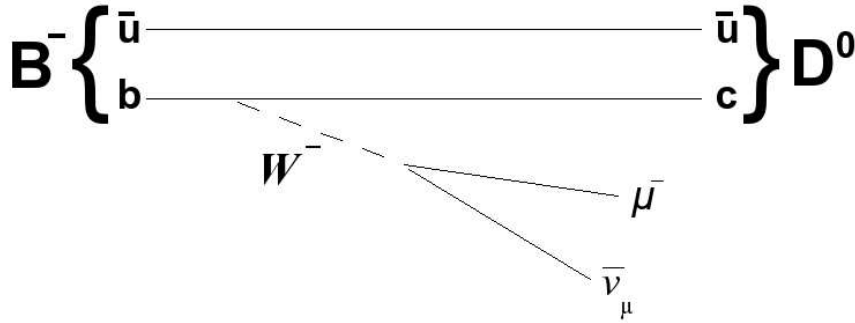
Figure 2.13: Hadron decay $B^- \to \mu^- \bar{\nu}_\mu D^0$
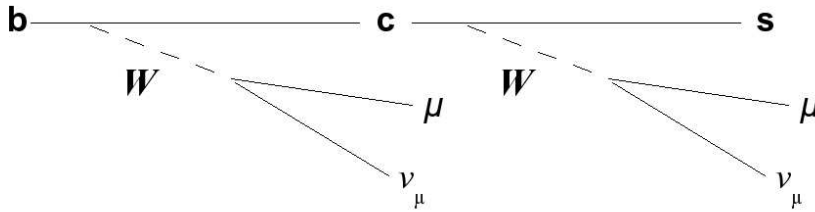
Figure 2.14: Cascade decay of a beauty quark.

the probability for the process $b \to u$, which is given by $\Gamma \sim |V_{ub}|^2$. The emitted W-boson subsequently decays to a muon and a muon-neutrino with a probability of

$$BR(W \to \mu\nu_\mu) = 10.57 \pm 0.15\%. \tag{2.39}$$

In addition to the direct muon production, *cascade decays* provide a source of muons from beauty quark decay, as shown in Fig. 2.14. The requirement of two muons in the final state provides a clearer experimental signature, since only a few processes can be a source of muon pairs.

Sources of muon pairs in ep collisions

Muons are considered as beauty signal muons if they originate from the direct decay of a beauty quark or from a cascade decay, i.e. the decay from a charm quark originated from the decay of a beauty quark. Signal dimuons can be produced in four ways as depicted in Fig. 2.15:

1. Both beauty quarks decay directly into muons, thus one obtains unlike-sign dimuons.

2. Both charm quarks from beauty quarks decay into muons, delivering also unlike-sign dimuons.

---

[4]The term *open* means that particles with the beauty flavour quantum number $B \neq 0$ are produced.

3. One beauty quark decays directly into a muon while the second beauty quarks decays indirectly into a muon via a charm quark (cascade decay). This yields like-sign dimuons.

4. The cascade decay of one beauty quark into a muon and the beauty decay charm quark decays also into a muon, yielding unlike-sign dimuons.
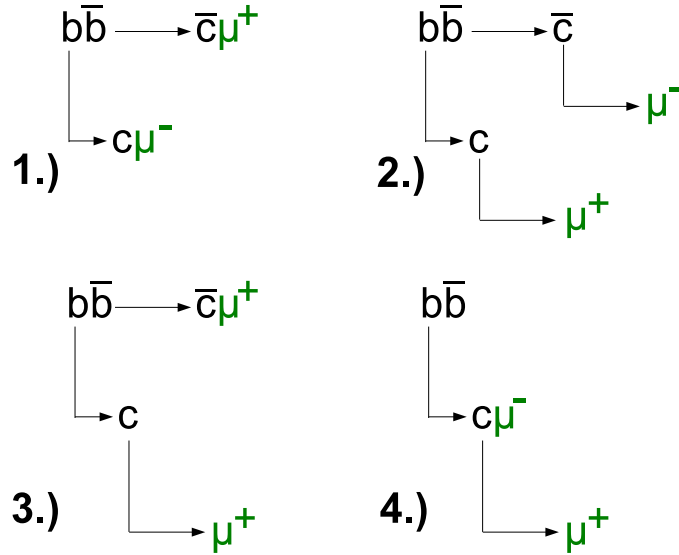
Figure 2.15: Sources of muons from beauty decay: **1.)** the direct decay of both beauty quarks and **2.)** the indirect decay of both charm quarks from beauty quarks into muons produce unlike-sign muon pairs; **3.)** the direct decay of one beauty quark into a muon and the decay a charm quark from the second beauty quark yields like-sign muon pairs. The cascade decay of one beauty quark into a muon and of the beauty-decay charm quark into a muon as well produce unlike-sign muon pairs (shown in **4.)**).

In general, all processes with prompt muons from B-hadron decays are considered as signal, which includes e.g. a small fraction of muons originating from indirect b or cascade c decays ($b \rightarrow c \rightarrow \mu$) and decays via intermediate tau leptons ($b \rightarrow \tau \rightarrow \mu$). The branching ratios of direct and cascade muon production are given below (taken from [2]):

$$
\begin{aligned}
BR(b \rightarrow \mu) &= (10.95^{+0.29}_{-0.25})\% \\
BR(b \rightarrow c \rightarrow \mu) &= (8.02 \pm 0.19)\% \\
BR(b \rightarrow \bar{c} \rightarrow \mu) &= (1.6^{+0.4}_{-0.5})\% \\
BR(b \rightarrow \tau \rightarrow \mu) &= (0.43 \pm 0.05)\%
\end{aligned}
$$

The weak force is able to change the type of neutral beauty mesons. This is referred to as $B^0 - \bar{B}^0$ oscillation, where the b quark oscillates into its antiparticle, as illustrated in Fig. 2.16. This process also changes the charge of the final state muons, e.g. muons from process 1.) can lead to like-sign dimuons if one of both B mesons has oscillated.
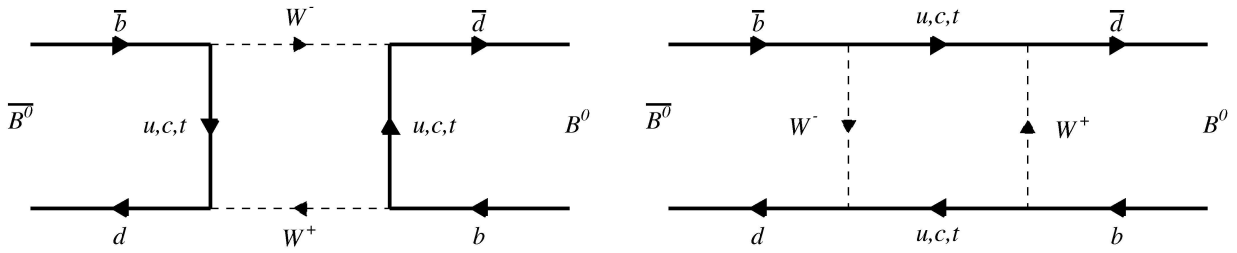
Figure 2.16: Example diagram for $B_d^0 \bar{B}_d^0$ mixing. Mediated by the weak CKM flavour transition, the quarks change their flavour sign.

The time integrated probability of χ of the oscillation process for a mixture of all B mesons is measured to $\chi = 0.1284 \pm 0.0069$ [2].

The decays from charm quark events can produce only unlike sign prompt dimuon events. Cascade-like decays of charmed mesons yielding like-sign muon pairs contain only non-prompt muons and are therefore not counted as signal muons.

Semileptonic decays of heavy flavour quarks have the feature that the muons are in general accompanied by hadrons. These muons are referred to as *non-isolated*, while muons from quarkonia states (bound $q\bar{q}$ states of equal type quarks) are *isolated*.
The reconstruction of the beauty or charm quark mass is not possible because the muon neutrinos from the weak decay can not be observed. Still the beauty mass sets an upper limit on the invariant mass for muons from the same beauty quark. The dimuon invariant mass from the process 1. to 3. is not limited by the beauty quark mass. The mass of the charm quark does not set an upper limit on the invariant dimuon mass as well, since muons from cascade-like charm decays are not considered as signal.

Quarkonium decays

Muonic decays of quarkonia are source of unlike sign muon pairs (illustrated in Fig: 2.17). The invariant mass of the muon pair represents the mass of the original bound state. Therefore, these dimuons can be identified by mass peaks in the invariant mass distributions.
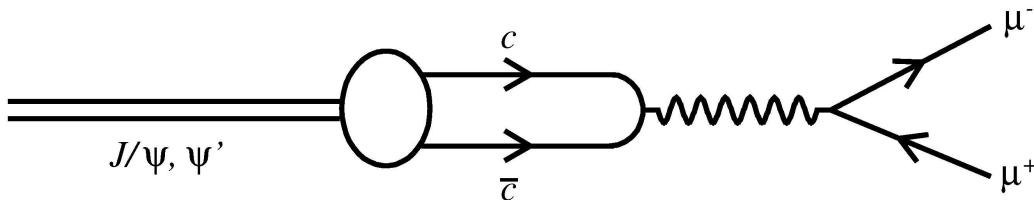
Figure 2.17: Diagram for the charmonium decay into a muon pair (created with [38]). Υ mesons decay similarly.

Bound states of two beauty quarks are referred to as Υ mesons. There exist several states

of the ground state $\Upsilon(1S)$ like $\Upsilon(2S)$, $\Upsilon(3S)$ etc. Their masses and muon branching ratios are given by [2]:

$$
\begin{aligned}
m_{\Upsilon(1S)} &= 9460.30 \pm 0.26 \text{ MeV} & BR(\Upsilon(1S) \to \mu^+\mu^-) &= 2.48 \pm 0.05\% \\
m_{\Upsilon(2S)} &= 10.02326 \pm 0.00031 \text{ MeV} & BR(\Upsilon(2S) \to \mu^+\mu^-) &= 1.93 \pm 0.17\% \\
m_{\Upsilon(3S)} &= 10.3552 \pm 0.0005 \text{ MeV} & BR(\Upsilon(3S) \to \mu^+\mu^-) &= 2.18 \pm 0.21\%
\end{aligned}
$$

Muon pairs produced by the decay of the Υ mesons are unlike-sign and in general not accompanied by hadronic activity, i.e. they are isolated. Therefore, the three states $\Upsilon(1S)$, $\Upsilon(2S)$ $\Upsilon(3S)$ are considered as background in this analysis.

Like $b\bar{b}$ states, corresponding $c\bar{c}$ states exist, referred to as J/ψ and ψ'. Besides the direct $c\bar{c} \to J/\psi X$ production, $b\bar{b}$ pairs can also decay into J/ψs. Muons from both $c\bar{c}$ states are considered as background if they are the result of a direct process, otherwise they are part of the signal in case of beauty-induced charmonia. These two cases can be distinguished by means of muon isolation requirement (muons from beauty-induced charmonium states are non-isolated). The charmonium masses as well as decay ratios of J/ψ and ψ' into muons are:

$$
\begin{aligned}
m_{J/\psi} &= 3096.919 \pm 0.011 \text{ MeV} & BR(J/\psi \to \mu^+\mu^-) &= 5.93 \pm 0.06\% \\
m_{\psi'} &= 3686.093 \pm 0.034 \text{ MeV} & BR(\psi' \to \mu^+\mu^-) &= 0.76 \pm 0.08\%
\end{aligned}
$$

Finally, muons can also be the rare decay product of light flavour quarkonia states ($\phi, \rho^0, \omega, \eta$ and η'). The masses of all these mesons are around or below 1 GeV. In order to remove this background, one sets a lower limit on the dimuon mass.

Bethe-Heitler and Drell-Yan events

A source of isolated muon pairs with no restriction on the dimuon invariant mass is given by muon pair production in Bethe-Heitler and Drell-Yan events, illustrated in Fig. 2.18. The
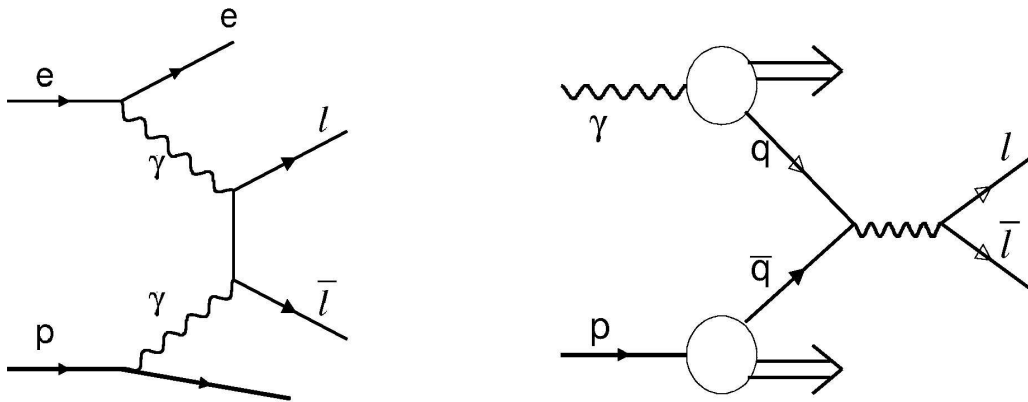
Figure 2.18: Diagrams for Bethe-Heitler (left) and Drell-Yan (right) muon pair production (taken from [4]).

muon Drell-Yan process is the electroweak production of a muon pair in the s-channel, where the boson originates from the anihilation of a $q\bar{q}$ pair. This process is strongly suppressed due to the necessity of a resolved photon in the initial state as a source for quarks. The Bethe-Heitler process, a boson-gluon-fusion in the t-channel, dominates the dimuon production at HERA. This background contribution can be separated by means of a muon isolation requirement.
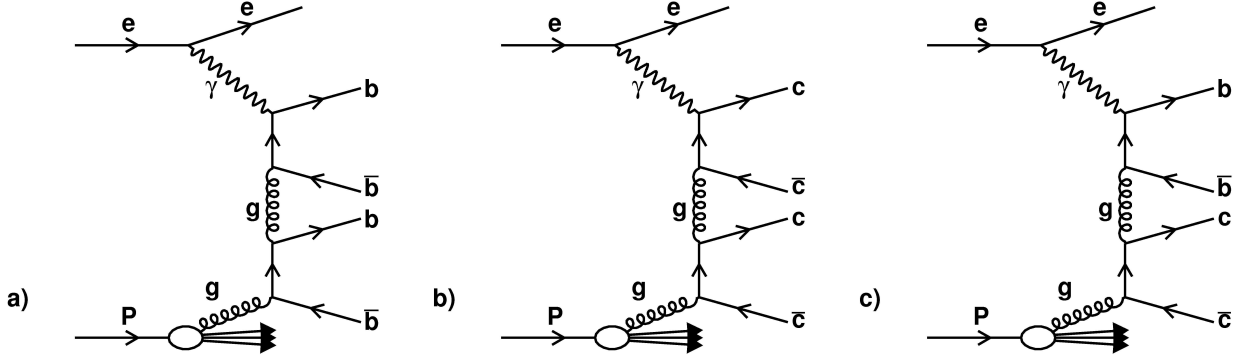
Multi-heavy-flavour events

Besides open heavy flavour events with one $q\bar{q}$ pair, also processes exist where 4 beauty quarks ($b\bar{b}b\bar{b}$), four charm quarks ($c\bar{c}c\bar{c}$) or one beauty quark pair _and_ one charm quark pair ($b\bar{b}c\bar{c}$) can be produced in the hard subprocess, as shown for ep collisions in Fig. 2.19.

Figure 2.19: Feynman diagrams for the production of **a)** four beauty quarks, **b)** four charm quarks and **c)** one $b\bar{b}$ and $c\bar{c}$ pair (created with [38]).

The production of four charm quarks has been observed in e^+e^- collisions at the BELLE and BABAR experiments [39, 40] with the surprising result that this process accounts for approximately 60% of continuum J/ψ production. The measured cross sections are:

$$\begin{aligned}
\sigma(e^+e^- \rightarrow J/\psi + \eta_c)_{BELLE} &= (25.6 \pm 2.8 \pm 3.4) \text{ fb} \\
\sigma(e^+e^- \rightarrow J/\psi + \eta_c)_{BABAR} &= (17.6 \pm 2.8 \pm 2.1) \text{ fb} \\
\sigma(e^+e^- \rightarrow J/\psi + c\bar{c})_{BELLE} &= (0.87^{+0.21}_{-0.19} \pm 0.17) \text{ pb} \\
\sigma(e^+e^- \rightarrow J/\psi + X)_{BELLE} &= (1.47 \pm 0.10 \pm 0.11) \text{ pb} \\
\sigma(e^+e^- \rightarrow J/\psi + X)_{BABAR} &= (2.52 \pm 0.21 \pm 0.21) \text{ pb}
\end{aligned}$$

The four beauty quark- as well as $b\bar{b}c\bar{c}$ production has not been observed up to now, but cross sections have been predicted e.g. for the double bottomonium process in e^+e^- collisions at a center-of-mass energy of $\sqrt{s} = (25\text{-}30)$ GeV [41]:

$$\sigma(e^+e^- \rightarrow \Upsilon(1S) + \eta_b) = (0.06 - 0.16) \text{ fb},$$

and for different final state heavy quarkonia processes in $p\bar{p}$ as well as pp collisions [42]:

Final State	σ_{Tevatron} [nb]	σ_{LHC} [nb]
$\eta_c\eta_c$	$3.32 \cdot 10^{-3}$	2.73
$J/\psi J/\psi$	$5.63 \cdot 10^{-2}$	2.83
$\eta_b\eta_b$	$1.87 \cdot 10^{-5}$	$7.36 \cdot 10^{-3}$
$\Upsilon\Upsilon$	$1.23 \cdot 10^{-4}$	$1.51 \cdot 10^{-2}$
$B_c\bar{B}_c$	$3.86 \cdot 10^{-3}$	$2.72 \cdot 10^{-1}$

Table 2.2: The predicted cross section of pair production of $J/\psi, \Upsilon$ and B_c at the Tevatron and LHC [42].

For *ep* collisions, the production of these so-called multi-heavy-flavour events has not been observed but first cross-section calculations have been performed by use of the MadGraph program [43, 181, 182]. The cross sections for the three processes were determined to be:

$$\sigma(e^\pm p \rightarrow b\bar{b}b\bar{b}) = 1.0999 \text{ pb},$$
$$\sigma(e^\pm p \rightarrow c\bar{c}c\bar{c}) = 511.75 \text{ pb},$$
$$\sigma(e^\pm p \rightarrow b\bar{b}c\bar{c}) = 29.113 \text{ pb}.$$

Muons of these multi-heavy-flavour processes are expected to be non-isolated and can be both, like- and unlike-sign.
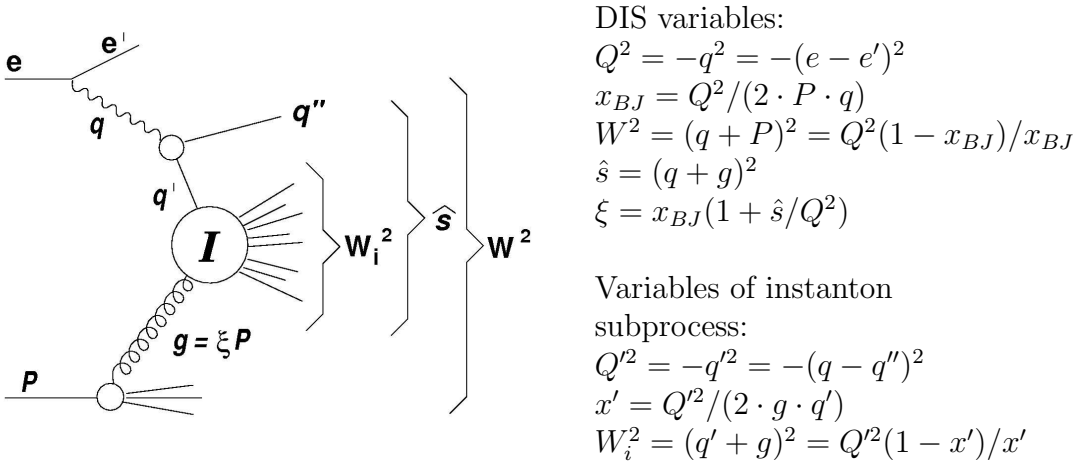
Instantons

An additional source for muon pairs is provided by instanton-induced events, or instantons [5,6] for short. Here the kinematics and features are briefly described. More information about the theoretical background of instantons can be found in Appendix E.

Instanton processes in *ep* interactions occur predominantly in boson-gluon fusion as depicted in Fig. 2.20. A photon emitted by the incoming electron fluctuates into a $q\bar{q}$ pair in the instanton background. One of these quarks (with four-momentum q') fuses with a gluon out of the proton, while the other quarks forms a so-called *current jet*. The instanton subprocess is characterised by the virtuality Q'^2 of the incoming quark and x', which is defined in analogy to the DIS variable x.

In the hard subprocess, exactly one $q\bar{q}$ pair of each kinematically accessible flavour n_f is produced as illustrated in Fig. 2.21. This feature is often referred to as *flavour democracy*. The $2n_f-1$ (anti-)quarks give rise to a higher amount of final-state particles compared to normal QCD processes. Particles from the instanton process are expected to be distributed isotropically in their center-of-mass frame. The most important feature of instanton events is the violation of chirality, i.e. all quarks produced in the hard subprocess have the same chirality. The cross section of instanton processes is exponentially suppressed by $\sigma_{\text{Instanton}} \sim \exp\left(-\frac{4\pi}{\alpha_s}\right)$, however, it is still expected to be sizable at HERA in deep inelastic scattering and photoproduction [178, 205, 206]. The cross section of heavy-flavour instantons is suppressed additionally

DIS variables:
$$Q^2 = -q^2 = -(e - e')^2$$
$$x_{BJ} = Q^2/(2 \cdot P \cdot q)$$
$$W^2 = (q + P)^2 = Q^2(1 - x_{BJ})/x_{BJ}$$
$$\hat{s} = (q + g)^2$$
$$\xi = x_{BJ}(1 + \hat{s}/Q^2)$$

Variables of instanton
subprocess:
$$Q'^2 = -q'^2 = -(q - q'')^2$$
$$x' = Q'^2/(2 \cdot g \cdot q')$$
$$W_i^2 = (q' + g)^2 = Q'^2(1 - x')/x'$$

Figure 2.20: Kinematics of instanton-induced processes at HERA.
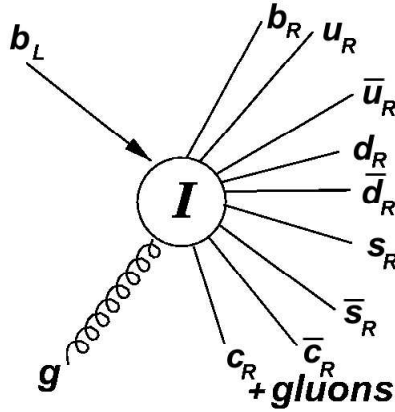
Figure 2.21: Production of a QCD instanton-induced event. A left-handed beauty quark and a gluon enter the instanton-subprocess, producing one right-handed $q\bar{q}$ pair of each kinematic allowed flavour.

by an unknown factor, which depends on the masses of the heavy quarks [207] and has to be determined empirically. The cross section becomes sizeable, if the suppression factor is not greater about 2 orders of magnitude, as it was found out in [15].

Muons from heavy-flavour instantons should be non-isolated due to the expected higher particle multiplicity (compared to beauty and charm events). Furthermore, non-isolated muon pairs from instantons can be both, like- and unlike-sign, since the beauty quarks in Fig. 2.21 can decay in the same way as in Fig. 2.15. A separation between beauty- and heavy-flavour instanton events is possible by means of so-called *event shape variables*, explained in Sec. 5.12.1.

2.8   Monte-Carlo simulation

Simulation programs based on Monte-Carlo (MC) methods serve as an essential tool for understanding the complexity of high energy physics processes and particle detectors. MC programs

are used to check the detector performance and the response of different detector components. Furthermore, MC generators are used to determine the efficiencies and acceptances necessary for unfolding cross sections. In this analysis, the MC generators PYTHIA [44] and RAPGAP [45], which are also referred to as leading-order plus parton shower (LO+PS) event generators, were used to describe signal distributions. The simulation of a particle collision event is done in two main steps. In the first step, the *ep*-collision process is simulated using an event-generator which provides a complete list of the four-momenta of the final-state particles. In the second step, these events are passed through a simulation of the detector. In the following, the general structure of an event generator and the detector simulation are described.

2.8.1 Event generation

ALL LO+PS Monte-Carlo generators use the factorisation theorem. Thus, an *ep*-collision process can be separated into several stages as illustrated for a BGF event in Fig. 2.22. The different stages are:
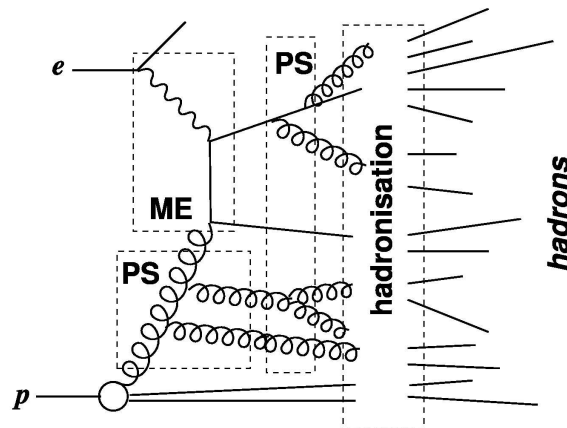
Figure 2.22: Structure of an *ep* event generator for a BGF process. The matrix element (ME) of the hard subprocess is calculated at leading order. Parton showers (PS) are applied for initial- and final-state radiation and finally the outgoing partons form hadrons in the hadronisation process.

- **Hard subprocess:** This is the main part of the event simulation. It describes the interaction between incoming beam particles. In *ep* collisions, it is the interaction between a parton extracted from the proton and the photon emitted by the electron. The flavour and momentum of the incoming parton are chosen according to chosen PDFs and are used as an input to the calculations. This part of the process can be calculated in fixed order perturbative expansion since it involves a hard scale. The hard momentum transfer μ sets the boundary condition for initial- and final-state parton showers.

- **Initial- and final-state radiation:** The parton showering (cf. Sec. 2.6), not included in leading-order calculations, uses QCD based models for describing higher order corrections

to the event topology. Processes, which contain charged and coloured objets are influenced by the emission of gluons and photons. Radiation of photons or gluons as well as gluon splitting into $q\bar{q}$ pairs are included before and after the hard subprocess. This refers to as *initial-* and *final-state radiation* .

- **Hadronisation:** In this process, colourless hadrons are formed out of the coloured partons. This non-perturbative part is described by phenomenological models (cf. Sec. 2.6).

- **Particle decay:** Here, unstable hadrons formed during the hadronisation process decay according to their branching ratios.

2.8.2   Next-to-leading order predictions

In heavy flavour production up to NLO, two main schemes are considered. In the fixed flavour number scheme (FFNS), also referred to as *massive scheme*, the photon and proton have a hadronic substructure with only the three light quarks u, d and s as active flavours. Heavy quarks are produced only in the hard subprocess and have masses. In the *massless scheme*, the heavy quarks are considered as active flavours in the photon and proton and are massless. Choosing the optimal scheme for NLO QCD predictions depends on the dominant scale. If the virtuality Q^2 and the squared transverse momentum $p_T^{b\,2}$ are of the order of m_b^2, threshold effects due to the beauty quark mass have to be taken into account and the massive scheme should be used. In case of Q^2 of $p_T^{b\,2}$ are much larger than m_b^2, the massless scheme could be considered.

For NLO QCD calculations in this analysis, the FMNR program [46] incorporated with the FMNR⊗PYTHIA interface [47] was used. It gives predictions for cross sections in photoproduction events relying on the WWA approximation and is based on the massive approach. The parameters used by the FMNR program are:

- Beauty quark mass: $m_b = 4.75$ GeV.

- Proton PDFs: CTEQ5M.

- Photon PDFs: GRV-G HO.

- Q^2 range: $Q^2 < 1$ GeV^2.

- Beauty production renormalisation and factorisation scale: $\mu_r = \mu_f = \sqrt{p_T^{b\,2} + m_b^2}$.

Final state muons from the beauty quarks are produced in the following way: First, the beauty quarks fragment to B hadrons, which then decay into muons using the muon momentum decay spectra applied in PYTHIA. The muons are emitted isotropically in the rest frame of the B hadron.

Chapter 3

Beauty quark production

The measurement of $b\bar{b}$ production is a longstanding and important topic in the framework of the Standard Model. Since the discovery in the year 1977 of the Υ meson [48], a beauty quark pair bound state, the measurement of beauty quark production plays an important role for particle physics and theory. In this chapter, a selection of beauty measurements from different collider experiments is presented.

3.1 Beauty quark production at the $Sp\bar{p}S$

The UA1 collaboration was the first measuring beauty-quark cross sections in single muon and dimuon final states in $p\bar{p}$ collisions [49, 50]. Beauty quarks were identified at the $Sp\bar{p}S$ collider at CERN at a centre-of-mass energy of 630 GeV by means of the semileptonic decay into muons, which were required to have a tranverse momentum of $p_T^\mu > 6$ GeV in the single muon and $p_T^\mu > 3$ GeV in the dimuon case. Furthermore, the dimuon system was restricted to have an invariant mass $m^{\mu\mu} < 35$ GeV. The measured inclusive single beauty-quark cross-section in an η range[1] of $|\eta| < 1.5$ is compared to next-to-leading order QCD predictions [51] and found to be in good agreement (Fig. 3.1). The extracted cross sections using single muons from beauty quark events as well as dimuon events from subsequent J/ψ decays [52] are also well described by the NLO calculation.

The importance of higher order contributions to the cross sections is confirmed by measurements of $b\bar{b}$ correlations in $\Delta R_{b\bar{b}} = \sqrt{\Delta\eta_{b\bar{b}}^2 + \Delta\phi_{b\bar{b}}^2}$ and $\Delta\phi_{b\bar{b}}$ in two different momentum ranges $p_{T_b}^{max} > 6$ respective 11 GeV of the beauty quark, as illustrated in Fig. 3.2. The leading order contribution to produce back-to-back configurations yields a peak at $\Delta\phi_{b\bar{b}} = 180°$ whereas higher order contributions also produce configurations with lower $\Delta\phi$. The good description of the measurement by the NLO QCD calculation especially at lower values of $\Delta\phi$ confirms the importance of the higher order contributions in the QCD calculation [51, 53].

---

[1]η stands for the pseudorapidity and is defined as $\eta = -\ln(\tan\frac{\theta}{2})$
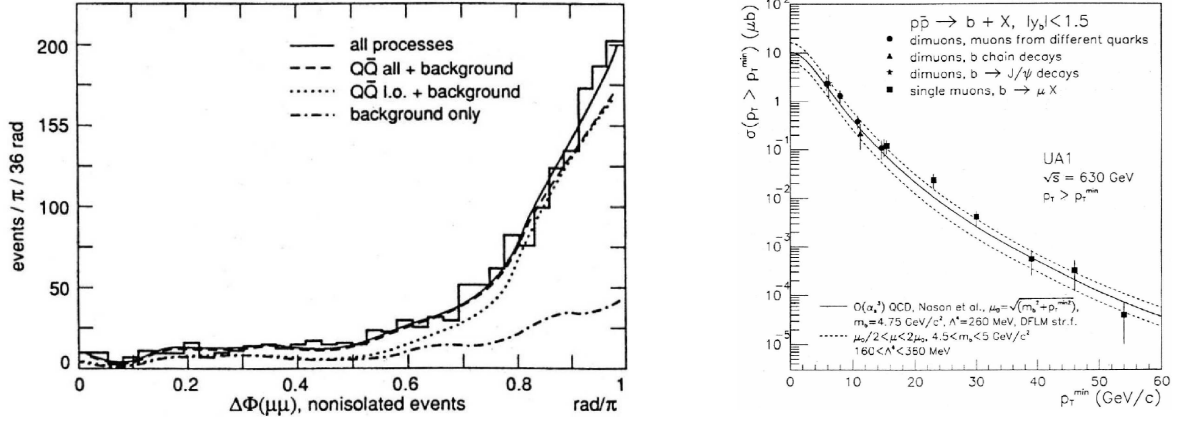
Figure 3.1: Left: Dimuon azimuthal distance for non-isolated dimuons with $p_T^\mu > 3$ GeV and $m^{\mu\mu} > 4$ GeV as part of the overall mass and angle fit, measured at UA1 [50]. **Right:** Inclusive single beauty quark cross section for $|\eta| < 1.5$ and $p_T > p_T^{min}$ from UA1. Presented are the cross section measurements extracted from single muon and dimuon events originating from different beauty quarks and from beauty chain decays as well as measurements extracted from single muon events originating from J/ψ from beauty quarks and the comparision to a next-to-leading order calculation [51].
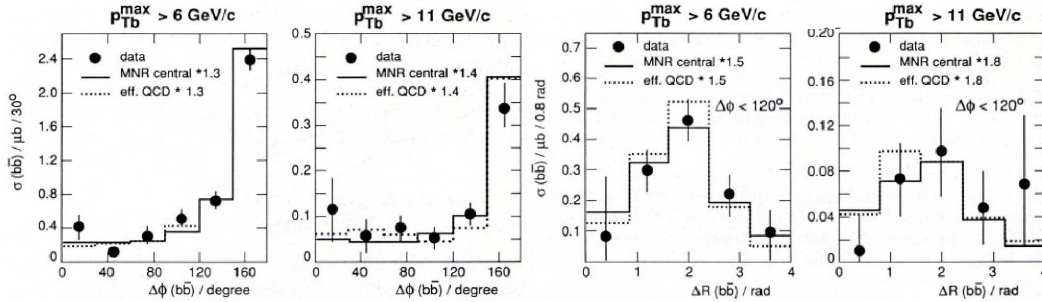
Figure 3.2: Beauty quark correlations from dimuon events in $\Delta R^{b\bar{b}}$ and $\Delta\phi^{b\bar{b}}$ in two different p_T ranges of the beauty quarks compared to NLO calculations [53] (picture taken from [50]).

3.2 Beauty quark production at Tevatron

Studying heavy flavour production is a very active research topic for the CDF and D∅ experiments at the Tevatron $p\bar{p}$ collider at Fermilab. Both the CDF and the D∅ group measured the cross section for the process $pp \to \bar{b} + X$ using Run I data (see Tab. 3.1) and obtained results above the NLO QCD predictions [54–56].

Since then new data from Run II have become available and many theoretical developments have been introduced (full NLO calculations, resummation of $\log(p_T/m_b)$ terms, substantial

Period	Time	Centre-of-mass Energy
Run Ia	1992-1993	$\sqrt{s} = 1.8$ TeV
Run Ib	1993-1995	$\sqrt{s} = 1.8$ TeV
Run II	since 2001	$\sqrt{s} = 1.96$ TeV

Table 3.1: Tevatron running periods.

changes in the fragmentation functions and improved PDFs). Comparisons of this new theory (FONLL [57]) with the RunII data at CDF [58] delivers a good agreement as shown in Fig. 3.3. The same dataset was also compared to the MC@NLO[2] [59] predictions, where also a good agreement was observed.
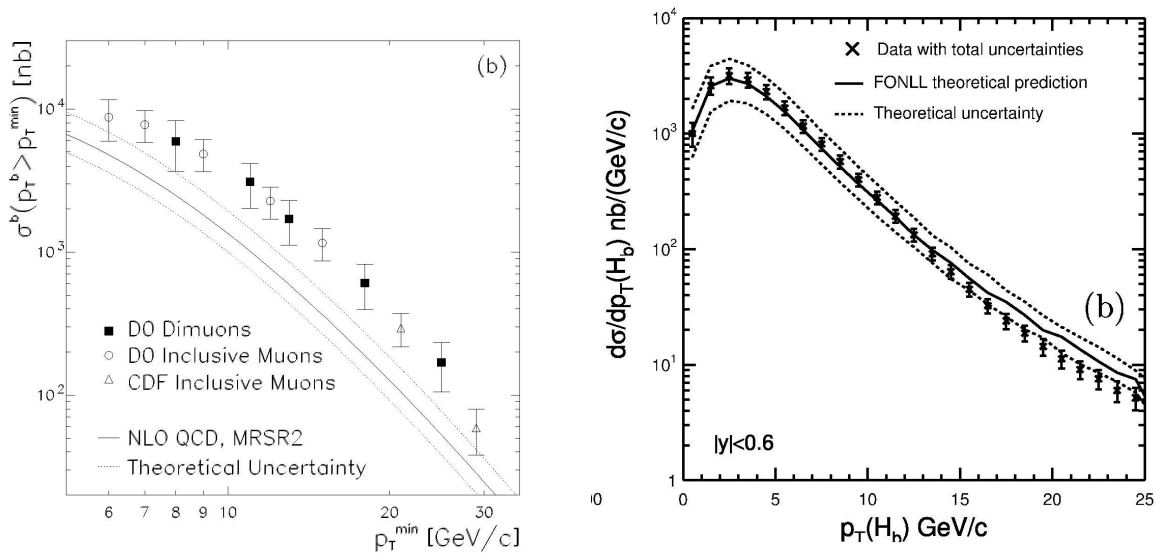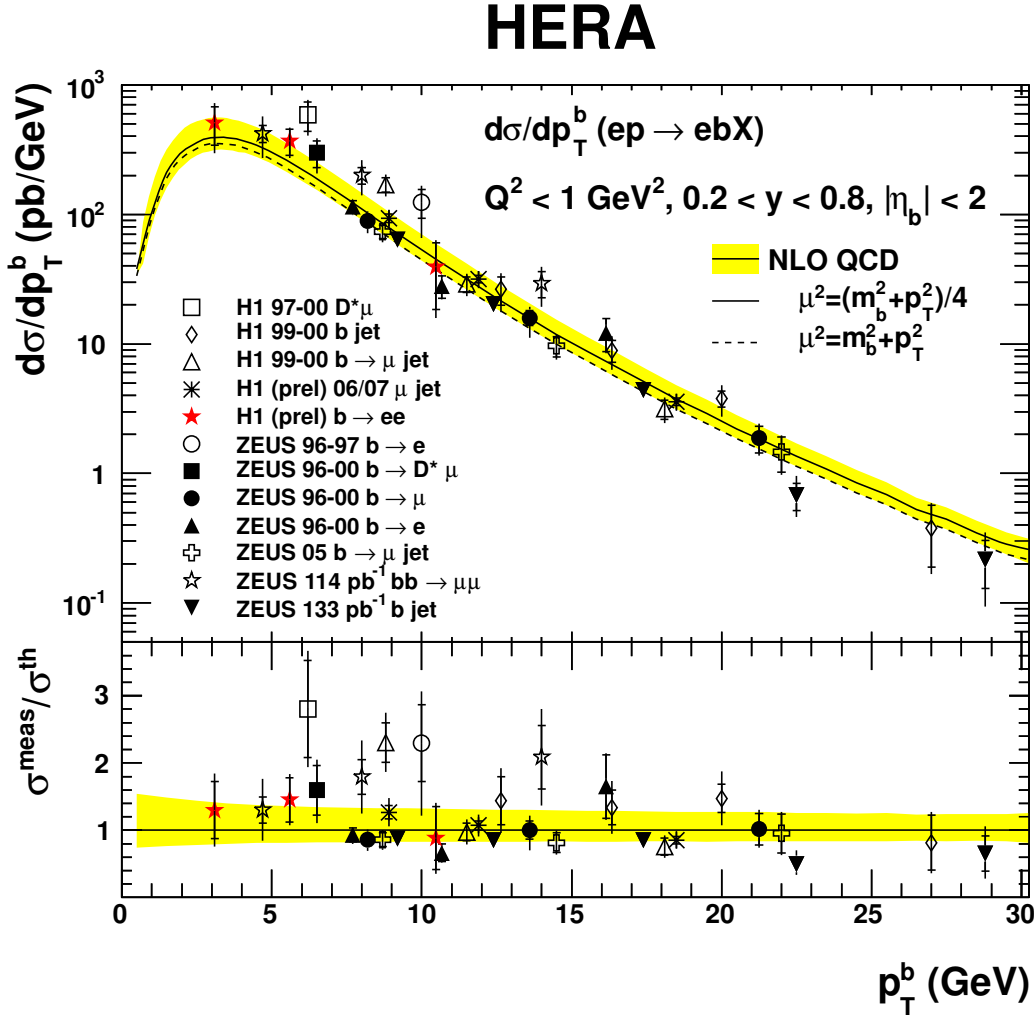

Figure 3.3: Beauty production cross section measured at Tevatron as a function of p_T^b (left) and p_T of the J/ψ from B decays (taken from [54]).

3.3   Beauty quark production at HERA

Both the ZEUS and H1 collaborations measured beauty quark cross sections in deep inelastic scattering and photoproduction [60–69]. In general, events were considered with two jets and a muon or electron from semileptonic b-decays. The beauty signal was separated from the charm and light-flavour backgrounds by use of the transverse momentum of the lepton relative to the axis of the associated jet and the impact parameter of the muon. Double-tagging methods by means of dimuons and $D^*\mu$ were also performed. Analyses were performed or are still in progress exploiting the long lifetime of B-hadrons by use of secondary vertices [70–73] in order to measure beauty production without any additional final-state particle.

---

[2]MC@NLO is a HERWIG based programme combining NLO QCD calculations with parton shower Monte Carlo.

Fig. 3.4 shows a summary of published differential cross sections for beauty quark photoproduction at HERA as a function of the mean transverse momentum p_T^b of the beauty quark, measured by the ZEUS and H1 collaborations in various independent analyses.

Figure 3.4: Summary of differential cross sections $d\sigma/dp_T^b$ for beauty quark photoproduction measured by the ZEUS and H1 collaboration (taken from [188]). The theoretical prediction were extracted by the FMNR program with two different choices of scale: $\mu^2 = \frac{1}{4}(m^2 + p_T^2)$ (solid black line) and $\mu^2 = m^2 + p_T^2$.

The measured cross sections were compared to theoretical predictions in next-to-leading order and found to be agreeing reasonably well.

3.4   Beauty production at the LHC

Since the start of data taking at the Large Hadron Collider in september 2009, the ATLAS [74], CMS [75] as well as the LHCb collaboration [76] have measured beauty quark production in pp-collisions at a centre-of-mass energy of $\sqrt{s} = 7$ TeV. Measurements of heavy-quark production at this higher energy offers a new testing ground for theoretical calculations. At the LHCb experiment, the $b\bar{b}$ cross section was measured by the decay of b hadrons into a D^0 meson and a muon [77] and compared to NLO predictions from MCFM [78] and FONLL [57] as well as to results of measurements at the Tevatron and found to be consistent with the theoretical predictions. The CMS collaboration measured e.g. $B\bar{B}$ angular correlations in $\Delta\phi$ and ΔR by means of reconstruced secondary vertices [79], as illustrated in Fig. 3.5.
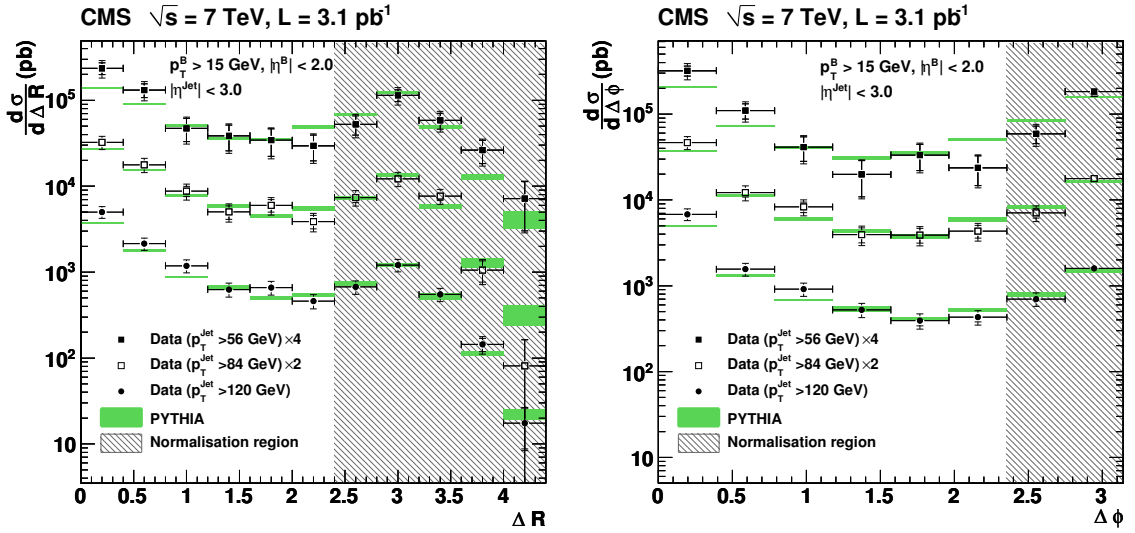
Figure 3.5: Differential $B\bar{B}$ production cross sections in ΔR (left) and $\Delta\phi$ (right) measured at CMS for different jet p_T regions at a centre-of-mass energy of $\sqrt{s} = 7$ TeV. The data (solid points) is compared to predictions from PYTHIA (shaded bars) (taken from [79]).

Furthermore, the inclusive b hadron production cross section in single muon [80] and $b\bar{b}$ cross section in dimuon events [81] were measured by the CMS collaboration. In Fig. 3.6, differential cross sections as a function of the muon transverse momentum and pseudorapidity measured in [75] are illustrated. The observed shapes are well described by the theoretical predictions of the MC@NLO program [59].

At the ATLAS experiment, the cross section of b-jet production was measured with muons associated to jets [82] and compared to NLO QCD predictions from the POWHEG program [83] as well as to a different ATLAS b-jet measurement with secondary vertices [84]. This is illustrated in Fig. 3.7. In general, the measured cross sections in these analyses were found to be consistent with the NLO QCD predictions.
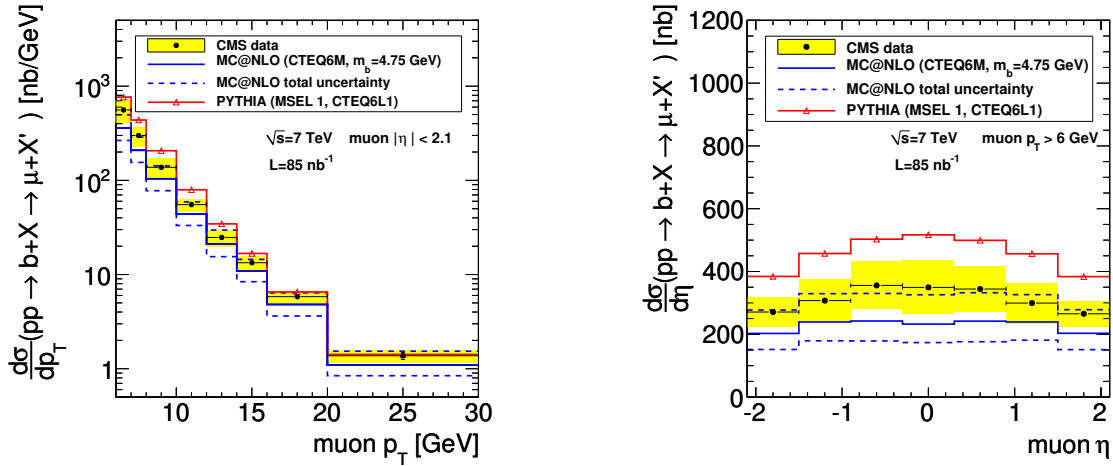
The three collaborations LHCb, CMS and ATLAS have also measured the production cross

Figure 3.6: Differential cross sections $d\sigma/dp_T^b$ measured by the CMS collaboration for the process $pp \to b + X \to \mu + X'$ at a centre-of-mass energy of $\sqrt{s} = 7$ TeV. The data (points) is compared to predictions from PYTHIA (triangles) and MC@NLO (solid and dashed line) (taken from [80]).
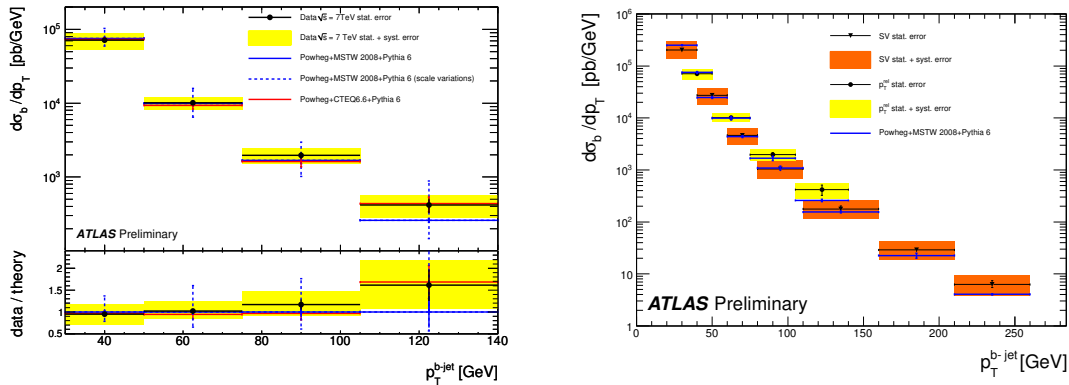

Figure 3.7: Differential b-jet production cross section as a function of p_T^{b-Jet} based on p_T^{rel} of muons in jets (left) measured at the ATLAS experiment at a centre-of-mass energy of $\sqrt{s} = 7$ TeV. The data (points) are compared to NLO predictions from the POWHEG and PYTHIA program (lines). This measurement was compared to a different ATLAS b-jet measurement based on reconstructed secondary vertices (triangles), as shown in the right picture (taken from [82]).

section of B_d^0 and B_s^0 mesons. The search for both mesons was performed on the one hand by their direct decay into a muon pair [85, 86]. This very rare decay channel of the B mesons is very interesting since it occurs only via loop diagrams and is helicity suppressed. Upper limits on the branching fractions have been determined at 95% confidence level by the CMS and LHCb collaboration.

On the other hand, the B mesons were identified by the processes:

$$
\begin{aligned}
B_s^0 &\rightarrow J/\psi + \phi, \quad J/\psi \rightarrow \mu^+\mu^-, \quad \phi \rightarrow K^+K^-, \\
B_d^0 &\rightarrow J/\psi + K^{*0}, \quad J/\psi \rightarrow \mu^+\mu^-, \quad K^{*0} \rightarrow K\pi, \\
B_d^0 &\rightarrow J/\psi + K_s^0, \quad J/\psi \rightarrow \mu^+\mu^-, \quad K_s^0 \rightarrow \pi^+\pi^- \\
B^\pm &\rightarrow J/\psi + K^\pm, \quad J/\psi \rightarrow \mu^+\mu^-
\end{aligned}
$$

as measured e.g. in [87–91]. The decay processes of neutral B mesons into a J/ψ and a kaon or ϕ are of significant interest as they allow the measurement of the B_s^0 and B_d^0 mixing phase, which is responsible for $\mathcal{CP}$ violation. The reconstructed invariant masses of both B mesons in these measurements, as illustrated in Fig. 3.8, were found to be consistent with the world average values.
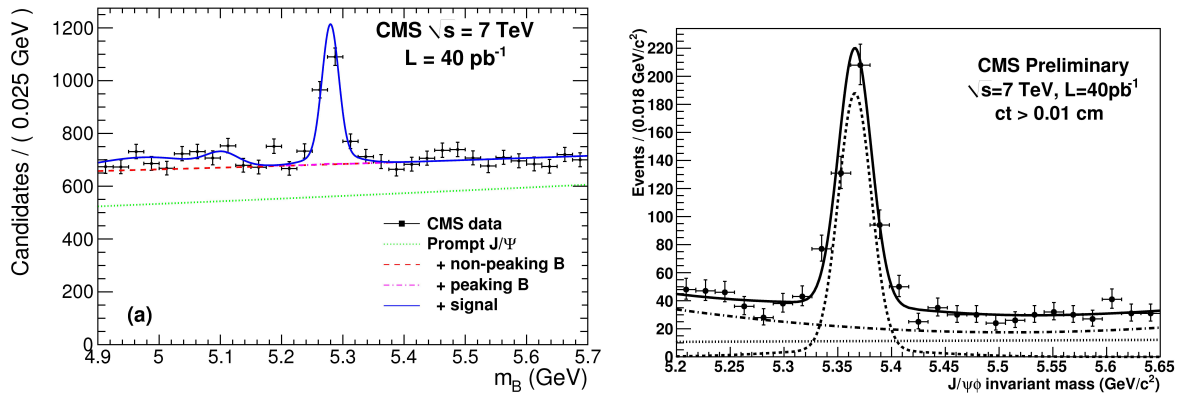
Figure 3.8: Reconstructed B_d^0 mass by the invariant $J/\psi K_s^0$ mass (left, taken from [87]) and reconstructed B_s^0 mass by the invariant $J/\psi\phi$ mass (right, taken from [88]), measured by the CMS collaboration at a centre-of-mass energy of $\sqrt{s} = 7$ TeV.

Differential cross sections as a function of the transverse momentum and pseudorapidity of the B mesons have been measured as well by the CMS collaboration [87–89] and were compared to NLO QCD predictions from MC@NLO. The obtained results were found to be in reasonable agreement with the theory in terms of shape and absolute normalisation. A summary of the B meson cross section measurements performed by the CMS collaboration at $\sqrt{s} = 7$ TeV in pp collisions at the LHC with comparison to NLO QCD predictions is illustrated in Fig. 3.9. In the same picture, the b hadron fraction measured by the CMS, ATLAS and LHCb as well as the CDF collaboration (latter at lower energies), is shown.
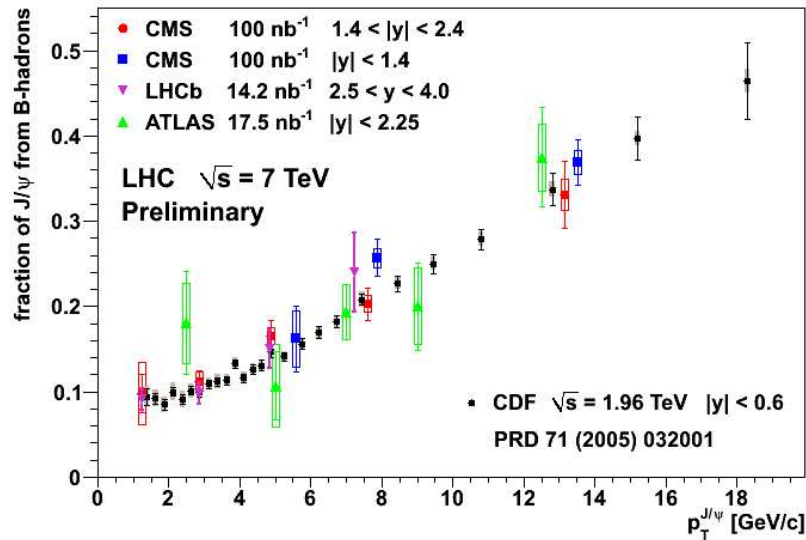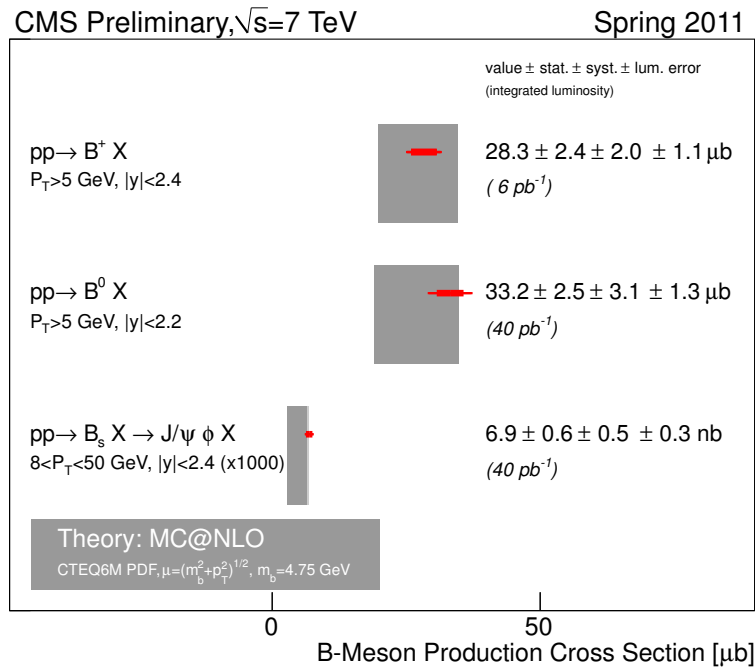
Figure 3.9: Summary of B meson cross section measurements from the CMS experiment (upper plot) at a centre-of-mass energy of $\sqrt{s} = 7$ TeV at pp collisions. The obtained cross sections are compared to NLO prediction from MC@NLO. In the lower plot, b hadron fraction measurements from CMS are illustrated and compared to results of ATLAS, LHCb and CDF (both pictures are taken from [92]).

Chapter 4

HERA and the ZEUS detector

In this chapter the HERA collider as well as the ZEUS detector are described briefly. Furthermore, parts of the detector, which are used in this analysis, are described more in detail.

4.1 The HERA collider

HERA (**H**adron-**E**lektron-**R**ing-**A**nlage) was the first and only lepton-proton collider and is located at the DESY (**D**eutsches **E**lektron-**SY**nchrotron) Research Centre in Hamburg, Germany. Built between 1984 and 1990, the machine was operating since 1992 and closed down after 15 years of data taking on June 30th 2007.
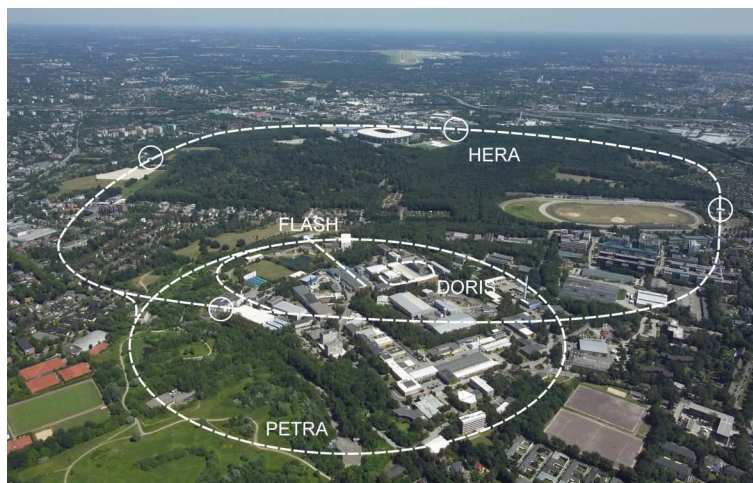
Figure 4.1: Aerial view of the DESY Research Centre in Hamburg, Bahrenfeld. The location of the HERA and PETRA accelerators is indicated by dashed lines (taken from [93]).

HERA consisted of two storage rings on top of each other, located in a 6.3 km long tunnel between 10 and 25 m under ground level. Electrons or positrons could be accelerated to an

energy of 27.5 GeV and protons to 920 GeV[1]. Electrons and protons were brought to collision at two interaction points yielding a centre-of-mass energy of $\sqrt{s} \approx 318$ GeV (300 GeV till 1998, respectively), which could be observed and analysed by the two detectors H1 [94] and ZEUS [95]. Furthermore, two fixed target experiments, HERMES [96] and HERA-B [97], were added. The main focus of the HERMES experiment was the study of the spin structure of the proton by means of the polarised electron beam, which is brought into collision with a polarised gas target. The HERA-B experiment was designed to investigate $\mathcal{CP}$ violation in beauty quark production by using the proton beam scattered at a wire target.
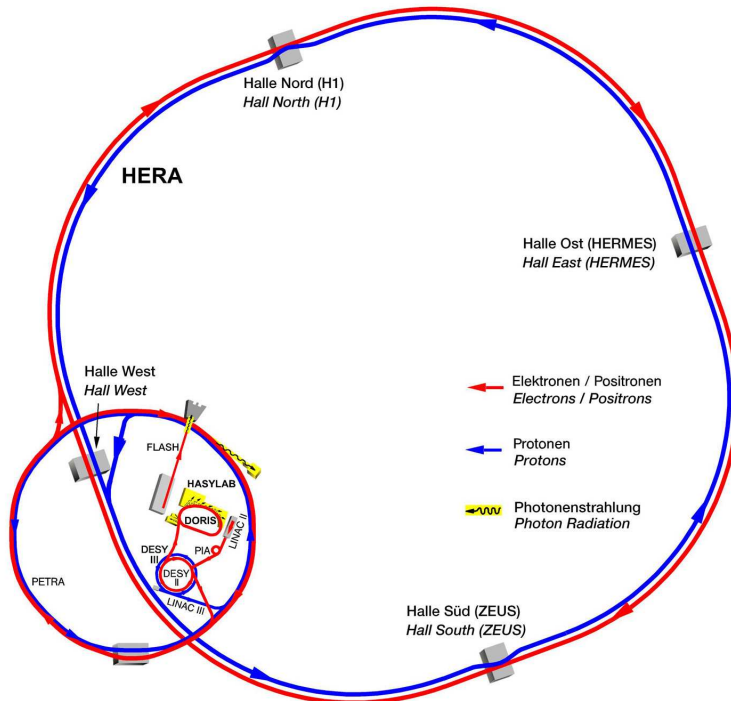
Figure 4.2: Schematic view of the HERA storage rings (taken from [93]).

During the shutdown in the years 2000 and 2001 HERA was upgraded in order to deliver a five times higher luminosity[2], defining two periods of data taking: HERA I before and HERA II after the upgrade. In the last few months of data taking, the proton energy was lowered to $E_P = 575$ GeV and $E_P = 460$ GeV. These data were used in order to measure the longitudinal structure function F_L of the proton [100]. At the end of the HERA data-taking, an integrated luminosity of ~ 500 pb^{-1} for each collider experiment was delivered, shown in Fig. 4.3. Tab. 4.1 lists furthermore a summary of HERA design parameters for both periods.

---

[1]820 GeV till the year 1998.

[2]Additionally, spin rotators were implemented and in the middle of 2003, a further longer shutdown was necessary due to severe background problems [4].

Type	HERA I design		typical in 2000		HERA II design	
Luminosity	$1.5 \cdot 10^{31}$ cm^{-2} s^{-1}		$1.7 \cdot 10^{31}$ cm^{-2} s^{-1}		$7.0 \cdot 10^{31}$ cm^{-2} s^{-1}	
Centre-of-mass energy	300 GeV		318 GeV		318 GeV	
	Lepton	Proton	Lepton	Proton	Lepton	Proton
Energy	27.5 GeV	820 GeV	27.5 GeV	920 GeV	27.5 GeV	920 GeV
Nr. bunches	180	180	180	180	180	180
Beam current	58 mA	160 mA	45 mA	100 mA	58 mA	140 mA
Particles per bunch	$3.6 \cdot 10^{10}$	10^{11}	$3.5 \cdot 10^{10}$	$7.3 \cdot 10^{10}$	$4 \cdot 10^{10}$	10^{11}
Beam width	247 μm	247 μm	190 μm	190 μm	118 μm	118 μm
Beam height	78 μm	78 μm	50 μm	50 μm	32 μm	32 μm

Table 4.1: Main design parameters of HERA. Typical values in the year 2000 are also shown [98, 99].
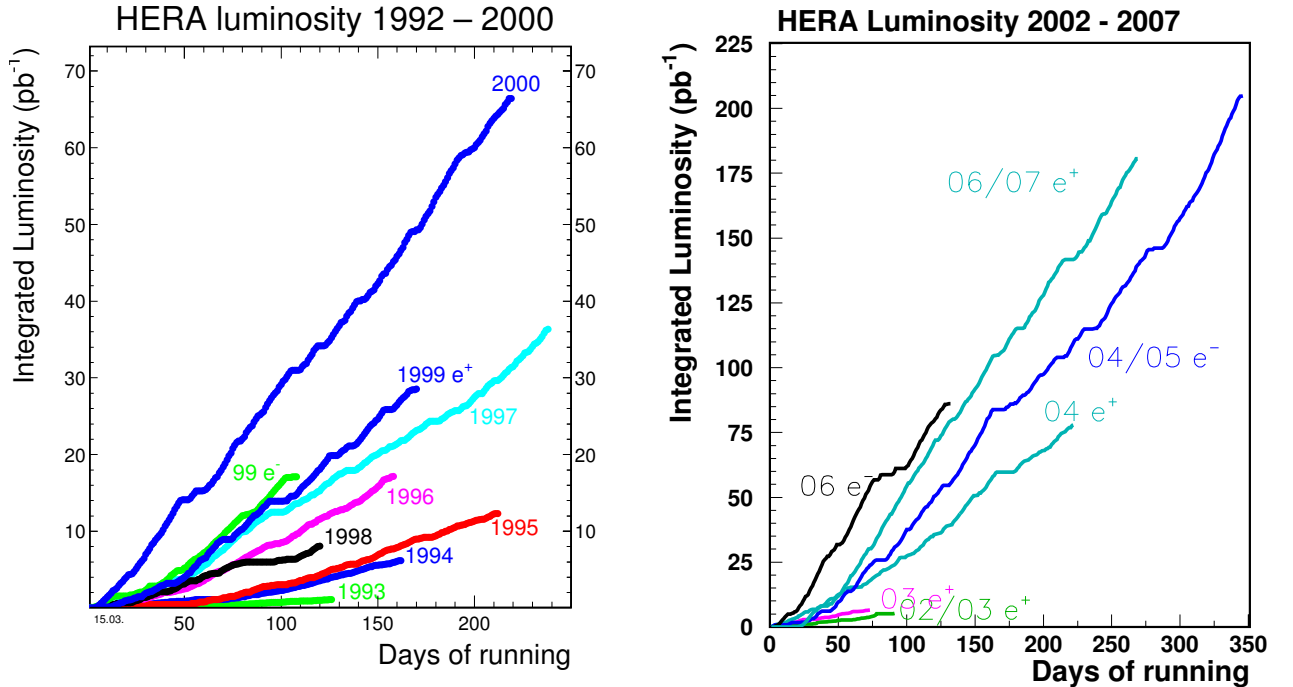
Figure 4.3: Integrated luminosity delivered by HERA for the HERA I and HERA II period (taken from [112]).

4.2   The ZEUS detector

The ZEUS detector [101], a general purpose detector with a size of 12m x 10m x 19m and a weight of 3600 tons, was designed to measure energy, momentum and kind of final-state particles produced in *ep*-collisions. Due to the higher energy of the proton relative to the electron the centre-of-mass system is boosted into the proton direction, yielding an asymmetric design of the detector. Figs. 4.4 and 4.5 illustrate the cross section of the ZEUS detector along and orthogonal to the beam axis, respectively.
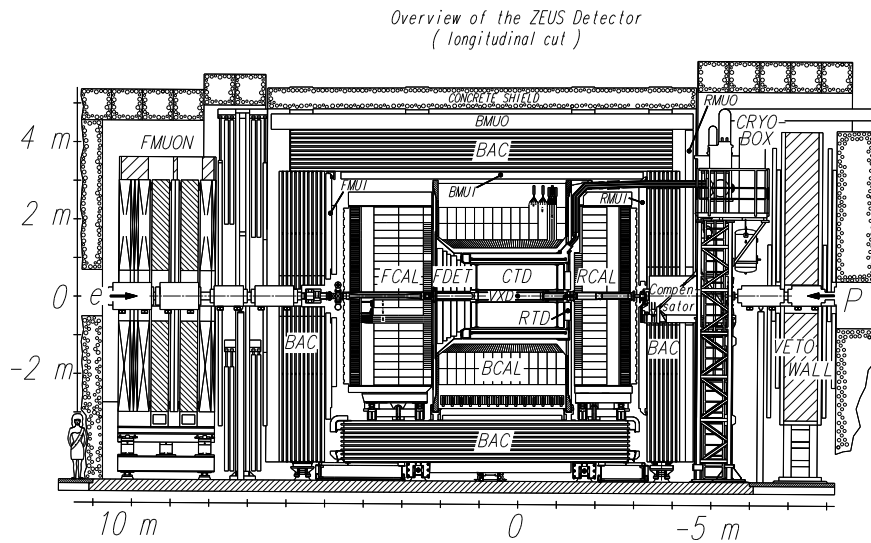
Figure 4.4: Cross section of the ZEUS detector along the beam axis (HERA I configuration) [95]. In HERA II, the VXD was replaced by the MVD.
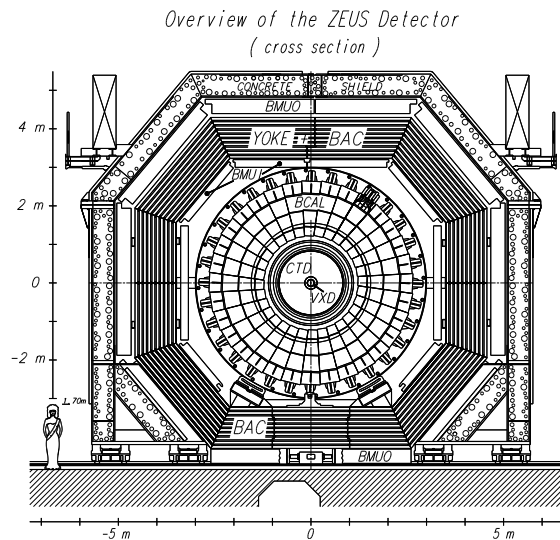
Figure 4.5: Cross section of the ZEUS detector orthogonal to the beam axis [95] (HERA I configuration). In HERA II, the VXD was replaced by the MVD.

The ZEUS coordinate system (cf. Fig. 4.6) is a right-handed orthogonal system, whose origin

is at the nominal interaction point. The x axis is pointing horizontally towards the centre of the HERA ring, the y axis upwards and the the z axis in the direction of the proton beam.

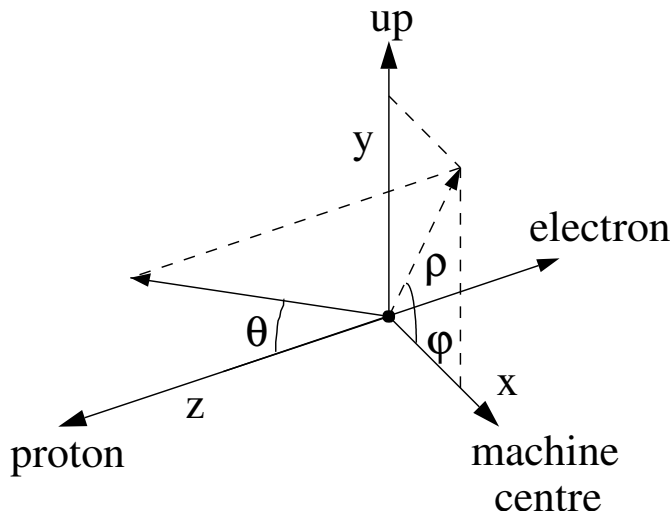**Figure 4.6:** The ZEUS coordinate system. The z axis points along the positive direction of the proton, the origin is located at the nominal interaction point.

The polar angle θ is measured relative to the z axis and the azimuth angle ϕ relative to the x axis. Instead of the polar angle θ, one uses generally the so-called *pseudorapidity* η, which is given by

$$\eta = -\ln\left(\tan\left(\frac{\theta}{2}\right)\right). \tag{4.1}$$

This definition has the advantage that the difference between two values of η is longitudinally Lorentz-invariant. In the following, a short description of the main detector components is given. Components most relevant for this analysis are described in more detail in the later sections.

The innermost part around the interaction point was covered since HERA II by a silicon-strip micro vertex detector (MVD, cf. Sec. 4.4) which was surrounded by the central tracking detector (CTD, cf. Sec. 4.3), a cylindrical drift chamber. The CTD was enclosed by a super-conducting solenoid magnet, providing a magnetic field of 1.43 T parallel to the beam pipe to determine the charges and momenta of charged particle tracks. In the forward direction, the CTD was supplemented by the forward detector (FDET). The tracking system was surrounded by a compensating high resolution uranium-scintillator calorimeter (CAL, cf. Sec. 4.5) which was used as the main device for energy measurements. It was divided into forward (FCAL), barrel (BCAL) and rear (RCAL) sections with different thickness. The calorimeter was enclosed by an iron yoke providing the return path for the magnetic field flux and serving as absorber for the backing calorimeter (BAC, cf. Sec. 4.7), which measured energy escaping detection from the main detector. Due to the high penetration power of the muon, the BAC also contributed to muon identification and reconstruction. Dedicated muon identification detectors (cf. Sec. 4.6) were located inside (FMUI, BMUI and RMUI) and outside (FMUO, BMUO and RMUO) the iron yoke.

The VETO wall was located in the rear direction at about z = -7.5 m from the interaction point. It consisted of an iron wall supporting scintillator hodoscopes and was used to reject proton beam related background. The luminosity measurement detector (LUMI, cf. Sec. 4.8), a small lead-scintillator calorimeter at z = -107 m (HERA I), was used to detect photons from bremsstrahlung events for the luminosity measurements. In HERA II, the LUMI system had been complemented with a spectrometer system in order to cope with the increased instantaneous collider luminosity.

4.3   Central Tracking Detector

The Central Tracking Detector (CTD) [102] was a gas-filled[3] cylindrial wire drift chamber used to measure direction and momentum of charged particles and to estimate the energy loss by ionisation dE/dx, which is used for particle identification. The inner radius of the CTD chamber was 18.2 cm and the outer 79.4 cm. Its active region covered the longitudinal interval from z = -100 cm and z = 104 cm, resulting in a polar angle coverage of $15° < \theta < 164°$ and a complete azimuthal coverage. The chamber was radially organised into nine superlayers of eight sense wire layers each as illustrated in Fig. 4.7. The odd superlayers had wires parallel to the chamber axis and were called *axial superlayers* while the wires of the even layers, so-called *stereo superlayers*, were mounted with angles of about $±5°$ with respect to the beam axis in order to allow track reconstruction of the z coordinate. The obtained resolutions were 180 μm in the $r - \phi$ plane and 2 mm in the z-direction.
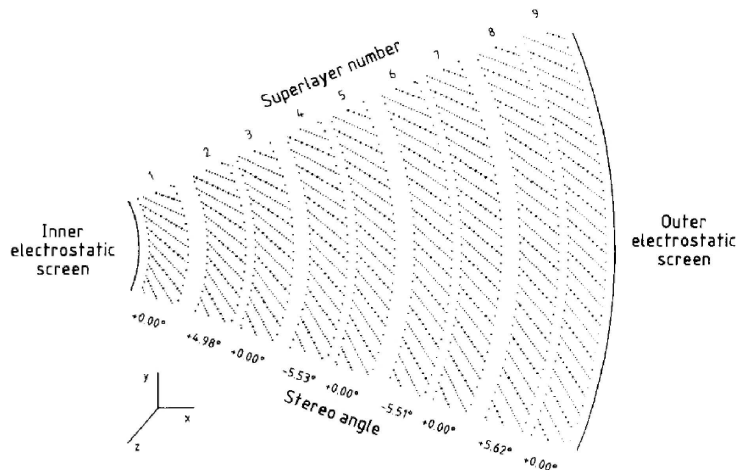
Figure 4.7: Layout of a CTD octant. The superlayers are numbered and the stereo angles of their sense wires are illustrated.

Charged particles traversing the CTD ionised gas molecules in the chamber and created electron-ion pairs along its trajectory. The electrons were attracted by the positively charged sense wires while the positive ions were attracted by the negative field wires. The drift velocity of the electrons was approximately constant at 50 μm/ns. Due to the increase of the electric field in the

---

[3]Mixture of argon, CO_2 and ethane.

immediate vicinity of a drift chamber's sense wire, the electrons near the wires were strongly accelerated and thus created secondary electron-ion pairs. Avalanche-like multiplication of electrons occured which led in the case of the CTD to an amplification factor of about 10^4. The resulting electric pulse was read out and digitised by 8-bit Flash ADCs. For trigger purposes, the three inner axial superlayers were equipped with a z-by-timing system. In these layers, the electric pulses were read out at both ends of the wires. The z position was then determined from the difference in the arrival times. The obtained resolution was approximately $\sigma_z = 4$ cm.

For tracks crossing at least three superlayers, originating from the nominal vertex position with a transverse momentum of $p_T > 150$ MeV, the relatice transverse momentum resolution could be parameterised by [103]

$$\sigma(p_T)/p_T = 0.0058p_T \oplus 0.0065 \oplus 0.0014/p_T, \tag{4.2}$$

where p_T is given in GeV and $\oplus$ indicates the quadratic sum. The first term gives the contribution from the position resolution of the hits, while the other two terms depend on the mutiple scattering before and inside the CTD, respectively. In the HERA II data taking period, the conditions at which the CTD operated changed. Due to the additional information of the MVD, installed 2001, the overall track transverse momentum and vertex resolution improved and can be parameterised as [104]

$$\sigma(p_T)/p_T = 0.0029p_T \oplus 0.0081 \oplus 0.0012/p_T. \tag{4.3}$$

4.4   Micro Vertex Detector

During the HERA upgrade shutdown in 2001, a silicon-strip micro vertex detector (MVD) [105] was installed in order to significantly improve the precision of the ZEUS track reconstruction and forward acceptance. Thus, it allowed the identification of events with secondary vertices originating from the decay of heavy flavour particles which have a long lifetime ($c\tau \approx 100$ μm or larger). The design of the MVD was determined by the restricted available space between the beampipe and the CTD as well as the following technical requirements:

- radial extension smaller than 32.4 cm (CTD inner diameter),

- polar angular coverage between $10°$ and $150°$,

- measurement of three points per track in two projections each,

- at least 20 μm hit resolution for normal incident tracks,

- two-tracks separation of 200 μm,

- hit efficiency better than 95%,

- noise occupancy better than 10^{-3}.

The MVD was divided into two regions: The barrel (BMVD) and forward MVD (FMVD) [106]. The BMVD had a length of 64 cm and covered the average longitudinal event vertex distribution which was determined mainly by the average proton bunch length of ~ 20 cm. Consisting of three layers of double silicon strip sensors, called barrel modules, arranged in concentric cylinders around the interaction point, the coverage of the polar region amounted to 30° till 150°. The internal layer was not complete due to the elliptic shape of the beam pipe which was not centred around the interaction point (cf. Fig. 4.8).
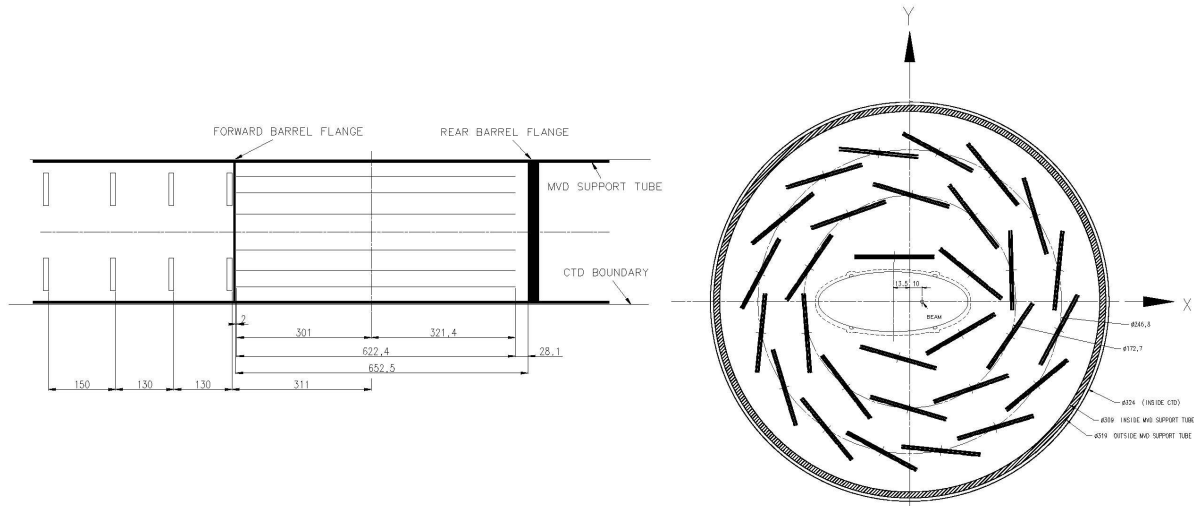
Figure 4.8: Left: Cross section of the MVD, parallel to the beam pipe with the barrel region on the right and the forward region on the left. **Right:** Cross section of the MVD, perpendicular to the beam pipe.

The single sided silicon sensors of the BMVD were square shaped (64.2×64.2 mm^2), 320 μm thick and arranged in *half modules* with strips parallel and perpendicular to the beam pipe. Two half modules were placed on top of each other in order to form a module with 1024 readout channels providing two coordinates for each particle traversing it. The ambiguity due to the connected sensors per half module could be solved at reconstruction level.

The FMVD covered the polar region between 10° and 30°. It consisted of four wheels perpendicular to the beam axis, where each wheel was made of two back-to-back layers with silicon strip sensors of the same type as in the barrel region. Those sensors had a trapezoidal shape with strips parallel to one tilted edge and contained 480 readout channels per strip. Two overlapping sensors of a wheel form a module providing two coordinates of a particle traversing a wheel.

4.5   Uranium Calorimeter

The ZEUS calorimeter (CAL) [107] was a compensating sampling calorimeter consisting of alternating layers of depleted uranium (absorber), wrapped in steel foils, and scintillator plates

(active material). The thickness of the plates[4] had been chosen to provide linear and equal response for electrons and hadrons over a wide range of energies.
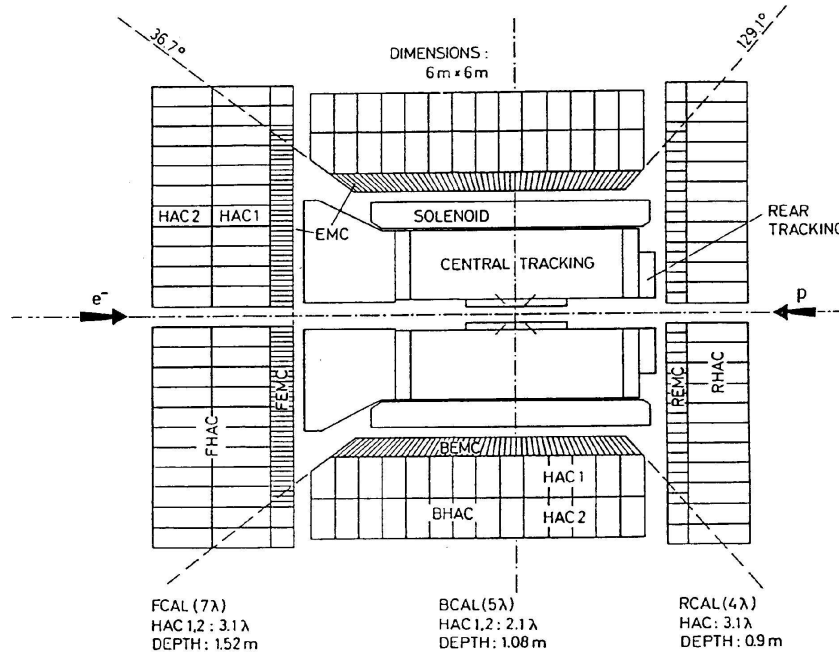

Figure 4.9: Schematic view of the UCAL along the beam axis.

The CAL was geometrically divided into three parts: The forward (FCAL), the barrel (BCAL) and the rear calorimeter (RCAL), covering together 99.8% of the forward and 99.5% of the backward hemisphere. The depth of the calorimeter was determined by the maximum energy that had to be absorbed, requiring 99% energy containment [108]. The maximum energy depended on the polar angle and ranged from 30 GeV in the RCAL to 800 GeV in the FCAL. The containment of the highest energetic jets was achieved by the low resolution backing calorimeter.

The FCAL covered polar angles from $2.2°$ to $36.7°$ and was divided into 23 modules numbered with increasing x. Each module consisted of towers with a front surface dimension of 20 x 20 cm^2, subdivided longitudinally into one electromagnetic (EMC) and two hadronic sections (HAC1, HAC2). Each hadronic section of a tower was identified as one calorimeter cell while the electromagnetic sections were subdivided into four transverse cells with a front surface dimension of 20 x 5 cm^2. The structure of one FCAL module is illustrated in Fig. 4.10.

The RCAL covered polar angles from $129.1°$ to $176.5°$. While its design was very similar to the FCAL, the RCAL contained only one hadronic section and the electromagnetic sections were only divided into two transverse cells yielding a front surface dimension of 20 x 10 cm^2. The BCAL covered polar angles from $36.7°$ to $129.1°$ and contained one electromagnetic and two hadronic sections. It was divided into 32 wedge-shaped modules, whereof each module was subdivided into 14 towers along the z-axis.

---

[4]Uranium: 3.3 mm, scintillator: 2.6 mm
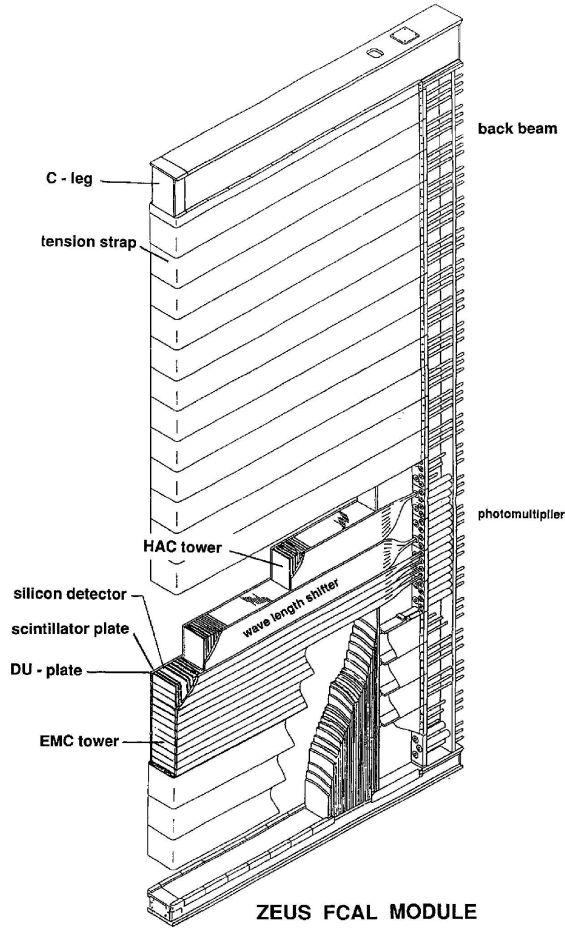
Figure 4.10: View of an FCAL module.

Each cell of the CAL was read out on opposite sides via wavelength shifters by two photomultiplier tubes. While the sum of signals of both photomultipliers was approximately independent of the impact point of the impinging particle, the horizontal position could be determined by comparing the two signals.

Under test beam conditions, the electromagnetic energy resolution had been determined to be

$$\frac{\sigma_E}{E} = \frac{18\%}{\sqrt{E}} \oplus 2\%, \tag{4.4}$$

and for the hadronic resolution

$$\frac{\sigma_{Had}}{E} = \frac{35\%}{\sqrt{E}} \oplus 1\%, \tag{4.5}$$

where E is the particle energy measured in GeV. The calorimeter energy response was calibrated with an accuracy of about 1%. Angles could be measured within a precision of about 10 mrad. The time resolution of the CAL (< 1 ns for energy depositions greater than 4.5 GeV) was used

to reject non-*ep* background with characteristic timing patterns (e.g. particles from the beam halo) already at the trigger level (cf. Sec. 4.9.)

4.6 Muon Detectors

Muons can traverse large amounts of material without being absorbed since they lose energy mainly by ionisation. The muon detectors had to measure tracks produced in the interaction region which crossed the whole calorimeter thickness and the iron yoke. The momenta of the muons differed depending on their polar angle due to the boosted system in the forward region. Muons with a momentum greater than 10 GeV were frequently produced in this region. In the barrel and rear region the average momentum of the muons was expected to be much smaller. Therefore, the muon detection system was divided into two sub-detectors, the forward muon detector (FMUON, cf. Sec. 4.6.1) and the barrel and rear muon detector (BMUON and RMUON, cf. Sec. 4.6.2).
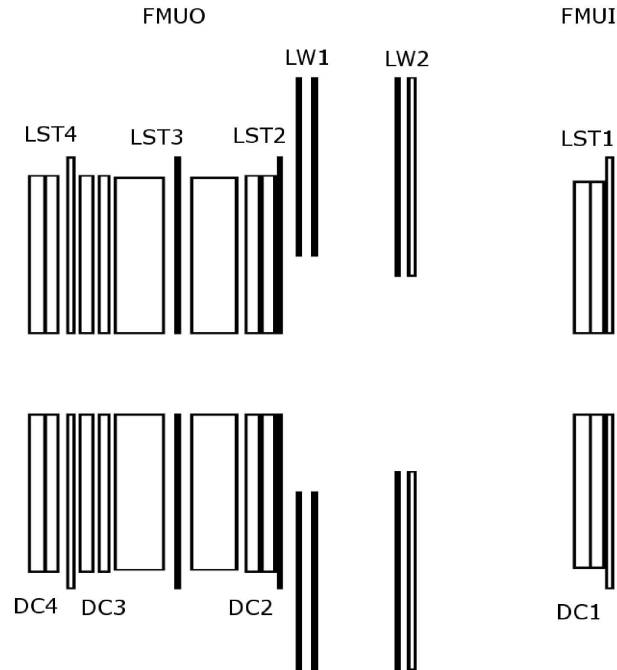
4.6.1 Forward Muon Detector

The forward muon detector [101] was longitudinally divided into two regions (cf. Fig. 4.11). The inner region (FMUI) was located between the FCAL and the iron yoke, the outer region (FMUO) was positioned outside the forward iron yoke. The components of the FMUON detector were:

- a system of 4 planes of limited streamer tubes (LST) [109] trigger planes (LST1 - LST4), providing digital radial ρ and azimuthal ϕ readout,

- 2 larger planes of LSTs with digital (ρ, ϕ) and analogue (ρ) readout in the large polar angle region (LW1, LW2),

- 4 planes of drift chambers (DC1 - DC4),

- 2 large toroidal iron magnets providing a magnetic field of 1.7 T for the momentum separation and measurement in the angular region $5° < \theta < 16°$.

The first plane of LST and drift chambers made up the FMUI detector, placed inside the iron yoke while the rest of the system was located outside the iron yoke. The individual components of the FMUON detector are described in the following.

The limited streamer tube planes: The limited streamer tube planes were used both for triggering on events with muons and reconstructing the azimuthal and radial position of muon candidates. A trigger plane was made of four LST chambers grouped in two half-planes. A quadrant consisted of two layers of LSTs. On the outer side, copper strips were attached in polar geometry. On particle passage, the LSTs induced a signal in the radial and azimuthal copper strips. The number of radial strips was 132 while each strip was 1.9 cm wide. They were divided along the bisector of the quadrant so that the simplest readout unit of the trigger

Figure 4.11: Schematic view of the forward muon detector along the beam axis.

plane was an octant. The number of strips was 32 per octant. Each strip covered an interval of $1.4°$ in the azimuthal angle.

The drift chambers: The drift chambers were needed in order to obtain a good momentum resolution. Each plane consisted of four chambers grouped two by two in two half planes fixed on a support panel. The basic element of the chamber was a cell made of four sense wires and of the layers generating the electric drift field. The four sense wires measured the radial coordinate.

The large angle coverage planes: The two large angle coverage planes (LW) were used to achieve the desired geometrical acceptance also in the region left uncovered by the toroids $(16° < \theta < 32°)$. Each plane consisted of eight LST layers. The LST signal was induced on copper strips radially separated by $0.7°$ in the ϕ coordinate and by 1.8 cm in the ρ coordinate. There were 64 ϕ strips and 192 ρ strips per octant. Using a centre of gravity algorithm, a resolution of ~ 1 mm was achieved for the ρ coordinate.

4.6.2   Barrel and Rear Muon Detector

The barrel and rear muon detector [110] covered a large area of ~ 2000 m^2, consisting of LST chambers. Inner barrel muon chambers (BMUI) were arranged on the inner barrel part of the BAC, outer barrel muon chambers (BMUO) were located on the outer barrel part. The rear region was divided into RMUI and RMUO chambers in a similar way (cf. Fig. 4.12).
While varying in shape and dimension, the different chambers had the same internal structure.
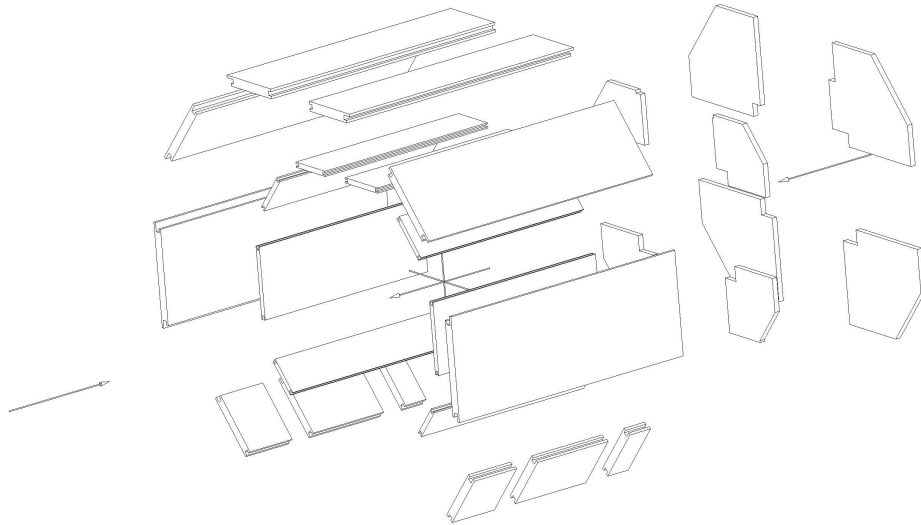
Figure 4.12: Layout of the barrel and rear muon detectors.

A hexagonal aluminium structure with a witdh of 20 cm in BMUI and 40 cm in BMUO supported a double layer of LST chambers on both sides. Each LST was made of a plastic profile with eight cells. In each cell a copper-beryllium wire of 100 μm diameter was located. The distance between two sense wires was 1 cm. Each LST plane was equipped with 13 mm wide readout strips on one side with a pitch of 15 mm running perpendicular to the wires. In the BMUI and BMUO chambers the LSTs were directed parallel to the beam direction whereas in RMUI and RMUO they were placed parallel to the ZEUS x direction. With the analog strip readout the achievable spatial resolution on the coordiante perpendicular to the wires was 200 μm and 700 μm for the coordinate parallel to the wires.

4.7 Backing Calorimeter

The iron yoke in between the inner and outer muon chambes was interleaved with aluminium proportional tubes which made it a tracking calorimeter, called backing calorimeter (BAC) [111]. The BAC was used to handle events with shower leaks of high energy jets penetrating the CAL. Such events could be vetoed or corrected for using the BAC. Furthermore, the BAC was used to tag muons wich was specially useful in regions scarcely covered by the muon chambers (e.g. the lower barrel region).

The BAC modules inserted into the yoke consisted of 7-8 tubes (channels) with a cross section of 11x 15 mm^2 each and a longitudinal length of 1.8 - 7.3 m. Gold plated tungsten wires with a diameter of 50 μm were streched in the centre of the tubes and supported every $\sim$ 50 cm in the longitudinal direction. Flat aluminium cathodes with a length of 50 cm were mounted on top of the modules. The wires were read out on one side and provided both analogue and digital signals while the pads had analogue read out only.
Energy was measured by summing up the analogue signals from the wires grouped in addition into towers of a width of 25-50 cm (2-4 modules) over the full depth of the BAC. The pads of

2-4 neighbouring modules were added to pad towers with an area of 50 x 50 cm^2 (4 modules) similar to the wire towers. They provided a measurement of the location of the energy deposit along the wires. The signals from the wires provided patterns of hit positions in the BAC to reconstruct muon trajectories. Details on the dimensions and numbers of the BAC's modules, pads and wires are listed in the following Tab. 4.2.

	Barrel	Bottom	Forward	Rear
Area $[m^2]$	1902	296	460	322
Number of layers	9	9	10	7
Gas volume $[m^3]$	38.0	5.9	9.2	6.4
Number of 8-tube modules	2246	193	840	572
Number of 7-tube modules	658	120	280	112
Module length $[m]$	4.5 and 5.5	7.3	$1.8 \rightarrow 3.6$	$1.8 \rightarrow 3.6$
Number of wires	22574	2384	7980	5360
Wire towers	100	10	32	36
Pad towers	1100	150	222	230

Table 4.2: Dimensions and numbers of BAC components.

The spatial resolution of the BAC is ~ 1 mm perpendicular to the wires while the resolution parallel to the wires was constrained by the pad size. Under test beam conditions the energy resolution was determined by

$$\frac{\sigma_E}{E} \sim \frac{1.1}{\sqrt{E}}, \tag{4.6}$$

whereby E is the particle energy given in GeV.

4.8 Luminosity measurement

The luminosity measurement at ZEUS [112–115] was made by using the Bethe-Heitler QED Bremsstrahlung process [116]:

$$ep \rightarrow e'p\gamma. \tag{4.7}$$

This process has a large cross section ($\sigma_{BH} \approx 20$ mb) yielding sufficient statistics and can be calculated differentially as a function of the photon energy with an accuracy of $\sim 0.5\%$ by

$$\frac{d\sigma_{BH}}{dk} = 4\alpha r_e^2 \frac{E_e'}{kE_e} \left(\frac{E_e}{E_e'} + \frac{E_e'}{E_e} - \frac{2}{3} \right) \left(\ln \frac{eE_pE_eE_e'}{m_em_pk} - \frac{1}{2} \right). \tag{4.8}$$

α is the fine structure constant, r_e the classical electron radius, k the energy of the photon and E_e and E_e' the energy of the incoming respectively outgoing electron. With a well-known cross section σ_{BH} and N_{BH}, the corresponding number of events observed over a period of time is given by

$$\mathcal{L} = \frac{N_{BH}}{\sigma_{BH}}. \tag{4.9}$$

4.8.1 Photon Calorimeter

The photon calorimeter [117] measured the rate of Bethe-Heitler photons using a lead-scintillator sampling calorimeter positioned at z = -107 m from the interaction point. To shield the calorimeter from synchrotron radiation, a set of carbon filters was installed in front of it. Since these filters worsened the energy resolution, two Cherenkov detectors measured the number of e^+e^--pairs produced by the Bethe-Heitler photons as the passed through the filters.
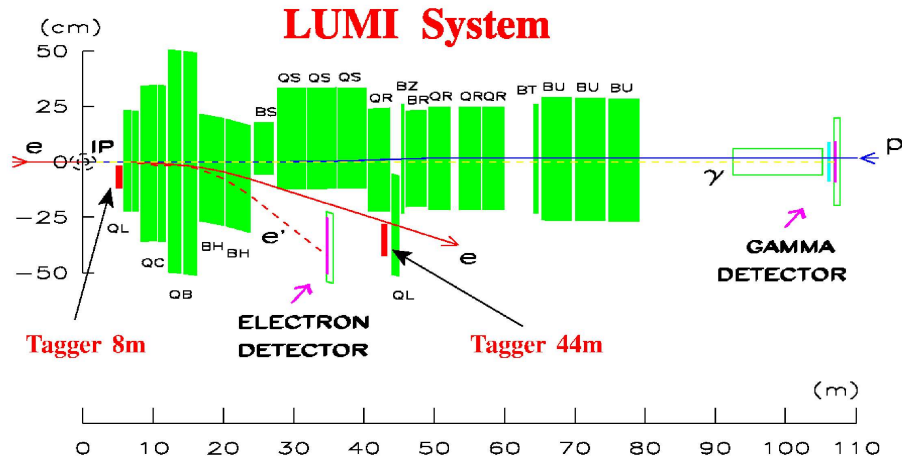
Figure 4.13: The layout of the ZEUS Luminosity Monitor (HERA I). The nominal interaction point is located at (0,0).

The electron scattered in the Bethe-Heitler process had a lower energy than the beam electrons and thus was bent at a different angle by the beam magnets. It was detected in another lead-scintillator sampling calorimeter positioned 35 m from the interaction point. The detection of Bethe-Heitler electrons was used for systematic studies of the photon calorimeter measurement, whereby the systematic uncertainty on the luminosity measurement is given by 1.8 %.

4.8.2 Spectrometer System

The spectrometer system [118] detected Bethe-Heitler photons through their pair conversion in material. When photons left the beam pipe about 92 m from the nominal interaction point, they passed through a 3 mm thick window made of copper (90 %) and Beryllium (10 %) and around 10 % of the photons converted into e^+e^--pairs which were split by a dipole magnet and detected by two tungsten-scintillator calorimeters. The luminosity was measured from the rate of coincidence in both calorimeters, whereby the systematic uncertainty is 2.6 %.

4.9 Trigger and Data Acquisition system (DAQ)

The HERA beam bunch structure leads to a beam crossing every 96 ns which corresponds to a nominal bunch crossing rate of 10.4 MHz. The rate of *ep* events ranges from about 0.1 Hz for

NC DIS events with $Q^2 > 100 \, \text{GeV}^2$ to 250 Hz for soft photoproduction. The rate of background events, however, exceeded the rate of *ep* physics events by several orders of magnitude. The dominant part of the background was caused by interactions of electrons or protons with the residual gas nuclei or elements from the beam pipe (*beam gas events*), which occured typically at a rate of 10 kHz. An additional background was caused by cosmic ray muons passing the CTD. The rate which the ZEUS data acquisition system (DAQ) was able to write to tape was about 10 Hz. Therefore, a significant reduction of the number of events was required. For this reason, a three level trigger system [119] was used. The complexity of the trigger selection rose from level to level while the data throughput was reduced. Fig. 4.14 illustrates a schematic diagram of the ZEUS trigger and data acquisition system. In the following, the different levels of the trigger system are described.
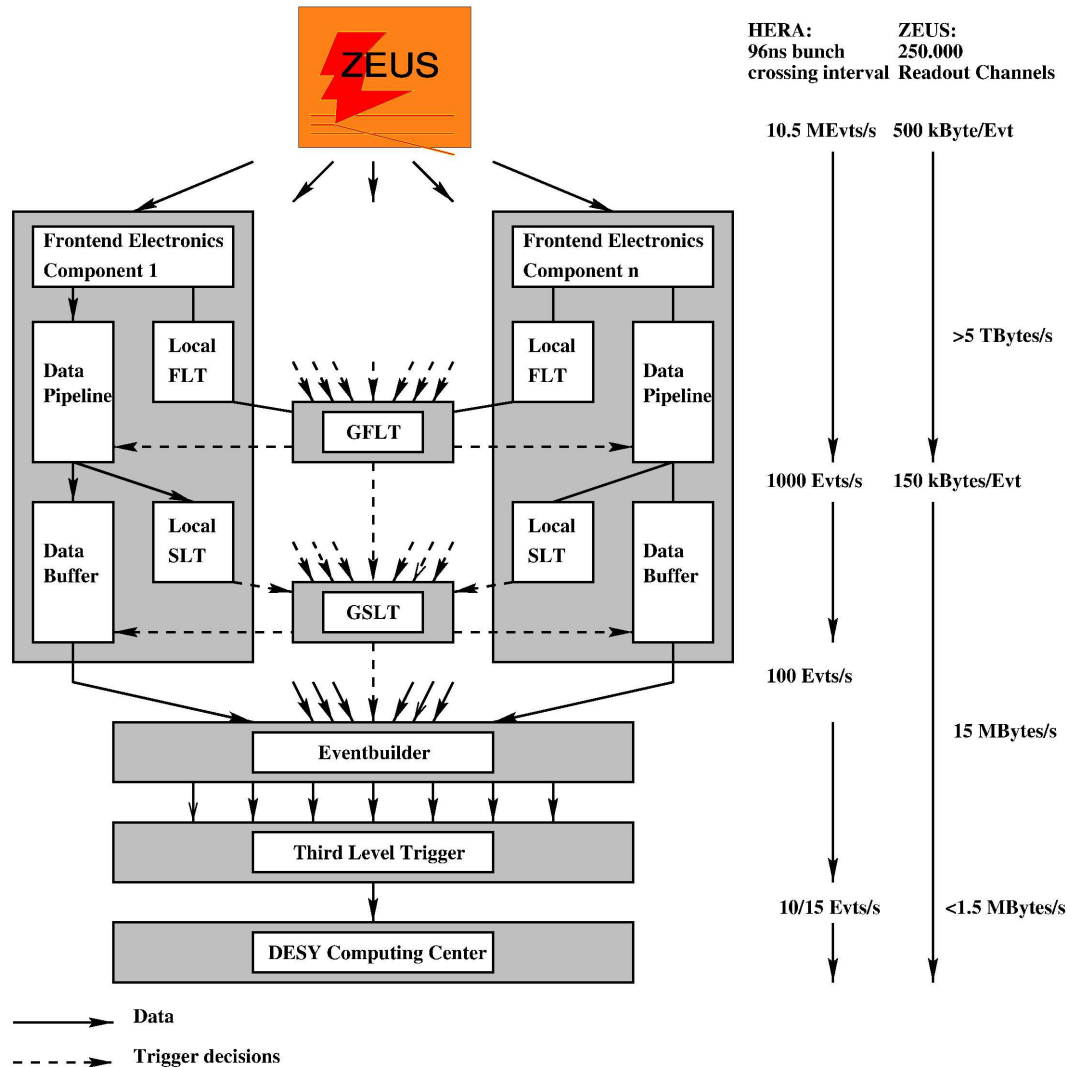

Figure 4.14: The ZEUS trigger and aquisition system.

4.9.1 Global First Level Trigger (FLT)

The FLT [120] was a hardware trigger used to reduce the event rate below 1 kHz. Thus, each detector component was equipped with its own FLT providing a fast trigger information (within 2 μs after bunch crossing) based on properties like energy sums, thresholds or timing information, which were passed to the global first level trigger (GFLT). The GFLT decided by combining different trigger information whether to accept or reject an event within 4.4 μs. Since the event data were stored in analog or digital pipelines, the trigger processing was almost deadtimeless.

4.9.2 Global Second Level Trigger (SLT)

The SLT was implemented on a transputer[5] network. Events accepted by the GFLT were analysed further and their quantities were recalculated to a higher degree of precision. Beam gas background was rejected by using CAL timing information. The decisions of several branches of the SLT were collected by the global second level trigger (GSLT) [121], which provided a decision after 7 ms and reduced the event rate to 50-100 Hz. After the HERA upgrade, the GSLT was supplemented by an additional tracking trigger, referred to as global tracking trigger (GTT) [122], which was developed in order to take advantage of the additional tracking information provided by the MVD. The MVD hits were combined with the track segments from the CTD and were then used for a more precise determination of the primary vertex position. The processing of the GTT algorithm is performed on a Linux PC farm. The combined trigger decision could be used to efficiently reduce the rate on the second level trigger.

4.9.3 Global Third Level Trigger (TLT)

For accepted events the data of all components were combined in a single record of ADAMO [123] database tables by the event builder and passed on the TLT [124] which used a computer farm for the analysis and classification of each event. Based on physical quantities of the fully reconstructed events, such as kinematic variables, output of electron and muon finding algorithms, topologies of the hadronic final state etc., a decision was made and the accepted events were classified. Accepted events (with a size of approximately 100-150 kb) were written to disk at a rate of ~10 Hz and fully reconstructed offline by the ZEUS software.

4.9.4 Detector simulation

All event generators commonly used at ZEUS (e.g. RAPGAP, PYTHIA etc.) are integrated in a software package called AMADEUS. This software package converts the output of the event generator (like the four-momenta of the produced particles in the *ep* interaction) into the so-called ADAMO format (Aleph DAta MOdel [125]), which can be handled by the programmes in the following steps: For the simulation of the detector response, the event-generator output is passed to the MOZART (Monte Carlo for ZEUS Analysis, Reconstruction and Trigger)

---

[5]A microprocessor optimised for parallel processing by INMOS (UK).

program. MOZART is based on the GEANT 3.21 package [128], which contains a description of all relevant physics processes for electromagnetic and hadronic interactions of particles traversing an arbitary detector geometry. After MOZART, the trigger logic used during data recording was simulated by the CZAR package (Complete ZGANA Analysis Routines) [127], which combines the programmes ZGANA (ZEUS Geant Analysis), wich is responsible for the FLT and SLT simulation, with the TLT simulation software TLTZGANA. In the next step, which is common for both MC simulated events and ZEUS raw data, the offline reconstruction is performed by the reconstruction package ZEPHYR (ZEUS Physics Reconstruction). As a consequence, the structure of a MC simulated event and a data event are identical, thus both can be analysed in the same way, e.g. by the ORANGE framework [129]. More information about the event simulation at ZEUS can be found in [130].

Chapter 5

Event reconstruction

The aim of this analysis is the measurement of beauty quark production with two muons in the final state from the semileptonic b-decay:

$$e^{\pm}p \to b\bar{b}X \to \mu\mu X'. \tag{5.1}$$

Fig. 5.1 shows such a dimuon event. The reconstruction of event properties needed to identify such events consists of the reconstruction of the hadronic system as well as the muon reconstruction. The reconstruction of the hadronic system is based on track and energy information combined into energy flow objects (EFOs) which are the input for the jet algorithm.
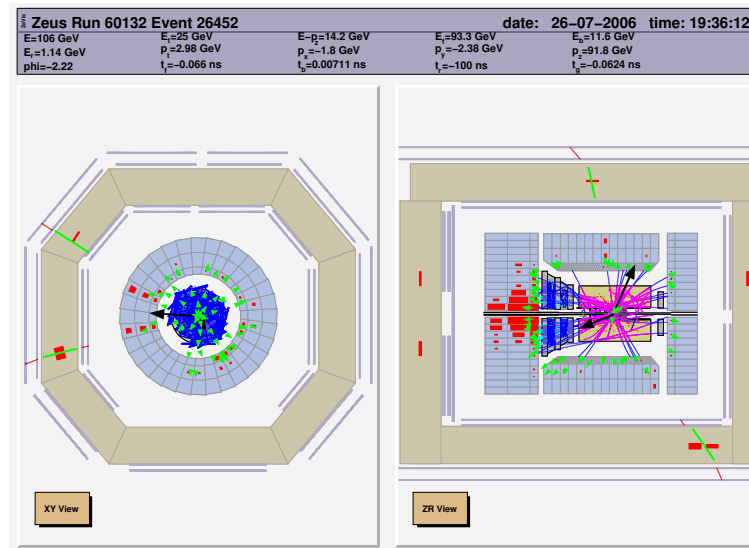
Figure 5.1: Event display of a dimuon event from semileptonic beauty quark decay in the **left:** $X - Y$ plane, **right:** $Z - R$ plane. Shown are reconstructed tracks (red lines), CAL energy (red cells in the CAL), EFOs (green arrows), reconstructed jets (black arrows) as well as muons (green lines in the muon chambers).

For the identification of muons a set of muon finder algorithms using the inner tracking chambers, the calorimeters and the muon chambers is used. These finders are combined into a

general muon finder, called GMUON, in order to improve the efficiency and to benefit from redundancies.

In the following, different parts of the event reconstruction are described. Beginning with the inner tracking, followed by the calorimeter energy measurement and the combination of both, the main part of this chapter lays emphasis on the muon reconstruction. Finally, the jet algorithm as well as the methods for the identification of beauty and instanton events are described.

5.1   Track and vertex reconstruction

Tracks of charged particles are reconstructed by combining hit information from the inner tracking detectors taking into account the errors on the hit measurement, the dead material distribution and effects of multiple scattering. The track reconstruction enables the measurement of the momentum and charge of a particle. In addition, the energy loss dE/dx along the track can also be used for particle identification. Since the implementation of the MVD, three different track types can be found:

- **CTD only tracks:** This track type has been used predominantly for the HERA I data period and uses only the CTD information.

- **Regular tracks:** This track type is available for the HERA II data period and uses both, the CTD and MVD information.

- **ZTT tracks:** This track type uses the CTD and MVD information as well but the track parameter accuracy near the vertex is improved by using the Kalman filter technique [132].

All track types are described by a five parameter parametrisation [131], as illustrated in Fig. 5.2. This parametrisation was chosen in order to describe trajectories of charged particles in a magnetic field parallel to the beam axis.

- ϕ_H, the azimuthal angle of the helix tangent at the distance-of-closest-approach (DCA) to the z-axis,

- Q/R, where Q denotes the charge of the track given by the directon of curvature and R the local radius of curvature of the helix,

- QD_H, where D_H is the DCA to the z-axis.

- Z_H, the z-coordinate at this point and

- $\cot\theta_H$, where θ_H is the polar angle of the helix.

The first three parameters describe a circle in the $X - Y$ plane and the latter two represent the location and pitch in Z.

The track finding and reconstruction is performed in three steps. The first step uses the pattern recognition package VCTRACK [131], which consists of a multi-step algorithm combining
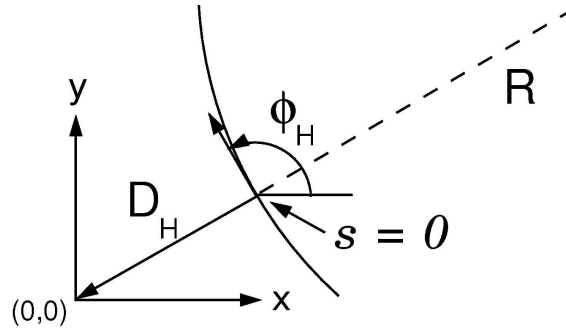
Figure 5.2: Helix parameter in the $X - Y$ plane for a positively charged track.

information from different tracking detectors. In this first stage, starting from the outermost CTD superlayer, each track candidate begins as a track seed which consists of three CTD hits from an axial superlayer. The second step assigns the seed hits, together with all other hits picked up in the same superlayer, to initial trajectories and combines matched track segments in the CTD with hit-clusters in the MVD. By this procedure, tracks with combined CTD and MVD hits as well as hits in only one of these detectors are stored[1]. In the third step, the track information by VCTRACK is passed to a track-fitting package referred to as rigorous track fit (RTFIT [133]), which is based on Kalman filter techniques [132]. This approach improves the tracking accuracy by considering inhomogeneities in the magnetic field, multiple scattering and ionisation energy loss of particles. Finally the track helix parameters and their covariances are determined.

After the track reconstruction, the primary vertex and secondary vertices originating from the decay of long-lived particles (i.e. $K_S^0 \rightarrow \pi^+\pi^-$ or $\Lambda^0 \rightarrow p\pi^-$), photon conversion ($\gamma \rightarrow e^+e^-$) or particle interactions in the detector material, can be reconstructed.
The primary vertex is reconstructed by the VCTRACK package. Track pairs compatible with a common vertex are combined with other track pairs and a vertex is determined based on the overall χ^2 of the best combination, followed by a deterministic annealing filter (DAF) [134]. Secondary vertices are fitted in a similar way, but only tracks fulfilling the criteria

- $p_T > 0.5$ GeV,

- number of MVD hits: $N_{MVD} \geq 4$ and

- number of CTD superlayer hits: $N_{SL,CTD} \geq 3$,

are considered for vertex-fitting. Tracks contributing too much to the χ^2 of the vertex are discarded one by one until the quality of the fit is acceptable. If a secondary vertex is found by this fit procedure, one obtains three vertex coordinates, the covariance matrix as well as the χ^2.

---

[1]Tracks with hits only in the CTD or MVD are referred to as *CTD-only* and *MVD-only* tracks, respectively.

5.2 Reconstruction of calorimetric variables

The CAL energy measurement needs to be corrected for several detector effects. So-called *hot cells* corresponding to a malfunction in the CAL electronics or the photomultipliers (PM) have been excluded. Noisy channels are suppressed by setting energy thresholds for cells and using redundant information of both PMs of a CAL cell. Initially, a cell energy cut of 60 MeV is applied in order to suppress noise in the EMC (110 MeV in the HAC) sections. For isolated cells, this threshold is set to 100 MeV in the EMC and 150 MeV in the HAC. These thresholds were determined in order to correspond to approximately four standard deviations of the noise distributions. Occasionally, a PM in the CAL fires, resulting in a spark which induces a large signal. Each cell of the CAL is mointored by two PMs, therefore sparks can in general be rejected by analysing the imbalance in the two readings.

Studies comparing the calorimetric reconstruction in data and MC simulations resulted in a discrepancy which can be corrected by multiplying the energies measured in the data events by a correction factor [135–139], which are summarized in Tab. 5.1 for the electromagnetic and hadronic parts of the forward, barrel and rear CAL.

CAL section	Cell type	energy correction 1996-1997	energy correction 1998-2004	energy correction 2005-2007
FCAL	electromagnetic	+4.0%	+2.4%	+5.0%
	hadronic	-5.0%	-5.9%	-3.5%
BCAL	electromagnetic	+4.0%	+5.3%	+6.4%
	hadronic	+8.2%	+9.6%	+10.7%
RCAL	electromagnetic	+2.2%	+2.2%	+2.2%
	hadronic	+2.2%	+2.2%	+2.2%

Table 5.1: Energy correction factors for the electromagnetic and hadronic parts of the FCAL, BCAL and RCAL for the running periods 1996-2007.

From the corrected CAL information, the total transverse energy E_T^{CAL} is calculated as the scalar sum of the transverse energy of each cells:

$$E_T^{CAL} = \sum_{i=1}^{N_{cells}} E_i \sin(\theta_i). \tag{5.2}$$

Dead material in front of the CAL as well as the presence of particles which do not release all their energy in the CAL (like muons) cause a systematic shift of the calorimetric reconstruction towards lower values and require additional corrections. They are applied to energy flow objects, so-called EFOs (cf. Sec. 5.3).

5.3 Reconstruction of the hadronic system

The energy measurement of particles is fundamental for the reconstruction of event properties. For the CAL energy measurement the resolution improves with increasing energy of the parti-

cles ($\sigma_E/E \sim 1/\sqrt{E}$), while the resolution of the CTD gives better energy estimation for lower energy particles.
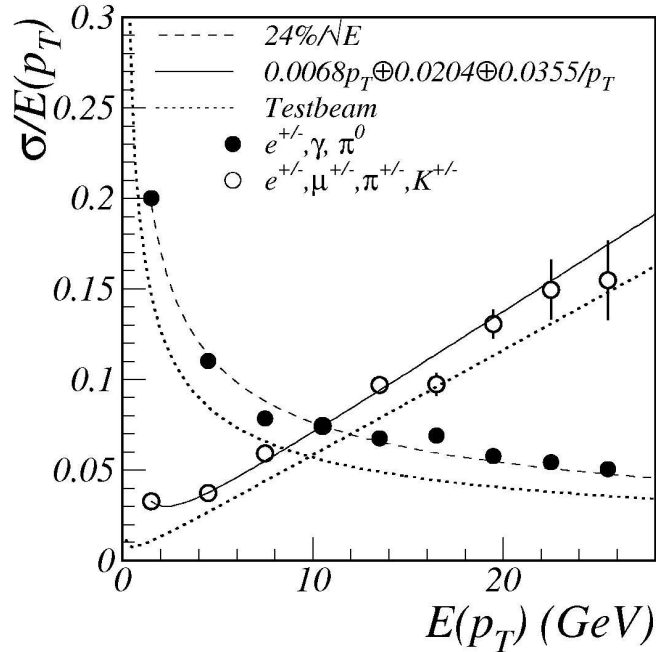
Figure 5.3: Resolutions from single particle MC simulations. The track transverse momentum resolution in the CTD (open markers) and the CAL energy resolution (close markers) is shown.

In order to benefit from the most accurate energy determination in both energy ranges, the track reconstruction and the CAL energy measurement are combined to *energy flow objects* (EFOs)[2] [140]. The resolution dependence on the electromagnetic energy and the transverse momentum of the track is presented in Fig. 5.3 with the typical resolutions used in the tuning of the combination algorithm.

The tracking information is mainly used below 10-15 GeV and the calorimeter energy measurement for higher energies in order to form four-vectors representing the oriented energy deposition of particles traversing the detector. In the following, the combination process as well as corrections due to the influence of dead material and the presence of muons are described.

5.3.1 Reconstruction of energy flow objects

The use of EFOs is justified by the fact that the hadronic energy posesses both a charged and a neutral particle component. Both are measured by the calorimeter, but a large fraction of the charged particles are also measured by the tracking detectors. In many cases the resolution of the tracking devices is better than that of the calorimeter, especially if the charged particles have

---

[2]In ZEUS nomenclature, they are also referred to as ZUFOs, ZEUS Unidentified Flow Objects

low energies or if they cross a large thickness of dead material before being detected in the CAL.

The use of EFOs rather than the usual energy deposits in the CAL is also driven by the design of the ZEUS calorimeter (cf. Sec. 4.2), which is divided in three parts (FCAL, BCAL and RCAL). This separation is a serious complication for local clustering algorithms in handling the energy deposits of a single particle which is not confined within a single part of the CAL since the energy will be split in two or more clusters. Therefore, the reconstruction procedure of EFOs is done in two steps:

Step 1: Energy cell measurements are clustered separately in the three CAL sections and the different cell layers (electromagnetic and hadronic cells). Each cell with sufficient energy is considered a candidate to be connected with one of its neighbours. The connection is made with the nearest neighbour with the highest energy or with the highest energy cell next to the neighbour. This procedure is iterated for each cell and produces a unique assignment of a cell to a *cell island*, as shown in Fig. 5.4.
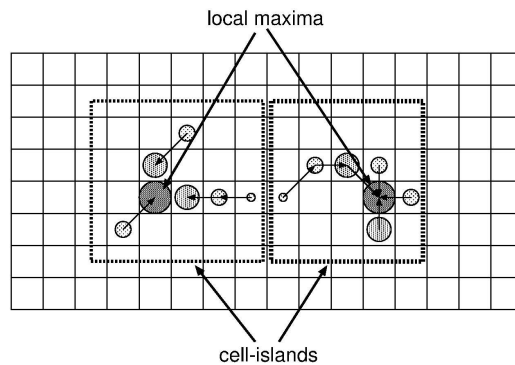

Figure 5.4: A schematic diagram showing how cell-islands are formed.

Step 2: Cell islands belonging to a shower of a single particle or a jet of particles are collected into so-called *cone islands*. The matching of cell islands starts from the outermost hadronic layer of the calorimeter and proceeds inwards. The angular separation between cell islands of different layers is calculated in $\theta - \phi$ space and transformed to a probability according to a distribution determined by a single pion MC simulation. Links with high probabilty are accepted provided that the probability is larger than a threshold. Once the linking procedure is completed, the cone islands are generated by combining all calorimeter cells which point to the same cone island in the electromagnetic sections. The cone island centre is calculated as the energy weighted mean of the cell centres which have been corrected for the imbalance of the two photomultiplier measurements per cell. The energy weight is determined logarithmically rather than linearly to cope with the observed systematic bias due to the varying cell projectivity resulting from the CAL geometry.

For the track reconstruction, vertex-fitted tracks which pass at least 4 superlayers in the transverse momentum range $0.1 < p_T^{track} < 20$ GeV are selected. If the track has hits in more than

7 superlayers, the upper transverse momentum cut is raised to $p_T^{track} < 25$ GeV. The tracks are extrapolated to the inner CAL surface taking the magnetic field into account and further into the CAL by a linear approximation using the track momentum vector at the CAL surface. The matching criterion used for the track-island matching is the distance-of-closest-approach (DCA) of the track and the position of the island. A track is matched to the island, if the DCA is smaller than the island radius or lower than 20 cm (cf. Fig. 5.5).
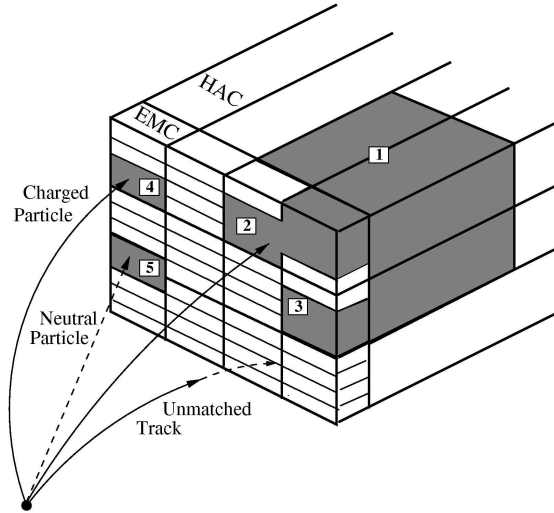
Figure 5.5: Reconstruction of EFOs by a match between CAL cells clustered into cone islands (HAC cell 1 and EMC cell 2 and 3 are joined to form a cone island) and tracks (taken from [140]). The different match categories of a charged particle (track is matched to cone island 4), neutral particle (no track is matched to cone island 5) and unmatched track are shown.

The track information is used in the following cases:

- The relative uncertainty on the momentum measurement is smaller than the relative uncertainty of the calorimeter measurement:

$$\sigma(p)/p < \sigma(E_{CAL})/E_{CAL}, \tag{5.3}$$

where $\sigma(p)$ and $\sigma(E_{CAL})$ are the measured resolutions of the momentum of the tracking and the energy in the CAL respectively.

- The track momentum exceeds the energy measurement in the CAL within the resolution on the measured ratio E_{CAL}/p:

$$E_{CAL}/p < 1.0 + 1.2 \cdot \sigma(E_{CAL}/p), \tag{5.4}$$

where the uncertainty $\sigma(E_{CAL}/p)$ is given by

$$\sigma(E_{CAL}/p) = (E_{CAL}/p^2) \cdot \sigma(p) \oplus (1/p) \cdot \sigma(E_{CAL}). \tag{5.5}$$

Since muons are minimum ionising particles (MIPs) and lose their energy predominantly by ionisation, the measured energy in the CAL is not proportional to the momentum. Therefore, EFOs with the properties of a muon are treated differently and the tracking information is favoured over the energy measurement if:

- $E_{CAL} < 5$ GeV,

- $E_{CAL}/p < 0.25$,

- $p_T < 30$ GeV.

In addition to the described clean matches of one track to one island, the following three categories exist:

- Tracks without an associated island are treated as charged particles and the CTD information is used on the assumption that the particle is a pion,

- Cone islands not matched to a track are treated as neutral particles and the CAL energy measurement is used,

- Cone islands with more than three associated tracks are treated as jets and the CAL information is used.

The more complicated 1-to-2, 1-to-3, 2-to-1 and 2-to-2 track-island matches are treated similary to the 1-to-1 match, substituting the CAL energy and the CTD momentum with the sum of the energies of the islands and the sum of the momenta of the tracks respectively. In case of a single track is matched to two or more islands and the CAL energy is favoured, the more precise angular information of the track is used.

5.3.2   Cone island correction

Comparisions between data and MC simulations have shown discrepancies in the reconstruction of EFOs using calorimetric islands [141]. Therefore, the following corrections have been applied to the EFOs:

Energy loss in dead material: Energy losses due to dead material in general are difficult to implement fully into MC simulations. A detailed dead material map, shown in Fig. 5.6, has been used to correct the contribution to the energy loss of mainly the beam pipe, the tracking detectors and the solenoid.

The dead material contribution between the interaction point and the calorimeters varies with the polar angle between 1 and 3 radiation lengths X_0 and is more significant for low energy particles. Corrections on the EFOs are introduced depending on the polar angle and the cone island energy.
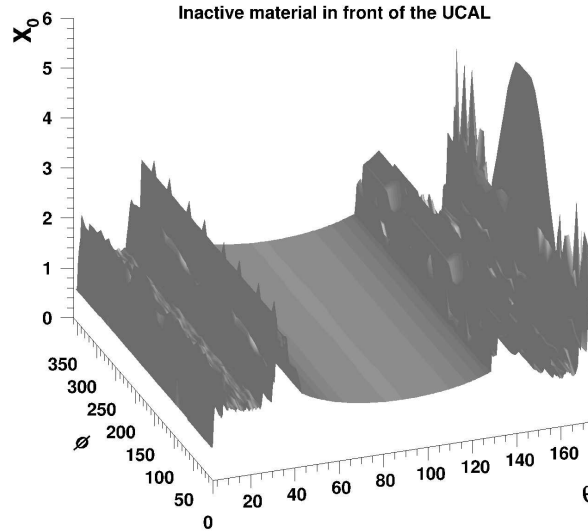
Figure 5.6: Map of the dead material distribution between the interaction region and the CAL as a function of θ and ϕ [141].

Calorimeter geometry: The zones of the cracks between the calorimeter sectors are not well simulated and corrections are introduced offline.

Energy overestimation of low-momentum hadrons: Protons and pions with momenta below ~ 1 GeV lose energy mainly through ionisation without hadronic interactions. In this case, the CAL is not compensating anymore ($e/h \sim 0.6$). This effect causes an overestimation of the energy of low-momentum hadrons which has to be corrected.

5.3.3 Corrections for the presence of a muon

The reconstruction of the hadronic system of an event only from the calorimeter would underestimate the energy in the presence of a muon. For a muon, the energy loss while traversing the CAL is dominated by ionisation and therefore the measured energy is not proportional to and in general less than the momentum.

If EFOs are used to reconstruct the hadronic system, this effect is compensated since EFOs have been optimised to take the muonic energy signature in the CAL correctly into account and favour the tracking information over the CAL measurement. This is only sufficient for semi-isolated muons. In the case that the muon is contained in a hadron-jet and the corresponding EFOs represent more than one particle, further corrections have to be implemented. The energy release of a muon in the CAL is parametrised as a function of the polar angle θ using single muon MC simulations (cf. Fig. 5.7)

A correction of the EFO associated to a muon is applied using the expected energy loss in the calorimeter. The correction is applied to EFOs consisting at least of a track. The muons are extracted from the general muon reconstruction and are preselected by the following cuts to
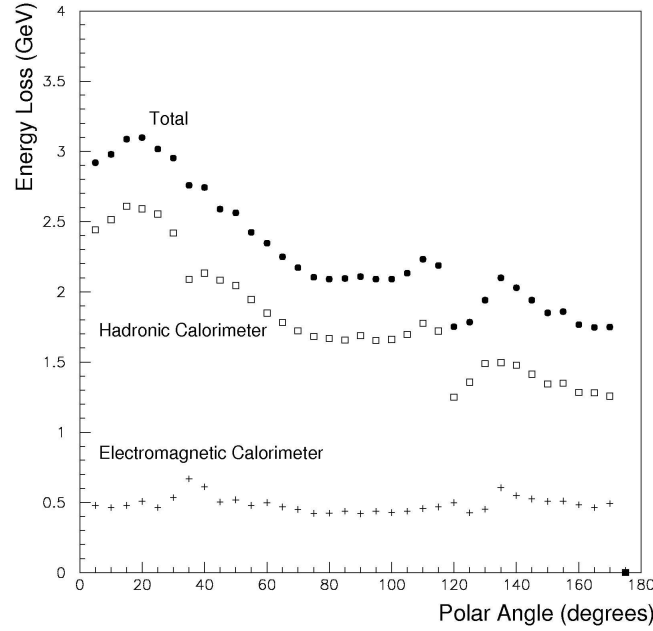
Figure 5.7: Energy loss of a muon in the CAL as a function of the polar angle θ (full circles) and the energy fractions in the electromagnetic (crosses) and hadronic (open squares) calorimeter sections [141].

ensure a good quality muon:

- Muon quality ≥ 4,

- Muon track is fitted to a vertex,

- $p > 1$ GeV.

The association of the muon the EFO is carried out by the used track. The following corrections to the EFOs are applied per muon:

- If the EFO uses the track information for the energy determination, no correction is needed.

- If the EFO uses the CAL information for the four-vector determination and the energy of the EFO is between 50% and 150% of the predicted energy loss of a muon, the EFO four-vector is determined from the reconstructed muon properties, as given by the CTD.

- If the EFO uses the CAL information for the four-vector determination and the energy of the EFO is larger than 150% of the predicted energy loss of a muon, $E_{EFO} > 1.5E_{MIP}$, the EFO is split into two EFOs. One EFO is set to the four-vector of the muon track while the other holds the difference between the initial and the muon EFO to separate the muonic and hadronic system of the event.

- If the EFO energy is less than 50% of the predicted energy loss of a muon, $E_{EFO} < 0.5E_{MIP}$, a new EFO of the muon four-vector is added to the EFO list.

5.4 Modification of the EFO reconstruction algorithm

The first iteration of the HERA II data set and corresponding Monte Carlo samples from the Grand Reprocessing procedure used in this analysis contains EFOs from the combination of CAL measurements and the information of tracks, which are associated to the primary vertex or secondary vertices, while the resulting muon EFOs originate only from primary vertex tracks. As a result, muon candidates from tracks with some displacement from the primary vertex (e.g. muons from the decay of B hadrons) are not considered as possible muon EFOs. As technical task in this thesis, the EFO reconstruction algorithm [140] was modified in that way, that tracks are taken into account, which are close to, but not associated to the primary vertex. Since the measurement of beauty quark production by means of muons in the final state is the main topic of this thesis, a beauty Monte Carlo sample generated with PYTHIA [44] with 100.000 events was used in order to estimate the effect of the modification of the EFO reconstruction algorithm with respect to the reconstruction of muon EFOs.

In principle, the criteria to match a non-vertex track to an EFO is similar to those of vertex-associated tracks (cf. Sec. 5.3.1). However, most of all non-vertex tracks are not suited for the matching to EFOs since some of them can be the result of misidentified kaons or pions, cosmic ray muons, interaction with detector components or beam gas, etc. and can be localised far away from the interaction point. Thus, the impact parameter δ of all vertex- and non-vertex associated tracks in the $X - Y$ plane as well as in Z was considered, as shown in Fig. 5.8, in order to determine an adequate upper limit on both quantities for non-vertex tracks, which should be used for the EFO matching.
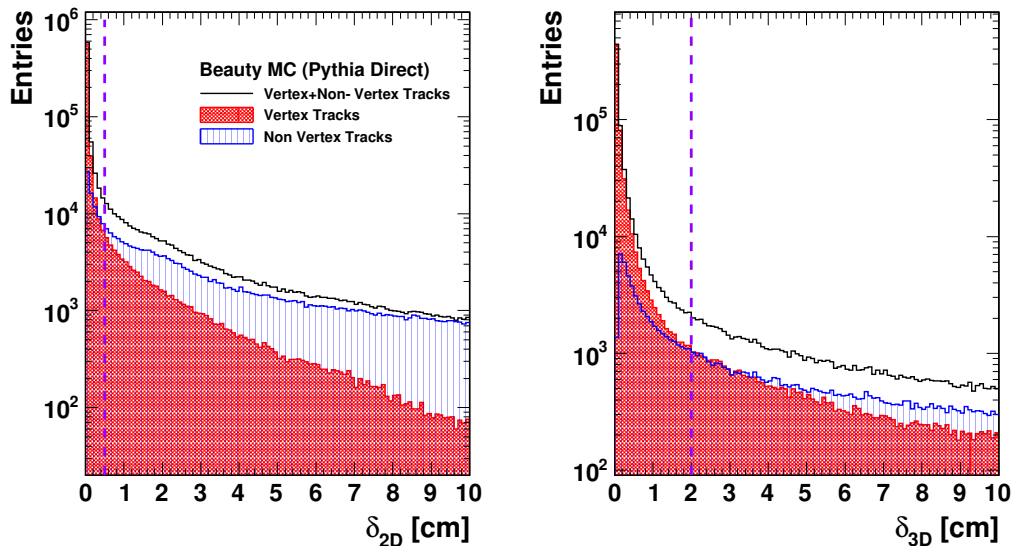

Figure 5.8: Impact parameter δ in the $X - Y$ plane and in Z direction for vertex- (filled area), non-vertex (area with vertical lines) and the sum of all tracks (solid line) from a beauty MC photoproduction subsample. Also shown are the proposed cuts on δ_{2D} and δ_{3D} for the non-vertex tracks (dashed lines).

Reasonable upper limits on both impact parameter quantities were found to be

$$\delta_{2D} \leq 0.5 \text{ cm} \qquad \text{and} \qquad \delta_{3D} \leq 2.0 \text{ cm}. \qquad (5.6)$$

In Fig. 5.9, different quantities, which are sensitive to the EFO reconstruction, are shown before (filled area) and after (area with horizontal lines) taking non-vertex tracks into account. Displayed are the total number of tracks used for the EFO-track matching, the amount of EFOs per event, the quantity $E - p_z$ of the hadronic system as well as the transverse energy of all jets (cf. Sec. 5.8).
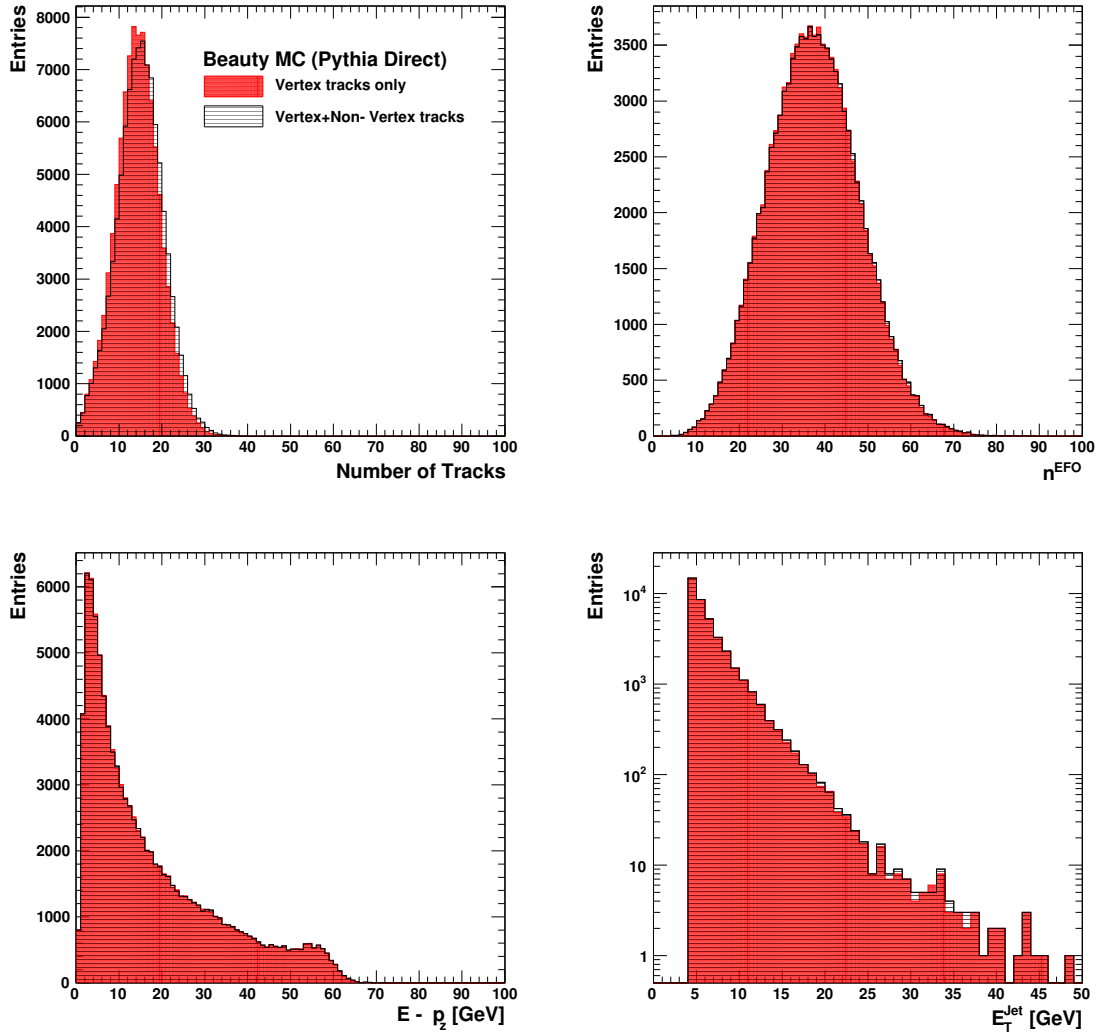
Figure 5.9: Control distribution for EFO dependent quantities with all tracks (area with horizontal lines) and only with vertex-associated tracks (filled area) in the used beauty MC photoproduction subsample. Shown are the amount of tracks used for the EFO reconstruction, the amount of EFOs per event, $E - p_z$ of the hadronic system as well as the transverse energy E_T^{Jet} of all jets.

As one can see from these distributions, the shapes of these quantities change slighty, only the

amount of tracks used for the EFO reconstruction shifts to larger values, as expected. In total, approximately 2% additional EFOs are reconstructed from non-vertex tracks. A further look at the different EFO types reveals that the predominant contribution of all additional tracks is assigned to EFOs, while the remaing unassigned tracks change the type of already existing ones, as shown in Fig. 5.10 (right). The different types of EFOs are listed in Tab. 5.2.
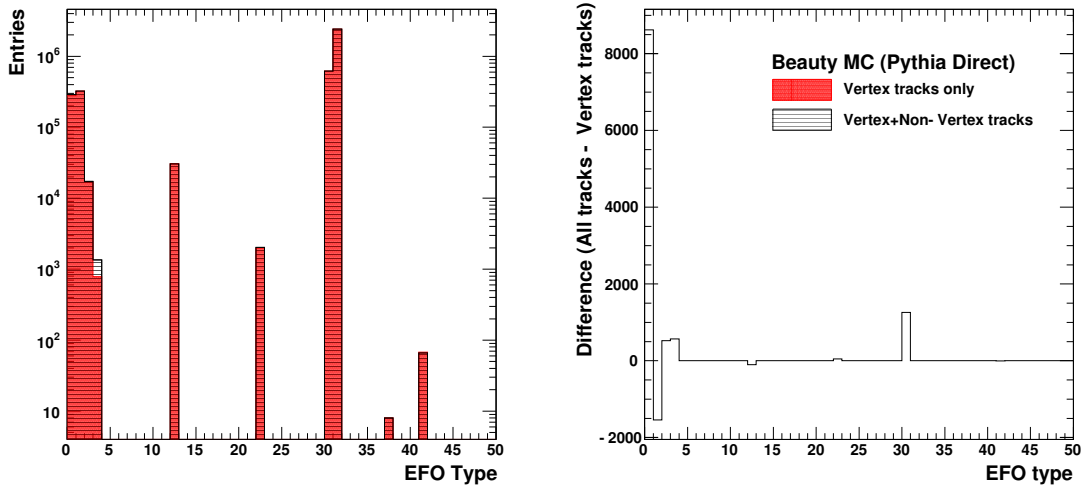

Figure 5.10: EFO types before (filled area) and after (area with horizontal lines) modification of the EFO reconstruction algorithm in the used beauty MC photoproduction subsample. In the right figure, the histogram without the EFO reconstruction modification was subtracted from the one containing these modifications in order to visualize the effect of the modification. The different EFO types and their corresponding bin-key is given in Tab. 5.2.

EFO type	Definition
0	1 track, not matched to island
1 or 10	1-to-1 match between track and CAL island
2	2 tracks match 1 island
3	3 tracks match 1 island
12	1 track matches 2 islands
22	2 tracks match 2 islands
30	some track match, but only CAL information used
31	1 island, not matched to track
32	1 island, not matched to track, leftover CAL energy from type 10
37	1 track matches 2 islands, CAL energy, tracking angle used
41	1-1 match, CAL energy, tracking angle used

Table 5.2: Definition of the different types of EFO [140].

Finally, it was checked, how many additional muons were reconstructed from non-vertex tracks. In Fig. 5.11, the impact parameter δ in both, the $X - Y$ plane and in Z, is illustrated for all reconstructed muons (area with horizontal lines) and for muons from tracks, which are not associated to a vertex (filled area). In total, the amount of reconstructed muons increased by $\sim 5.1\%$, where the additional muons have relativ high impact parameter.
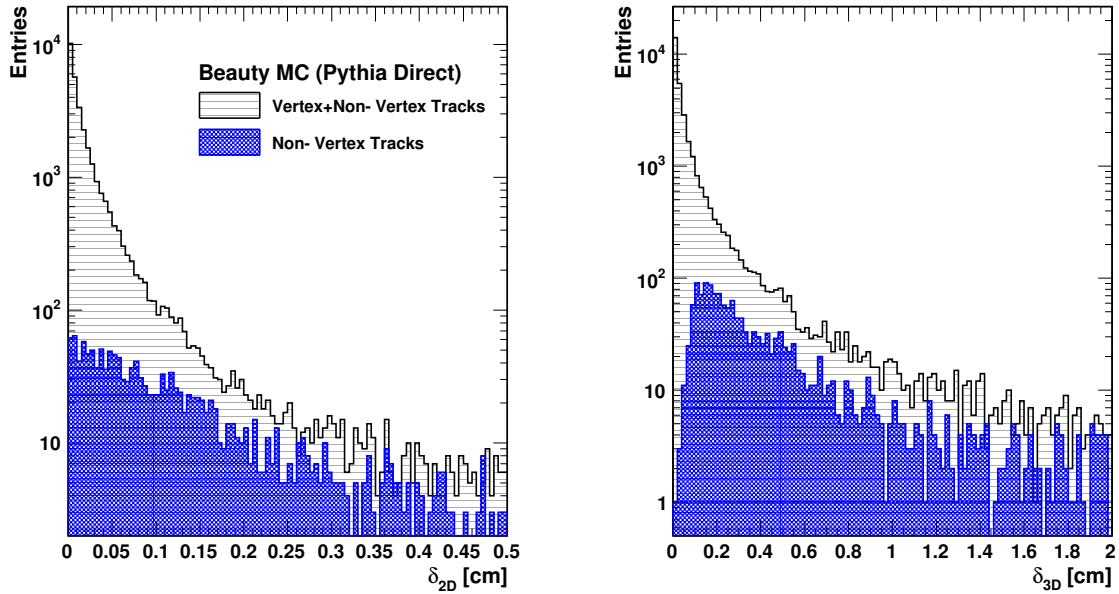
Figure 5.11: Impact parameter in the $X - Y$ plane and in Z direction muons reconstructed from all (area with horizontal lines) and from non-vertex tracks (filled area).

Although the additional contribution of reconstructed muons is quite satisfying, some improvements could be performed on the impact parameter-cut of the non-vertex tracks. Studies concerning this matter are in progress [142]. Nevertheless, in the currently produced next version of the HERA II data set and corresponding Monte Carlo samples from the Grand Reprocessing procedure, the modifications of the EFO reconstruction algorithm are implemented successfully.

5.5 Muon reconstruction

The selection and reconstruction of muons with a good signal-to-background ratio is important in order to measure muons from semi-leptonic beauty quark decays. This has been achieved due to the redundancy of the muon signature measured in several components of the ZEUS detector. First, the main characteristics of muon signatures as well as the corresponding backgrounds are described, followed by a description of different muon finder algorithms and their combination to a general muon finder package, called GMUON [143].

5.5.1 Muon signature

Muons are special particles concerning the penetration power in matter. They are minimal ionizing particles (MIPs), i.e. their energy loss in the uranium of the calorimeter is almost independent of the muon momentum. The energy deposit can be calculated as [144]:

$$\frac{dE}{dx} = 1.082 \frac{\text{MeV}}{\text{g/cm}^2} \tag{5.7}$$

yielding a range in iron of about 1 m/GeV.

Four main features are used in ZEUS to tag muons from semi-leptonic beauty decays:

1. The charge of the muons leads to a track which can be reconstructed by use of the tracking detectors. From this track, the muon momentum and direction can be determined.

2. Muons from beauty decays are produced very close to the primary vertex of the $e^{\pm}p$ collision. Within the CTD resolution, they are associated to the primary vertex (prompt muons). This requirement reduces the background from kaon and pion decays in flight. In HERA II, the MVD enables the possibility to determine the secondary vertex from the B meson decay. Muons can then be associated to this secondary vertex.

3. Due to the minimum ionising property, high-energy muons are not stopped in the CAL. They leave a relatively small amount of energy along their trajectory in the CAL and reach the muon chambers where they can be identified as charged tracks.

4. Muons from heavy flavour decays are accompanied by hadrons, therefore they are non-isolated.

5.5.2 Muon backgrounds

The fake muon background can be summarised as:

- **Muons from kaon and pion decays:** Despite the fact that kaons and pions are long-lived particles, they have a finite probability to decay within the CTD volume before they reach the CAL or in the CAL before they interact. Many of such muons can be rejected by the muon track momentum matching between the CTD and the muon chamber measurements or the CTD track vertex reconstruction. But some fake muons can pass through the rejection.

- **Sail-through:** Hadrons have a small, but finite probability to traverse the material in front of the muon detection system without interaction. In that case, they will be identified as a muon.

- **Leakage of hadronic shower:** Hadronic particles escaping the calorimeter can traverse the inner and outer muon chambers. This contribution is partially removed by the muon reconstruction algorithm and a cut based on the quality of the matching between tracks and muon segments. For hadronic-shower leakage and sail-throughs the detected muon is actually a hadron, hence these sources are treated together and called *punch-through*.

- **Cosmic ray muons:** A single cosmic ray muon traversing the detector close to the primary vertex can be misreconstructed as two unlike-sign muons originating from the same vertex. Since both the event timing and the vertex distribution are random for such events, most of them can be rejected by use of vertex and timing cuts, the remaining ones by requiring that both muons are not completely back-to-back in polar angle θ and azimuth angle ϕ.

- **Matching ambiguities:** Non-muon tracks reconstructed in the CTD can be accidentally associated to muon system hits or tracks produced either by a true muon or a background muon from one of the other background categories above. The momentum of this misassociated track will then be assigned to the muon candidate. Through the same mechanism, alternative reconstructions can exist for the same muon candidate, at most one of which is the true muon. This is called *matching ambiguity background.*

Hadron-related background, including matching ambiguities, are the dominant part of the background for semi-leptonic muons from heavy flavour decays. Cosmis rays dominate the background for elastic dimuon candidates.

5.5.3   Muon reconstruction algorithms

Different algorithms for muon identification are available for ZEUS. Most of them (like BRE-MAT and MPMATCH) are using the FMUON, BMUON and RMUON chambers, some the BAC (i.e. MUBAC) or only the CAL information (MV). The general methods of the different algorithms are summarised below followed by the methods of combining the result of these algorithms.

- **MV:** The MV algorithm [145] performs a CAL MIP signature with a CTD reconstructed track for muon identification. It is only suited for isolated muons with $p > 1$ GeV due to the large hadronic background for low momentum muons in the CAL. The MV algorithm evaluates the compatibility of the cluster shape and energy distribution with a MIP signature like a neural net. MV combines the energy deposit in different CAL sections (EMC, HAC1&2), the number of cells in these sections and the polar and azimuth angle θ and ϕ, and compares these variables to MC samples of muons and hadrons. Based on these quantities, it provides a probability for an energy deposit to be assosicated with a muon.

  MV is also useful for identification of very forward muons without a track because it is able to detect clusters without a track and it has a large geometric coverage with a low momentum threshold.

- **GLOMU:** The muon reconstruction algorithm GLOMU [146] is a muon finder for the TLT, which is also available for offline analysis. GLOMU combines the muon track segment reconstruction in the inner chambers of BMUON and RMUON with the tracking in the CTD and a MIP signature in the CAL. The following information from the three detector components are included in a χ^2 fit:

Muon track segments in the inner barrel and rear muon chambers: Muon track segments are reconstructed in the inner barrel and rear muon chambers to reconstruct track segments. For each track the point of entrance and the polar and azimuth angle θ and ϕ with the associated errors are available.

Good quality track in the CTD: A good quality track in the CTD satisfying the following requirements:

- $\chi^2 \leq 20$,
- DCA ≤ 10 cm,
- $|z| \leq 75$ cm,
- $\theta \geq 20°$,
- barrel region: $p_T \geq 1$ GeV,
- rear region: $p \geq 1$ GeV,

is extrapolated outwards to a fiducal volume outside the CTD. The fiducial volume is a cylinder of $R = 94$ cm radius between $z = $ -146 cm and $z = 180$ cm [146]. Each extrapolated track provides the position in space, the direction in polar and azimuth angle θ and ϕ, the momentum as well as the errors at the fiducial volume.

MIP in the CAL: Energy deposits compatible to a MIP are reconstructed by use of a specialised MIP finder. Output variables are the position and the timing information of each MIP.

The matching is performed in θ and ϕ separately for all combinations of the following properties. θ and ϕ are obtained by

- a CTD track
- a BRMUON track
- a segment connecting the CTD-CAL points
- a segment connecting the BMUI-CAL and RMUI-CAL points.

The total χ^2 is the sum of χ^2_θ and χ^2_ϕ. For matching, a total $\chi^2 \leq 20$ is required. The advantage of GLOMU is the low p/p_T threshold and a resonably low background. On the other hand, it is only suited for semi-isolated muons, has a reduced geometrical coverage due to the exclusive usage of the inner barrel and rear muon chambers and a moderate efficiency.

- **BREMAT:** The BREMAT algorithm [147] reconstructs muons by matching tracks extrapolated from the CTD to the BMUI and RMUI and reconstructed muon segments in the inner and/or outer muon chambers. The following CTD track preselection is applied within BREMAT:

  - Track momentum $p > 1$ GeV

- Track polar angle $\theta > 20°$
- Track should start from the first CTD superlayer and reach at least the third super-layer
- Distance-of-closest-approach (DCA) of the muon track to the interaction point $|DCA| <$ 10 cm
- z position of the DCA to the interaction point $|Z_{DCA}| < 75$ cm
- χ^2 per number of degrees of freedom (ndf) of the track fit $\chi^2/\text{ndf} < 5$
- Distance Δ between a central point on a barrel/rear muon segment and the crossing point of the straight line obtained by extrapolation of the track to the muon chambers should be less than 150 cm.

The possible scattering processes of the muon traversing the considerable amount of material on the way to the muon chambers (e.g. the magnet, CAL) as well as the variation of the magnetic field along the trajectory are simulated using the GEANE [148] package and also included in the error matrix of the extrapolated CTD track. The material in front of the inner muon chambers leads to an effective minimal momentum for BREMAT muons of about 1 GeV.

The reconstructed muon track segments can contain either hits of the inner muon chambers or, if muons reached the outer muon chamber, hits from both the inner and outer muon chambers. In the first case, extrapolated CTD tracks are matched to muon segments in position and angle in two projections (4 degrees of freedom (d.o.f.) match). In the second case, the muon momentum can be measured by the outer and inner muon chambers, yielding an additional degree of freedom and a higher quality matching (5 d.o.f match).

- **MPMATCH:** In order to reconstruct forward muons, the MPMATCH algorithm [149], which is similar to BREMAT, is used. It matches tracks in the forward muon chambers with tracks from the CTD in the overlap region of the CTD and the forward muon chambers. Muon tracks which are reconstructed in the FMUON system are defined by five parameters in the ZEUS reference system: $(x, y, dx/dz, dy/dz, Q/p)$. The matching starts with an FMUON track by opening a corridor in the polar angle θ and the azimuth angle ϕ around the track. If at least one CTD track is found, the FMUON track is extrapolated backwards to the z coordinate of the most outer hit of the CTD track. For the extrapolation, the GEANE package is used. A fit between the two tracks is performed using a Kalman filter [150]. In case of multiple CTD tracks in the corridor, the χ^2 of the fit is used to identify the best match. This procedure is iterative for each track. For the best match, a vertex refit is done for the FMUON track and it is extrapolated backwards to the z coordinate of the vertex. Finally, a fit between the extrapolated FMUON track and the CTD track including the vertex position is performed. Like BREMAT, MPMATCH is suited for high momentum non-isolated muons in the forward region but suffers from the low FMUON efficiency and a high momentum threshold.

- **MAMMA:** The MAMMA algorithm [143] matches isolated muons with a MIP signature to an inner forward muon chamber segment. Since the background is very high in the

forward region, this finder is only suited for low background analyses with well-isolated muons.

- **MUFO:** The MUFO reconstruction algorithm [151] matches a track segment from the FMUON to a track reconstructed in the CTD similar to MPMATCH. It can use MUBAC for additional background rejection and provides a momentum fit of the muon using the FMUON and CTD information. The algorithm can also provide matching between a FMUON segment and the primary vertex without CTD tracking. This can be used to reconstruct very forward muon tracks which can not be reconstructed by the CTD due to the tracking chamber acceptance.

- **MUBAC:** The MUBAC algorithm [152] provides BAC muon candidates to be further matched with a vertex fitted track reconstructed in the CTD by a simple DCA algorithm. In order to match both tracks, the DCA should be less than 120 cm, whereas for the case of high quality reconstructed muons the cut on the DCA is tightened to 50 cm.

The BAC provides a digital (hit) and an analog (pad) readout which are used in combination for muon reconstruction, taking into account the errors on the measurement. The BAC provides a clean muon signature with a larger geometrical coverage than the muon chambers, in particular the bottom part of the detector and the gaps between the forward and barrel muon chambers. The momentum threshold on reconstructed muons is high due to the amount of material along the trajectory of the muon from the interaction point to the BAC. Therefore, the minimum p_T of muons in the barrel to reach the BAC is 2 GeV. Muons in the forward region need $p > 2.8$ GeV and in the rear region $p > 1.6$ GeV.

5.5.4 GMUON - a general muon finder

All muon reconstruction algorithms mentioned above are suited for specific event topologies concerning for example muon isolation and have different thresholds and geometrical coverage. A general muon reconstruction benefits from redundancies by the combination of all algorithms. The GMUON package [143] collects the results of the reconstructions and combines their information in a general list of reconstructed muon candidates. The qualities of the individual reconstructions are taken as a reference to categorize the muons by assigning a quality factor to each candidate. If a candidate is reconstructed by more than one algorithm, the quality factor is increased to benefit from the simultaneous identification. If the reconstruction of a single algorithm does not yield a sufficiently accurate candidate on its own, the possible redundancy with other algorithms is used to recover the candidate. The GMUON package assigns quality factors in the range of 0 to 6 to the candidates from the general list. Quality 0 is the lowest quality while quality 6 describes the candidates with the highest reconstruciton accuracy. The quality factor stages were optimized on beauty and background MC samples such that the signal-to-background ratio increases approximately by a factor of two for each unit of quality. An overview of the different finder combinations and the resulting GMUON quality is given in Tab. A.1 and A.2 in Appendix A.

Forward muon corrections: Muons in the forward region are detected using the MPMATCH of MUFO finder. The original GMUON quality assignment does not treat some sources of background and overestimates the quality of the forward muon candidates. In the simulations, the noise in the muon chambers is not included, but sometimes high in the data. If an arbitrary track is matched to these noisy cells, the identification of muons can be faked. Additionally, the forward region suffers from secondary particles produced in the magnets and in material in the beam pipe.

In order to take this background into account, the default quality is reduced depending on the used finders. The reduction of spurios hits in the forward muon chambers is based on the number of detector planes used by the forward muon track fit. For less than five planes, the quality is reduced according to the following Tab. 5.3:

Found by	Property	value	quality change
MPMATCH or MUFO	Nr. d.o.f.	3	-2
MPMATCH or MUFO	Nr. d.o.f.	1	-3
MPMATCH or MUFO	Starting at innermost plane	no	-1
MPMATCH or MUFO	MUBAC match	yes	+1
MPMATCH or MUFO	MV match	yes	+2
MUBAC	not (MPMATCH or MUFO) and $\eta^\mu > 1.2$	-	-1

Table 5.3: Definition of the forward muon quality correction.

Also the abscence of a hit in the innermost chamber suggests a fake muon and the quality is reduced by one. The quality can be recovered if MUBAC and MV found the same muon candidate. An additional reconstruction in MUBAC increases the quality by one, in the case of MV, the quality is increased by two but only to a maximum of the initial quality. Therefore, the resulting quality is never higher than before the correction. For muon candidates found only by MUBAC, the quality is reduced by one to correct for noise in the BAC.

HAC2 energy deposit: The rejection of muon candidates produced by noisy muon chambers is important, in particular because this kind of misidentification is not simulated by the MC. When a fake hit in the muon chambers is associated to a track coming from another particle, usually this particle is not able to reach the secand part of the hadronic calorimeter (HAC2). Muons leave a MIP energy deposit in the HAC2. Therefore, all moun candidates in the forward region without an energy deposit in HAC2 are rejected. In the barrel region the muon probability calculated by the MV finder is used in addition to take into account the passage of muons through gaps in the coverage of the CAL. Only muon candidates without an HAC2 energy deposit and a MV probability $P < 0.01$ are discarded.

5.6   MC Muon efficiency corrections

For cross-section measurements in this analysis and other muon related analyses, the muon reconstruction efficiency is essential. In the MC simulations, the efficiency of the muon cham-

bers is in general overestimated and therefore has to be corrected. The processes chosen for studying the muon efficiency are the decays J/ψ or $\psi' \rightarrow \mu^+\mu^-$ (cf. Fig. 5.12 and 2.17) and the Bethe-Heitler process (cf. Fig. 2.18) as sources of muons due to their simple and easily selectable topology of two isolated muons. Since the MV finder is well suited for isolated muons and uses for reconstruction the CAL, an independent, well simulated detector component, it can be used as the reference.

In order to obtain a clean dimuon sample for the evaluation of muon efficiency correction factors for the HERA II period, the following cuts were applied [154]:

- EVTAKE = 1, i.e. only events are required with reliable CTD, CAL and Solenoid,

- MBTAKE ON, i.e. only events are allowed with working BRMUON chambers,

- FMUTAKE OFF, i.e. good quality of the FMUON chambers is not required,

- exlude shifted vertex runs (run-range 37588 - 37639)

- cut on the global event timing determined by the CAL to reject cosmic ray candidates: $|T_g| \leq 10$ ns (applied to data only).

- at least two muons reconstructed with GMUON of a quality ≥ 1 and found at least by MV finder and with momentum taken from the CTD reconstruction package.

- cut on the vertex position (identical to cut in HERA I analyses) to reject cosmics and other non-ep background:

    - $|z_{vtx}| < 50$ cm and
    - $\sqrt{x_{vtx}^2 + y_{vtx}^2} \leq 3$ cm,

- maximal two tracks fitted to the primary vertex,

- any number of total tracks in the event,

- at least one dimuon system with

    - opposite charge,
    - dimuon mass $m^{\mu\mu} > 2$ GeV,
    - angular distance between the two muons: $\Delta R = \sqrt{\Delta\eta^2 + \Delta\phi^2} > 0.5$.
    - distance in polar angle θ between both muons: $\Delta\theta = |\pi - (\theta_{\mu_1} + \theta_{\mu_2})| > \frac{\pi}{200}$ and
    - distance in azimuth angle ϕ between both muons: $\Delta\phi = |\pi - |\phi_{\mu_1} + \phi_{\mu_2}|| \leq \frac{\pi}{200}$, in order to reject perfectly back-to-back muons from cosmic rays.

- no explicit trigger requirement
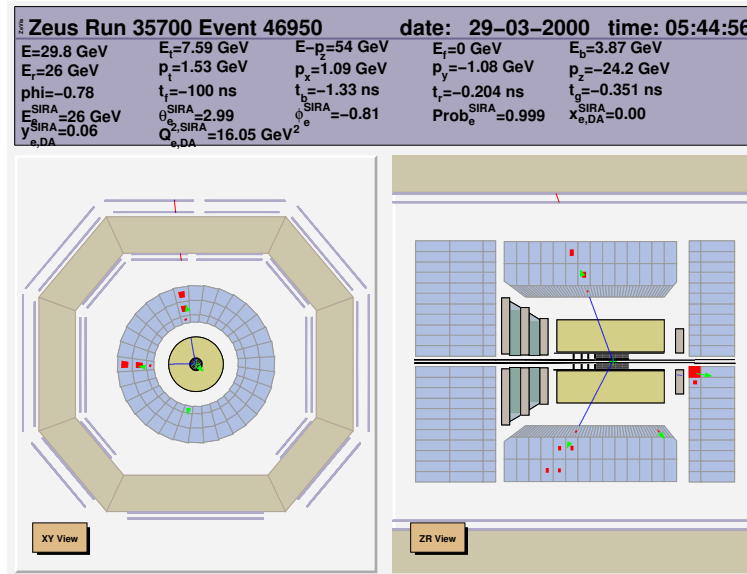
Figure 5.12: Eventdisplay of a $J/\psi \rightarrow \mu^{+}\mu^{-}$ event.

In order to avoid event-trigger biases, events triggered only by muon triggers were treated in a special way: If one of both muons triggered the event, only the other can be used for the efficiency determination. For events triggered by both muons, each muon is included.

In GMUON, two different configurations are used, referred to as *tight* and *loose*, which are defined for the finders MUBAC, BREMAT and MPMATCH as follows:

- **MUBAC:** For the tight selection, a distance cut of the MUBAC hit to the track extrapolated to the BAC ≤ 50 cm is required, ≤ 120 cm for the loose selection.

- **BREMAT:** For the tight selection, a track segment matching probability of $P > 0.01$ is required and no cut for the loose selection.

- **MPMATCH:** The tight selection requires a track segment matching probability of $P > 0.05$ and $P > 0.01$ for the loose selection.

The efficiency correction factor applied to the MC muons found by one of the three finders depends on the muon transverse momentum, p_T^{μ}, and pseudorapidity, η^{μ}, and is calculated as the ratio of data and MC efficiency:

$$f_{\text{corr., finderX}}\left(p_T^{\mu}, \eta^{\mu}\right) = \frac{\epsilon_{\text{data, finderX}}\left(p_T^{\mu}, \eta^{\mu}\right)}{\epsilon_{\text{MC, finderX}}\left(p_T^{\mu}, \eta^{\mu}\right)} \tag{5.8}$$

where the factor is evaluated for the tight or loose configuration, respectively. In Figs. 5.13-5.16, the evaluated efficiency correction factors for the BREMAT, MUBAC and MPMATCH finder used in this analysis are presented for each running period of the HERA II data taking.
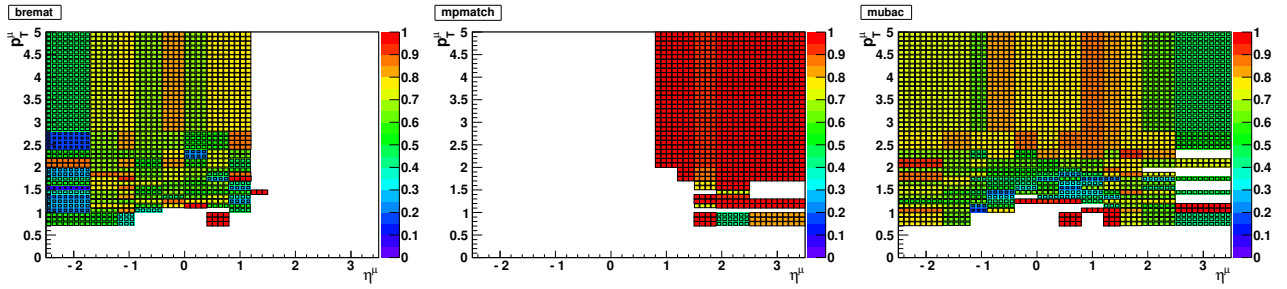
Figure 5.13: Muon efficiency correction factors for BREMAT, MPMATCH and MUBAC for 2003/04p.
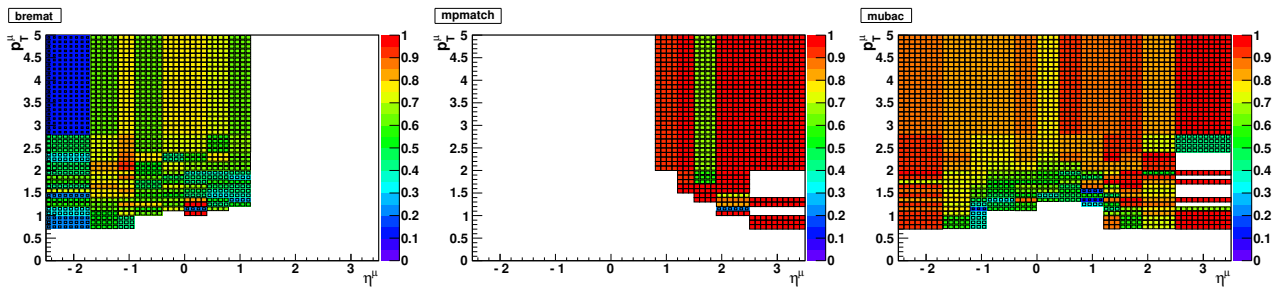
Figure 5.14: Muon efficiency correction factors for BREMAT, MPMATCH and MUBAC for 2005e.
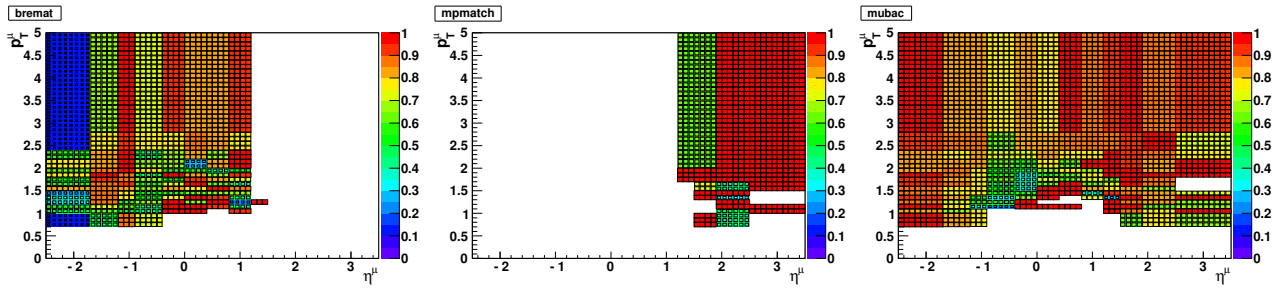
Figure 5.15: Muon efficiency correction factors for BREMAT, MPMATCH and MUBAC for 2006e.
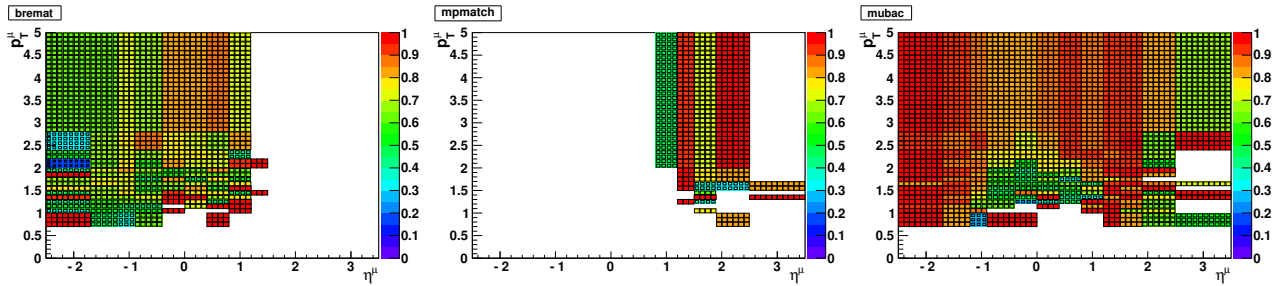
Figure 5.16: Muon efficiency correction factors for BREMAT, MPMATCH and MUBAC for 2006/07p.

The efficiencies were applied in a random number based scheme: If a randomly generated value x fulfills the requirement

$$x < f_{\text{corr., finderX}}, \tag{5.9}$$

the information of finderX for the corresponding muon is changed according to the application of the efficiency correction factor and the muon quality is recalculated based on the new finder information. Fig. 5.17 shows the rate of muons in dimuon events for different combnations of muon finders before and after application of the efficiency correction. In general, a good improvement can be observed.
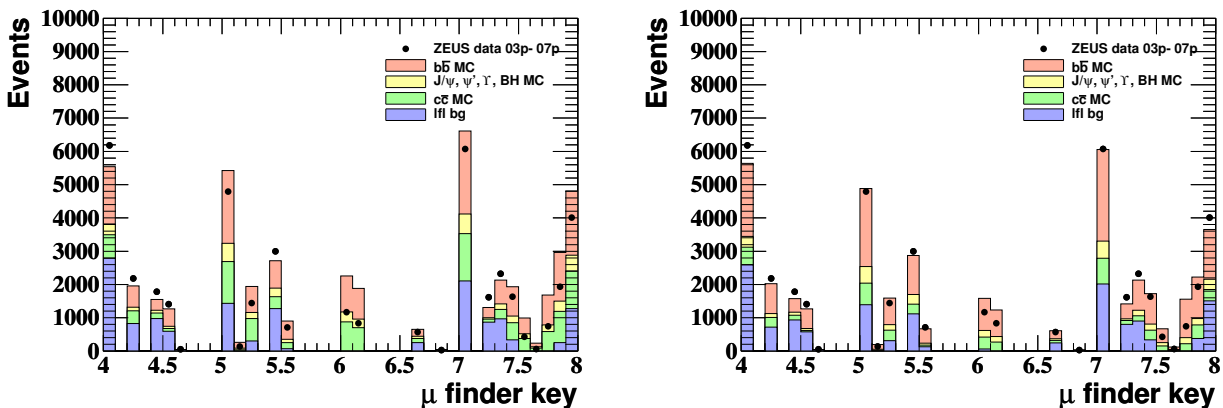
Figure 5.17: Distribution of muon finder combinations for dimuon events **left:** before and **right:** after applying the muon efficiency corrections. The meaning of the bin entries is given in Tab. F.1 in Appendix F.

Although the improvement is quite noticeable, it should be remarked that the current version of muon-efficiency-correction files used in this analysis were produced with data and MC samples before the Grand Reprocessing (referred to as *pre-Grand Reprocessing version*), where the reconstruction information was not yet completed. New efficiency corrections are in progress [155] and will be available soon for further muon analyses.

5.7   Muon and dimuon isolation

Dimuons from semi-leptonic beauty decays are accompanied by hadronic activity while dimuons from background events like $J/\psi, \psi'$ and Bethe-Heitler events usually lead to very isolated dimuons in the detector. In order to distinguish between both event classes, one defines a dimuon isolation. First, the single muon isolation I^μ was calculated from which then the dimuon isolation $I^{\mu\mu}$ was determined. The single muon isolation is defined as the total sum of the transverse momenta of all EFOs with an angular distance of

$$\Delta R = \sqrt{\Delta\eta^2 + \Delta\phi^2} < 1 \tag{5.10}$$

between the EFO and the muon excluding those EFOs associated to the muon. The single muon isolation is then calculated according to

$$I^{\mu_j} = \Sigma p_T^{EFO_i}, EFO_i \neq \text{muon}_j, \Delta R < 1. \tag{5.11}$$

An EFO is associated to a muon and thus not included in this sum if

- the muon track is identical to the EFO track or

- the muon and the EFO are separated by $\Delta R < 0.02$ (only for EFOs containing one track and one island) or

- it is the closest EFO to the muon inside a cone of $\Delta R = 0.4$ with a $p_T^{EFO} < 3.0$ GeV.

The dimuon isolation is the squre root of the squares of the single muon isolation

$$I^{\mu\mu} = \sqrt{I_{\mu_1}^2 + I_{\mu_2}^2}. \tag{5.12}$$

In Fig. 5.18, the isolation distributions of dimuons from heavy quarkonia, Bethe-Heitler processes as well as beauty events are shown. As expected, the background contributions are peaked at very low values of $I^{\mu\mu}$. It should be noted that the Υ contribution, simulated with PYTHIA [44], contains a larger fraction of non-isolated muons than the charmonia contribution, simulated with HERWIG [175]. Probably both Monte Carlo generators differ in simulation of inelastic heavy quarkonia events.
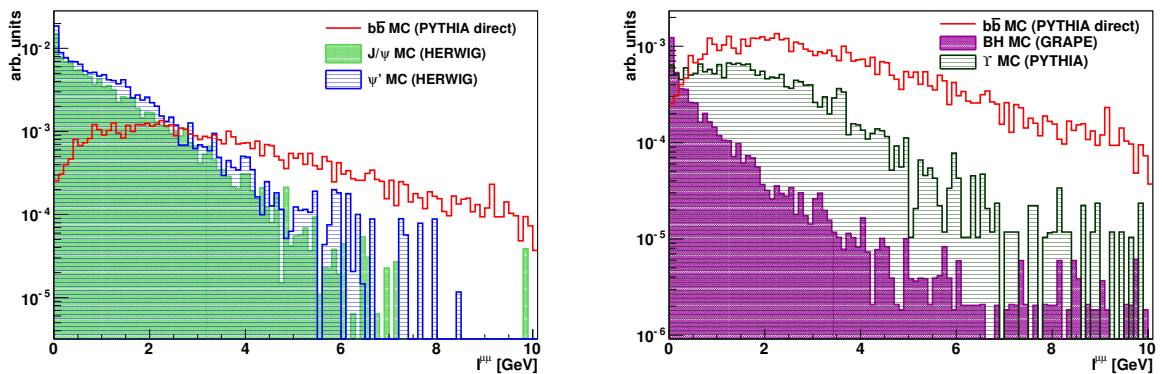
Figure 5.18: Isolation distribution for dimuons from heavy quarkonia, Bethe-Heitler processes as well as beauty events.

5.8 Jet reconstruction

In order to describe the dynamics on an interaction, final-state particles are grouped into jets of collimated particles using a jet algorithm. Although the dynamics of the jets in an event are closely related to the dynamics of the partons which are produced in the hard subprocess, the definition of a jet relies on the algorithm used for the reconstruction. An important feature of a jet algorithm is infrared safety, i.e. the output of the algorithm should be independent of soft or collinear emissions causing infrared divergences in the theoretical calculations. Cone-based jet algorithms are widely used at hadron-hadron colliders and are standardised according to

criteria set at the Snowmass meeting of 1990 [156]. Jets which were reconstructed by use of such algorithms consist of calorimeter cells (or partons in a theoretical description), i, with a distance, R_i, from the jet centre defined by:

$$R_i = \sqrt{(\eta_i - \eta_{jet})^2 + (\phi_i - \phi_{jet})^2} < R, \qquad (5.13)$$

where R is the jet cone radius. However, this method can be ambiguous in its treatment of overlapping jets. This ambiguity can be avoided by using the k_T clustering algorithm which is implemented in the KTCLUS library [157]. This has the advantage of being infrared safe to all orders [158].

In a cluster algorithm, a distance measure is defined determining which objects should be merged. This quantity is defined between two objects i and j to be

$$d_{ij} = \frac{\min(E_{T,i}^2, E_{T,j}^2)[(\eta_i - \eta_j)^2 + (\phi_i - \phi_j)^2]}{R^2}, \qquad (5.14)$$

where R is a parameter analogous to the cone radius. In the limiting case of the distance between object i and the proton remnant travelling in the z-direction, one defines

$$d_i = E_{T,i}^2. \qquad (5.15)$$

If $d_{min} = \min[d_i, d_j] = d_{ij}$, then objects i and j are merged into a single object k, according to the specific recombination scheme used. For example, in the E-recombination scheme the four-momentum of the composite object is the sum of the four-momenta of the objects from which it is formed, i.e.

$$P_k = P_i + P_j. \qquad (5.16)$$

The object k is then used in further iterations of the algorithm. However, if $d_{min} = d_i$ the object is a final state jet and removed from further clustering. This process is repeated until all objects have been removed in this way. In this analysis, the k_T-clustering algorithm in the longitudinally invariant mode was used on EFOs in the experimental data in order to produce jets in the final state. The E-recombination scheme was used, producing massive jets whose four-momenta were, therefore, the sum of the four-momenta of the clustered EFOs.

5.9   Electron reconstruction

In this analysis, the electron candidates are identified by use of the neural network package SINISTRA [159]. This package takes the transverse and longitudinal energy profiles of energy clusters from the entire calorimeter as input and calculates the probability that each electromagnetic cluster resulted from a real scattered electron. The program is trained on neutral current DIS MC and yields $\sim 80\%$ efficiency for finding electrons if the energy deposit in the EMC is larger than 10 GeV and the probability given by SINISTRA is larger than 0.9. Tab. 5.4 lists the cuts applied to the electron candidate and the finder output used in this analysis. After the scattered electrons were tagged, they were subtracted from the total E_T^{CAL} (cf. Sec. 6).

Property	cut value
electron momentum transfer	$Q^2 > 2$ GeV^2
inelasticity	$y \in [0.05,\ 0.7]$
finder probability (Sinistra)	$P_{\mathrm{si}} > 0.9$
energy of electron (sum of cells of electron island)	$E_{\mathrm{e}} > 10$ GeV
rear box cut around beam pipe	$|x_{\mathrm{e}}| > 12$ cm or $|y_{\mathrm{e}}| > 6$ cm
experimental DIS selection criterion	$E - p_z \in [40,\ 60]$ GeV

Table 5.4: The cuts applied to the reconstructed electron candidate are given. The electron candidate (if any) with the highest probability was chosen as the scattered electron in the event.

5.10   Reconstruction of kinematic variables

After the reconstruction of the hadronic final state and the scattered electron, as described in the previous sections, four measured quantities are available: The energy E'_e and polar angle θ_e of the scattered electron as well as the absolute value of the total transverse momentum $p_{T,h}$ and δ_h of the hadronic system, where

$$p_{T,h}^2 = \left(\sum_h p_{x,h} \right)^2 + \left(\sum_h p_{y,h} \right)^2 \text{ and} \tag{5.17}$$

$$\delta_h = \sum_h \left(E_h - p_{z,h} \right). \tag{5.18}$$

The sum runs over all particles in the final state except the scattered electron. The angle of the hadronic system γ_h is then given by:

$$\cos \gamma_h = \frac{p_{T,h}^2 - \delta_h^2}{p_{T,h}^2 + \delta_h^2}, \tag{5.19}$$

where γ_h can be interpreted as the angle of the scattered quark in the naive quark parton model.

The variables E'_e, θ_e, γ_h and $p_{T,h}$ can now be used for the reconstruction of the kinematic variables Q^2, x and y in DIS or only for the reconstruction of y in photoproduction, since $Q^2 \approx 0$ and $x \approx 0$ for such events. There are different methods whose choice depends on the kinematic region, the interaction type as well as the reference frame. Three of these reconstruction methods are described in the following.

The electron method

The electron method [160] uses the energy E'_e as well as the angle θ_e of the scattered electron and is therefore applicable only for DIS events. For given proton and electron beam energies, E_p and E_e, one obtains for the kinematic variables Q^2, y and x by neglecting the electron mass:

$$y_{el} = 1 - \frac{E'_e}{2E_e}(1 - \cos \theta_e), \tag{5.20}$$

$$Q_{el}^2 = 2E_e E_e'(1 + \cos\theta_e), \tag{5.21}$$

$$x_{el} = \frac{E_e'(1 + \cos\theta_e)}{2y_{el}E_p}. \tag{5.22}$$

The reconstructed values are very sensitive to the energy scale of the electron. At low Q^2, this method offers good resolution while at high values of Q^2, the *double angle method* has a better precision.

The double angle method

This method [161] uses the angles of the hadronic system, γ_h, as well as of the scattered electron, θ_e, therefore it is only applicable for DIS events as well. The kinematic variables can be written as:

$$Q_{DA}^2 = 4E_e^2 \frac{\sin\gamma_h(1 + \cos\theta_e)}{\sin\gamma_h + \sin\theta_e - \sin(\gamma_h + \theta_e)}, \tag{5.23}$$

$$y_{DA} = \frac{\sin\theta_e(1 - \cos\gamma_h)}{\sin\gamma_h + \sin\theta_e - \sin(\gamma_h + \theta_e)}, \tag{5.24}$$

$$x_{DA} = \frac{E_e}{E_p}\frac{\sin\gamma_h + \sin\theta_e + \sin(\theta_e + \gamma_h)}{\sin\gamma_h + \sin\theta_e - \sin(\theta_e + \gamma_h)}. \tag{5.25}$$

The sensitivity of to the absolute energy scale is minimised by this reconstruction method but the resolution of all reconstructed kinematic variables depends on the measurement of the angle γ_h of the hadronic system.

The Jacquet-Blondel method

This method [162] is used if no scattered electron could be observed like in photoproduction and CC DIS events. For the reconstruction of the kinematic variable y_{JB}, only the information of the hadronic final state is considered:

$$y_{JB} = \frac{\delta_h}{2E_e}, \tag{5.26}$$

In this analysis, both the electron method for the DIS contribution and the Jacquet-Blondel method for photoproduction events were chosen. Furthermore, the Jacquet-Blondel method was used for the reconstruction of the kinematics of instanton-induced events (cf. Sec. 5.12).

5.11   Beauty quark identification methods

For the measurement of the cross sections of beauty quark production, several methods are used in order to separate beauty quark events from background constisting of charm and light flavour events. In the following, a brief description of the discriminating observables used in this analysis is given.

5.11.1   The p_T^{rel} method

Beauty quarks are significantly heavier than charm and light flavour quarks. This is reflected in their decay kinematics especially in the muon decay channel. An observable reflecting the characteristics of the quark masses in semi-leptonic decays into muons is the transverse momentum of the muon relative to the direction of its parental quark. As a result of the heavy beauty quark mass, it is to be expected that the p_T^{rel} spectrum of muons originating is harder compared to the p_T^{rel} spectra from charm and light flavour quarks. As quarks are not experimentally observable, jets are reconstructed to represent the momentum of the quarks and define the reference for the calculation of the p_T^{rel} of the muon, as illustrated in Fig. 5.19.
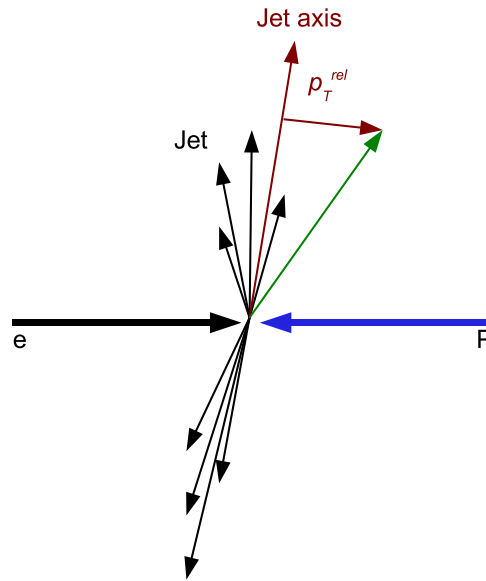
Figure 5.19: Illustration of the transverse muon momentum relative to its associated jet.

Two definitions of p_T^{rel} are available which both are valid to exploit the heavy mass of the beauty quark in order to determine the fraction of beauty events. The first definition calculates the p_T^{rel} of the muon relative to its associated jet:

$$p_T^{rel} = |\vec{p}_T^{\,\mu}| \cdot \sin\left(\arccos\left(\frac{\vec{p}_T^{\,\mu} \cdot \vec{p}_T^{\,jet}}{|\vec{p}_T^{\,\mu}| \cdot |\vec{p}_T^{\,jet}|}\right)\right). \tag{5.27}$$

The second definition, which is used in this analysis as an independent cross check for the normalisations of the beauty and background contribution for dimuon events with jets, uses

a slightly modified jet axis as a reference by subtracting the muon momentum from the jet momentum, thus shifting the p_T^{rel} spectrum to larger values:

$$p_T^{rel} = |\vec{p}_T^{\,\mu}| \cdot \sin\left(\arccos\left(\frac{\vec{p}_T^{\,\mu} \cdot (\vec{p}_T^{\,jet} - \vec{p}_T^{\,\mu})}{|\vec{p}_T^{\,\mu}| \cdot |(\vec{p}_T^{\,jet} - \vec{p}_T^{\,\mu})|}\right)\right). \tag{5.28}$$

5.11.2 Impact parameter method

The impact parameter δ is a tracked-based variable which can be used to separate primary vertex tracks from tracks originating from a long-lived particle, resulting in some displacement from the primary vertex. In principle, the impact parameter is defined as the distance of closest approach (DCA) of a track to the primary vertex. While δ is a positive quantity by definition, it turns out to be useful to introduce a sign to the impact parameter. As illustrated in Fig. 5.20, the sign of δ is positive if the track intercepts the axis of the associated jet and negative otherwise. Impact parameters with positve sign reflect the lifetime of heavy flavour hadrons,
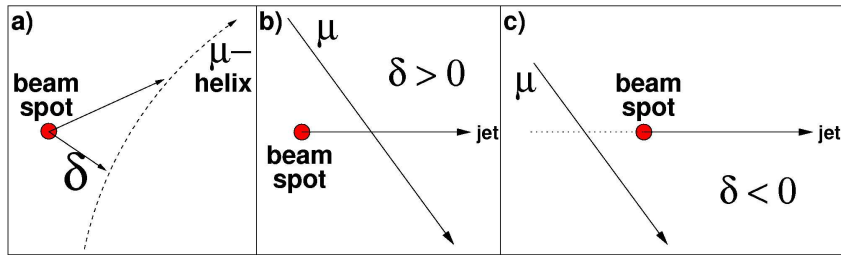
Figure 5.20: Sketch of the impact parameter δ of a muon track. If the muon track intercepts the jet axis downstream the primary vertex/beam spot, the impact parameter has a positive sign, otherwise it is negative.

while negative signed impact parameters are the result of resolution effects of particle tracks coming from the beamspot. For a better control of these resolution effects, the significance of the impact parameter is calculated:

$$S_{IP} = \frac{\delta}{\sigma_\delta} \tag{5.29}$$

where σ_δ is the uncertainty on the impact parameter calculated from the beamspot and the helix uncertainties. This quantity is only used for the association of tracks, which are not fitted to the primary vertex or to secondary vertices, to the reconstruction of EFOs (cf. Sec. 5.4).

5.11.3 Decay length

Another quantity, which exploits the lifetime information as well, is the projected decay length L_{XY}, a jet-based variable and defined as the distance between the primary vertex (or beamspot) and the secondary vertex. The decay length is restricted to two dimensions by calculating its

projection onto the $X - Y$ plane:

$$L_{XY} = \begin{pmatrix} \Delta X \\ \Delta Y \end{pmatrix} = \begin{pmatrix} X_{VTX} - X_{BSP} \\ Y_{VTX} - Y_{BSP} \end{pmatrix} \tag{5.30}$$

The sign of the decay length is obtained by using the axis of the associated jet.
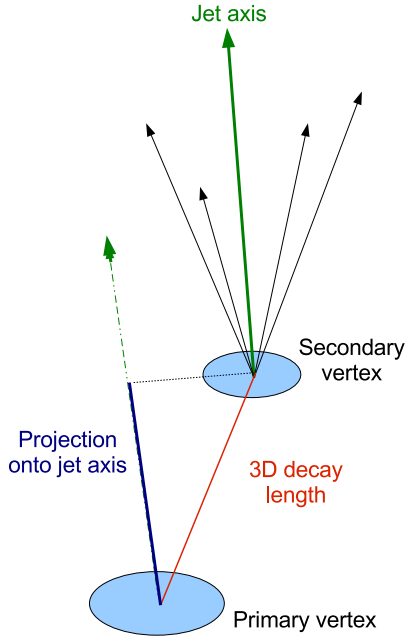
Figure 5.21: Illustration of the decay length calculation and its projection on the jet axis.

If the two-dimensional vector pointing from the primary to the secondary vertex is located in the same hemisphere as the two-dimensional jet-axis, a positive sign is assigned to the decay length and a negavite otherwise. Negative decay lengths originating from secondary vertices, which are reconstructed opposite to the direction of the associated jet are unphysical and caused purely by detector resolution effects. In order to avoid discontinuities for vertices where the decay vector is perpendicular to the jet direction, the two-dimensional decay length is further projected onto the jet axis. The projected decay length is then given by:

$$L_{XY}^{proj} = \begin{pmatrix} \Delta X \\ \Delta Y \end{pmatrix} \cdot \frac{\vec{j}}{|\vec{j}|}. \tag{5.31}$$

Fig. 5.21 shows a schematic view of the decay length and the procedure of its projection.

The decay length significance $S_{L_{XY}^{proj}}$ is defined as the projected decay length L_{XY}^{proj} divided by its error $\sigma_{L_{XY}^{proj}}$:

$$S_{L_{XY}} = \frac{L_{XY}}{\sigma_{L_{XY}}}, \tag{5.32}$$

where the error on the decay length is calculated from the covariance matrices of the beamspot and the secondary vertex [72]. The decay length as well as its significance possess more separation power than the impact parameter δ as more information is combined in one quantitiy. On the other side, the impact parameter δ does not require information about hadron decay vertices and therefore a reconstruction of secondary event vertices.

The reconstruction of secondary vertices provides an additional quantity, referred to as invariant mass of the secondary vertex, for the separation of beauty from charm and light-flavour contributions. This quantity is reconstructed by means of the four-momenta of the tracks entering the secondary vertex fit. In inclusive secondary vertex analyses [70–73], this variable was combined with the decay length significance in order to increase the discriminating power. Splitting the samples into different mass regions yields beauty, charm and light-flavour enriched regions, as illustrated in Fig. 5.22. In this thesis, the decay length L_{XY}^{proj}, its significance $S_{L_{XY}^{proj}}$ as well as the invariant mass of each secondary vertex, m_{vtx} are used as an additional independent cross check for the normalisations of the beauty and background contributions.
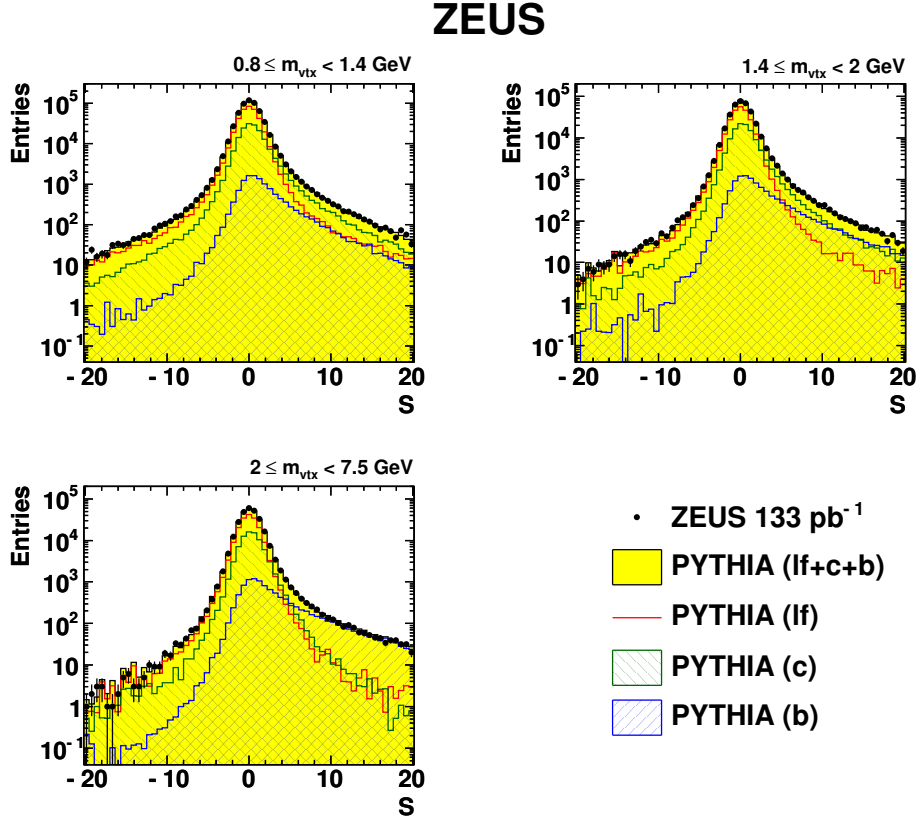
Figure 5.22: Decay length significance $S_{L_{XY}}$ for a) light-flavour, b) charm and c) beauty enriched region (taken from [70]).

5.12   Reconstruction of instanton kinematics

For the experimental verification of instanton-induced events at HERA, the reconstruction of both, the kinematic variable Q'^2, which is the virtuality of the quark entering the instanton-subprocess, and the *instanton band*, a limited area in the $\eta - \phi$ plane, in which the particles of the instanton-decay are distributed, is essential. In Fig. 5.23, the kinematics of the instanton process in *ep* collisions is shown: The photon with four-momentum q fluctuates into a $q\bar{q}$ pair, one of which with four-momentum q' enters the instanton subprocess and the other quark with four-momentum q'', referred to as *current quark*, forms a jet with high transverse energy. Analogous to the photon virtuality Q^2, the virtuality of the quark q' is given by

$$Q'^2 = -q'^2 = -(q - q'')^2 \tag{5.33}$$

Several instanton analyses have shown [7–10,15], that the current quark q'' and the hadronic jet with highest transverse energy, E_T^{Jet}, are well correlated. Using this identity and the Jacquet-Blondel method (cf. Sec. 5.10) yields for the reconstructed quark virtuality Q'^2 [8,15]:

$$Q'^2_{rec} = \sum (E_i - p_{z,i}) \cdot (E_{Jet} + p_{z,Jet}) - m_{Jet}^2. \tag{5.34}$$
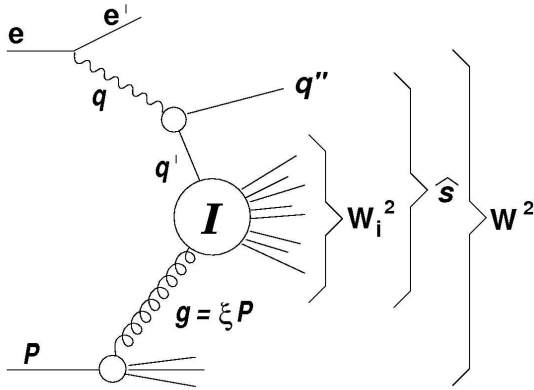
Figure 5.23: Reminder: Feynman diagram of instanton-induced processes in *ep* collisions at HERA.

All EFOs, which are neither part of the proton remnant nor of the jet with highest E_T, "form" the instanton. As a consequence of the homogeneous energy and parton distribution in the instanton rest-frame, a band structure in the $\eta - \phi$ plane is expected, referred to as instanton band. The band is defined to have a width of ± 1.1 units in η around a mean $\bar{\eta}$, the middle of the instanton band [7]:

$$\bar{\eta} = \frac{\sum E_{T,h}\eta_h}{\sum E_{T,h}}. \tag{5.35}$$

The sum of all EFOs in this band will be defined as *particle multiplicity* N_{Band}. Since heavy-flavour instantons contain both, a $b\bar{b}$ and $c\bar{c}$ pair, the expected parton multiplicity in instanton-induced events should be higher than in charm or beauty events, as shown in Fig. 5.24
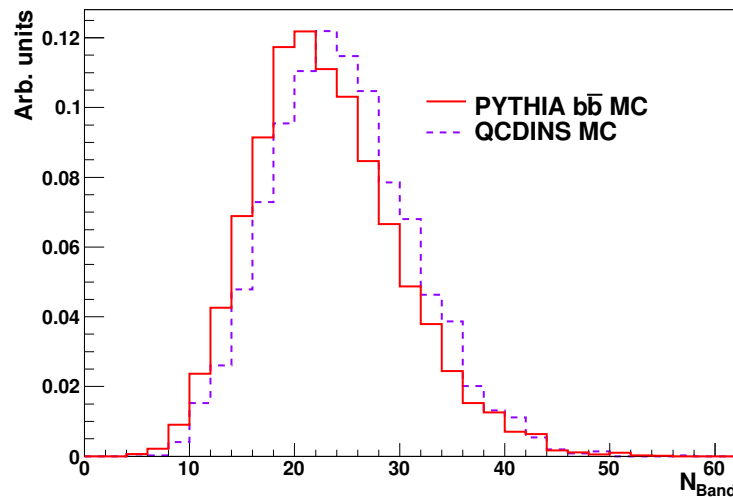
Figure 5.24: Particle multiplicity in the reconstructed instanton band from instantons (dashed line) and beauty events (solid line). The distributions of both processes is normalised to unity.

5.12.1   Separation from beauty quark events

Besides the reconstruction of the kinematic variables of instanton-induced events, so-called
event shape variables [163], e.g. the (pseudo) thrust, sphericity, isotropy, oblateness, aplanarity
etc., have proven to be very useful for the separation of instanton events from normal DIS
and photoproduction events. In principle, instantons are expected to "decay" isotropically
in their rest-frame. As a result, hadrons from the instanton-subprocess should be distributed
homogeneously in the instanton-band and in the detector. Event shape variables are quanitities
sensitive to the distribution of particles in the lab- and specific center-of-mass frames, allowing
to separate isotropic events from dijet-systems (e.g. charm and partially beauty) events. Three
of these quantities, which are used in this analysis, are described in the following.

Sphericity

The sphericity Sph [164, 165] is calculated for all EFOs in the lab frame which are neither part
of the proton remnant nor of the current jet. The diagonalised *sphericity tensor*, given by

$$Sph^{\alpha\beta} = \frac{\sum\limits_{i} p_i^\alpha p_i^\beta}{\sum\limits_{i} |p_i^2|}, \quad \alpha, \beta = x, y, z \tag{5.36}$$

yields three different positive eigenvalues $\lambda_{1,2,3}$ fulfilling the following relations:

$$0 \leq \lambda_1 \leq \lambda_2 \leq \lambda_3 \quad \text{and} \quad \lambda_1 + \lambda_2 + \lambda_3 = 1. \tag{5.37}$$

Then the sphericity quantity can be defined as:

$$Sph = \frac{3}{2}(\lambda_1 + \lambda_2). \tag{5.38}$$

In the case of (di)jet-like events, the sphericity has values close to 0, in the case of isotropic
events values close to 1.

Isotropy

The isotropy Δ_B [166] is calculated for all EFOs within the reconstructed instanton band after
a Lorentz-boost into the instanton rest-frame. This quantity is defined as:

$$\Delta_B = \frac{E_{\text{in,B}} - E_{\text{out,B}}}{E_{\text{in,B}}}, \tag{5.39}$$

with

$$E_{\text{in,B}} = \max \sum_h |\vec{p_h} \cdot \vec{i}| \quad \text{and} \quad E_{\text{out,B}} = \min \sum_h |\vec{p_h} \cdot \vec{i}|, \tag{5.40}$$

where h denotes the EFOs in the instanton band and $\vec{p_h}$ their momenta. The maximum of
$E_{\text{in,B}}$ and the minimum of $E_{\text{out,B}}$, respectively, are obainted by trying out all orientations of the
unit-vectors $\vec{i}$. For (di)jet-like events, the isotropy variable has values close to 1 and approaches
0 for isotropic events.

Pseudo thrust

The pseudo thrust T_{pseudo} is inspired by the *thrust* variable [167] initially used in e^+e^- collisions to select dijet-like events and was used in the HERA I dimuon analysis [4] as an independent check for the normalisations of the beauty and background contributions for dimuon events without reconstructed jet. The pseudo thrust is defined by:

$$T_{pseudo} = \frac{\sum\limits_{i=1}^{\text{nEFO}} \vec{p}_i \cdot \vec{T}_1 + \sum\limits_{i=1}^{\text{nEFO}} \vec{p}_i \cdot \vec{T}_2}{\sum\limits_{i=1}^{\text{nEFO}} \vec{p}_i}. \tag{5.41}$$

The sums runs over all reconstructed EFOs where $\vec{p}_i$ are the momenta of the EFOs and the unit vectors $\vec{T}_1$ and $\vec{T}_2$ are iterated until the scalar T_{pseudo} is maximised:

- First T_{pseudo} is maximised in ϕ for $\theta = \pi/2$.

- The plane perpendicular to the now determined axis in ϕ divides the detector in two hemispheres.

- In these two hemispheres, $\vec{T}_1$ and $\vec{T}_2$ are iterated separately in θ while keeping the previously found ϕ fixed allowing a kink in the zx plane, as illustrated in Fig. 5.25.
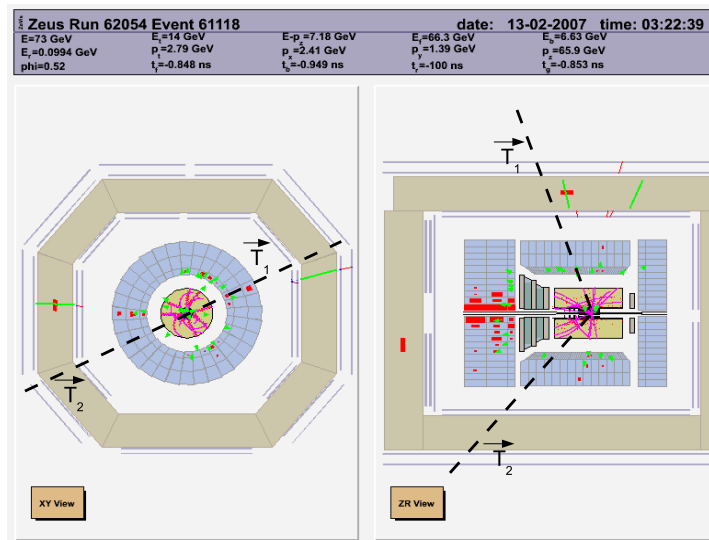
Figure 5.25: Illustration of the pseudo thrust in a dimuon event in ZEUS. The lines $\vec{T}_1$ and $\vec{T}_2$ give the measured pseudo-thrust axes. The kink in θ compensates the longitudinal boost of the initial $b\bar{b}$ system.

For back-to-back events, the value of T_{pseudo} is close to 1 and approaches 0.5 for isotropic events. Fig. 5.26 shows the pseudo thrust distribution for non-isolated, unlike-sign dimuon events from beauty and charm MC. As expected, charm events behave more dijet-like than beauty events. This quantity is not directly used for the separation of instanton from beauty events, since the
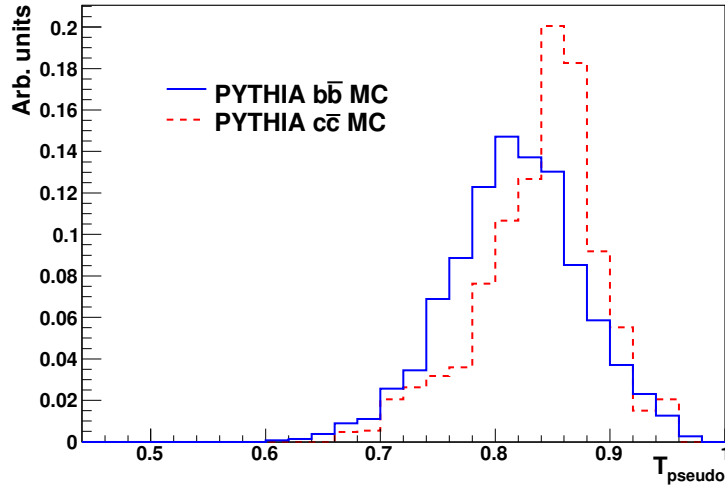
Figure 5.26: Pseudo thrust distributions for non-isolated, unlike-sign muon pairs in charm (dashed line) and beauty MC (solid line).

reconstruction of instanton kinematics requires the presence of a reconstructed jet. However, the resulting pseudo thrust axes $\vec{T}_1$ and $\vec{T}_2$ can be used as reference axes for the reconstruction of secondary vertices in events without jets [168]. First investigations after the successful implementation of a modified version of the pseudo thrust algorithm (the modifications were necessary in order to consider DIS events as well) into the ORANGE framework [129] looked promising [169]. Therefore, the currently produced next iteration of the HERA II data set and corresponding MC samples contain secondary vertices reconstructed by means of the pseudo thrust axes.

Chapter 6

Event selection

In this analysis, beauty quark production is measured by requiring two well reconstructed muons in the final state. In this chapter, the data and MC samples used in this analysis are listed, followed by a detailed description of the event and muon candidate selection.

6.1 Data and Monte Carlo Samples

For this analysis, data of the HERA II period (2003-2007) collected by the ZEUS detector were used, listed in Tab. 6.1. As the muons are the most important ingredient of this analysis, only runs with reliable barrel and rear muon chamber performance (cf. Sec. 4.6.2) have been selected using the MBTAKE routine combined with the requirement of a good state of the CTD, CAL, trigger chain and luminosity measurement, done by the EVTAKE routine, and of a agood state of the MVD, done by the MVDTAKE routine. In total, an integrated luminosity of (376 ± 6.5) pb^{-1} was used.

Running period	Hadron	Lepton	$\sqrt{s}$ [GeV]	$\mathcal{L}$ [pb^{-1}] EVTAKE+MBTAKE +MVDTAKE
2003/2004	p	e^+	318	35.39
2005	p	e^-	318	125.14
2006	p	e^-	318	53.49
2006/2007	p	e^+	318	136.12

Table 6.1: Data samples collected with the ZEUS detector between 2003 and 2007.

This data sample was the first version of the *Grand Reprocessed* data processed with a version of the reconstruction software ZEPHYR which included the latest corrections, detector alignments and tracking developements. For the simulation of dimuon signal and background events, needed to determine the cross section for beauty quark production in this analysis, various generators have been used. In the following, a brief description of all samples is given, for detailed information see Tab. B.1, B.2 and B.3 in Appendix B.

Charm and beauty events were simulated using the generators PYTHIA [44] for the photoproduction (PHP) and RAPGAP [45] for the DIS regime. Both MC generators used the CTEQ-5L [170] parametrisation for the proton PDFs and the GRV-G LO parametrisation [171] for the photon PDFs. The beauty and charm PHP samples were separated into four subsamples for direct, resolved and excitation in photon and proton processes with a cut of $Q^2_{Gen.} < 1$ GeV^2 on the virtuality of the exchanged photon. The beauty and charm quark masses were set to $m_b = 4.75$ GeV and $m_c = 1.35$ GeV, respectively. Inclusive beauty and charm MC samples in DIS were produced by the BGF process. Beauty and charm events were generated with a lower cut on the photon virtuality $Q^2_{Gen.} > 1$ GeV^2 and $Q^2_{Gen.} > 1.5$ GeV^2, respectively. The masses of the heavy flavours were set to $m_b = 4.75$ GeV for the beauty and $m_c = 1.5$ GeV for the charm quark. For the estimation of the systematic uncertainty caused by the Monte Carlo simulation, additional RAPGAP samples were generated with the same lower Q^2 cuts, where beauty and charm were produced by the excitation process $bg \rightarrow bg$ and $cg \rightarrow cg$, respectively.

Since the beauty sample contains the signal events for which production cross sections are intended to be measured, they are required to be available in a sufficient quantity to ensure a satisfactory statistical precision. Therefore, the inclusive beauty MC sample in PHP is ∼6-10 times the data statistics in photoproduction and the inclusive beauty MC sample in DIS ∼16-18 times larger than the data. The cross section for charm quark production is much higher than for beauty quark production. Since the time as well as storage space consumed by the event simulation is not negligible, an inclusive charm sample in PHP and DIS was generated with similar integrated luminosities to those of the data.

Different generators were used for the heavy quarkonia samples, which were also used in other analyses [154, 172–174]: Inelastic J/ψ and ψ' events were generated with HERWIG [175] and the inelastic Υ sample by means of PYTHIA, while elastic quarkonia processes were simulated with DIFFVM [176]. Furthermore, the inelastic charmonia sample was reweighted in $p_T^{\mu\mu}$ in order to describe the data (cf. Sec. 7.2.1).

Bethe-Heitler processes were simulated using the generator GRAPE [177]. Elastic, quasi-elastic and DIS events were generated with a lower muon transverse momentum cut of $p_T^\mu > 0.5$ GeV. The light-flavour background was not directly simulated since the loose data selection cuts would have required producing a very large inclusive sample which was technically not feasible. Instead, the light-flavour background was obtained from the data in the same way as in the previous HERA I analysis [4].

The instanton sample was simulated using the generator QCDINS [178] with the JETSET programme [179]. Since the default version of this generator simulates only instanton-induced events with light-flavour quarks in DIS, a modification was required as done in [15, 180] for the production of an instanton-sample containing beauty- and charm-quark pairs in photoproduction as well.

Multi-heavy-flavour events were generated with a special package called MG2ZEUS [181, 182], consisting of the MadGraph program [43] and the FORMOZA generator [183]. Since the cross sections of these processes, predicted by MadGraph, are very small, the samples for $b\bar{b}b\bar{b}$ and

$b\bar{b}c\bar{c}$ events are 10 times the data luminosity while the $c\bar{c}c\bar{c}$ sample was generated, due to technical reasons, with twice the data luminosity. No cuts were applied on generator level.

6.1.1 Trigger selection

For this analysis, a combination of several triggers was chosen in order to obtain a high trigger selection efficiency. The predominant part consists of muon triggers in open charm and beauty, dijet, photoproduction and deep inelastic scattering events. The trigger selection consists of at least one of the following third-level trigger slots:

- HFL01: Open charm and beauty in PHP

- HFL05: Inclusive dijet

- HFL06: Dijets in DIS

- HFL13: Inclusive semi-leptonic μ

- HFL14: Inclusive μ in DIS

- HFL16: Inclusive μ in BAC

- HFL25: μ + dijets

- HFL27: MVD inclusive trigger

- HFL30: J/ψ candidate

- HFL31: Isolated $\mu\mu$ from MV

- HFL32: Inclusive double-tagged $\mu\mu$

- DIS03: Medium Q^2 DIS

- HPP31[1]/SPP02/SPP09: Inclusive low Q^2 DIS

- EXO11/12: Barrel/rear μ

- MUO03: Semi-isolated barrel/rear μ

- MUO01/02/04-09: forward μ

- MUO10-14: μ in BAC.

Detailed information of the triggers used in this analysis are given in Appendix D.

---

[1]HFL17 could also be used, since both triggers are very similar. However, HPP31 was chosen for historical reasons.

6.1.2   General event requirements

The large mass of a $b\bar{b}$ pair ($\sim$10 GeV) leads to a significant amount of energy deposited in the central parts of the detector. A cut on the hadronic transverse energy was applied with

$$E_T \geq 8 \text{ GeV}, \tag{6.1}$$

where

$$E_T = \begin{cases} E_T^{\theta>10°} & \text{for } \gamma p \text{ events} \\ E_T^{\theta>10°} - E_T^e & \text{if a DIS electron is found,} \end{cases} \tag{6.2}$$

in order to suppress backgrounds from false-muon and charm events. The transverse energy is calculated as $E_T^{\theta>10°} = \Sigma_{i,\theta_i>10°}(E_i \sin\theta_i)$, where the sum runs over all energy deposits in the CAL with the polar angle greater than 10° in order to remove proton-remnant effects. The transverse energy of the detected scattered DIS electron is also subtracted. The detection criteria for the scattered electron are given in Tab. 5.4.

6.1.3   Dimuon selection

Dimuon events were selected by requiring two muons with transverse momenta of

$$p_T^\mu \geq \begin{cases} 1.5 \text{ GeV} & \text{for muons with quality} = 4 \\ 0.75 \text{ GeV} & \text{for muons with quality} \geq 5. \end{cases} \tag{6.3}$$

depending on the muon quality. Additionally, a cut with a similar scope as the initial E_T cut was applied on the fraction of the total transverse energy carried by the muon pair:

$$0.1 < \frac{(p_T^{\mu_1} + p_T^{\mu_2})}{E_T} < \begin{cases} 0.5 & \text{for } m_{\text{inv}}^{\mu\mu} < 4 \text{ GeV} \\ 0.7 & \text{for } m_{\text{inv}}^{\mu\mu} \geq 4 \text{ GeV}. \end{cases} \tag{6.4}$$

This E_T-fraction cut removes events where the hadronic activity is very high (false-muon background) or low (quarkonia and Bethe-Heitler events), respectively. In Fig. 6.1, the total calorimetric E_T before and after applying the dimuon E_T fraction cut is illustrated. The region removed by this cut contain predominantly background events from heavy quarkonia as well as Bethe-Heitler and almost no beauty contribution. The region above the E_T cut of 8 GeV is well described.

6.1.3.1   Mass and charge separation

In order to distinguish between muon pairs from cascade decays of the same b quark and those from different b quarks, the distributions were separated corresponding to the invariant mass of the muon pairs. Events were separated into a subsample of low-mass dimuons with

$$m_{\text{inv}}^{\mu\mu} < 4 \text{ GeV}, \tag{6.5}$$
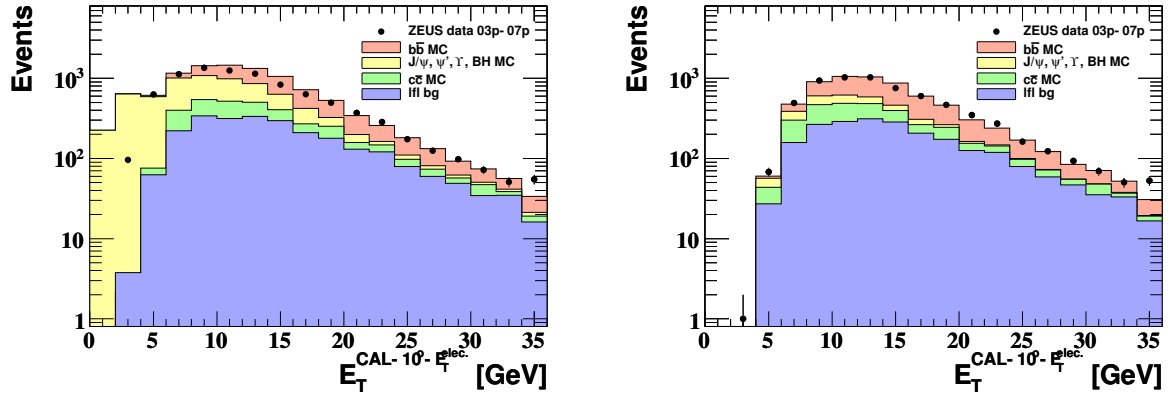
Figure 6.1: The corrected total calorimetric E_T for high and low mass dimuons before (left) and after application of the dimuon E_T fraction cut (right). The breakdown into the expected contributions from different processes is also illustrated.

containing dimuons predominantly from the same b quark, and of high-mass dimuons with

$$m_{\mathrm{inv}}^{\mu\mu} \geq 4 \text{ GeV,} \tag{6.6}$$

a sample enriched in dimuons originating from the decay of different b quarks. Furthermore, events were divided by the charge of the muon pairs into like- and unlike-sign events. In Fig. 6.2, the corresponding invariant mass distributions for like- and unlike-sign dimuons in the low- and high-mass region are presented. The dominant signal and background contributions to the four subsamples are summarised in Tab. 6.2

	unlike-sign $\pm/\mp$	like-sign $++/--$
low inv. mass $m^{\mu\mu} < 4$ GeV	**muons from same b,** muons from $J/\psi, \psi'$ and false-muon background	**false-muon background** few muons from different b
high inv. mass $m^{\mu\mu} \geq 4$ GeV	**muons from different b** muons from $c\bar{c}, \Upsilon$, BH and false-muon background	**muons from different b** and false-muon background

Table 6.2: Classification of events using mass and charge correlation of dimuons. The main contributions to each class are given.

6.1.3.2 Isolation cuts

As mentioned before, muons from semileptonic decays are in general accompanied by hadrons from the same decay, thus, they can be separated from muons of quarkonia and Bethe-Heitler
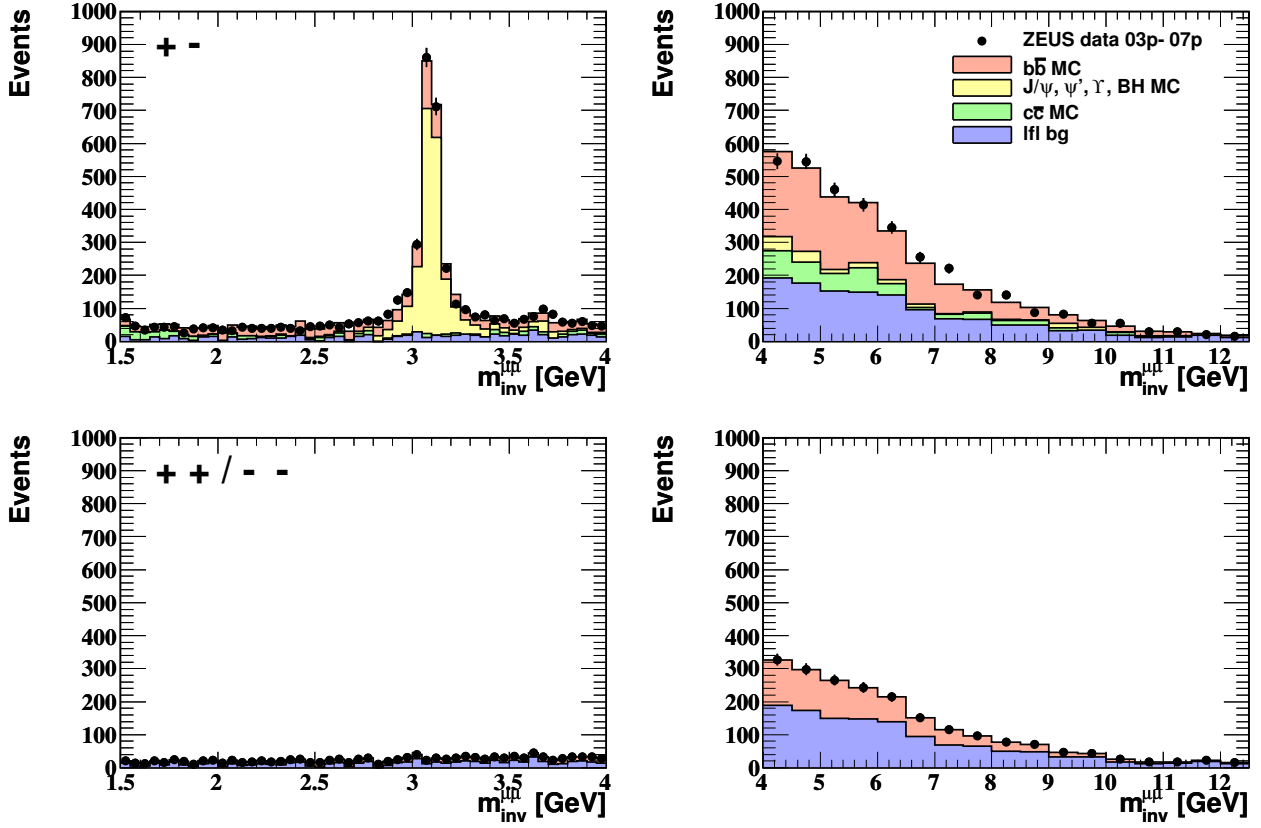
Figure 6.2: Dimuon mass distributions of like- and unlike-sign muon pairs in the low- and high-mass subsamples. The breakdown into the expected contributions from different processes is also illustrated.

processes by requiring a muon isolation cut. The dimuon isolation variable $I^{\mu\mu}$, defined in Sec. 5.7, was required to exceed 0.25 GeV, reducing the elastic quarkonia and Bethe-Heitler contributions to an almost negligible level. Inelastic quarkonia and Bethe-Heitler events can pass this cut since hadrons from the proton remnant can be accidentally within the isolation cone. Therefore, the isolation cut was raised to 2.0 GeV in the J/ψ and ψ' mass region, where this background is predominant.

Summarising, dimuon events fulfilling the relation

$$
I^{\mu\mu} \geq \begin{cases} 2.0 \text{ GeV} & \text{for } m^{\mu\mu}_{J/\psi} \in [2.9,\ 3.25] \text{ or } m^{\mu\mu}_{\psi'} \in [3.6,\ 3.75] \\ 0.25 \text{ GeV} & \text{otherwise.} \end{cases} \tag{6.7}
$$

are called non-isolated, while the remaining events become part of the isolated background sample.

Fig. 6.3 shows the dimuon mass distributions for the isolated and non-isolated samples.
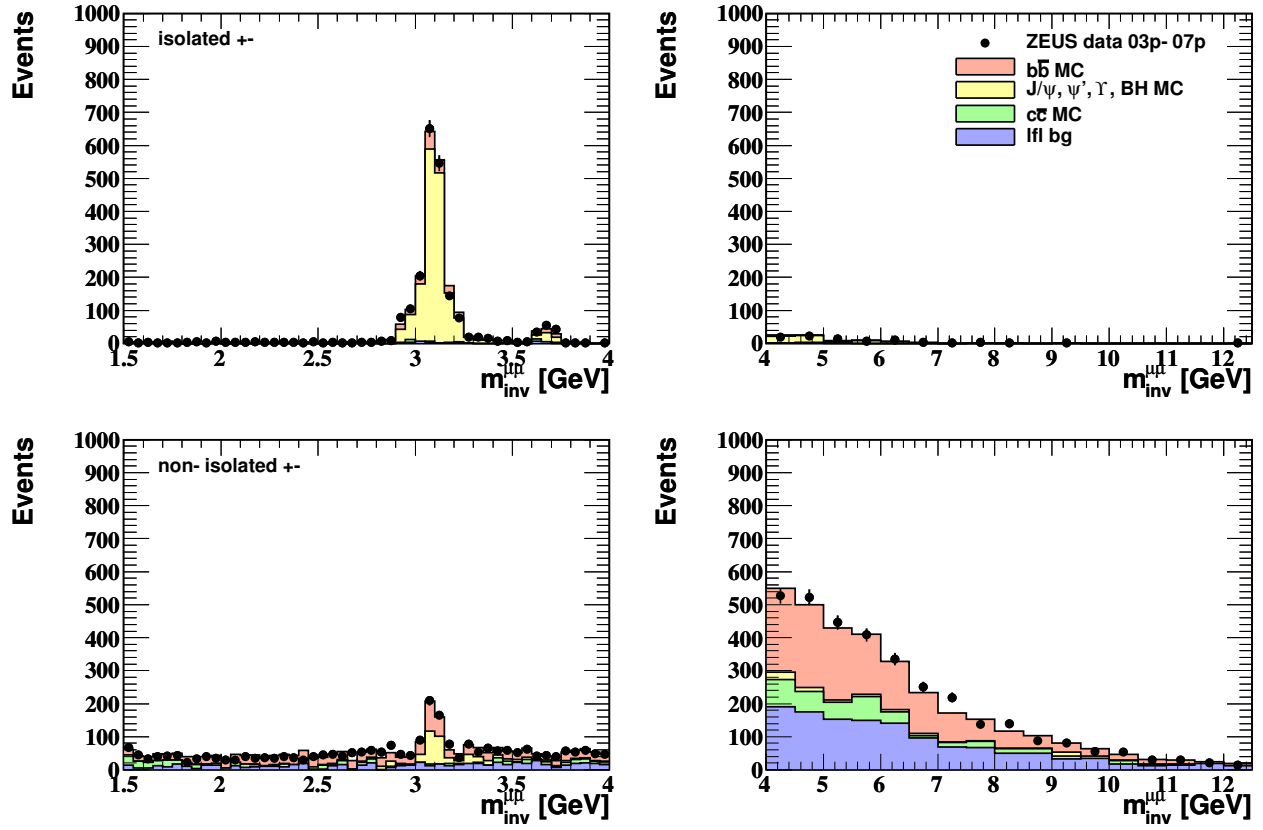
Figure 6.3: Dimuon mass distributions of unlike-sign isolated and non-isolated muon pairs in the low- and high-mass subsamples. The breakdown into the expected contributions from different processes is also illustrated.

6.1.4 Background and cleaning cuts

In order to suppress events with ambigous matches between tracks and muon chamber segments as well as light-flavour background from this sample of muons, a lower invariant mass cut of

$$m_{\text{inv}}^{\mu\mu} > 1.5 \text{ GeV} \tag{6.8}$$

was applied, implying a minimum opening angle between both muons. A cut on the difference in pseudorapidity of the two muon candidates of

$$|\eta^{\mu_1} - \eta^{\mu_2}| < 3.0 \tag{6.9}$$

removes a large fraction of light-flavour background events with a very forward and backward muon candidate as well as a small fraction of Bethe-Heitler background in the non-isolated sample.

Furthermore, muon candidates with badly measured momenta (predominantly from false-muon background) were rejected by means of the imbalance between the transverse momenta of the muon pair:

$$\frac{(|p_T^{\mu_1} - p_T^{\mu_2}|)}{(|p_T^{\mu_1} - p_T^{\mu_2}|)} \leq 0.7 \tag{6.10}$$

Muons from cosmic rays were suppressed by rejecting events with back-to-back muons and events where the average calorimeter timing differs more than 10 ns from the nominal collision time, large showers were removed by means of the BAC total energy and number of BAC muon segments (cf. Sec. 6.1.5).

6.1.5 Summary of selection cuts

In the following, all cuts for the event selection in this analysis are summarised:

- **Event selection:**

  - Transverse energy measured in the CAL: $E_T \geq 8$ GeV
  - well reconstructed vertex: $|z_{vtx}| < 30$ cm and $\sqrt{x_{vtx}^2 + y_{vtx}^2} < 3$ cm

- **Muon selection:**

  - Number of muons: $N^\mu \geq 2$
  - Transverse momentum:
    $p_T^\mu > 0.75$ GeV (GMUON quality ≥ 5),
    $p_T^\mu > 1.5$ GeV (GMUON quality $= 4$)
  - Dimuon isolation:
    $I^{\mu\mu} > 0.25$ GeV outside J/ψ and ψ' mass peak
    $I^{\mu\mu} > 2.0$ GeV inside J/ψ and ψ' mass peak
  - Muon E_T fraction:
    $\frac{(p_T^{\mu_1} + p_T^{\mu_2})}{E_T} > 0.1$ and
    $\frac{(p_T^{\mu_1} + p_T^{\mu_2})}{E_T} < 0.5$ for $m^{\mu\mu} < 4$ GeV or
    $\frac{(p_T^{\mu_1} + p_T^{\mu_2})}{E_T} < 0.7$ for $m^{\mu\mu} \geq 4$ GeV
  - Difference in η: $|\eta^{\mu_1} - \eta^{\mu_2}| < 3.0$
  - Invariant mass: $m_{\text{inv}}^{\mu\mu} > 1.5$ GeV
  - p_T asymmetry cut: $\frac{\left(|p_T^{\mu_1} - p_T^{\mu_2}|\right)}{\left(|p_T^{\mu_1} - p_T^{\mu_2}|\right)} \leq 0.7$

- **Background cuts:**

  - Cosmics rejection:
    $T_{CAL} < 10$ ns,
    $E_{BAC} < 100$ GeV or $N_{BAC}^\mu < 15$,
    $||\phi^{\mu_1} - \phi^{\mu_2}| - \pi| < \frac{\pi}{200}$,
    $|\theta^{\mu_1} - (\pi - \theta^{\mu_2})| < \frac{\pi}{200}$

After all selection cuts, a sample of 11587 dimuon events from the HERA II data was obtained.

Chapter 7

Beauty signal determination

7.1 Principle of the measurement

Two principle event classes contribute to the beauty signal. The first class are events where both muons originate from the same parent b quark, e.g. via the sequential decay chain $b \rightarrow c\mu X \rightarrow s\mu\mu X'$ (cf. Fig. 2.14). These yield unlike-sign muon pairs produced in the same event hemisphere and with a dimuon invariant mass of $m^{\mu\mu} < 4$ GeV, corresponding to a partially reconstructed B meson mass. The second class of beauty events consists of events in which both muons originate from different beauty quarks of a $b\bar{b}$ pair. These events can yield like-sign and unlike-sign muon pairs, depending on whether the muons originate from the primary beauty decay or from the secondary charm decay (cf. Fig. 2.15) and whether $B^0\bar{B}^0$ mixing has occured. Muons from different beauty quarks are predominantly produced in different hemispheres and will therefore have a large dimuon invariant mass.

The first background contribution arises from primary charm-quark pair production where both charm quarks decay into muons. This yields unlike-sign muon pairs where the two muons are predominantly produced in different hemispheres. Cascade-like decays of charm mesons yields only non-prompt like-sign dimuons which were simply rejected by the selection criteria in Sec. 6. The charm contribution is too small in order to be measured directly from the data. Therefore, it was normalised to the charm contribution from a $D^* + \mu$ sample, which has a similar event topology. Double charm pair production can yield like-sign dimuons as well (cf. Sec. 2.7), but the contribution of this process is essentially negligible, which will be shown in Sec. 7.2.4.

Backgrounds like heavy quarkonia decays ($J/\psi, \psi', \Upsilon$) and Bethe-Heitler processes yield unlike-sign muon pairs. Contrary to muons from semileptonic beauty and charm decays, muons from these processes are not directly accompanied by hadronic activity, thus giving a well-isolated muon signature.

Since the contribution of like-sign dimuons from charm production is negligible, beauty quark production is the only source of genuine like-sign muon pairs. Background contributions from light flavour, where one or both muons are fake, contribute to both like-sign and unlike-sign

muon combinations. The like-sign false-muon background can be obtained from the data by subtracting the MC like-sign beauty contribution, properly scaled to the measurement, from the total like-sign sample, whereas the unlike-sign background is a simple reflection of the like-sign background.

In the HERA I dimuon analysis [4], it was shown that the charge of these false-muon pairs is almost uncorrelated, i.e. the contributions to the like- and unlike-sign dimuon distributions are, with small corrections, almost equal. Consequently, the difference between the unlike-sign and like-sign distributions is essentially free from light-flavour background and no simulation of this background using Monte Carlo methods is required. Once the other background contributions from open charm, heavy vector mesons and Bethe-Heitler are determined, the beauty contribution can be measured using this difference in the same way as it was done in [4].

7.2   Signal and background normalisation

For a later measurement of the cross section for beauty quark production (cf. Sec. 8), the beauty contribution in the dimuon sample needs to be determined. This is only possible after the determination of the background contributions, which is described in the following.

7.2.1   Normalisation of heavy quarkonia and Bethe-Heitler MC

The isolated dimuon sample contains predominantly dimuon events from heavy quarkonia and Bethe-Heitler processes while the beauty contribution there is very small. Therefore, the heavy quarkonia MC were normalised to describe the $J/\psi, \psi'$ and Υ mass peaks and the Bethe-Heitler MC for the description of the isolated high-mass region. Furthermore, it is known from previous analyses [4, 172–174] that HERWIG generates a too soft p_T spectrum for inelastic J/ψs, hence a reweighting of the HERWIG MC was mandatory in order to describe the dimuon p_T distribution in the isolated low-mass region before the normalisation of the heavy quarkonia contributions. By fitting the data over MC ratio of the $p_T^{\mu\mu}$ distribution, the following reweighting function was determined:

$$f_{\text{weight}}(p_T^{\mu\mu}) = 0.7064 \cdot \min(\exp(0.5604 \cdot p_T^{\mu\mu}), 8.64). \tag{7.1}$$

This reweighting correlates e.g. with the distance in pseudorapidity-azimuth ΔR between the two muons, therefore, the $p_T^{\mu\mu}$ and $\Delta R^{\mu\mu}$ (as an additional control) distributions for low-mass, isolated muon pairs before and after applying this reweighting are illustrated in Fig. 7.1. The reweighted distributions show good agreement between data and MC. It should be noted that this reweighting procedure is applied on both, isolated- and non-isolated muon pairs in the J/ψ sample genereated by the HERWIG MC. After the normalisation of the heavy quarkonia and Bethe-Heitler contributions, the resulting scaling factors were then used for the non-isolated dimuon sample (cf. Fig. 6.2).
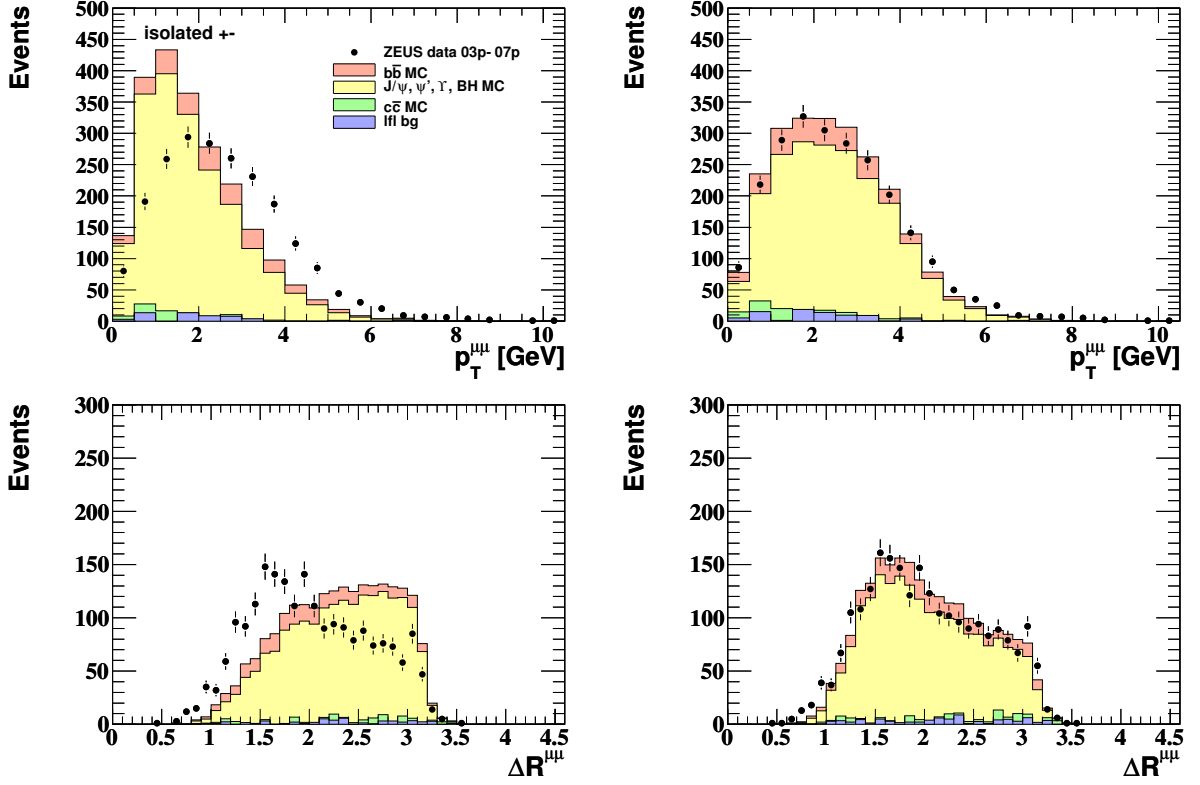
Figure 7.1: Dimuon p_T and ΔR spectra for low-mass, isolated muon pairs before (left) and after (right) reweighting the J/ψ $p_T^{\mu\mu}$ spectra.

7.2.2 Charm MC normalisation

Only non-isolated unlike-sign muon pairs contribute to the background for this analysis. As mentioned before, a direct measurement of the charm contribution from the dimuon data is not possible, therefore, the same procedure for the scaling as in the HERA I analysis was used: Considering the topology of $D^* + \mu$ and $\mu\mu$ events from charm (cf. Fig. 7.2), one observes that both topologies are very similar. Thus, the same scale factor $s_{MC,charm}$ for describing the D^* mass peak is used for this analysis and was determined to [4]

$$s_{MC,charm} = 1.37 \tag{7.2}$$

7.2.3 Light-flavour background determination

The light-flavour background was obtained by means of the subtraction method where two essential assumptions are made:

1. In the considered phase space, only beauty-quark decays can produce like-sign muon pairs.

2. There is no charge correlation between like-sign and unlike-sign muon pairs from light-flavour background.
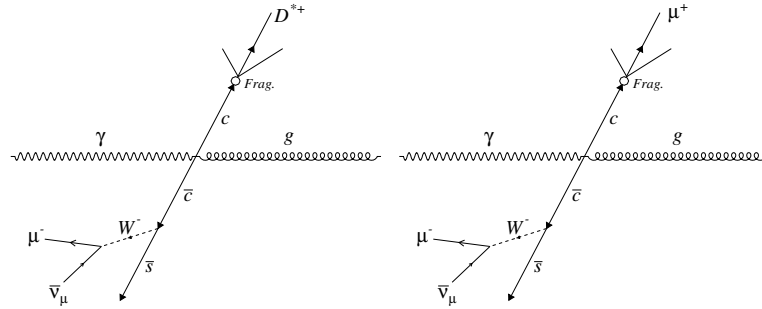
Figure 7.2: Topology of $D^*\mu$ pair (left) and $\mu\mu$ pair (right) from $c\bar{c}$ event. Dimuons from those events are unlike-sign and non-isolated.
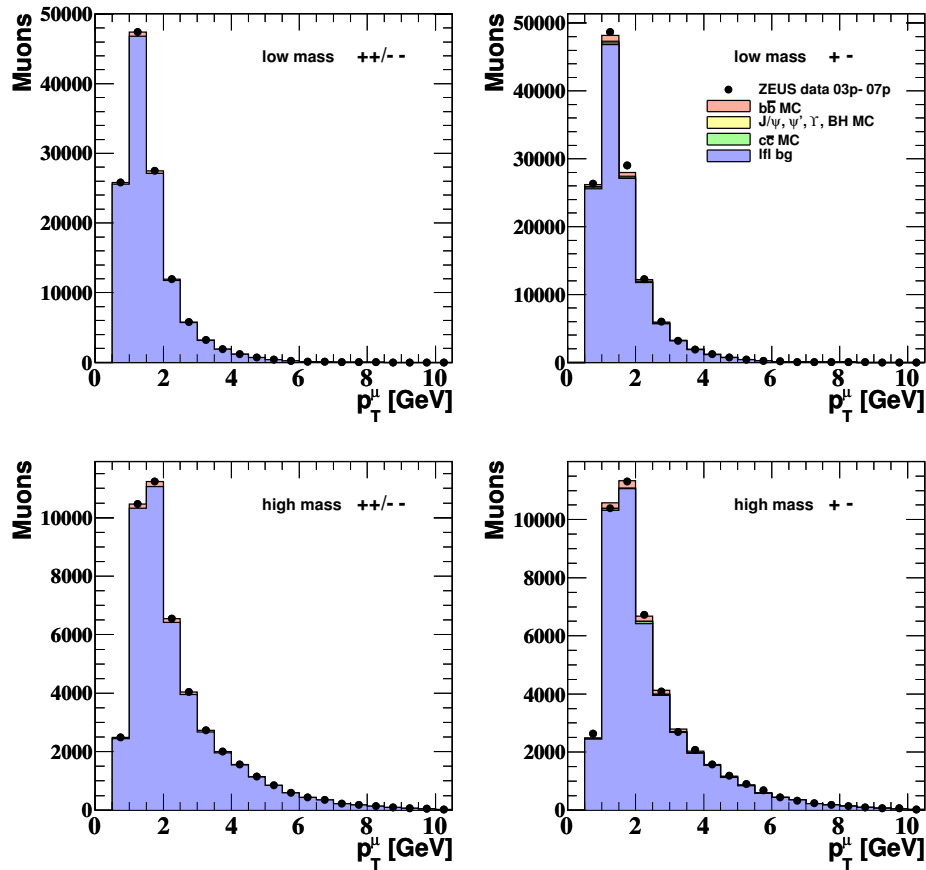
Figure 7.3: Muon transverse momentum p_T^μ for like- (left) and unlike-sign (right) dimuons in the low- and high-mass range. The light-flavour background obtained from the like-sign sample was applied to the data in the unlike-sign sample, shown in the dominating contribution. The almost negligible remaining contributions from beauty, charm, heavy quarkonia and Bethe-Heitler processes are also shown.

The first assumption is based on the standard model and was not tested further. The second assumption was briefly checked on a dimuon sample highly enriched in false dimuon candidates

(GMUON quality > 0) to ensure that the subtraction method can still be applied for this analysis on the HERA II data sample. Figs. 7.3 - 7.6 show control distributions for this sample. The unlike-sign dimuon data is quite well described by the shape of the like-sign distribution from the light-flavour background, however, small corrections for the unlike-sign light-flavour background in the high ($\sim 1\%$) and low mass region ($\sim 4\%$) sample were required.
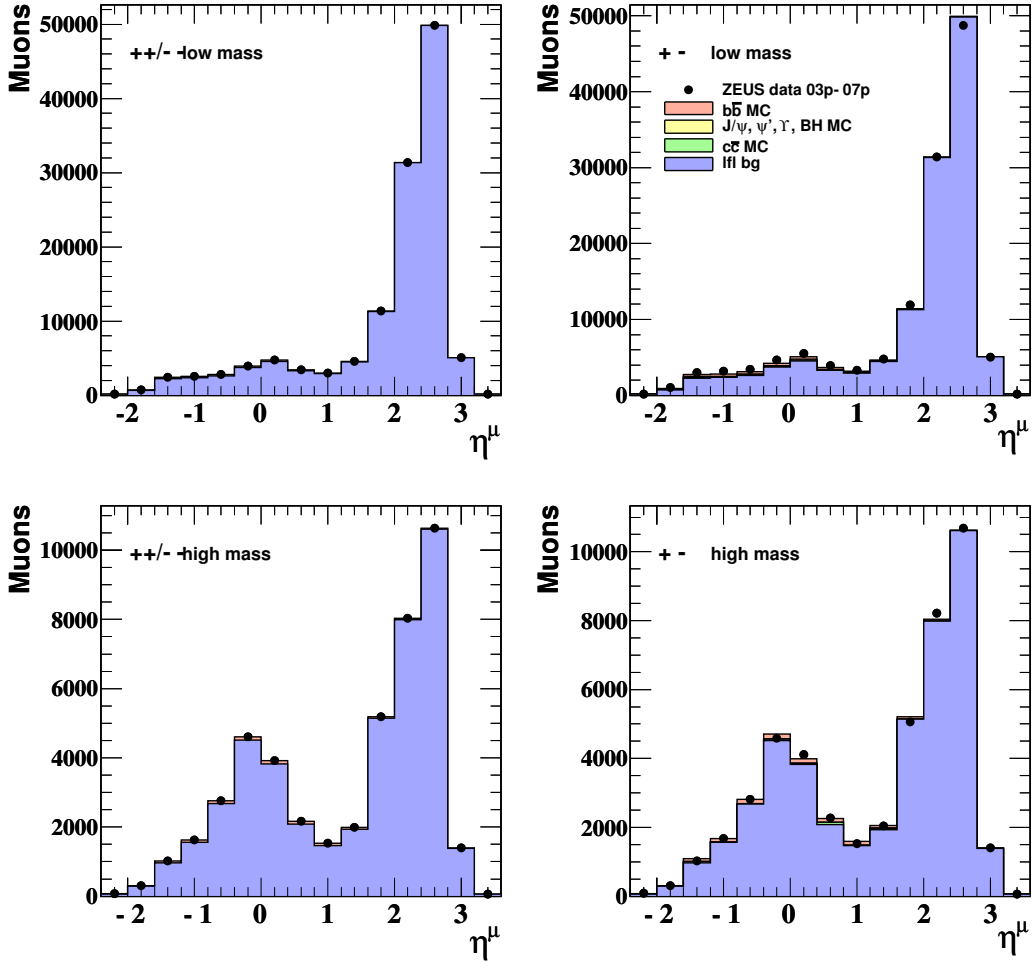
Figure 7.4: Muon pseudorapidity η^{μ} for like- (left) and unlike-sign (right) dimuons in the low- and high-mass range. The light-flavour background obtained from the like-sign sample was applied to the data in the unlike-sign sample, shown in the dominating contribution. The almost negligible remaining contributions from beauty, charm, heavy quarkonia and Bethe-Heitler processes are also shown.
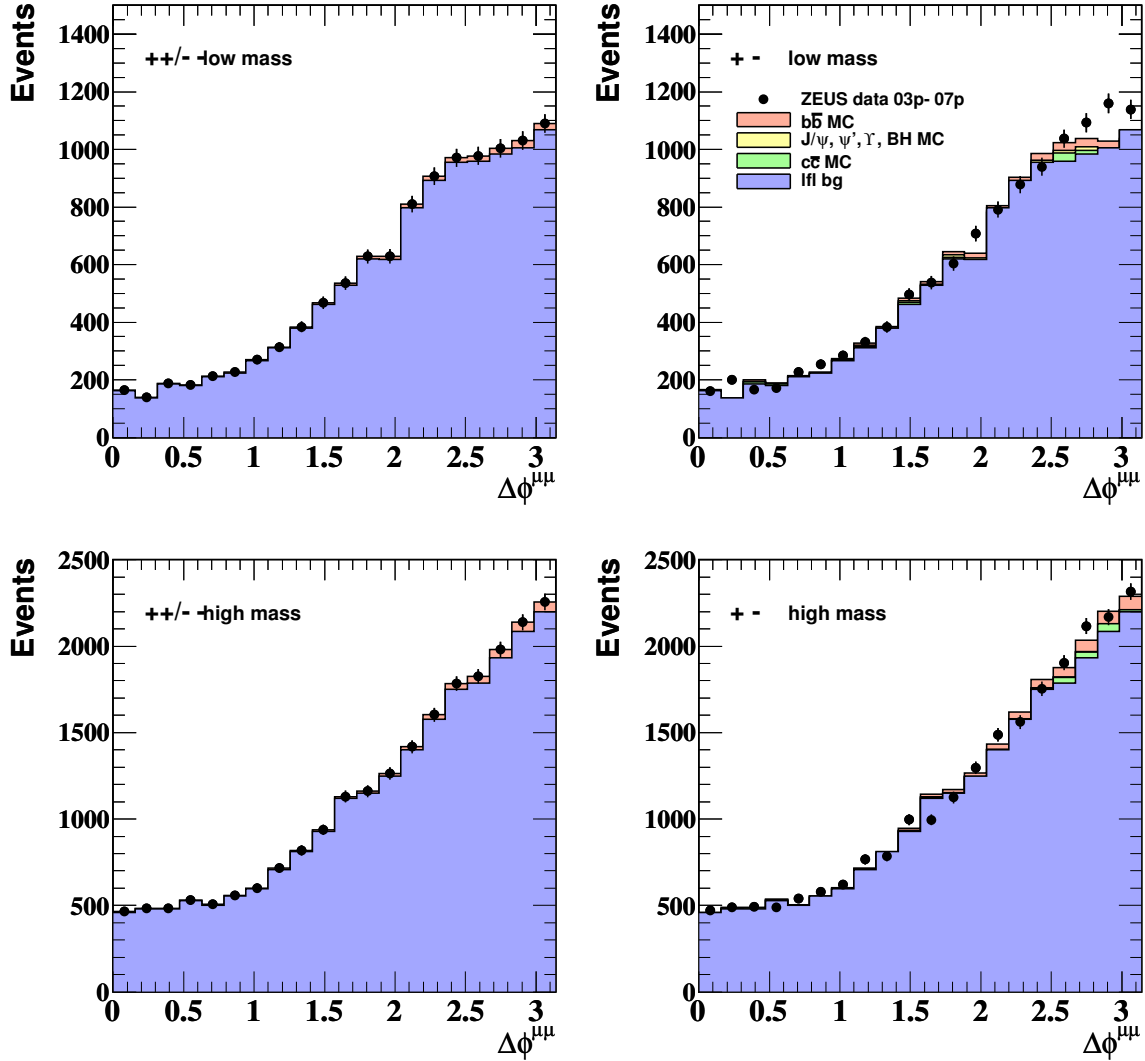
Figure 7.5: Azimuthal distance $\Delta\phi^{\mu\mu}$ of both muons for like- (left) and unlike-sign (right) dimuons in the low- and high-mass range. An additional mass cut of $m_{\text{inv}}^{\mu\mu} \geq 3.25$ GeV was applied in these plots since angular muon cross sections in $\Delta\phi$ and ΔR for muons from different b quarks were measured in the later part of this thesis. The light-flavour background obtained from the like-sign sample was applied to the data in the unlike-sign sample, shown in the dominating contribution. The almost negligible remaining contributions from beauty, charm, heavy quarkonia and Bethe-Heitler processes are also shown.

7.2.4 Multi-heavy flavour contribution

The contributions of all three multi-heavy-flavour processes after all selection cuts listed in Sec. 6 to the dimuon data are only 0.03 % for the $b\bar{b}b\bar{b}$ process, 0.19 % for the production of $c\bar{c}c\bar{c}$ and 0.25 % for the $b\bar{b}c\bar{c}$ process, hence in principle essentially negligible. Corresponding dimuon invariant mass distributions for like- and unlike-sign muon pairs in the low- and high-mass region from these processes with comparison to the dimuon data can be found in Appendix G.
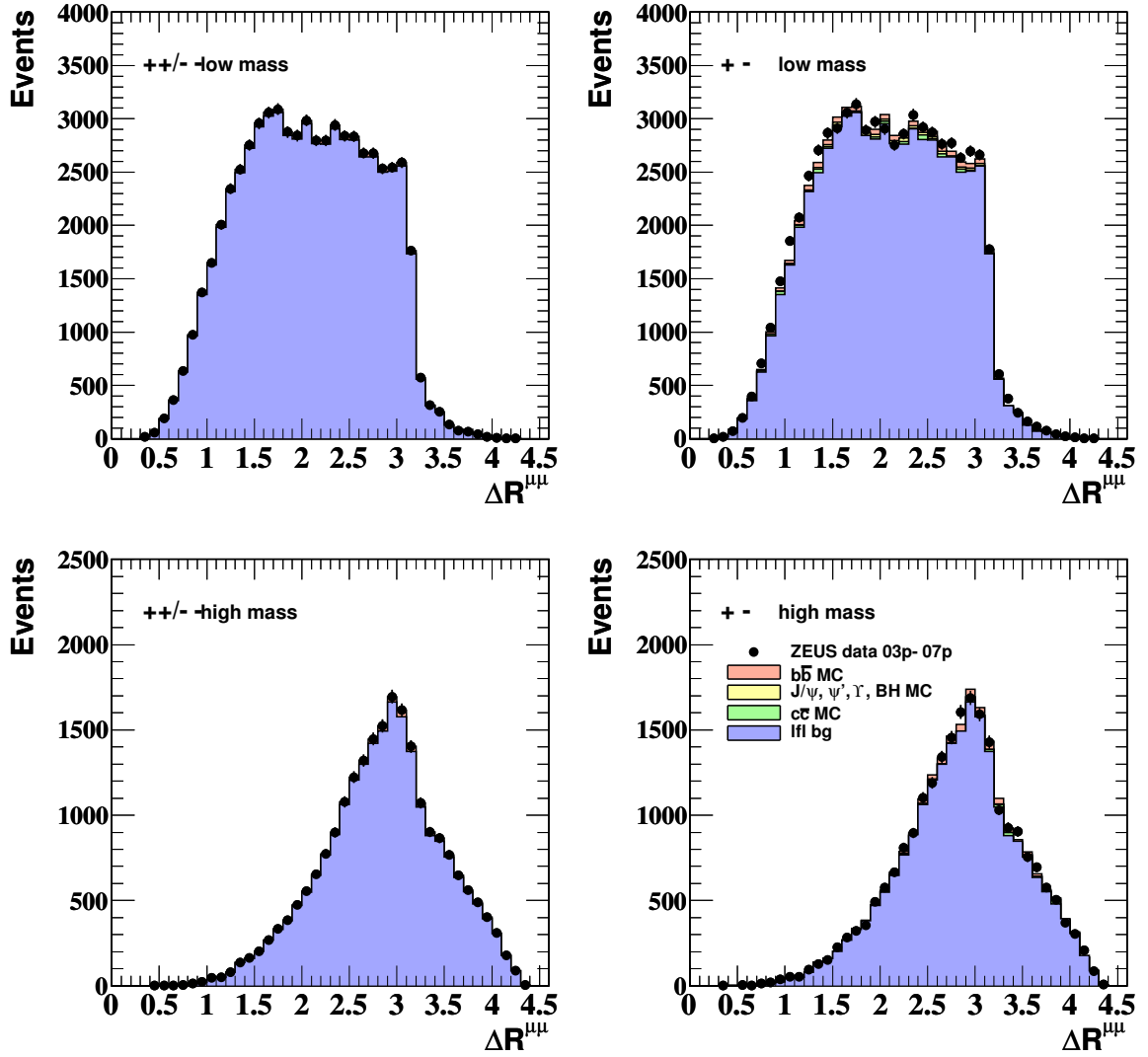
Figure 7.6: Angular correlations in $\Delta R^{\mu\mu}$ of both muons for like- (left) and unlike-sign (right) dimuons in the low- and high-mass range. An additional mass cut of $m^{\mu\mu}_{\mathrm{inv}} \geq 3.25$ GeV was applied in these plots since angular muon cross sections in $\Delta\phi$ and ΔR for muons from different b quarks were measured in the later part of this thesis. The light-flavour background obtained from the like-sign sample was applied to the data in the unlike-sign sample, shown in the dominating contribution. The almost negligible remaining contributions from beauty, charm, heavy quarkonia and Bethe-Heitler processes are also shown.

7.2.5 Beauty MC normalisation

After determining the background normalisations, the scale factor for the beauty signal MC is obtained by the following procedure:

The unlike-sign dimuon data d^{unlike} consists of the unlike-sign contributions of beauty, charm,

heavy quarkonia, Bethe-Heitler as well as the light-flavour background

$$d^{\text{unlike}} = b^{\text{unlike}} + c^{\text{unlike}} + VM + BH + LF^{\text{unlike}}, \qquad (7.3)$$

while the like-sign dimuon data d^{like} is the sum of the like-sign beauty and light-flavour background contributions:

$$d^{\text{like}} = b^{\text{like}} + LF^{\text{like}}. \qquad (7.4)$$

Due to assumption 2.) of the light-flavour background-estimation, one has:

$$LF^{\text{unlike}} = C \cdot LF^{\text{like}}, \qquad (7.5)$$

where C is the correction factor applied to the unlike-sign light-flavour contribution (cf. Sec. 7.2.3). The beauty scale factor, defined by $b^{\text{unlike/like}} = s^b_{\text{MC}} \cdot b^{\text{unlike/like}}_{\text{MC}}$ is then obtained by means of Eq. 7.3, 7.4 and 7.5.

$$s^b_{\text{MC}} = \frac{d^{\text{unlike}} - C \cdot d^{\text{like}} - VM - BH}{b^{\text{unlike}}_{\text{MC}} - C \cdot b^{\text{like}}_{\text{MC}}} \qquad (7.6)$$

For this analysis, the normalisation factor for the beauty MC was determined to be:

$$s^b_{\text{MC}} = 1.85 \pm 0.04 \text{ (stat.)}. \qquad (7.7)$$

7.2.6   Control distributions

The normalisations of the beauty and background contributions were checked with several different kinematic variables used in this analysis. In the following, a selection of control distributions for muon and jet kinematics, event properties as well as secondary vertex information is presented.

Fig. 7.7 shows the transverse momentum p_T^μ and the pseudorapidity η^μ of muons for the sum of low- and high-mass non-isolated dimuons as a control for muon spectra. In the η^μ distribution, an apparent shift of the data to larger values of η with respect to the MC can be seen. This shift has been observed in previous beauty quark measurements with semi-leptonic decays of the beauty quark into muons [184, 185].

Also illustrated in Fig. 7.7 (lower left) is the $\log(Q^2)$ distribution. This quantity was used to check both, the photoproduction and DIS contribution in dimuon events, which were normalised with the same scaling factors for the beauty and background contributions since no separation is done between PHP and DIS in this analysis. The quantity $E - p_z$, shown in Fig. 8.3 (lower right), relates to the center-of-mass energy W of the photon-proton system in photoproduction.

Angular correlations in $\Delta R^{\mu\mu}$ and $\Delta^{\mu\mu}$ of both muons in dimuon events are shown in Fig. 7.8 for the low- and high-mass range as control plots for the event topology. Additionally, the dimuon isolation $I^{\mu\mu}$ (cf. Sec. 5.7) is illustrated in Fig. 7.8 as a check for the hadronic activity around the muons. Both, isolated and non-isolated events for the low- and high-mass dimuon sample entered this control plot. It can be observed that the heavy quarkonia and Bethe-Heitler
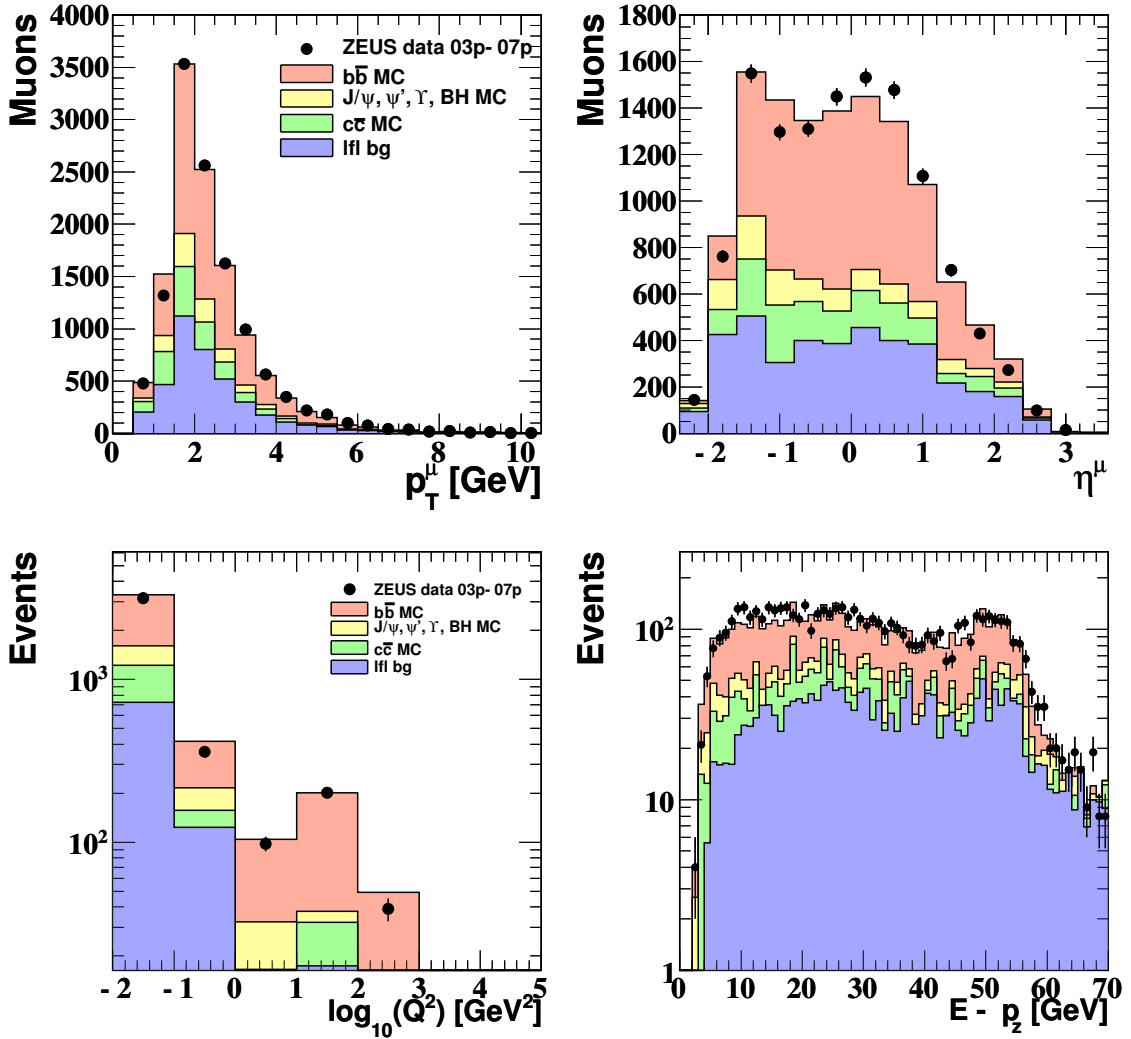
Figure 7.7: Muon transverse momentum (upper left) and pseudorapidity distributions (upper right) from non-isolated, unlike-sign dimuons in the low- and high-mass region. For each event, two muons entered. Furthermore, the distributions for Q^2 (lower left) and $E - p_z$ (lower right) for the same dimuon events are shown. The lower two bins of the Q^2 distribution contain non-DIS events: The first bin contains events with $E - p_z < 34$ GeV (predominantly photoproduction events) and the second bin contains events with $E - p_z > 34$ GeV, which did not pass the DIS electron requirements. Also illustrated is the breakdown into the expected contributions from different processes.

contributions peaks at low values of $I^{\mu\mu}$, as expected, while the beauty, charm and light flavour contributions have higher values of $I^{\mu\mu}$.

Other control distributions were presented in Chapter 6, i.e.

- the unlike-sign dimuon mass for isolated and non-isolated muon pairs in the low- and high-mass region, shown in Fig. 6.3, as a check for the normalisation of the isolated and non-isolated dimuon samples,
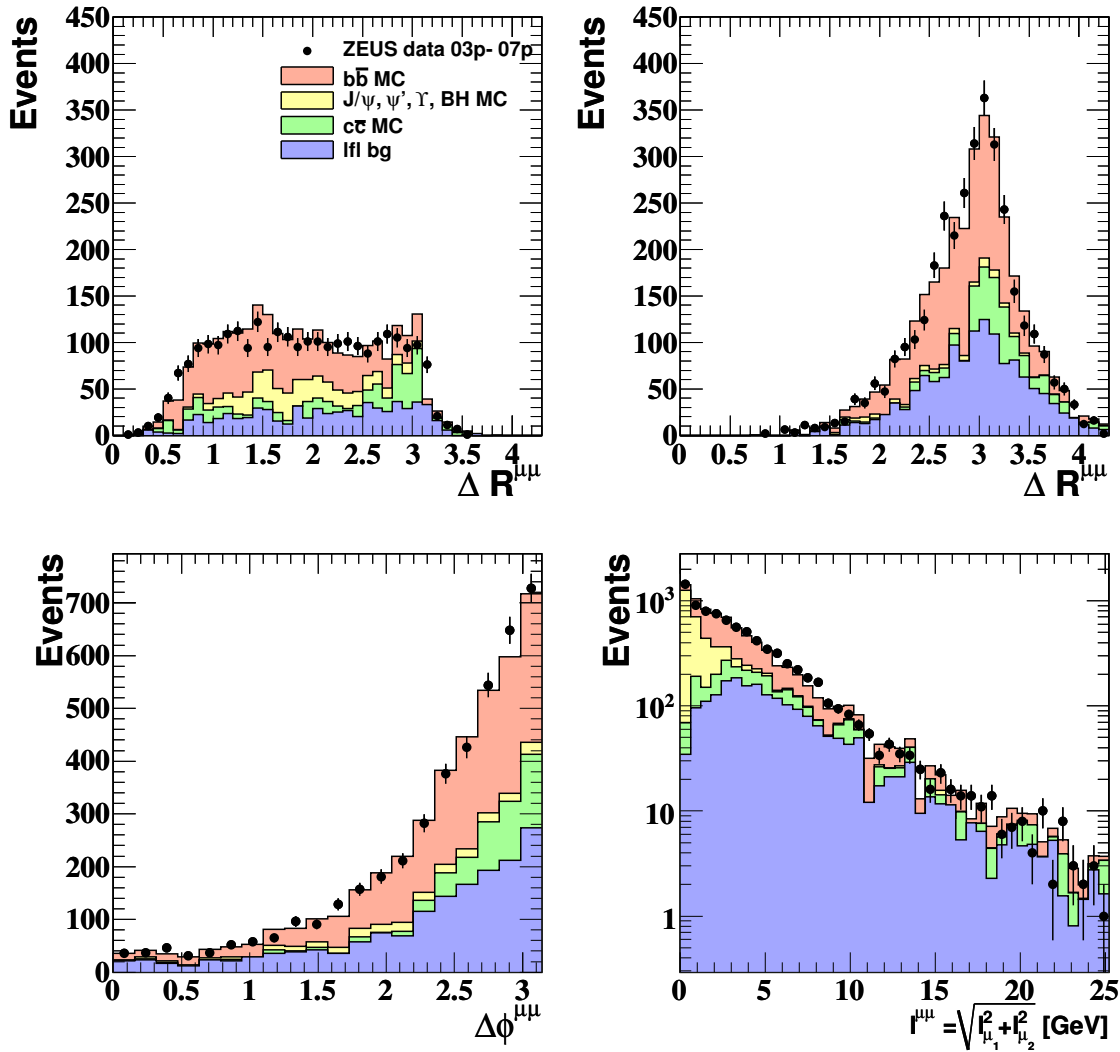
Figure 7.8: Angular correlations in ΔR of both muons in dimuon events for low-mass (upper left) and high-mass (upper right) unlike-sign dimuons in the non-isolated subsample. Furthermore, angular correlations in $\Delta\phi$ of both muons in dimuon events for the sum of low-mass and high-mass unlike-sign dimuons in the non-isolated subsample (bottom left) as well as the dimuon isolation $I^{\mu\mu}$ for low- and high-mass unlike-sign dimuon events (bottom right) are presented.

- the like- and unlike-sign dimuon mass for the sum of isolated and non-isolated muon pairs, illustrated in Fig. 6.2, as a control for the total normalisation.

- the transverse energy measured in the CAL, E_T^{CAL}, before and after applying the dimuon-E_T fraction cut, which is shown in Fig. 6.1.

In general, good agreement with the data was achieved.

Jets in dimuon events

The normalisations of the beauty and background contributions were checked furthermore on dimuon events containing jets. Approximately 76% of all dimuon events contain at least one jet candidate. For these events, the p_T^{rel} distribution (cf. Sec. 5.11.1) is shown in Fig. 7.9. In the same figure, the pseudo thrust, T_{pseudo}, (cf. Sec. 5.12.1) is illustrated for the remaining events without jets.
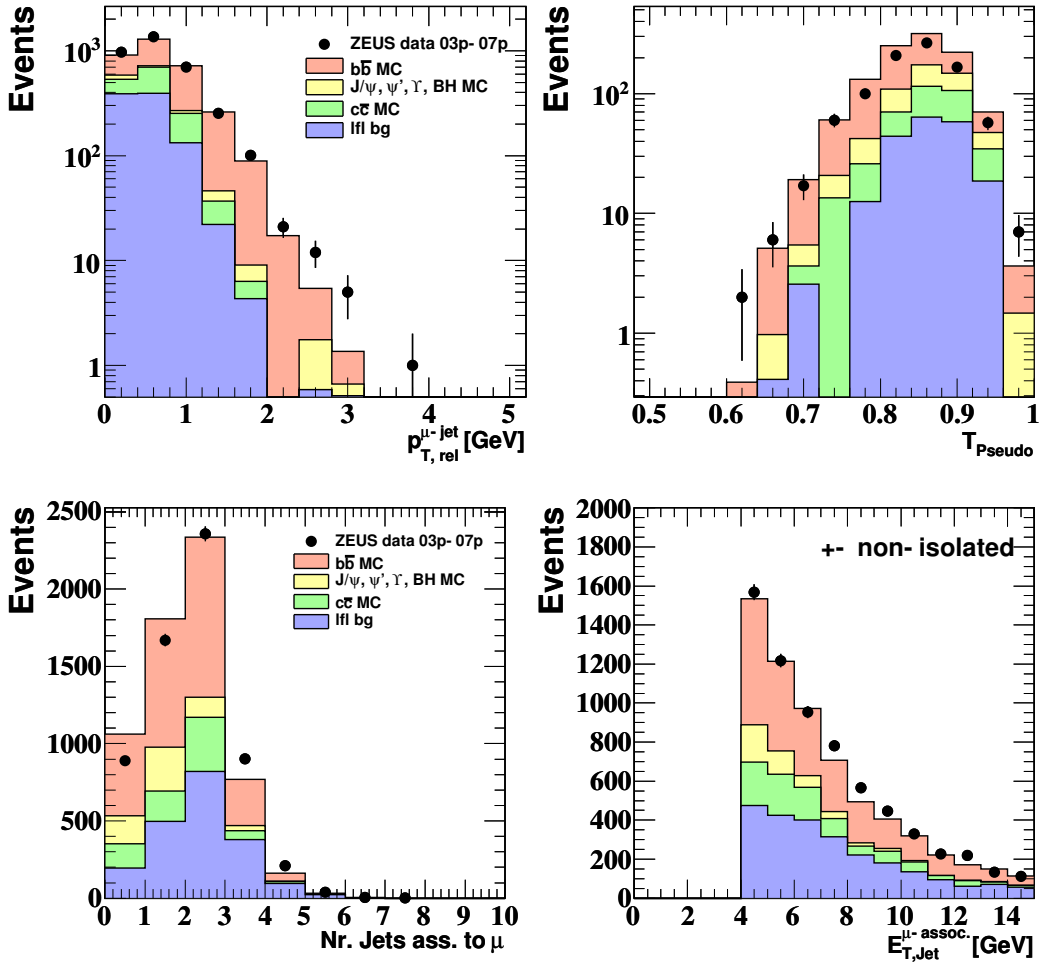
Figure 7.9: p_T^{rel} (upper left) distribution for non-isolated, unlike-sign dimuon events with jets and pseudo thrust, T_{pseudo} (upper right) distribution for non-isolated, unlike-sign dimuon events without jets. Shown are furthermore the number of muon-associated jets (lower left) as well as the corresponding transverse energy, E_T^{Jet} (lower right). The breakdown into the expected contributions from different processes is also illustrated.

Fig. 7.9 as well as Fig. 7.10 show further control distributions for events with non-isolated, unlike-sign muon pairs, where at least one muon is associated to a jet with $E_T^{Jet} > 4$ GeV and $|\eta^{Jet}| \leq 2.5$. Displayed are the transverse energy, E_T^{Jet}, and momentum, p_T^{Jet}, as well as the pseudorapidity, η^{Jet}, the jet-muon distance in the $\eta - \phi$ plane, ΔR, and mass, m^{Jet}, of all muon-associated jets. For all jet variables, the MC contributions agree reasonably with the
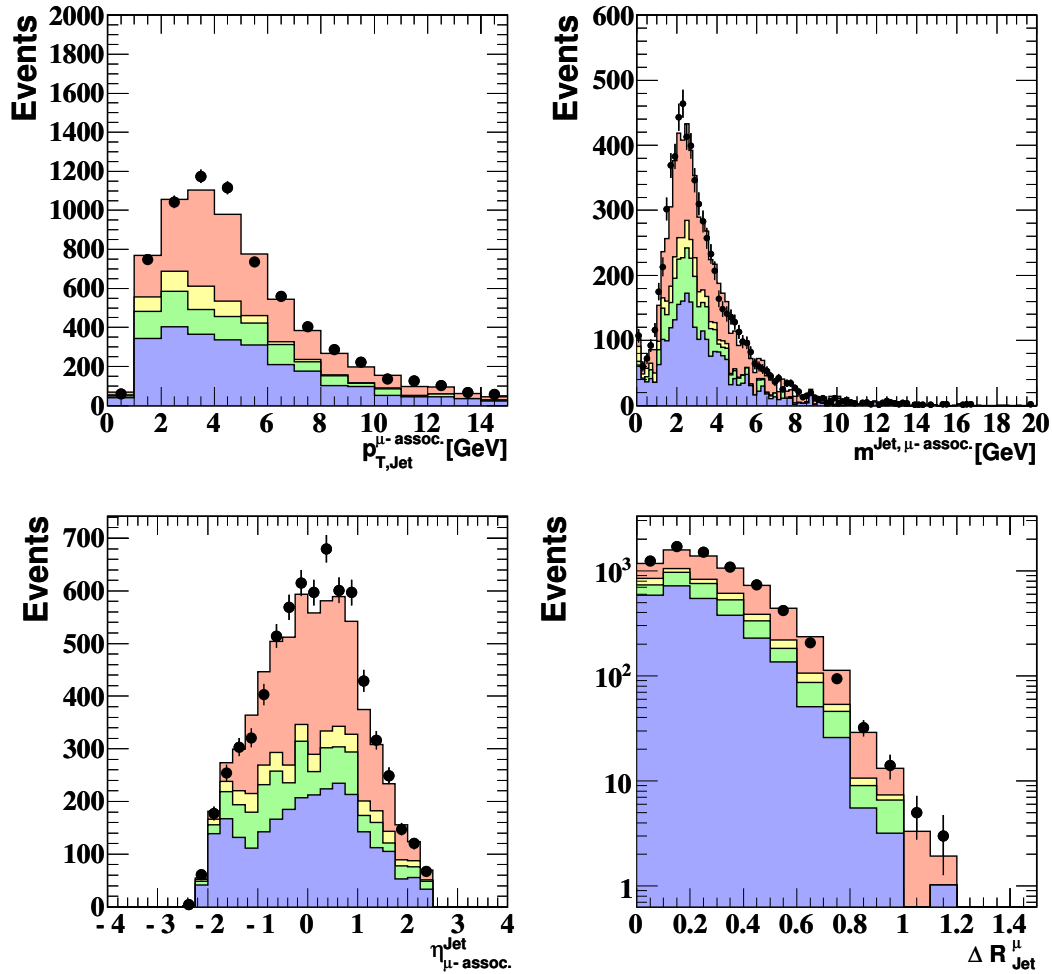
Figure 7.10: Kinematics of muon-associated jets in the non-isolated, unlike-sign dimuon sample. Shown are the transverse momentum, p_T^{Jet}, mass, m^{Jet}, the pseudorapidity, η^{Jet} as well as the jet-muon distance in the $\eta - \phi$ plane, ΔR. The breakdown into the expected contributions from different processes is also illustrated.

data.

Secondary vertices in dimuon events

The last part of control distributions consists of quantities relating to the life-time information of heavy hadrons. In Fig. 7.11, the number of secondary vertex candidates per event, the track multiplicity and invariant mass m_{vtx} as well as the corresponding χ^2/ndf per secondary vertex for the sum of like- and unlike-sign dimuon events are illustrated. While the vertex mass region below 1.5 GeV seems to be underestimated by the MC, the region above 1.5 GeV as well as the remaining secondary vertex quantities show good agreement between data and MC.

As mentioned before in Sec. 5.11, beauty hadrons have longer lifetimes than charm hadrons,
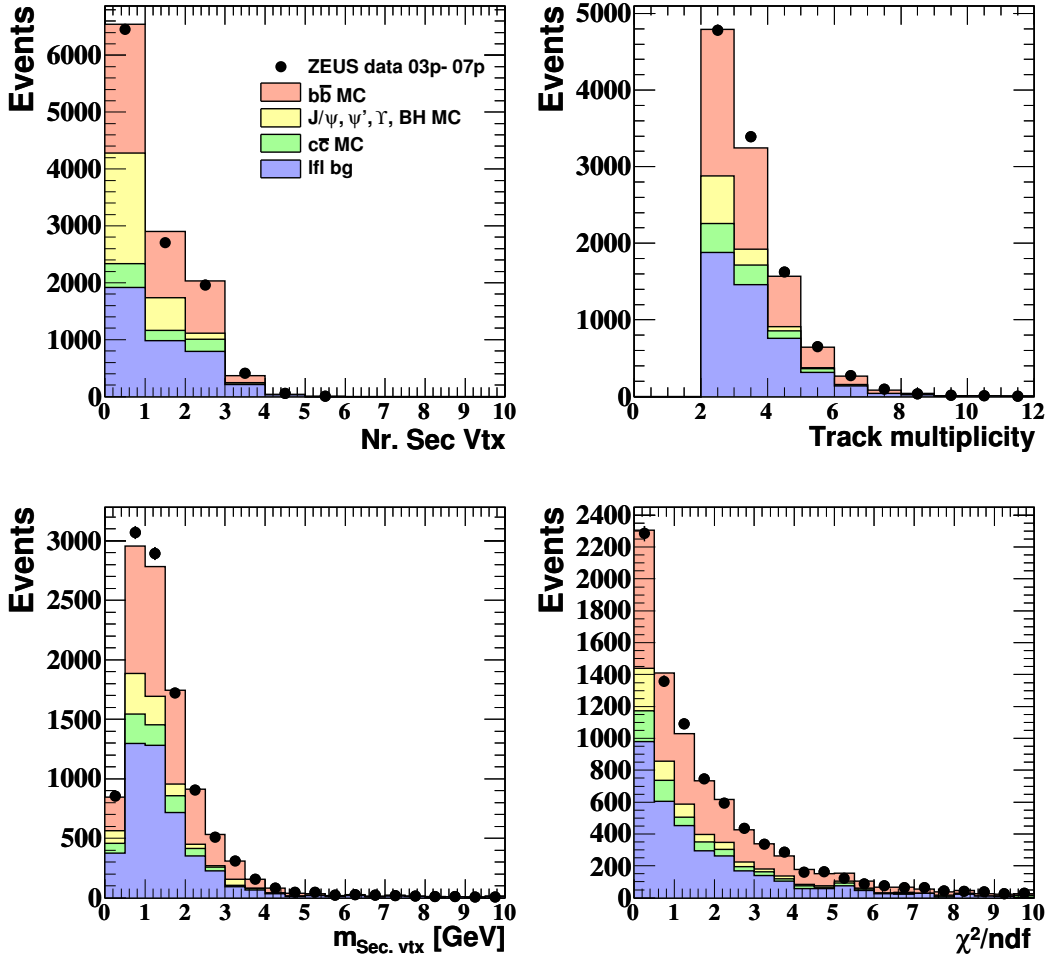
Figure 7.11: Number of secondary vertex candidates, track multiplicity, invariant mass m_{vtx} as well as χ^2/ndf for each secondary vertex for like- and unlike-sign dimuon events. The breakdown into the expected contributions from different processes is also illustrated.

which is reflected in their decay length L_{XY}. This quantity as well as its significance $S = L_{XY}/\sigma_{L_{XY}}$ are shown in Fig. 7.12 for the sum of like- and unlike-sign dimuon events. The decay length L_{XY} is well described by the MC, but, in contrast to other analyses using life-time information of the heavy hadrons [70–73], where the light-flavour background distribution is expected to be symmetric around zero, the shape of the dimuon light-flavour contribution is asymmetric, which is the result of the subtraction method (cf. Sec. 7.2.3). The beauty contribution was varied from s^b_{MC}=1.85 to 0.9 in order to obtain a fairly symmetric shape of the light-flavour contribution in the tail of the decay length distribution, but in that case, the data is not described by the MC anymore. The decay length significance is not fully described by the MC, hence a so-called *smearing* of the MC would be necessary. This method has also been applied in the analyses mentioned before.

The negative part of the decay length significance distribution is unphysical and caused by the detector resolution. Thus, it was mirrored onto and then subtracted from the positive
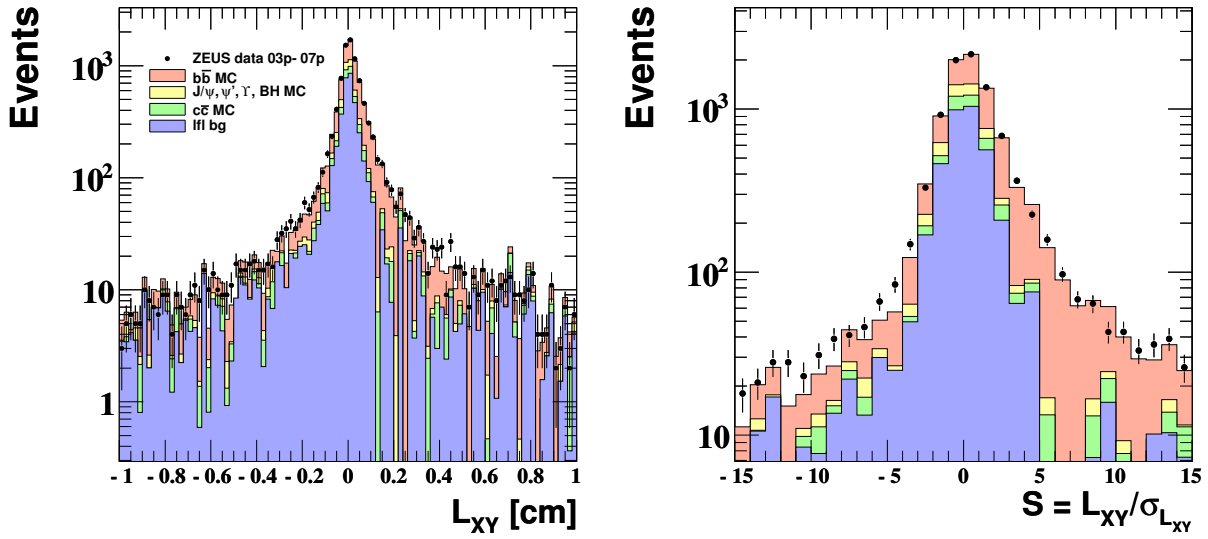
Figure 7.12: Decay length L_{XY} and decay length significance $S = L_{XY}/\sigma_{L_{XY}}$ for the sum of like- and unlike-sign dimuon events. The breakdown into the expected contributions from different processes is also illustrated.

part of the significance distribution, yielding the so-called *mirrored decay length significance* $S^+ - S^-$, which is illustrated in Fig. 7.13 in both, logarithmic and linear scale.
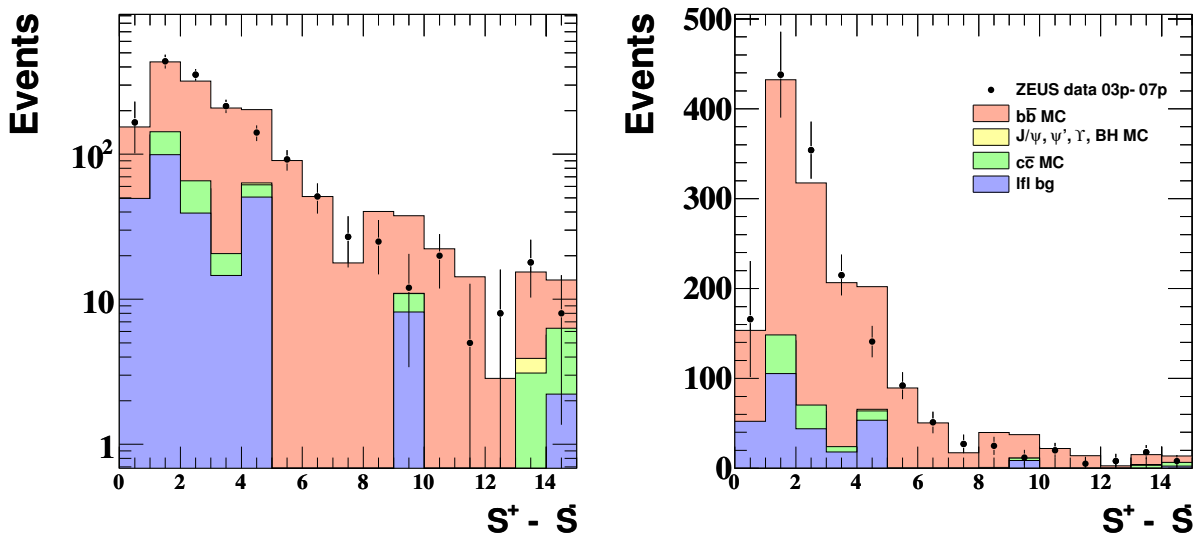
Figure 7.13: Mirrored decay length significance $S^+ - S^-$ for the sum of like- and unlike-sign dimuon events in logarithmic and linear scale. The breakdown into the expected contributions from different processes is also illustrated.

With this procedure, the contribution of heavy quarkonia and Bethe-Heitler processes is almost rejected since the significance distribution is symmetric around zero. Contributions of

light-flavour and charm background are also reduced enormously while the beauty purity is very high, which can be well observed in the linearly scaled $S^+ - S^-$ distribution. With the normalisation factors determined in the previous part of this chapter, the $S^+ - S^-$ distribution is reasonably described by the MC.

While the beauty scaling factor determined in this thesis (s_{MC}^b =1.85) is roughly of the same order (but still greater) than in other beauty production measurements with muons or electrons [4, 62, 65, 185], the beauty scaling factor in inclusive measurements in photoproduction without restriction on a particle in the final state [70–72] is approximately 50% smaller (s_{MC}^b =1.05). It was checked that the mirrored significance for dimuon events in Fig. 7.13 is still reasonably described by the MC if the beauty normalisation is reduced to $s_{\mathrm{MC}}^b \approx$1.6, but the agreement between MC and dimuon data in the remaining control distributions for the muon spectra or secondary vertices becomes worse. One possibility in order to compensate this disagreement could be e.g. the inclusion of instanton-induced events with heavy flavours, as explained in the following section.

7.3   Search for instantons in dimuon events

In the first step for the search of heavy-flavour instantons, the same selection criteria for dimuon events as described in Sec. 6 has been used. Both, the production and decay of J/ψ and Υ mesons are not well described by the JETSET programme [179] implemented in QCDINS [178]. Therefore, events with muon pairs originating from heavy quarkonia decays were rejected. While the theoretical cross section for heavy-flavour instantons contains an unknown mass-suppression factor [207], the QCDINS MC generator is only able to predict cross section for instanton processes without this factor. Albeit, in order to obtain the upper limit of instanton events to the dimuon data, the unsuppressed instanton contribution predicted by QCDINS was first normalised to once the data luminosity. As a consequence, a reduction of the beauty normalisation factor in Eq. 7.7 was necessary.

First it was checked if the dimuon data is described by the sum of the normalised beauty, charm, heavy quarkonia, Bethe-Heitler, light-flavour background and instanton MC. While the instanton scaling factor was set to $s_{\mathrm{MC}}^{\mathrm{Instanton}}$ =1.0, the beauty scaling factor was varied from s_{MC}^b =1.85 to ≈0.8, the normalisations of the remaining contributions did not change. It was found out that the sum of the dimuon MC including QCDINS overestimates in all cases the dimuon data. In Figs. 7.14 and 7.15, control distributions for muon and secondary vertex quantities are illustrated, where the QCDINS contribution is implemented as well. The beauty normalisation in these distributions was set to $s_{\mathrm{MC}}^b = 1.1$, which is of the same size of to the beauty scaling factor determined in inclusive beauty production measurements in photoproduction ($s_{\mathrm{MC}}^b = 1.05$) [70–72]. As mentioned before, the MC contribution to the dimuon data is somewhat overestimated in these quantities. Therefore, the QCDINS normalisation needed to be corrected to lower values, while the beauty scaling factor was adjusted accordingly in order to describe the shape of the control distributions presented in the previous part of this chapter.

For a reasonable description of the dimuon data by the sum of all MC contributions, the
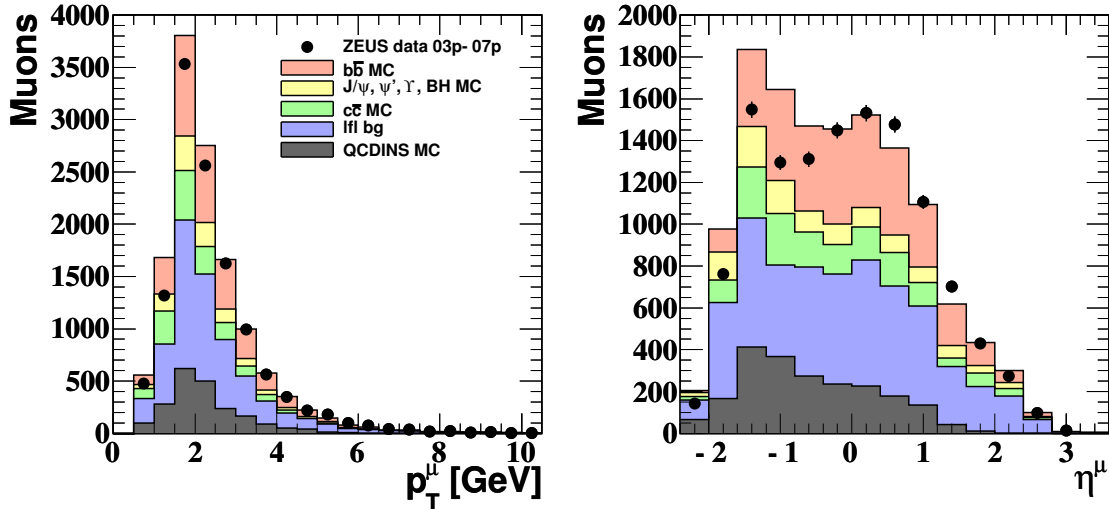
Figure 7.14: Muon transverse momentum (upper left) and pseudorapidity distribution (upper right) from low- and high-mass unlike-sign dimuons in the non-isolated sample. The instanton contribution, normalised to once the data luminosity, is shown as well. The beauty contribution is scaled by $s_{\text{MC}}^{b} = 1.1$.
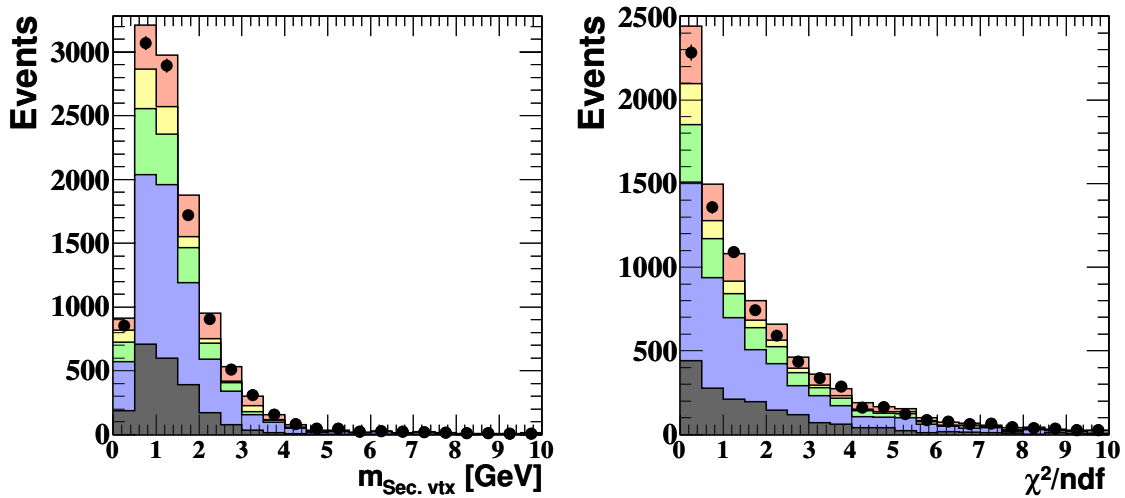
Figure 7.15: Invariant mass, m_{vtx}, (left) and the χ^2/ndf (right) for each secondary vertex for like- and unlike-sign dimuon events. The instanton contribution, normalised to once the data luminosity, is shown as well. The beauty contribution is scaled by $s_{\text{MC}}^{b} = 1.1$.

instanton scaling factor was assumed to be:

$$s_{\text{MC}}^{\text{Instanton}} = 0.5, \tag{7.8}$$

while the beauty scaling factor changed to:

$$s_{\text{MC}}^{b} = 1.5. \tag{7.9}$$

Figs. 7.16 and 7.17 show the invariant mass for like- and unlike-sign as well for isolated and non-isolated muon pairs in the low- and high-mass region with the re-scaled beauty and instanton fraction. As expected, muon pairs from instantons are predominantly non-isolated as well as like- and unlike-sign. It should be noted that, in contrast to the like- and unlike-sign dimuon contribution from the light-flavour background, which is almost equal, the unlike-sign contribution from heavy-flavour instantons is significantly higher than the like-sign contribution ($\sim$25% higher) and not identical in shape.
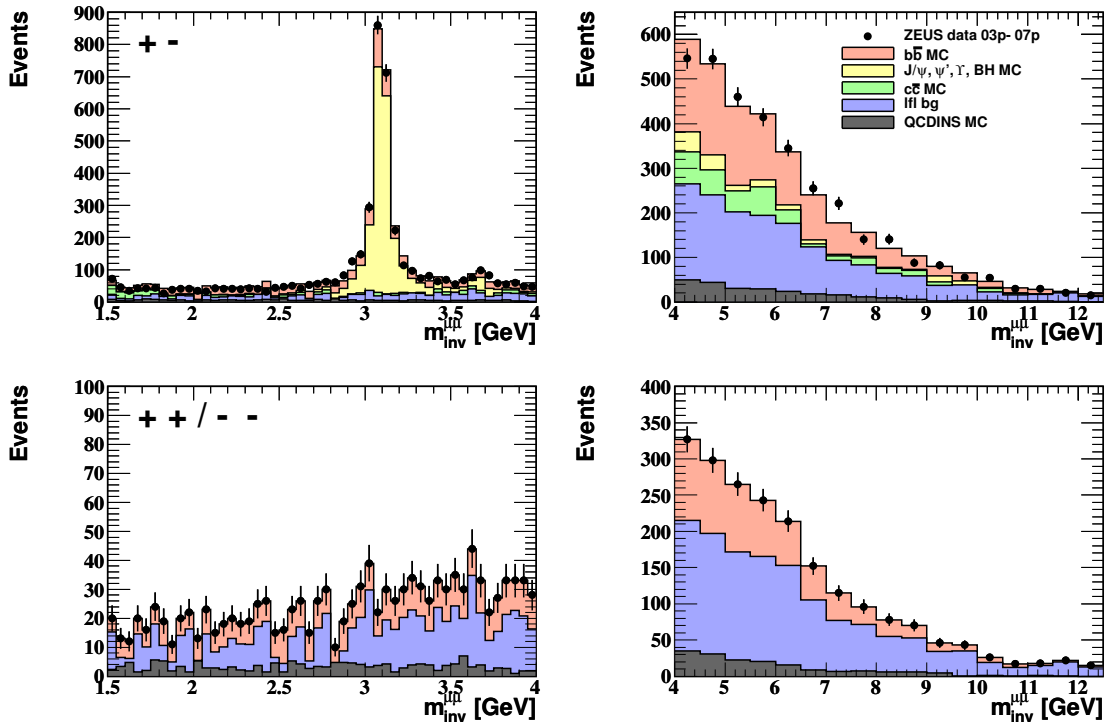
Figure 7.16: Invariant dimuon mass for like- and unlike-sign muon pairs with the instanton contribution scaled by 0.5 and the beauty contribution scaled by 1.5. The breakdown into the expected contributions from different processes is also illustrated.

In the following Figs. 7.18 - 7.20, further control distributions concerning the muon spectra as well as secondary vertex quantities are shown as a control for the normalisation factors for the instanton and beauty MC. With exception of the muon pseudorapidity, which is better described by the MC without instanton contribution (cf. Fig. 7.7), some of the remaining control quantities show a slightly better agreement between the MC and the data when taking the instanton contribution into account, e.g. muon transverse momentum, p_T^μ, the invariant secondary vertex mass, m_{vtx}, or the decay length significance, L_{XY}. Especially in the decay length distribution, the shape of the light-flavour background becomes slighlty more symmetric in the tail region. In the remaining quantities, the agreement between MC and data does not change or worsens slightly, thus, a dimuon contribution from heavy-flavour instantons for these quantities is not explicitly necessary.
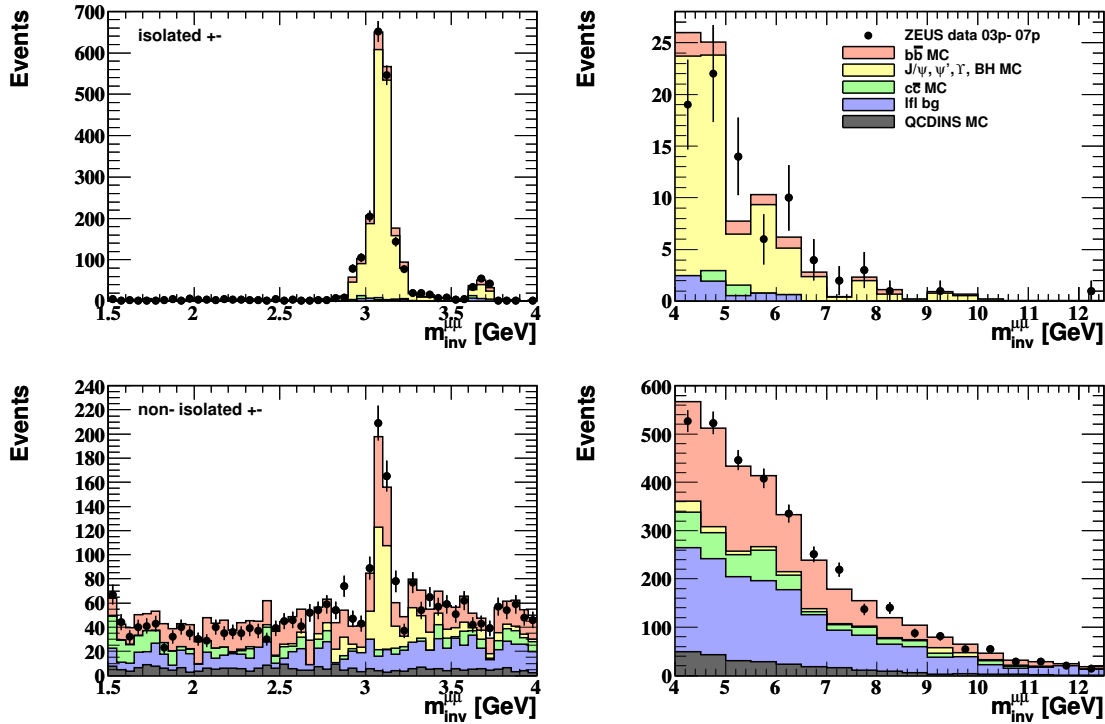
Figure 7.17: Invariant dimuon mass for isolated and non-isolated muon pairs with the instanton contribution scaled by 0.5 and the beauty contribution scaled by 1.5. The breakdown into the expected contributions from different processes is also illustrated.

Nevertheless, it was shown in [15] that dimuon events from heavy flavour instantons could be separated from normal MC dimuon events by using a combination of variables describing the kinematics of instanton-induced events and event shape variables (cf. Sec. 5.12 and Sec. 5.12.1). The used variables in the analysis presented here are the reconstructed virtuality Q'^2 of the quark entering the instanton subprocess, the number of particles in the reconstructed instanton-band N_{Band}, the sphericity Sph and isotropy Δ_B for unlike-sign, non-isolated dimuon events with at least 1 jet candidate with $E_T \geq 4$ GeV[1] and shown in Fig. 7.21. In these distributions, the instanton contribution from QCDINS is not considered and the beauty contribution was normalised with the scale factor as determined in Eq. 7.7 (cf. Sec. 7.2.5). Reasonable agreement between the dimuon data and MC can be observed. The same distributions are illustrated in Fig. 7.22, where the instanton contribution scaled by 0.5 is taken into account and the beauty normalisation was changed again to $s^b_{\mathrm{MC}} =1.5$. In these distributions, the contribution of heavy-flavour instantons leads to a slightly better agreement between the dimuon MC and the dimuon data.

It is possible to enrich the instanton contribution in dimuon events by applying different cuts and combination of cuts on Q'^2, N_{Band}, Sph and Δ_B, as inspired [15]. In Fig. 7.23, the quantities

---

[1]The requirement of the presence of a jet is necessary for the reconstruction of the kinematics of instanton-induced events. If an event contains more than one jet, the jet with the highest E_T was chosen as *current jet* candidate.
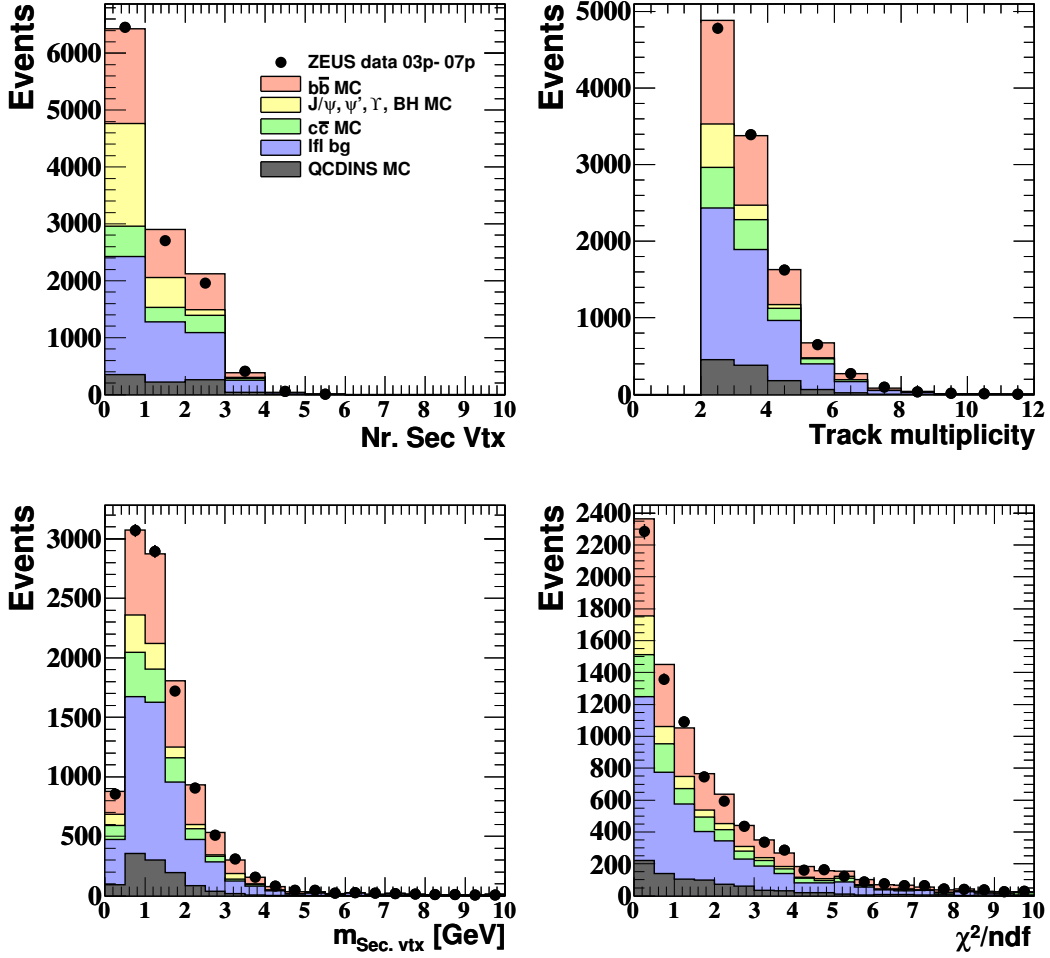
Figure 7.18: Number of secondary vertex candidates, track multiplicity, invariant mass m_{vtx} as well as χ^2/ndf for each secondary vertex for like- and unlike-sign dimuon events with the instanton contribution scaled by 0.5 and the beauty contribution scaled by 1.5. The breakdown into the expected contributions from different processes is also illustrated.

Q'^2, N_{Band}, Sph and Δ_B with the requirements

- $Q'^2 \geq 60$ GeV^2 and

- $N_{\mathrm{Band}} \geq 25$

for unlike-sign, non-isolated dimuons are illustrated. These cuts lead to a high reduction of the beauty dimuon MC, since it dominates at $Q'^2 < 60$ GeV^2 and the instanton fraction just starts at this threshold. Furthermore, a lower limit of $Sph \approx 0.1$ and an upper limit of $\Delta_B \approx 0.9$ can be observed. Thus, the requirement of at least 25 particles in the reconstructed instanton band discards events with a perfect back-to-back particle configuration. Again, the dimuon data is reasonably described by the MC, including the predicted contribution of QCDINS. But an excess of dimuon events in the data, which is described only by the instanton contribution and not by the remaining dimuon MC can not by observed and therefore, a clear signal of
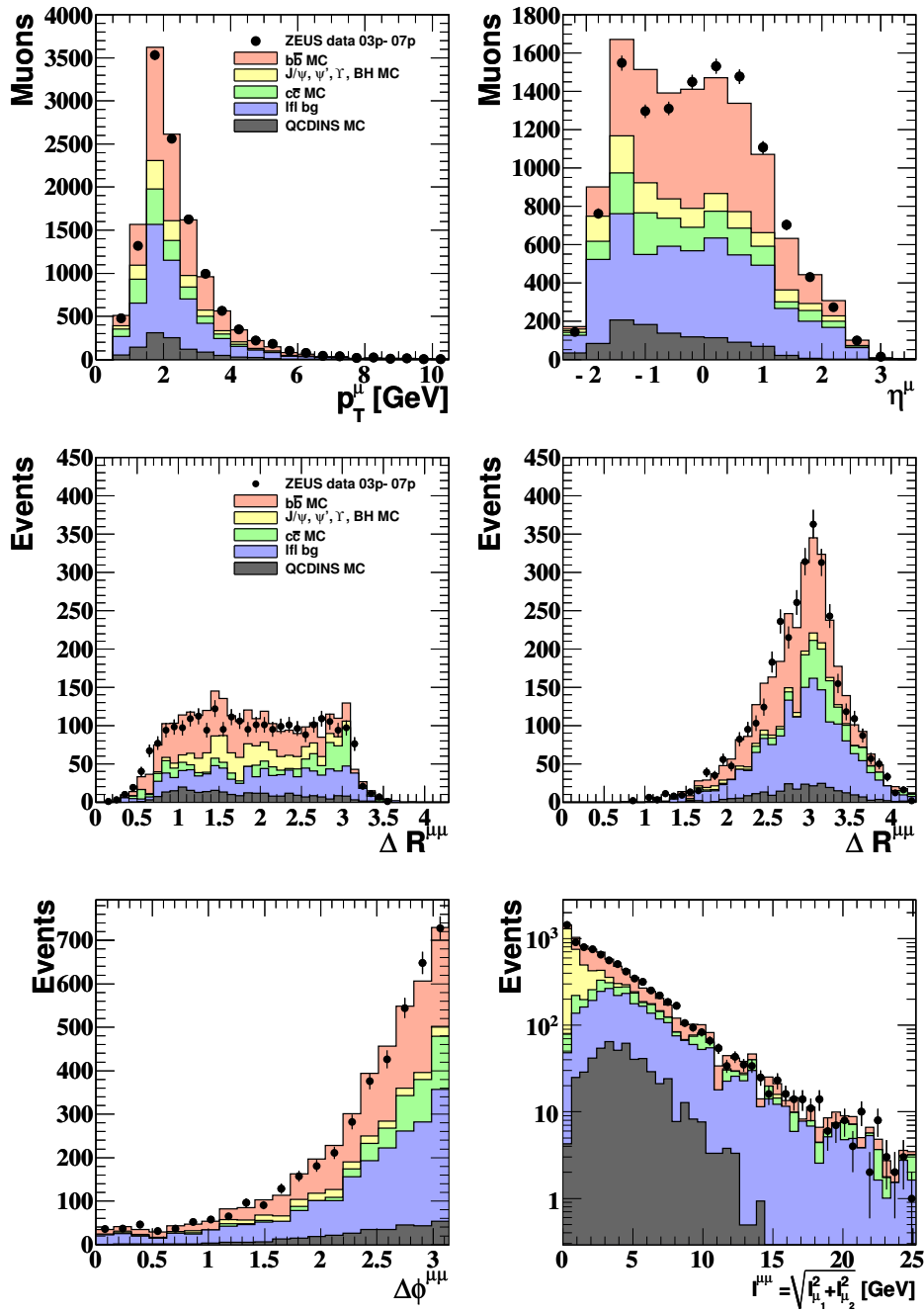
Figure 7.19: Muon transverse momentum, p_T^μ, (upper left) pseudorapidity, η^μ, (upper right) angular correlations in ΔR of both muons in dimuon events for low-mass (center left) and high-mass (center right) unlike-sign dimuons in the non-isolated subsample. Furthermore, angular correlations in $\Delta\phi$ of both muons in dimuon events for the sum of low-mass and high-mass unlike-sign dimuons in the non-isolated subsample (bottom left) as well as the dimuon isolation $I^{\mu\mu}$ for low- and high-mass unlike-sign dimuon events (bottom right) with the instanton contribution scaled by 0.5 and the beauty contribution scaled by 1.5 are presented.
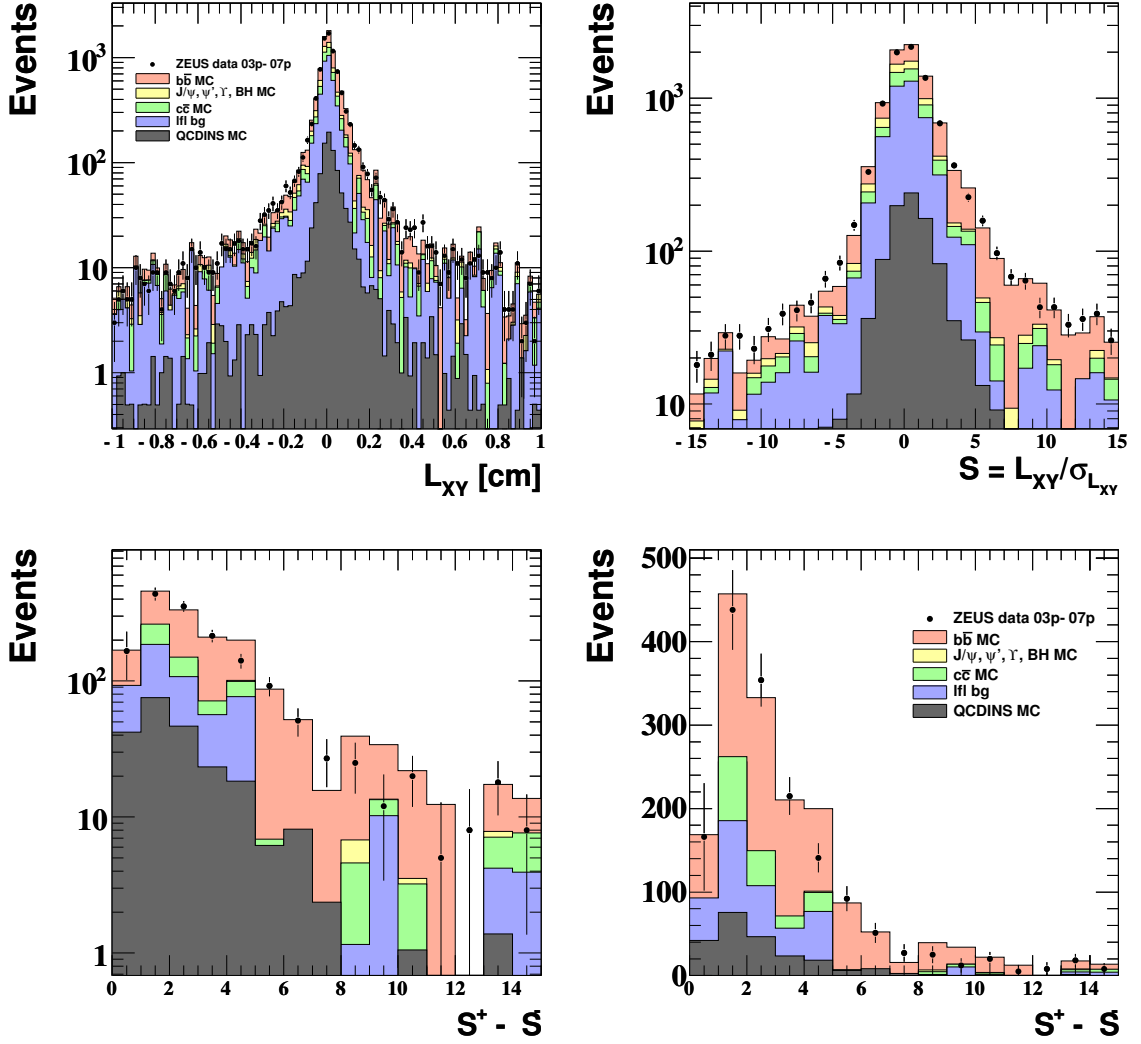
Figure 7.20: Decay length L_{XY}, decay length significance $S = L_{XY}/\sigma_{L_{XY}}$ as well as the mirrored decay length significance $S^+ - S^-$ (in logarithmic and lineare scale) for the sum of like- and unlike-sign dimuon events with the instanton contribution scaled by 0.5 and the beauty contribution scaled by 1.5. The breakdown into the expected contributions from different processes is also illustrated.

instanton-induced events at HERA can not be veryfied. Nevertheless, it is possible, based on the good description of the dimuon data by the sum of the normal dimuon and instanton MC, that the dimuon data contains approximately 7-8% heavy-flavour instanton-induced events. In this dimuon analysis and in previous muon (and electron) analyses [4, 62, 65], the beauty scaling factor was determined to be almost a factor 2 higher than in inclusive beauty-production measurements [70–72]. One possible explanation for this excess in beauty production measurements with leptons would be the omission of instanton-induced events. The inclusion of a certain contribution of instantons with heavy flavours in this analysis for example reduces the beauty scaling factor from 1.85 to 1.5 ($\approx$18%).
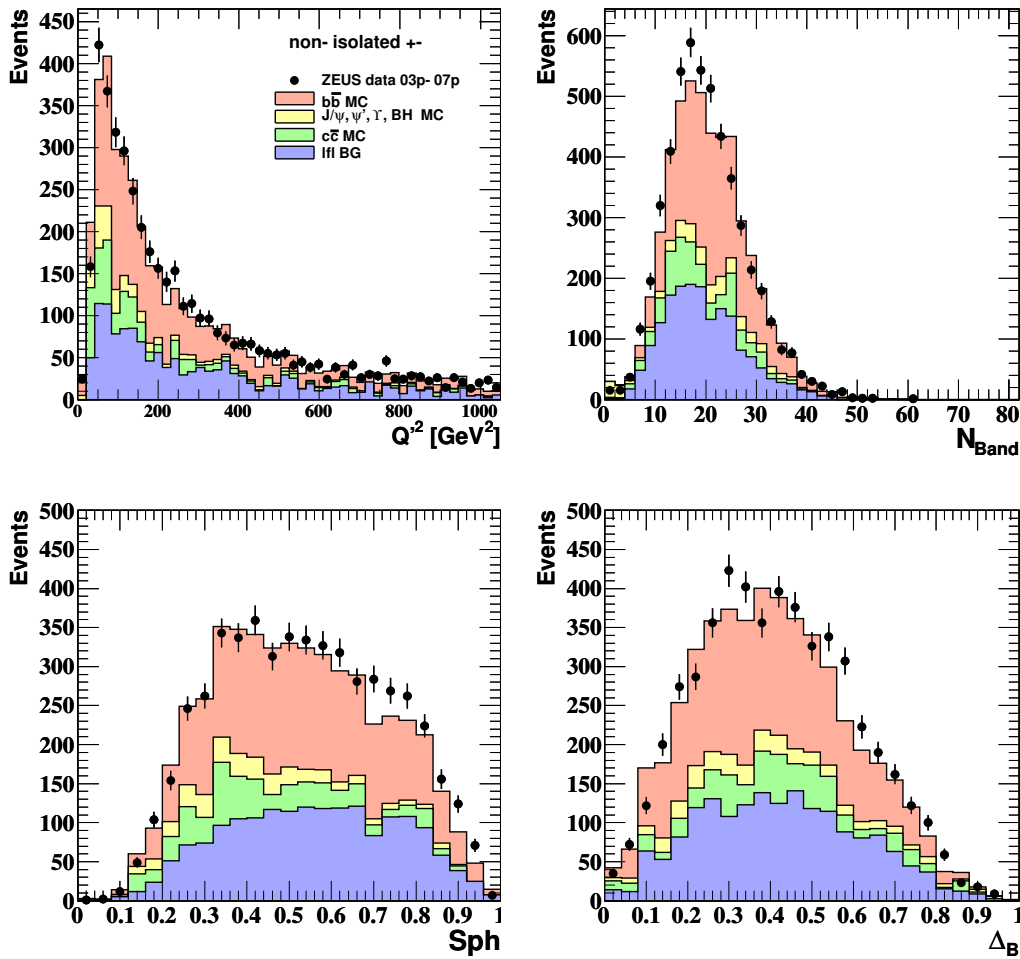
Figure 7.21: Event shape variables for unlike-sign, non-isolated muon pairs. Shown are Q'^2, the virtuality of the quark entering the instanton subprocess, the number of particles in the reconstructed instanton band, n_{Band}, the sphericity Sph, as well as the isotropy Δ_B. The breakdown into the expected contributions (without instantons) from different processes is also illustrated.

For future analyses on instanton-induced events with (or without) heavy flavours, following analysis techniques and improvements are suggested:

- Additional event shape variables, e.g. the pseudo thrust, Fox-Wolfram moments or the mean $p_T - \eta$ correlation of all EFOs in the instanton band should be used in combination with adequate cuts to separate the instanton signal from background contributions [186, 187]. The existing cuts on the discriminating observables used in this analysis should be improved as well.

- A search for heavy flavour instantons with a triple-tag method has also been performed. The requirement of three muons in the final state rejects almost all background contributions from heavy-quarkonia and Bethe-Heitler events. Unfortunately, the trimuon data
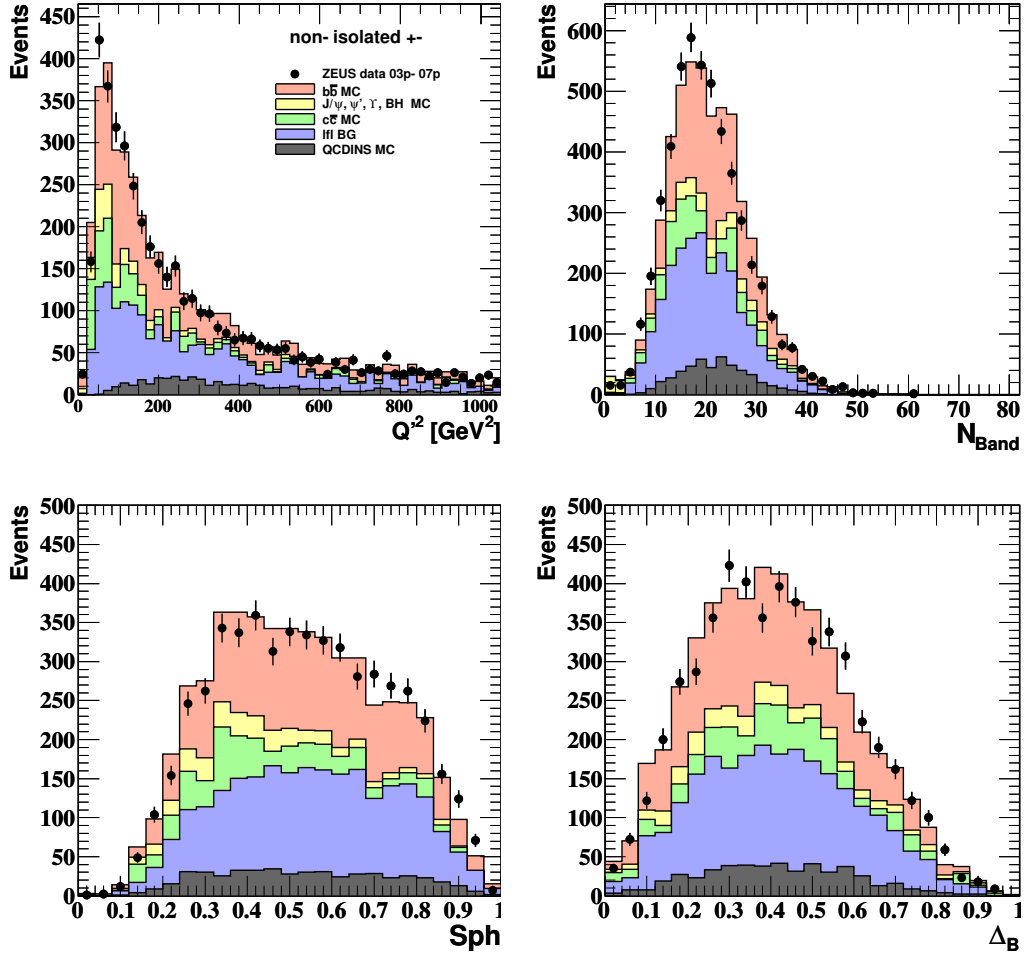
Figure 7.22: Event shape variables for unlike-sign, non-isolated muon pairs with the instanton contribution scaled by 0.5 and the beauty contribution scaled by 1.5. Shown are Q'^2, the virtuality of the quark entering the instanton subprocess, the number of particles in the reconstructed instanton band, n_{Band}, the sphericity Sph, as well as the isotropy Δ_B. The breakdown into the expected contributions from different processes is also illustrated.

statistics is reduced to an almost negligble level. The expansion to events with three leptons (electrons <u>and</u> muons) in the final state instead would yield a sufficient data statistic with small background contributions.

Although this part of the analysis presented in this thesis has shown that the dimuon data could contain a significant instanton contribution, this contribution was assumed to be zero for the measurement of the cross sections for beauty quark production in the next chapter in order to compare these results with those from previous measurements [4, 62].
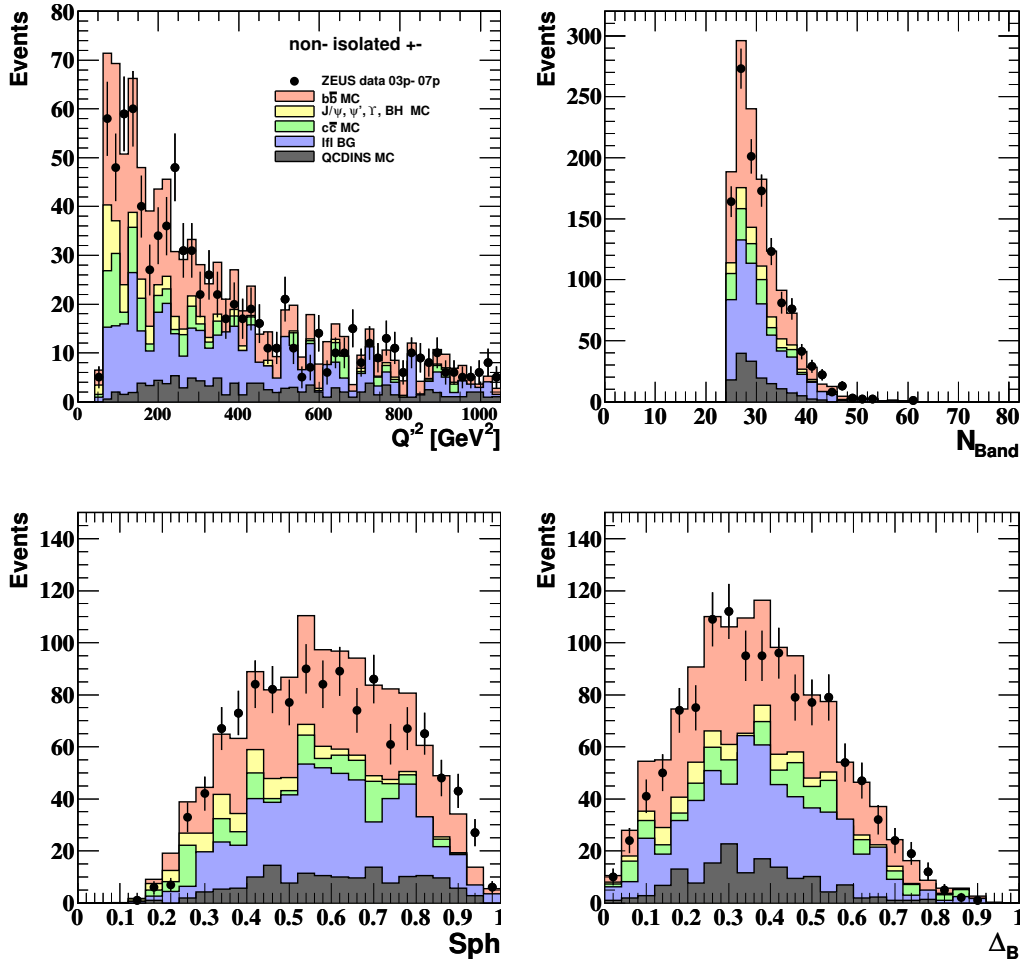
Figure 7.23: Event shape variables for unlike-sign, non-isolated muon pairs with $Q'^2 \geq 60$ GeV^2 and $n_{\text{Band}} \geq 25$ and with instanton contribution scaled by 0.5 and the beauty contribution scaled by 1.5. Shown are Q'^2, the virtuality of the quark entering the instanton subprocess, the number of particles in the reconstructed instanton band, n_{Band}, the sphericity Sph, as well as the isotropy Δ_B. The breakdown into the expected contributions from different processes is also illustrated.

Chapter 8

Cross section measurement

After the determination of the normalisations of the beauty MC and the background contributions in Sec. 7, the beauty signal, required for the measurements of the $b\bar{b}$ production cross section, can be extracted by using the subtraction method [4, 64], which will be explained in the following Sec. 8.1. Measurements of the visible cross section for beauty quark production from dimuon events as well as the total $b\bar{b}$ cross section are presented in Sec. 8.2 and the determination of differential muon cross sections in $p_T^\mu, \eta^\mu, \Delta\phi^{\mu\mu}$ and $\Delta R^{\mu\mu}$ in Sec. 8.4. All measured cross sections were compared to LO+PS and NLO QCD predictions as well as to results of the previous measurement [4, 64].

8.1 Total and differential cross section definition

The total cross section σ_X of a given process X is defined by

$$\sigma_X = \frac{N_X}{\mathcal{L} \cdot \mathcal{A}},\tag{8.1}$$

where N is the number of events determined for the process X, $\mathcal{L}$ the luminosity of the corresponding data sample and $\mathcal{A}$ is referred to as acceptance, which is given by

$$\mathcal{A} = \left(\frac{N_{\text{rec}}}{N_{\text{true,X}}}\right)^{\text{MC}},\tag{8.2}$$

where N_{rec} is the number of reconstructed MC events and $N_{\text{true,X}}$ the number of events of the process X on generator (true) level. The single differential cross section as a function of a given variable Y is defined accordingly by

$$\frac{d\sigma_X}{dY} = \frac{N_X}{\mathcal{L} \cdot \mathcal{A} \cdot \Delta Y},\tag{8.3}$$

where ΔY refers to the width of the given Y bin.

The cross section for the process $e^{\pm}p \rightarrow b\bar{b}X \rightarrow \mu\mu X'$ can be measured by determining the fraction of dimuon events in the data sample coming from this process, which is done by the following procedure: Since the contributions of the false-muon background in the like- and unlike-sign dimuon sample are almost equal (with small corrections, cf. Sec. 7.2.3), the difference of both samples is free from this background. From this difference sample, the remaining normalised background contributions from charm, heavy quarkonia and Bethe-Heitler are subtracted, yielding the beauty contribution to the difference of like- and unlike-sign dimuon events. This contribution is extrapolated to the sum of both dimuon samples by means of the beauty MC:

$$N_{b\bar{b}\rightarrow\mu\mu} = \left[N^u_{\text{data}} - N^l_{\text{data}} - (N_{c\bar{c}} + N_{\text{VM}} + N_{\text{BH}}) \right] \times \left(\frac{N^u_{b\bar{b}} + N^l_{b\bar{b}}}{N^u_{b\bar{b}} - N^l_{b\bar{b}}} \right)^{\text{MC}}, \qquad (8.4)$$

where $N^l_{b\bar{b}}$ and $N^u_{b\bar{b}}$ are the predicted like- and unlike-sign beauty MC contributions. As mentioned before, there is a small residual excess of the unlike-sign over the the like-sign background. This excess is corrected in this analysis by a multiplicative correction factor C of 1.04 in the low- and 1.01 in the high-mass dimuon sample. With this correction, the beauty fraction is then determined by:

$$N_{b\bar{b}\rightarrow\mu\mu} = \left[N^u_{\text{data}} - C \cdot N^l_{\text{data}} - (N_{c\bar{c}} + N_{\text{VM}} + N_{\text{BH}}) \right] \times \left(\frac{N^u_{b\bar{b}} + N^l_{b\bar{b}}}{N^u_{b\bar{b}} - C \cdot N^l_{b\bar{b}}} \right)^{\text{MC}}, \qquad (8.5)$$

yielding 3904 dimuon events from beauty production in the HERA II data.

8.2 Visible and total cross section

In order to be comparable with the results of the HERA I analysis [4, 64], the visible cross section for the process $e^{\pm}p \rightarrow b\bar{b}X \rightarrow \mu\mu X'$ was determined in the same phase space region having high single muon-detection efficiency. This region, as illustrated in Fig. 8.1, is defined as:

- for both muons: $-2.2 < \eta < 2.5$,

- for one of the muons: $p_T > 1.5$ GeV,

- for the other muon: $p_T > 0.75$ GeV and

    - $p^\mu > 1.8$ GeV for $\eta^\mu < 0.6$ or
    - ($p^\mu > 2.5$ GeV or $p^\mu_T > 1.5$ GeV) for $\eta^\mu > 0.6$,

for both, the photoproduction or DIS regime and is therefore valid for the whole phase space in Q^2 and y. In this phase space, the visible cross section for dimuon production from beauty decays at HERA II was measured to:

$$\sigma^{\text{HERA II}}_{\text{vis}}(e^{\pm}p \rightarrow b\bar{b}X \rightarrow \mu\mu X') = 50 \pm 4 \text{ (stat.)} {}^{+14}_{-13} \text{ (syst.)} \text{ pb}, \qquad (8.6)$$
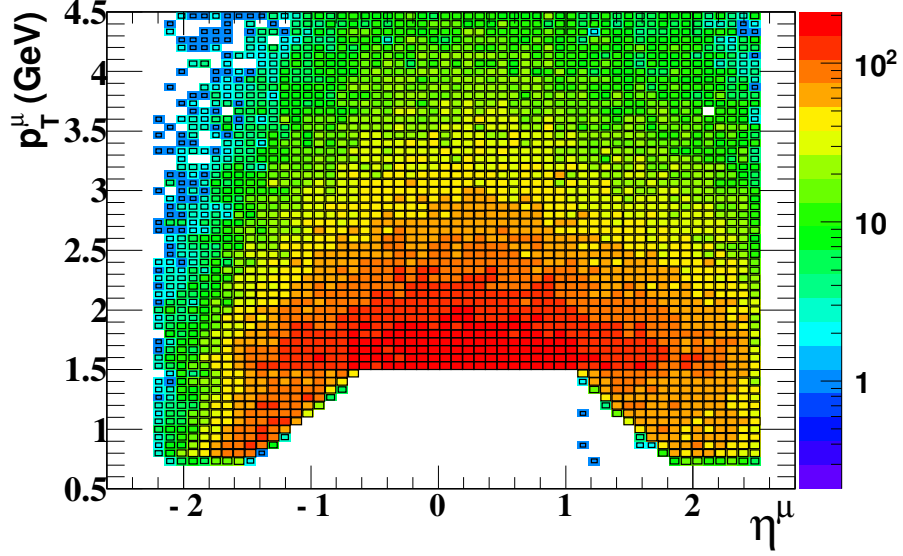
Figure 8.1: Muons from beauty decays in the visible kinematic p_T and η range.

where the first uncertainty is statistical and the second systematic. The determination of the systematic uncertainties is described in Sec. 8.3.

The measured visible cross section in this analysis is smaller but in good agreement with the published result of the HERA I dimuon analysis [64]:

$$\sigma_{\text{vis}}^{\text{HERA I}}(e^{\pm}p \to b\bar{b}X \to \mu\mu X') = 55 \pm 7 \text{ (stat.) } {}^{+14}_{-15} \text{ (syst.) pb.} \tag{8.7}$$

This cross section includes both, muons from direct $B-$hadron decays and indirect muonic decays, e.g. $b \to c \to \mu$, $b \to J/\psi \to \mu\mu$ or muons from intermediate τ leptons. The two muons can originate from the same beauty quark of from different quarks of the $b\bar{b}$ pair. Decay muons from kaons, pions of other light hadrons are not included. Events with more than one muon pair enter only once.

The measured cross section in Eq. 8.6 is larger than, but compatible with the NLO predictions from FMNR⊗PHYTHIA [47]:

$$\sigma_{\text{vis}}^{\text{NLO}}(e^{\pm}p \to eb\bar{b}X \to \mu\mu X') = 33^{+18}_{-8} \text{ pb.} \tag{8.8}$$

The next step after determing the visible cross section is the extrapolation to the total cross section for beauty quark production with the following procedure identical as in [4, 64]: The effective fraction of a $b\bar{b}$ pair decaying into at least two muons is 6.3% [2]. The probabiltity for such a muon pair to be in the visible kinematic range, evaluated from the beauty MC, is on average $\sim$6%. Thus, the combined probability for a beauty quark pair to yield a muon pair in the visible range is [4, 64]

$$P_{\text{vis}}^{b\bar{b} \to \mu\mu} \approx 0.38\%. \tag{8.9}$$

This value is quite small, but it is almost entirely determined by quantities measured with good precision at e^+e^- colliders, including the b-fragmentation functions as well as the $B \to \mu X$ de-

cay spectra. Dividing the visible cross section in Eq. 8.6 by the combined probability in Eq. 8.9 yields the total cross section for beauty quark production measured in this analysis:

$$\sigma_{\text{total}}^{\text{HERA II}}(e^{\pm}p \to b\bar{b}X) = 12.6 \pm 1.0 \text{ (stat.) } {}^{+3.6}_{-3.3} \text{ (syst.) nb.} \tag{8.10}$$

which is in good agreement with the HERA I result:

$$\sigma_{\text{total}}^{\text{HERA I}}(e^{\pm}p \to b\bar{b}X) = 13.9 \pm 1.5 \text{ (stat.) } {}^{+4.0}_{-4.3} \text{ (syst.) nb.} \tag{8.11}$$

The total cross section predicted by NLO QCD calculations is

$$\sigma_{\text{total}}^{\text{NLO}}(e^{\pm}p \to b\bar{b}X) = 7.5^{+4.5}_{-2.1} \text{ nb} \tag{8.12}$$

and a factor 1.7 lower than, but compatible within the large uncertainties with the measured total cross section value. In Fig. 8.2, the total cross section measured in this analysis compared to the result of the HERA I analysis and NLO predictions as well as to slightly less inclusive cross sections from a $D^*\mu$ measurement in HERA I is illustrated.
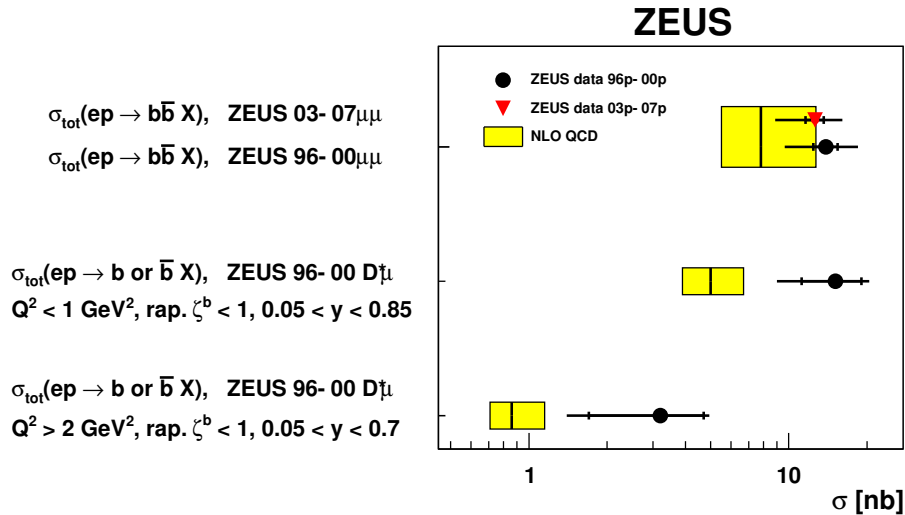
Figure 8.2: Comparison of measured cross sections of beauty quark production to NLO predictions. The $b\bar{b}$ cross section from this analysis is shown on top (triangle) and compared to the HERA I result. Related beauty quark cross sections from the ZEUS $D^*\mu$ analysis are illlustrated as well.

8.3   Systematic uncertainties

The systematic uncertainties on the measurement of the beauty quark cross section presented in this thesis were estimated by varying different parameters, e.g. the selection criteria or background contributions within their uncertainties, and repeating the determination of the visible cross section. The same procedure was also applied in each bin in which differential cross sections were measured.

- **Muon efficiency correction:** The systematic uncertainties of the muon efficiency corrections were estimated by determing the cross section by using all dimuons found by the muon chambers regardless of the BAC information and using the BAC without the muon chamber information. The error on the total cross section is $^{+20.2}_{-18.4}\%$.

- **Normalisation of the heavy quarkonia and Bethe-Heitler contributions:** The normalisation of the contributions from Bethe-Heitler processes and heavy quarkonia events was varied by $\pm 50\%$. The effect on the visible cross section is $^{+9.1\%}_{-9.2\%}$.

- **Charm contribution:** The relative contribution of charm in the dimuon background sample was varied by $\pm 20\%$. The effect on the visible cross section is $^{+6.1\%}_{-9.6\%}$.

- **b spectral shape uncertainty:** The dependence on the details of the beauty quark spectra was estimated by using only the direct $b\bar{b}$ MC or doubling the non-direct MC contributions. The effect on the visible cross section is $^{+12.9\%}_{-11.3\%}$.

- **c spectral shape uncertainty:** The direct and non-direct fractions for the charm contribution in dimuon events were varied in the same way as for the beauty contribution. The effect on the visible cross section is $^{+1.6\%}_{-1.7\%}$.

- **Dimuon isolation $I^{\mu\mu}$:** The dimuon isolation cuts were varied by ± 500 MeV. The effect on the visible cross section is $^{+2.6\%}_{-2.9\%}$.

- **Contributions from double heavy quark pairs:** The contributions of $b\bar{b}b\bar{b}$, $b\bar{b}c\bar{c}$ and $c\bar{c}c\bar{c}$ production where found to be essentially negligble (cf. Sec. 7.2.4) and not considered for the determination of the systematic uncertainties on the visible cross section.

- **Variation of the CAL-E_T cut:** The cut on the hadronic transverse energy was varied within $E_T^{CAL} \in [7,9]$ GeV. The uncertainty in the visible cross section for this variation was determined to be $^{+3.6\%}_{-1.9\%}$.

- **Variation of the like-/unlike-sign light-flavour ratio:** The dimuon light-flavour background ratio of like- and unlike-sign dimuon events was varied by $\pm 3\%$. The resulting uncertainty on the visible cross section is $^{+3.0\%}_{-1.2\%}$

- **Luminosity uncertainty:** A $\pm 2.0\%$ overall normalisation uncertainty associated with the luminosity measurement was applied to the visible cross section.

The individual contributions from the systematic uncertainties were added in quadrature separately for the positive and negative variations of the cross sections.

The parameters in the NLO FMNR program used for the calculations of the theoretical predictions were already mentioned in Sec. 2.8.2. The uncertainty of the NLO calculations were evaluated by varying simultaneously the beauty quark mass within $4.5 < m_b < 5.0$ GeV and the renormalisation and factorisation scale within $\mu_r/2 < \mu_r < 2\mu_r$, such that the uncertainty was maximised($^{\sim +60\%}_{\sim -30\%}$). Variations of the parton densities and the strong coupling constant led to much smaller uncertainties compared to the uncertainties related to the mass and scale variations and were therefore neglected.

8.4 Differential muon cross sections in p_T and η, angular muon cross sections in $\Delta\phi^{\mu\mu}$ and $\Delta R^{\mu\mu}$

The muon direction of flight is correlated with the original direction of the beauty quark. Therefore, differential cross sections in bins of the muon transverse momentum, p_T^μ, and pseudorapidity, η^μ, were measured in order to have a detailed look at single muon and beauty quark properties. Angular correlations in the $b\bar{b}$ system were determined by measuring cross sections in $\Delta\phi^{\mu\mu}$ and $\Delta R^{\mu\mu}$. As for the visible cross section, all differential cross sections includes both, muons from direct $B-$hadron decays and indirect muonic decays.

The definition for the kinematic range in this analysis is identical to the one of the previous measurement in order to be comparable. For both muons, the phase space was restricted to

- $p_T^{\mu\,(1,2)} > 1.5$ GeV,

- $-2.2 < \eta^{\mu\,(1,2)} < 2.5$,

for both, the photoproduction and DIS regime and also valid for the whole phase space in Q^2 and y. The background contributions were normalised with the same procedure as described in Sec. 7. The scaling factor for the beauty normalisation has been determined to:

$$s_{\mathrm{MC}}^b = 1.90 \pm 0.05 \text{ (stat.)}. \tag{8.13}$$

In Fig. 8.3, the p_T^μ and η^μ for non-isolated, unlike-sign dimuon events with the harder cut on the muon transverse momentum is illustrated.
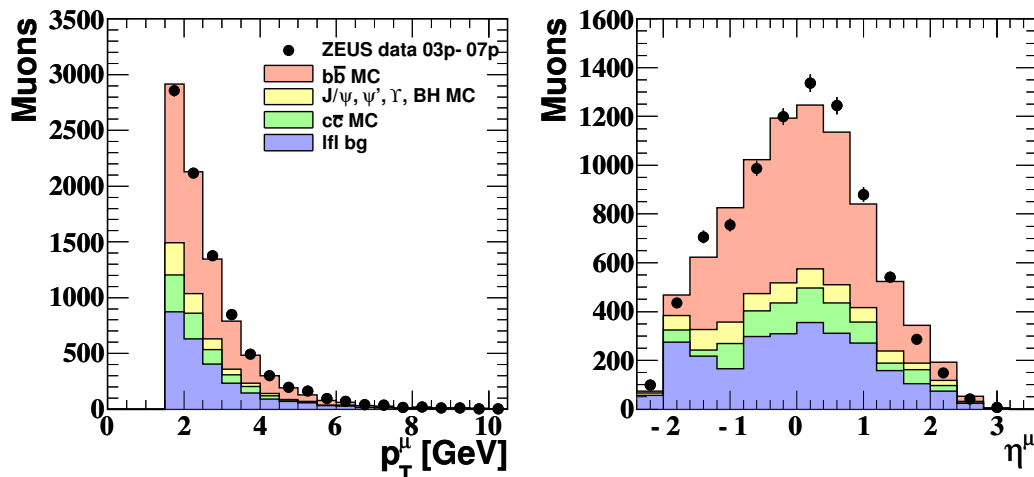
Figure 8.3: Muon transverse momentum (left) and pseudorapidity distribution (right) from low- and high-mass unlike-sign dimuons in the non-isolated sample with the higher p_T^μ cut of 1.5 GeV. For each event, two muons entered. The breakdown into the expected contributions from different processes is also illustrated.

In the following Figs. 8.4 and 8.5, the differential cross sections in bins of p_T^μ and η^μ are shown. The bin ranges and corresponding cross section values with statistical and systematic errors are summarised in Tabs. 8.1 and 8.2. The measured cross section values in both differential cross section spectra were compared to the values of the previous measurement, the scaled LO+PS prediction from PYTHIA and RAPGAP as well as to NLO QCD predictions from FMNR⊗ PYTHIA. In both differential cross-section spectra, very good agreement is
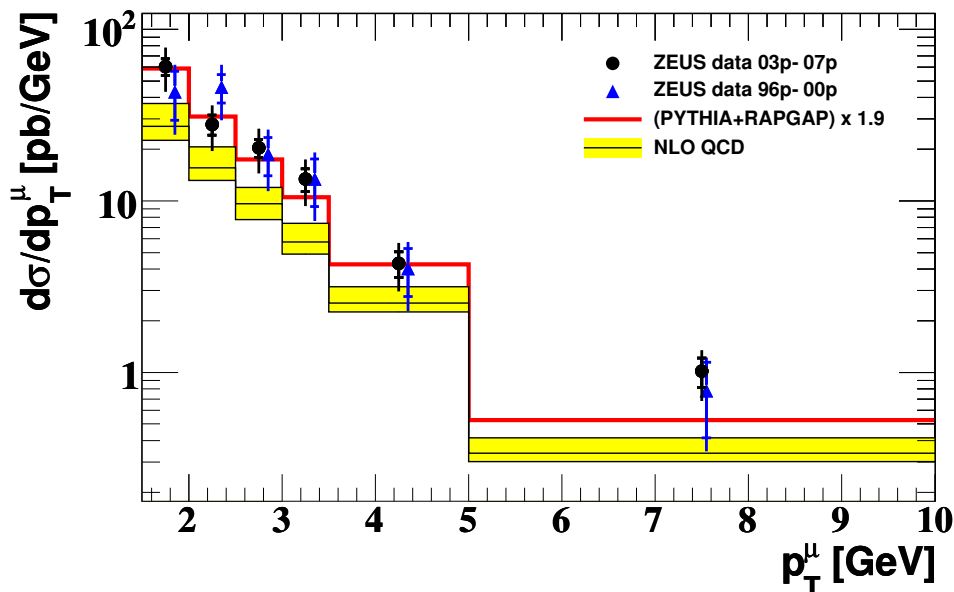
Figure 8.4: Cross section $d\sigma/dp_T^\mu$ for muons from b decays in dimuon events with $p_T^\mu >$ 1.5 GeV and -2.2 $< \eta^\mu <$ 2.5 for boths muons. For each event, two muons contribute. The HERA II data (solid points) are compared to the results of the HERA I analysis (triangles), to the scaled sum of the predictions by the LO+PS generators PYTHIA and RAPGAP (solid line) as well as to the NLO QCD prediction from FMNR⊗ PYTHIA (band).

p_T^μ Range [GeV]	Acceptance	$d\sigma/dp_T^\mu \pm$ stat. $\pm$ sys. [pb/GeV]
1.5 : 2.0	0.18	$60.63 \pm 6.86 \, ^{+16.49}_{-15.64}$
2.0 : 2.5	0.26	$27.83 \pm 3.76 \, ^{+7.57}_{-7.18}$
2.5 : 3.0	0.30	$20.34 \pm 2.49 \, ^{+5.53}_{-5.24}$
3.0 : 3.5	0.30	$13.38 \pm 2.04 \, ^{+3.64}_{-3.45}$
3.5 : 5.0	0.29	$4.33 \pm 0.73 \, ^{+1.17}_{-1.11}$
5.0 : 10.0	0.24	$1.02 \pm 0.20 \, ^{+0.28}_{-0.26}$

Table 8.1: p_T^μ cross-section numbers.

found with the scaled PYTHIA+RAPGAP predictions. The measured differential cross sections of this analysis (solid points) are compatible with the results of the previous measurement
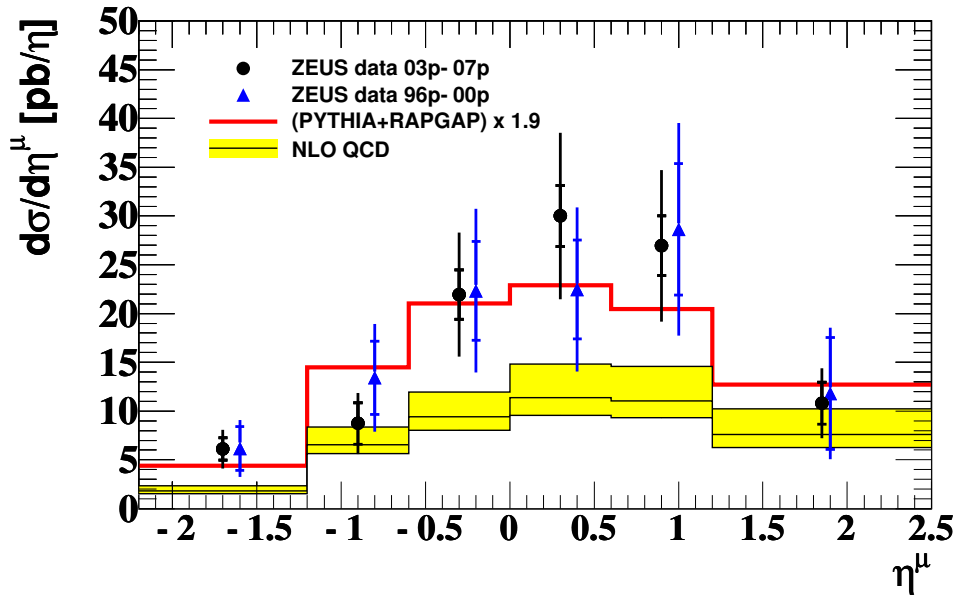
Figure 8.5: Cross section $d\sigma/d\eta^{\mu}$ for muons from b decays in dimuon events with $p_T^{\mu} >$ 1.5 GeV and -2.2 $< \eta^{\mu} <$ 2.5 for boths muons. For each event, two muons contribute. The HERA II data (solid points) are compared to the results of the HERA I analysis (triangles), to the scaled sum of the predictions by the LO+PS generators PYTHIA and RAPGAP (solid line) as well as to the NLO QCD prediction from FMNR$\otimes$ PYTHIA (band).

η^{μ} Range [GeV]	Acceptance	$d\sigma/dp_T^{\mu}\pm$ stat. $\pm$ sys. [pb/GeV]
-2.2 : -1.2	0.32	$6.11 \pm 1.15\ ^{+1.66}_{-1.58}$
-1.2 : -0.6	0.30	$8.72 \pm 2.13\ ^{+2.37}_{-2.25}$
-0.6 : 0.0	0.29	$21.94 \pm 2.53\ ^{+5.97}_{-5.66}$
0.0 : 0.6	0.27	$30.01 \pm 3.13\ ^{+8.16}_{-7.74}$
0.6 : 1.2	0.21	$26.96 \pm 3.06\ ^{+7.33}_{-6.95}$
1.2 : 2.5	0.12	$10.79 \pm 2.15\ ^{+2.93}_{-2.78}$

Table 8.2: η^{μ} cross-section numbers.

(triangles). Additionally, the measured cross sections are described reasonably by the shape of the FMNR$\otimes$ PYTHIA predictions with tendency to underestimate the data normalisation, as observed in previous measurements [64, 66].

To provide a detailed look at correlations between both beauty quarks, the event selection had to be optimised in order to obtain the largest possible fraction of dimuon events, where both muons come from different beauty quarks. Thus, the reconstructed invariant dimuon mass range was restricted to

$$m_{\text{inv}}^{\mu\mu} > 3.25 \text{ GeV,} \qquad (8.14)$$

which reduces the contribution of dimuons from the same beauty quark (e.g. $b \to J/\psi \to \mu\mu$) to an almost negligible level. The corresponding $\Delta\phi$ and ΔR data distributions between both muons were already presented in Fig. 7.8. Figs. 8.6 and 8.7 show the resulting differential cross sections, where the mass cut was replaced by the requirement that both muons originate from different beauty quarks. In Tabs. 8.3 and 8.4, the bin ranges and corresponding cross section values with statistical and systematic errors are summarised.
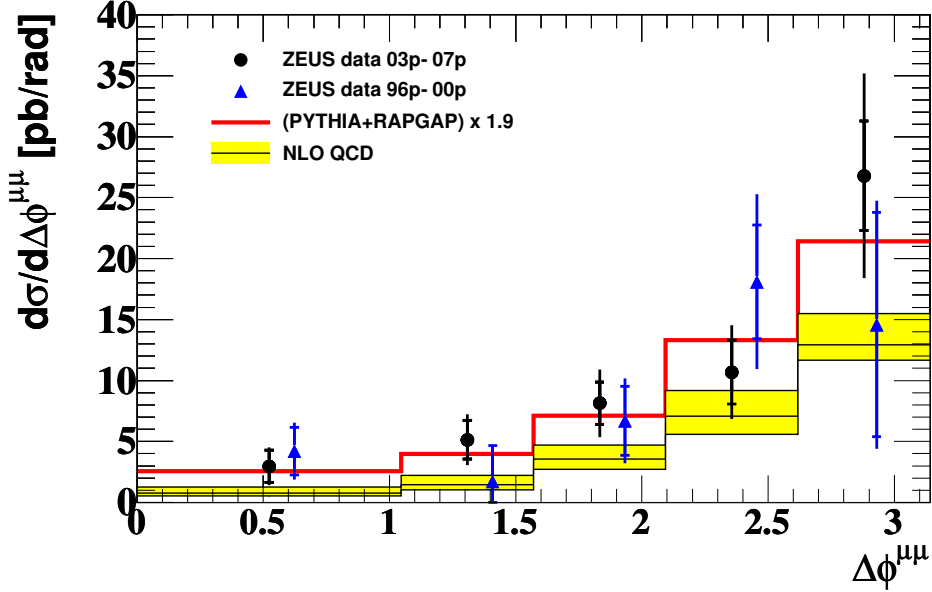
Figure 8.6: Cross section $d\sigma/d\Delta\phi^{\mu\mu}$ for muons from $b\bar{b}$ decays in which each muon originates from different b quarks, with $p_T^\mu > 1.5$ GeV and $-2.2 < \eta^\mu < 2.5$ for boths muons. The HERA II data (solid points) are compared to the results of the HERA I analysis (triangles), to the scaled sum of the predictions by the LO+PS generators PYTHIA and RAPGAP (solid line) as well as to the NLO QCD prediction from FMNR$\otimes$ PYTHIA (band).

$\Delta\phi^{\mu\mu}$ Range [GeV]	Acceptance	$d\sigma/d\Delta\phi^{\mu\mu}\pm$ stat. $\pm$ sys. [pb/GeV]
0.0 : 1.047	0.10	$2.96 \pm 1.32\ {}^{+0.81}_{-0.76}$
1.047 : 1.571	0.16	$5.13 \pm 1.58\ {}^{+1.39}_{-1.32}$
1.571 : 2.094	0.21	$8.14 \pm 1.75\ {}^{+2.19}_{-2.03}$
2.094 : 2.618	0.26	$10.68 \pm 2.61\ {}^{+2.88}_{-2.78}$
2.618 : 3.141	0.27	$26.79 \pm 4.50\ {}^{+7.23}_{-6.91}$

Table 8.3: $\Delta\phi^{\mu\mu}$ cross-section numbers.

Again, the distributions in $\Delta\phi^{\mu\mu}$ and $\Delta R^{\mu\mu}$ are well described by the scaled PYTHIA+RAPGAP predictions. FMNR$\otimes$ PYTHIA predictions for differential cross sections in $\Delta R^{\mu\mu}$ were not available, but for differential cross sections in $\Delta\phi^{\mu\mu}$. As for the differential cross sections in p_T^μ and η^μ, the measured cross sections are described reasonably by the shape of the FMNR$\otimes$ PYTHIA
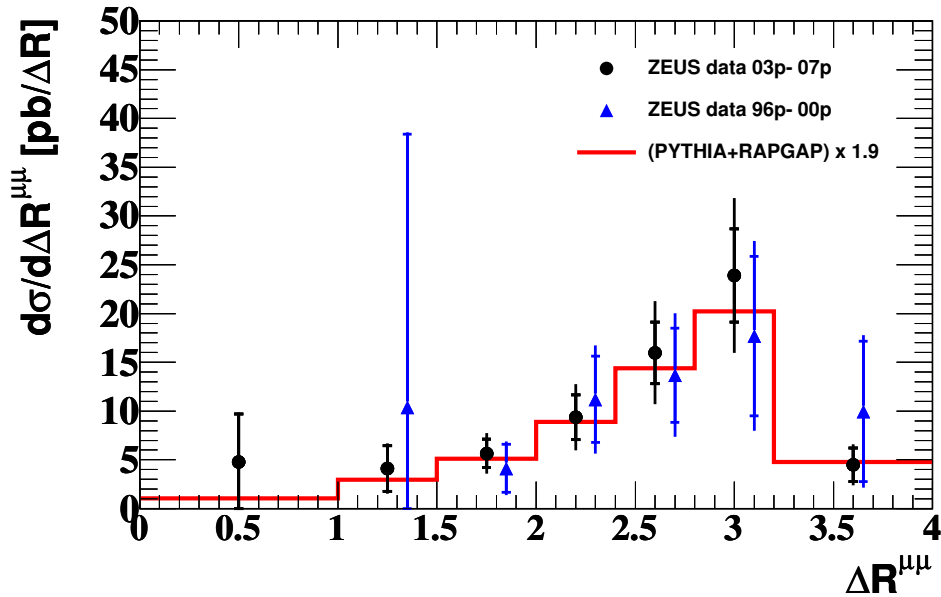
Figure 8.7: Cross section $d\sigma/d\Delta R^{\mu\mu}$ for muons from $b\bar{b}$ decays in which each muon originates from different b quarks, with $p_T^\mu > 1.5$ GeV and $-2.2 < \eta^\mu < 2.5$ for boths muons. The HERA II data (solid points) are compared to the results of the HERA I analysis (triangles) and to the scaled sum of the predictions by the LO+PS generators PYTHIA and RAPGAP (solid line).

predictions with a tendency to underestimate the data normalisation. It is interesting to note that the measured cross section at $\Delta\phi^{\mu\mu} \approx \pi$ is higher than in the previous measurement, but is still described by the LO+PS prediction. Differential cross sections for $\Delta R^{\mu\mu} \leq 1$ were also measured for the HERA II period, which was not possible (or with high statistical errors) for HERA I due to smaller statistics.

$\Delta R^{\mu\mu}$ Range [GeV]	Acceptance	$d\sigma/d\Delta R^{\mu\mu}\pm$ stat. $\pm$ sys. [pb/GeV]
0.0 : 1.0	0.01	$4.79 \pm 4.89 \, ^{+1.29}_{-1.23}$
1.0 : 1.5	0.07	$4.10 \pm 2.35 \, ^{+1.11}_{-1.05}$
1.5 : 2.0	0.18	$5.66 \pm 1.47 \, ^{+1.54}_{-1.46}$
2.0 : 2.4	0.24	$9.38 \pm 2.30 \, ^{+2.55}_{-2.42}$
2.4 : 2.8	0.27	$15.97 \pm 3.15 \, ^{+4.34}_{-4.12}$
2.8 : 3.2	0.28	$23.91 \pm 4.79 \, ^{+6.46}_{-6.17}$
3.2 : 4.0	0.25	$4.48 \pm 1.74 \, ^{+1.22}_{-1.15}$

Table 8.4: $\Delta R^{\mu\mu}$ cross-section numbers.

All in all, the measured total, visible and differential cross sections presented in this chapter confirm the results of the previous dimuon analysis.

Chapter 9

Summary and outlook

Open beauty quark production from dimuon events has been measured using the full data set collected by means of the ZEUS detector between the years 2003 and 2007, which corresponds to an integrated luminosity of 376 ± 6.5 pb^{-1} at a centre-of-mass energy of $\sqrt{s} = 318$ GeV.

As in the previous HERA I analysis, the beauty fraction from dimuon events was determined by using the difference of like- and unlike-sign dimuon events. The dimuon charm background was normalised to the charm contribution from a $D^* + \mu$ sample, which has a similar event topology. Background contributions from heavy quarkonia and Bethe-Heitler processes were normalised on an independent sample of isolated dimuon events to describe the mass peaks of $J/\psi, \psi'$ and Υ. The light-flavour background was obtained by the subtraction of the like-sign dimuon beauty contribution from the like-sign dimuon data and reflected to the unlike-sign dimuon sample, since there is almost no charge correlation between like- and unlike-sign muons from light-flavour events. The normalisation of the individual contributions was checked and confirmed on different variables describing e.g. the muon spectra, jet kinematics or quantities of reconstructed secondary vertices

For a comparision with results from the HERA I dimuon analysis, the measurement presented in this thesis was restricted to the identical kinematic region as defined in Sec. 8.2. The visible cross section for dimuon production in this phase space was determined to

$$\sigma_{\text{vis}}^{\text{HERA II}}(e^{\pm}p \to b\bar{b}X \to \mu\mu X') = 50 \pm 4(\text{ stat.}) {}^{+14}_{-13} \text{ (syst.) pb,} \qquad (9.1)$$

which is in good agreement with the result of the HERA I dimuon analysis:

$$\sigma_{\text{vis}}^{\text{HERA I}}(e^{\pm}p \to b\bar{b}X \to \mu\mu X') = 55 \pm 7(\text{ stat.}) {}^{+14}_{-15} \text{ (syst.) pb.} \qquad (9.2)$$

The visible cross section was furthermore extrapolated to a total cross section for beauty quark production. The obtained result is:

$$\sigma_{\text{total}}^{\text{HERA II}}(e^{\pm}p \to b\bar{b}X) = 12.6 \pm 1.0 \text{ (stat.)} {}^{+3.6}_{-3.3} \text{ (syst.) nb.} \qquad (9.3)$$

which is in good agreement with the HERA I result as well:

$$\sigma_{\text{total}}^{\text{HERA I}}(e^{\pm}p \to b\bar{b}X) = 13.9 \pm 1.5 \text{ (stat.)} {}^{+4.0}_{-4.3} \text{ (syst.) nb.} \qquad (9.4)$$

Both cross sections measured in this analysis are larger than, but compatible with the NLO predictions:

$$\sigma_{\mathrm{vis}}^{\mathrm{NLO}}(e^{\pm}p \to b\bar{b}X \to \mu\mu X') = 33^{+18}_{-8} \text{ pb and} \tag{9.5}$$

$$\sigma_{\mathrm{total}}^{\mathrm{NLO}}(e^{\pm}p \to b\bar{b}X) = 7.5^{+4.5}_{-2.1} \text{ nb.} \tag{9.6}$$

Differential cross sections in the transverse momentum, p_T^{μ}, and pseudorapidity, η^{μ}, of the muons were measured as well as $b\bar{b}$ correlations in the azimuthal distance $\Delta\phi^{\mu\mu}$ and $\Delta R^{\mu\mu}$ between both muons and compared to leading order plus parton showering NLO predictions and results of the HERA I dimuon analysis. The scaled predictions from PYTHIA and RAPGAP as well as the NLO predictions from FMNR⊗PYTHIA provide a good description of the shape of the differential cross sections. As for the visible and total cross section, the theoretical predictions underestimate the results of this measurement by a factor 1.9 (LO+PS MC) and 1.7 (NLO QCD), which has also been observed in previous muon analyses.

The reconstruction of muon candidates relies strongly on the reconstruction of so-called energy flow objects (EFOs), a combination of track information and energy measurements in the calorimeter. So far, muon candidates from EFOs originating only from primary vertex tracks were considered. The EFO reconstruction algorithm was successfully modified in order to consider tracks with some displacement from the primary vertex. While the amount of EFOs increases by 2%, the fraction of muon candidates with high impact parameter from tracks not associated to a vertex to all muon candidates is 5.1%, which is a large contribution. Further improvements on the selection criteria for tracks not originating from the primary vertex for the reconstruction of muon EFOs are in progress.

A search for instanton-induced events with heavy flavours in dimuon events has also been performed in this analysis. Instantons are expected to decay isotropically in their rest-frame with high particle multiplicity. In the lab frame, this feature is hypothetically observable via a homogeneous particle distribution in azimuth in a limited area of the pseudo-rapitidy η, referred to as *instanton band*. It was checked by means of different control distributions for the dimuon analysis presented in this thesis, that the instanton contribution predicted by QCDINS and scaled by $s_{\mathrm{MC}}^{Instanton} = 0.5$, combined with the dimuon contributions from beauty, charm, heavy quarkonia, Bethe-Heitler and light-flavour background still gives a reasonable description of the data. In addition, discriminating observables, which are sensitive to the hadronic final state, were used in combination with the requirement of both, like- and unlike-sign, non-isolated muon pairs, to separate beauty from instanton-induced events: The virtuality Q'^2 of the quark, which enters the instanton subprocess, the particle multiplicity N_{Band} in the reconstructed instanton band as well as the sphericity Sph and the isotropy Δ_B. For the reconstruction of these quantities, each dimuon event was required to have at least one jet candidate and different cuts on the kinematic variables of instanton-induced events were applied. For these discriminating variables, the dimuon data is also reasonably described by the dimuon MC including the instanton contribution. An excess of the dimuon data, which is only described by the QCDINS MC and not by the remaining dimuon contributions, which would be a clear signal for heavy flavour instantons in dimuon events, could not be observed. Albeit, based on the reasonable description of the dimuon data by the MC including the instanton contribution, it is not excluded that the dimuon data contains an instanton fraction of ~7-8%, which is very large. In that

case, the unknown mass-suppression factor for the calculation of the cross section of instanton induced events with heavy flavours would be determined to be of the order of ≈ 0.5 and the beauty scaling factor would decrease in this analysis from $s_{\mathrm{MC}}^b = 1.85$ to $s_{\mathrm{MC}}^b = 1.5$, hence the omission of instantons in heavy-flavour analyses with muons or electrons could be a possible explanation, why the beauty scaling factor (and as a result the measured cross section) in such analyses is almost a factor 2 higher (e.g. [62,64,65]) than in inclusive measurements [70–72].

This analysis offers some scope for further improvements:

- The beauty fraction of dimuon events in the data is still determined by subtracting the like-sign from the unlike-sign dimuon sample. An alternative would be to use the sum of both samples in combination with the life-time information of the charm and beauty hadrons provided by the MVD. Quantities describing this information, such as the invariant mass of secondary vertices, m_{vtx}, the hadron decay length L_{XY} and its significance S can be used to separate beauty from charm and light-flavour events. Control distributions for these quantities in the sum of like- and unlike-sign dimuon events show reasonable agreement between the dimuon data and MC contributions, thus, the method of secondary vertexing is in principle applicable in this analysis but, was not used in this thesis for the determination of the beauty fraction for lack of time.

- Secondary vertices in the HERA II data and corresponding Monte Carlo samples, which were used in this analysis, were reconstructed by requiring the presence of a reconstructed jet, since the jet axes were used as reference axes. Approximately 23% of the dimuon events in HERA II do not contain any jet candidates and have thus no reconstructed secondary vertex. The pseudo thrust, a quantity measuring the "(di-)jetness" of an event without reconstructed jet, provides alternative reference axes for the reconstruction of secondary vertices (cf. Sec. 5.12.1). The next iteration of HERA II data and MC samples, which are currently in production, contains, besides some optimised reconstruction information, additional secondary vertices which uses the pseudo-thrust axes as reference.

- The muon efficiency corrections used in this analysis are the dominant source of systematic uncertainty on the cross section measurement and were determined on dimuon data and MC samples before the Grand Reprocessing procedure. New efficiency correction tables based on dimuon samples of the Grand Reprocessing are in progress and will be available soon for further muon analyses and for a better estimation of the systematic uncertainties on muon-related cross sections.

- Differential cross sections were obtained for muons from beauty quarks. One of the next steps would be e.g. the measurement of dijet correlations for dimuon events. It was checked that approximately 17% of the dimuon events in HERA II contain at least two muon-associated jet candidates in a similar kinematic range as for other dijet analyses at HERA II performed at ZEUS [60–63], hence the statistics is still sufficient in order to measure differential dijet cross sections. However, the statistics can be increased by considering events with two electrons and/or one muon and one electron in the final state as well. Another step would be the extrapolation to differential cross sections of the beauty quark. This would allow comparisions with beauty production from other final states, e.g. the dielectron [188] or the dijet-dilepton channel [189].

Appendix A

Definition of the std. GMUON quality

qual-ity	finder combination	CTD match?	match prob/ DCA cut	vtx ass.	mip prob	mom. or rap.
6	BREMAT 5dof	yes	> 0.01	yes	-	-
	MPMATCH or MUFO	yes	> 0.05	-	-	-
	MPMATCH/MUFO + MV	yes	$> 0.01, < 0.05$	-	> 0.6	p>1
5	BREMAT 4dof + MV	yes	> 0.01	yes	> 0.6	$|\eta| > 0.6$
	MUBAC + MV	yes	-	yes	> 0.6	$|\eta| > 0.6$
	MUBAC+BREMAT4dof+MV	yes	> 0.01	yes	> 0.6	$|\eta| < 0.6$
	MUBAC+BREMAT5dof+MV	yes	> 0.01	no	> 0.6	-
	MPMATCH or MUFO	yes	$> 0.01, < 0.05$	-	-	-
	MUFO good vtx	no	—	yes	-	-
4	BREMAT 4dof	yes	> 0.01	yes	-	-
	MUBAC	yes	< 50 cm	yes	-	-
	MUBAC + MV	yes	< 120 cm	yes	> 0.6	$|\eta| < 0.6$
	MUBAC + MIP	yes	< 120 cm	-	impl.	pt>2
	MUFO other vtx	no	-	yes	-	-
	MCTS + MV	no	-	no	> 0.6	-

Table A.1: Default muon quality assignments (accepted muon candidates).

qual-ity	finder combination	CTD match?	match prob/ DCA cut	vtx ass.	mip prob	mom. or rap.
3	MV	yes	-	yes	> 0.95	p>1
	BREMAT 5dof	yes	> 0.01	no	-	-
	GLOMU + MV	yes	implicit	-	> 0.6	-
	MUBAC + MV	yes	< 120 cm	-	> 0.4	p>1
	MUBAC + GLOMU	yes	implicit	-	-	-
	MAMMA+CTD	yes	-	-	impl.	-
	MAMMA+vtx	no	-	yes	impl.	-
	MAMMA	no	-	-	impl.	-
2	MV	yes	-	yes	> 0.8	p>1
	MCTS	no	-	no	-	-
	BAC	yes	< 120 cm	yes	-	-
	BREMAT 4dof	yes	> 0.01	no	-	-
	GLOMU	yes	implicit	-	-	-
1	MV	yes	-	yes	> 0.6	p>1
0	MV	-	-	-	> 0.4	p>1
	MIP	yes	-	-	impl.	pt>2
-1	BREMAT 5dof	yes	< 0.01	-	-	-
-2	BREMAT 4dof	yes	< 0.01	-	-	-
	MCTS rec. problem	no	-	no	-	-
-3	any finder, same VC track	yes	-	-	-	-
-999	sim. μ, not rec.	-	-	-	-	p>1,pt> .5
-1000	sim. π/K decay, not rec.	-	-	-	-	p>1,pt> .5

Table A.2: Default muon quality assignments (rejected muon candidates).

Appendix B

Detailed list of MC samples

Beauty and Charm MC Samples in Photoproduction

Process	σ [nb]	Integrated luminosity $\mathcal{L}$ [pb^{-1}]			
		03/04p	05e	06e	06/07p
b direct	4.103	372	1304	494	1503
b resolved	0.708	353	1290	495	1556
b excitation in γ	1.343	466	1290	540	1417
b excitation in p	0.410	390	1290	547	1764
c direct	798	41	135	55	146
c resolved	111	41	135	55	146
c excitation in γ	374.8	41	135	55	146
c excitation in p	117.4	41	135	55	146

Table B.1: Beauty and Charm MC samples in photoproduction with corresponding integrated luminosities (approximated numbers) for different process types. All samples were generated in the region $Q^2 < 1$ GeV^2.

Beauty and Charm MC samples in DIS

Process	σ [nb]	Integrated luminosity $\mathcal{L}$ [pb^{-1}]			
		03/04p	05e	06e	06/07p
b direct BGF $\gamma g \rightarrow bb$	0.9077	1168	2115	925	2577
b excitation $bg \rightarrow bg$	1.2798	1167	2122	927	2500
c direct BGF $\gamma g \rightarrow c\bar{c}$	60.999	41	148	55	142
c excitation $cg \rightarrow cg$	26.487	41	147	55	498

Table B.2: RAPGAP Beauty and Charm MC samples in photoproduction with corresponding integrated luminosities (approximated numbers) for different process types.

Heavy Quarkonia, Bethe-Heitler, instanton and multi-heavy-flavour samples

Process	σ [pb]	Integrated luminosity $\mathcal{L}$ [pb^{-1}]			
		03/04p	05e	06e	06/07p
elastic J/ψ	500	813	2634	1047	2492
inelastic J/ψ	3570	49	148	65	152
elastic ψ'	500	813	2748	1092	2492
inelastic ψ'	817	153	153	122	153
$\Upsilon(1s, 2s, 3s)$	500	40	138	55	125
BH DIS	95	2964	8444	3439	7532
BH elastic	2052	96	775	310	365
BH inelastic	528	212	1358	419	758
instanton MC	6162	42	136	55	146
$b\bar{b}b\bar{b}$	1.0999	415	1364	555	1483
$c\bar{c}c\bar{c}$	511.75	85	277	109	272
$b\bar{b}c\bar{c}$	29.113	400	1324	553	1442

Table B.3: Background MC samples consisting of heavy quarkonia, Bethe-Heitler, instanton and multi-heavy-flavour events in photoproduction and DIS with corresponding integrated luminosities (approximated numbers) for different process types.

Appendix C

Monte-Carlo sample processes

Beauty Quark MC Samples

Direct processes:

$$\gamma g \;\rightarrow\; b\bar{b}$$

Resolved processes:

$$q\bar{q} \;\rightarrow\; b\bar{b}$$
$$gg \;\rightarrow\; b\bar{b}$$

Excitation in the proton processes:

$$b\gamma \;\rightarrow\; bg$$
$$bg \;\rightarrow\; bg$$
$$bq \;\rightarrow\; bq$$
$$b\bar{b} \;\rightarrow\; b\bar{b}$$

Excitation in the photon processes:

$$bg \;\rightarrow\; bg$$
$$bq \;\rightarrow\; bq$$

Charm Quark MC Samples

Direct processes:

$$\gamma g \;\rightarrow\; c\bar{c}$$

Resolved processes:

$$q\bar{q} \rightarrow c\bar{c}$$
$$gg \rightarrow c\bar{c}$$

Excitation in the proton processes:

$$c\gamma \rightarrow cg$$
$$cg \rightarrow cg$$
$$cq \rightarrow cq$$
$$c\bar{c} \rightarrow c\bar{c}$$

Excitation in the photon processes:

$$cg \rightarrow cg$$
$$cq \rightarrow cq$$

Appendix D

Trigger definition

TLT HFL01: Open charm and beauty trigger slot

TLT HFL05: Inclusive dijet trigger slot

- 2 jets with $E_T > 4.5$ GeV and $|\eta| < 2.5$,

- $p_z/E < 0.95$,

- $E - p_z < 100$ GeV (measured in the CAL).

TLT HFL06: Dijets in DIS trigger slot

- 2 jets with $E_T > 3.5$ GeV and $|\eta| < 2.5$,

- $p_z/E < 1.0$,

- $E - p_z < 100$ GeV (measured in the CAL).

TLT HFL13: Inclusive semi-leptonic muon slot

- at least one muon found at second level trigger,

- muon reconstructed in barrel respective rear muon chambers with a matching CTD track (matched with GLOMU),

- total $E_T > 9$ GeV (measured in the CAL).

TLT HFL14: Inclusive muon in DIS slot

- at least one muon found at second level trigger,

- muon reconstructed in barrel respective rear muon chambers with a matching CTD track (matched with GLOMU),

- presence of DIS electron.

TLT HFL16: Inclusive muon in BAC slot

- at least one muon + hadron found at second level trigger,

- muon reconstructed in BAC with a matching CTD track (matched with GLOMU),

- $p_T^\mu > 1.4$ GeV and $p > 3$ GeV and $r > 150$ cm (forward, rear) or

- $p_T^\mu > 2.0$ GeV (barrel) or

- very high quality BAC track without match (anywhere).

TLT HFL25: Muon plus dijet trigger slot

- at least one muon found at second level trigger,

- muon reconstructed in barrel respective rear muon chambers with a matching CTD track (matched with GLOMU),

- 2 jets with $E_T > 3.5$ GeV and $|\eta| < 2.5$,

- $p_z/E < 1.0$ (measured in the CAL),

- $E - p_z < 100$ GeV (measured in the CAL).

TLT HFL27: MVD inclusive trigger slot

- MVD vertex within -30 cm $< z_{vtx} < 30$ cm,

- at least four tracks fitted to primary vertex,

- $E_T > 8$ GeV (excluding first two inner rings around beam pipe),

- at least three tracks with

  - $p_T^{\text{Track 1}} > 0.75$ GeV,
  - $p_T^{\text{Track 2}} > 0.6$ GeV,
  - $p_T^{\text{Track 3}} > 0.45$ GeV,

- significance cut for the third-highest significance track. The significane is evaluated with respect to primary event vertex.

TLT HFL30: J/ψ candidate slot

- at least one muon found at second level trigger,

- muon reconstructed in barrel respective rear muon chambers with a matching CTD track,

- at least one additional track with $m^{\mu}_{\text{Track}} > 2$ GeV.

TLT HFL31: Two isolated muons from MV-TLT muon finder slot

- at least one moun + hadron found at second level trigger,

- two muon candidates from MV,

- p_T and mass requirements for J/ψ and Υ fulfilled.

TLT HFL32: Inclusive double-tagged (di)muon slot

TLT DIS03: Medium Q^2 DIS electron slot

- good electron with

  - $E_e > 4$ GeV and
  - $30 < E - p_z < 100$ GeV,

- box cut around beam pipe with $\sqrt{x^2 + y^2} \geq 35$ cm.

TLT HPP31: Inclusive low Q^2 DIS slot

- SLT SPP1,

- 12 cm $\times$ 12 cm electron box cut,

- $E_e > 7$ GeV,

- $E - p_z > 34$ GeV,

- $Q^2_{TLT} > 6$ GeV^2,

- one track from CTD with $p_T > 0.2$ GeV.

TLT EXO11/12: Barrel/Rear muon trigger slot

- one outer barrel respective rear muon reconstructed by GLOMU finder,

- cosmics rejection if:

  - $n_{\text{Tracks-CTD}} \leq 3$,
  - $E_{FCAL} < 1.0$ GeV,
  - two tracks with highest $p_T > 0.5$ GeV and $\cos(\theta_{\text{Tracks}}) < $ -0.9998,

- CAL timing cut compatible with physics event,

- includes a logical or of the first level trigger slots: FLT14 (barrel muon), FLT15 (rear muon),

- FLT14 and FLT15 use both, inner and outer muon chamber hits information,

- implicit requirement of any SLT physics slot.

TLT SPP02 (2003-2005): Inclusive low Q^2 DIS slot

- SLT SPP1,

- Sinistra or Emille electron finders,

- $30 < E - p_z < 100$ GeV,

- $E_e > 4$ GeV,

- 12 cm $\times$ 12 cm electron box cut.

TLT SPP09 (2006/07): Inclusive low Q^2 DIS slot

- SLT SPP1,

- only Sinistra electron finder,

- $30 < E - p_z < 100$ GeV,

- $E_e > 4$ GeV,

- 15 cm $\times$ 15 cm electron box cut.

TLT MUO01: Isolated muon filter

- ≥ 1 FMU matched to mip,

- no beam gas,

- vertex,

- SLT MUO 4 and FLT 0 must be required explicitely in addition.

TLT MUO02: High E_T filter

- ≥ 1 spline matched to MIP or CTD,

- $E_T > 10$ GeV,

- $E - p_z > 5$ GeV,

- vertex,

- SLT MUO 5 and FLT 6 required explicitely in addition.

TLT MUO03: Semi-isolated Muon in Barrel/Rear Muon Chambers

- one muon reconstructed by GLOMU finder,

- good inner barrel/rear muon found on second level trigger,

- muon-like CAL island (requires MIP coincidence),

- hit in barrel or rear inner muon chambers,

- $n_{\text{Tracks-CTD}} \geq 1$,

- track going into barrel or rear CAL with $p_T > 1$ GeV,

- second level trigger slot: till 2004 SLT MUO 1(replaced by SLT GTT 5 from 2005),

- SLT MUO 1 includes logical OR of the first level trigger slots FLT 8,9,10,11.

TLT MUO04: Old elastic J/ψ in FMU filter

- SLT MUO3,

- MAMMA match,

- $m^{\text{CTD-CTD, spline-CTD or spline-spline}} > 1.5$ GeV,

- logical OR of FLT 0 and FLT 18 explicitely required in addition.

TLT MUO05: New elastic J/ψ in FMU filter

- at least one spline matched to MIP or

- at least one hit in plane 1 matched to CTD and MIP,

- $n_{\text{CTD-VTX-Tracks}} \leq 3$,

- $E_{total} - E_e - E_{FCAL}^{\text{INR}} < 10$ GeV,

- vertex.

TLT MUO06: Dimuon filter

- ≥ 2 FMU, one of which spline matched to MIP or CTD,

- no beam gas,

- vertex.

TLT MUO07: DIS filter

- ≥ 1 FMU,

- scattered electron with $E_e > 4$ GeV,

- $E - p_z > 30$ GeV,

- logical OR of DIS SLTs,

- vertex.

TLT MUO08: Jets filter in FMU

- ≥ 1 FMU,

- at least 2 jets with $E_T > 3.5$ GeV and $|\eta| < 2.5$,

- logical OR of PHP SLTs,

- no beam gas,

- vertex.

TLT MUO09: Charged Current filter in FMU

- ≥ 1 FMU,

- logical OR of SLT HPP5, SLT EXO4 and SLT EXO5

- vertex.

TLT MUO10-MUO14: BAC muon filter

- track segment in BAC,

- caution: no built-in requirement on FLT and SLT bits.

Appendix E

Instanton theory

E.1   Introduction - instantons in quantum mechanics

Some basic properties of instantons can be illustrated in quantum mechanics. For this purpose, one considers the double-well potential [190]:

$$V(x) = g(x^2 - x_0^2)^2, \tag{E.1}$$

with minima at $x = \pm x_0$, shown in Fig. E.1 a). The total energy and Lagrange function of a particle with spin zero and mass $m = 1$ in this potential is

$$E = \frac{1}{2}\left(\frac{dx}{dt}\right)^2 + V(x), \quad L\left(x, \frac{dx}{dt}\right) = \frac{1}{2}\left(\frac{dx}{dt}\right)^2 - V(x). \tag{E.2}$$

In classical mechanics, the ground state is two-fold degenerate, i.e. the particle is either located at $x = x_0$ or at $x = -x_0$. In quantum mechanics, both states can be mixed by tunneling, so the ground state can be regarded as superposition of both:

$$|x\rangle_{E=0} = \frac{1}{\sqrt{2}}(|-x_0\rangle + |x_0\rangle).$$

The tunneling through the potential barrier restores the symmetry of the system and the expectation value $\langle x \rangle_{E=0}$ for the ground state is zero.

This tunneling effect can also be described classically. By use of a *Wick rotation* in Eq. E.2, one replaces real time t by *Euclidean* time τ, i.e. $t \to -i\tau$, and obtains:

$$E = -\frac{1}{2}\left(\frac{dx}{d\tau}\right)^2 + V(x) \tag{E.3}$$

or, respectively,

$$-E = \frac{1}{2}\left(\frac{dx}{d\tau}\right)^2 - V(x). \tag{E.4}$$
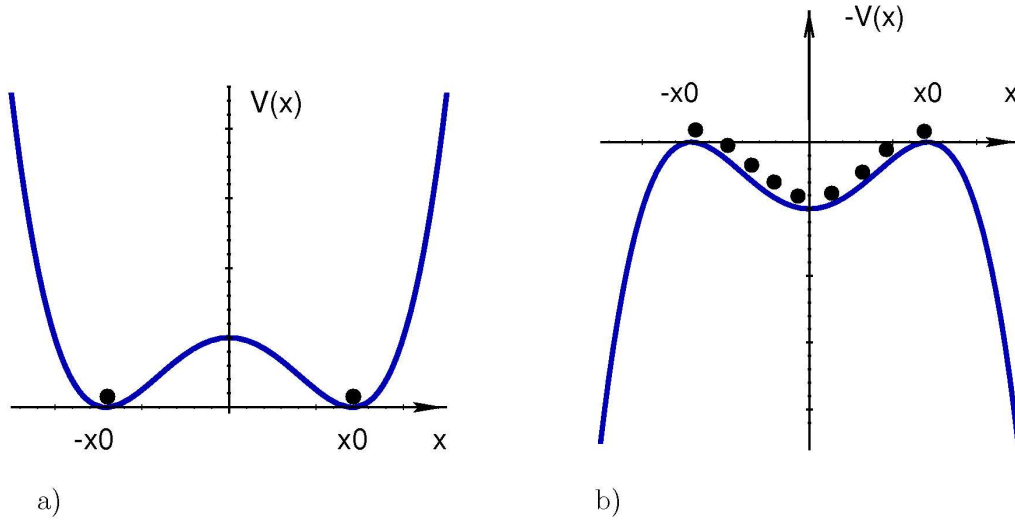
Figure E.1: a) Double-well potential: $-x_0$ and x_0 are the classical solutions of a particle in this potential. **b)** After a *Wick rotation*, one obtains a double-hill potential and both solutions can be connected with a trajectory the particle can move along [197].

This can be seen as a mirroring of the potential from $V(x)$ to $-V(x)$, thus the double-well potential becomes a double-hill potential, where the particle can move between both maxima, as shown in Fig.E.1 b). For the ground state $E = 0$, one finds the solution

$$x^{(I)}(\tau) = \pm x_0 \tanh\left[\sqrt{2g}x_0(\tau - \tau_0)\right],\tag{E.5}$$

which is referred to as *instanton solution* for positive sign and *anti-instanton solution* for negative sign. Fig. E.2 shows the instanton solution as well as its time derivative as a function of τ. One can see that instantons can describe tunneling between the classically degenerated ground states $x = \pm x_0$, identical to quantum mechanics. The time derivative of the instanton solution is sharply peaked at τ_0, i.e. the instanton solution is localised in Euclidean space-time. In real time, tunneling occurs almost instantaneously, therefore the term *instanton*.

Furthermore, by use of the *Feynman path integral method* [191], one can calculate the probability for the instanton process in the double-well potential. Thus, the transition amplitude between the initial state $x(t_i){=}x_i$ and the final state $x(t_f{=}x_f)$ can be calculated as integral over all paths $[Dx]$, weighted with their action $S(x)$:

$$\langle x_f|e^{-iH(t_f-t_i)}|x_i\rangle = N\int_{x_i}^{x_f}[Dx]e^{iS(x)},\tag{E.6}$$

where H is the Hamiltonian and N a normalisation factor. For Euclidean time, this turns into

$$\langle x_f|e^{H(\tau_f-\tau_i)}|x_i\rangle = N\int_{x_i}^{x_f}[Dx]e^{-S_E(x)}\tag{E.7}$$
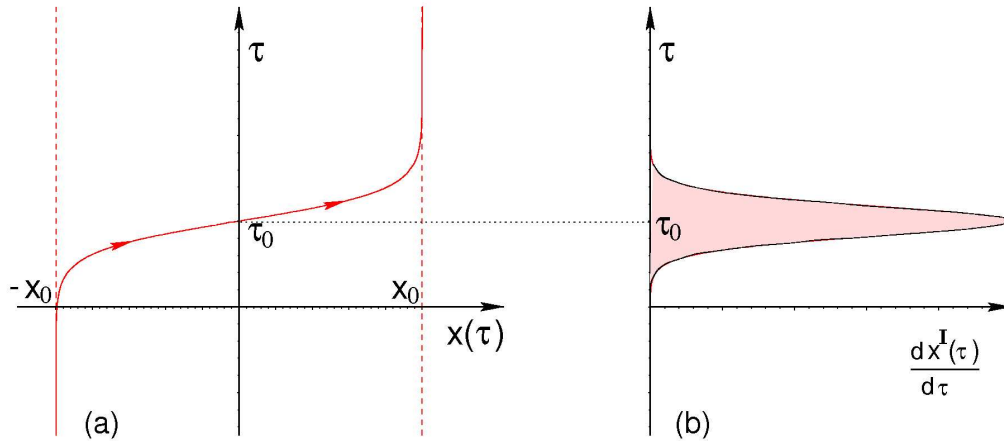
Figure E.2: a) Instanton solution of the equation of motion (equation E.5) in Euclidean time. **b)** Time derivative of x as a function of Euclidean time τ [197].

with S_E as *Euclidean action*, which is obtained from the one in Minkowsi space by means of a Wick rotation:

$$S = \int dt \ L(x, \dot{x}) \overset{t \to -i\tau}{\Longrightarrow} i \cdot S_E \tag{E.8}$$

With the Lagrangian of the double-well potential in Eq. E.2, one obtains finally for the Euclidean action:

$$S_E = \frac{4}{3}\sqrt{2g}x_0^3.$$

That means, the action is finite, therefore the instanton (I)or anti-instanton $(\bar{I})$solution possesses a finite transition probability. For the Feynman path integral method, the classical instanton solutions correspond to those paths with minimal action in Euclidean space-time and are the dominant part of the path integral. In quantum mechanics, where every path is allowed, one would have to integrate over numerous smaller contributions, which is for the most part unfeasible.

E.2 Instantons in Quantum Chromodynamics

The following part follows closely the introduction of QCD instantons given in the references [10, 190, 193].

The Langrangian of QCD is given by:

$$\mathcal{L} = -\frac{1}{4}G_{j,\mu\nu}G_j^{\mu\nu} + \sum_{n_f} \bar{\psi}(i\gamma^\mu D_\mu - m_{n_f})\psi, \tag{E.9}$$

where the sum runs over all six quark flavours, n_f. ψ is a generic fermion field and $G_{j,\mu\nu}$ the field strength tensor of the gluon field A_μ:

$$G_{j,\mu\nu} = \partial_\mu A_{j,\nu} - \partial_\nu A_{j,\mu} - f_{jkl}A_{k,\mu}A_{l,\nu}, \tag{E.10}$$

where f_{jkl} are the $SU(3)$ structure constants. For simplicity, the fermion fields are neglected in the following and the Langragian has the form:

$$\mathcal{L} = -\frac{1}{4}G_{j,\mu\nu}G_j^{\mu\nu}. \tag{E.11}$$

The Euclidean action S_E can then be written as:

$$S_E = \int d^4x \, \mathcal{L} = -\frac{1}{4}\int d^4x \, G_{j,\mu\nu}G_j^{\mu\nu}. \tag{E.12}$$

The Euclidean action in Eq. E.12 is finite, $G_{j,\mu\nu}G_j^{\mu\nu}$ is positive definite. Therefore, the gluon field strength tensor must vanish on a large sphere with radius $|x| = R \to \infty$ [192]:

$$G_{\mu\nu}(|x| = R) \stackrel{R \to \infty}{\Longrightarrow} 0. \tag{E.13}$$

This boundary condition is fulfilled by the trivial gauge field $A_\mu(x)=0$ as well as by gauge fields $A_\mu(x)$ with:

$$A_\mu(x = R) \stackrel{R \to \infty}{\Longrightarrow} \frac{i}{g}U(x)\partial_\mu U^\dagger(x), \tag{E.14}$$

where $U(x)$ is a transformation matrix of $SU(3)$. A general transformation of the gauge field $A_\mu(x)$ has the form:

$$A'_\mu(x) = U^\dagger(x)A_\mu(x)U(x) + \frac{i}{g}U^\dagger(x)\partial_\mu U(x), \tag{E.15}$$

therefore, the gauge field in Eq. E.14 is the result of the gauge transformation of $A_\mu(x)=0$. This is referred to as *pure gauge* [10, 193].

In $SU(3)$, one can distinguish between different gauge transformations $U(x)$, because some of them can be deformed continuously into each other, while this is not possible for the remaining ones. All gauge transformations which can be continuously deformated into each other form a so-called *homotopy class*. There is an infinite amount of such classes, which can be distinguished by means of their topological winding number

$$n = 0, \pm1, \pm2, ...$$

Furthermore, besides the different gauge tranformations $U(x)$, different vacua in those homotopy classes exists. Therefore, one introduces the so-called *Chern-Simons-number* [194], which represents the winding number of a gauge field A:

$$N_{CS} = \frac{g^2}{16\pi^2}\int d^3x \varepsilon_{ijk}\left(A_i^a\partial_j A_k^a - \frac{g}{3}\varepsilon_{abc}A_i^a A_j^b A_k^c\right), \tag{E.16}$$

where ε is the total antisymmetric tensor:

$$\varepsilon = \begin{cases} +1, & \text{for } ijk \text{ even permutation of 1,2,3} \\ -1, & \text{for } ijk \text{ odd permuation of 1,2,3} \\ 0 & \text{else} \end{cases}$$
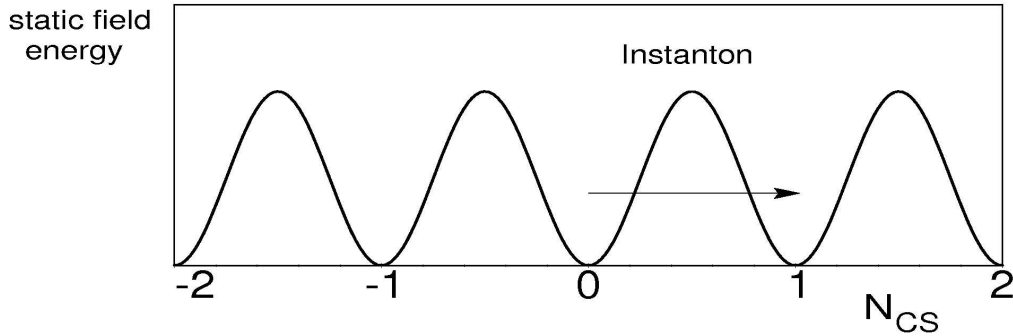
Figure E.3: Illustration of topological different QCD vacua. Plotted is the energy density of the gauge fields in dependence of the Chern-Simons number N_{CS} [196].

Thus, every homotopy class presents a specific vacuum with unique topology. It is not possible to move from one vacuum to neighbouring ones by means of continuously gauge transformations, since these vacua are separated from each other by energy barriers E_B [195], as illustrated in Fig. E.3.

Instanton solutions of the classical field equations in QCD are non-trivial gauge fields ($A_\mu^{(I)}$, $\mu = 1, 2, 3, 4$) with finite action connecting topologically different vacua. One obtains the solutions by changing, as in the quantum mechanical example, from real time into Euclidean time. Calculating the Lagrange density $\mathcal{L}$ of the Euclidean gauge field with these instanton solution [6] yields:

$$\mathcal{L}[A_\mu^{(I)}(x, \rho)] = \frac{12}{\pi \alpha_s} \cdot \frac{\rho^4}{(x^2 + \rho^2)^4}, \tag{E.17}$$

where α_s is the coupling constant of the strong interaction and ρ the size of the instanton[1]. The Lagrange density $\mathcal{L}$ depends only on x^2, i.e. there is a spherical symmetry, as illustrated in fig. E.4.

By integrating Eq. E.17, one obtains the Euclidean action S_E:

$$S_E = \frac{2\pi |Q|}{\alpha_s}, \tag{E.18}$$

which is independent of the size of the instanton ρ. Q is the topological charge:

$$Q = \Delta N_{CS} = \begin{cases} +1, & \text{instanton } I \\ -1, & \text{anti-instanton } \bar{I} \end{cases}$$

By means of the Feynman path integral method, the tunneling amplitude T can be determined:

$$T = f(\alpha_s) \cdot \exp(-S_E)(1 + \text{corrections}), \tag{E.19}$$

---

[1]The size of the instanton ρ characterises the spatiotemporal expansion of the instanton gauge field
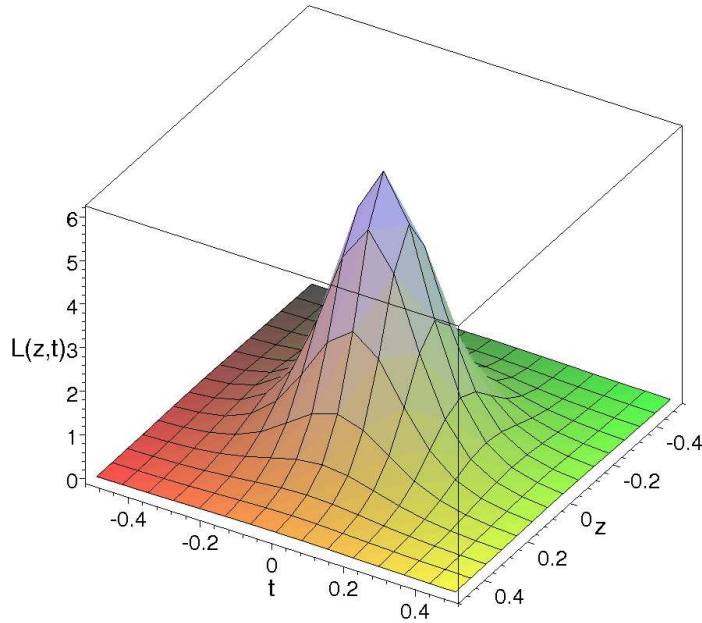
Figure E.4: Lagrange density of the instanton at $x_0=0$ [198].

and hence the dependence of the cross section (i.e. the square tunneling amplitude, thus dimensionless) of instanton-induced processes on the coupling constant α_s:

$$\sigma \propto \exp\left(-\frac{4\pi}{\alpha_s}\right). \tag{E.20}$$

One discovers that the tunneling process is on the one hand exponentially suppressed, but on the other hand it should be possible to measure the cross section due to the large QCD coupling constant α_s.

E.3   Cross sections of instanton-induced events

The differential cross section of instanton-induced processes can be written in I-pertubation theory as

$$\frac{d\sigma_{e^\pm p}^{(I)}}{dx'dQ'^2} \simeq \frac{d\mathcal{L}_{q'g}^{(I)}}{dx'dQ'^2} \cdot \sigma_{q'g}^{(I)}(Q',x') \text{ for } \begin{cases} Q'^2 = -q'^2 > 0 & \text{high} \\ 0 \leq x' = \frac{Q'^2}{2p\cdot q'} \leq 1 & \text{fixed} \end{cases}. \tag{E.21}$$

The differential luminosity $\mathcal{L}_{q'g}^{(I)}$ describes the amount of $q'g$-collisions per $e^\pm p$-collision and has been calculated in [199]. The total cross section $\sigma_{q'g}^{(I)}(Q',x')$ of the instanton subprocess is calculable by integrating over all free parameters of the instanton solution, the so-called *collective coordinates*, i.e. over the instanton size ρ and anti-instanton size $\bar{\rho}$, the spatiotemporal distance between instanton and anti-instanton, R_μ, and the relative $I\bar{I}$-colour-orientation matrix U:

$$\sigma_{q'g}^{(I)}(Q',x') = \int d\rho d\bar{\rho} \int d^4R \; e^{i(P+q')R} \int dU \; e^{-(\rho+\bar{\rho})Q'} D(\rho,\mu_r) D(\bar{\rho},\mu_r)...e^{-\frac{4\pi}{\alpha_s(\mu_r)}\Omega(U,\frac{R^2}{\rho\bar{\rho}},\frac{\rho}{\bar{\rho}})} \tag{E.22}$$

The function $\Omega(U, \frac{R^2}{\rho\bar{\rho}}, \frac{\rho}{\bar{\rho}})$ results from the emission of additional gluons and reduces the exponentiel suppression of the cross section. $\Omega(U, \frac{R^2}{\rho\bar{\rho}}, \frac{\rho}{\bar{\rho}})$ can be calculated by means of the $I\bar{I}$-valley method [200]. The instanton density $D(\rho, \mu_r)$ is perturbatively calculable as well [5, 201, 202]:

$$D(\rho, \mu_r) = d\left(\frac{2\pi}{\alpha_s(\mu_r)}\right)^{2N_C} e^{-\frac{2\pi}{\alpha_s(\mu_r)}} \frac{(\rho\mu_r)^{\beta_0\Delta_1-\Delta_2}}{\rho^5}, \tag{E.23}$$

where d is a constant depending on the renormalisation scheme and Δ_1, Δ_2 are constants depending on μ_r. β_0 is the first coefficient of the QCD β-function and given by

$$\beta_0 = \frac{11}{3}N_C - \frac{2}{3}n_f. \tag{E.24}$$

In first order, $\Delta_1 = 1$ and $\Delta_2 = 0$, therefore one obtains for the instanton density the relation $D \sim \rho^6$. As a consequence, the integral over the size of the (anti-)instanton diverges for large values of $\rho/\bar{\rho}$. But for large values of the quark virtuality Q'^2, only small instantons are taken into account for the calculation of the cross section due to the exponential factor $e^{-(\rho+\bar{\rho})Q'}$ [203].

For reliable results of the cross section of instanton-induced events, the kinematic region of x' and Q', in which instanton-pertubation theory can be safely applied has to be known. The determination of this region is possible by means of QCD lattice calculations, in which interactions between gluon fields on a discrete lattice are simulated [199, 204]. In fig. E.5, the instanton density $D(\rho)$ as a function of the size of the instanton ρ as well as the pertubatively calculated $D \sim \rho^6$ behaviour of the instanton density is illustrated.
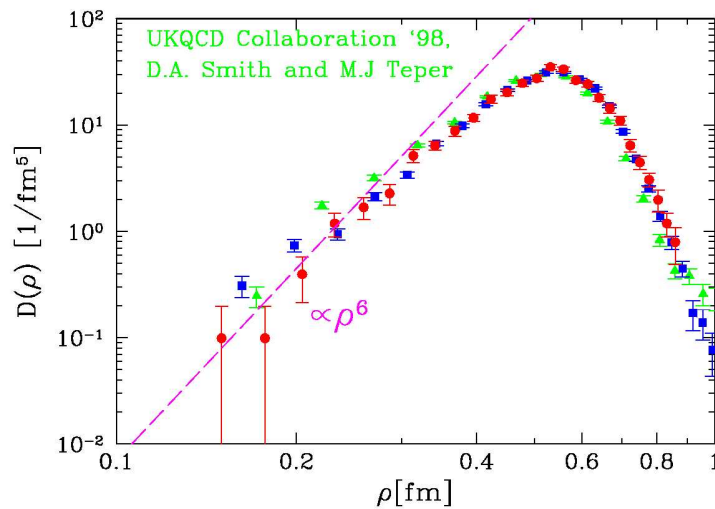
Figure E.5: Comparison between the perturbatively calculated instanton density $D(\rho, \mu_r) \sim \rho^6$ (dashed line) and those of several latticed calculations (dots) [199, 204]. The fiducial region for instanton pertubation is at $\rho \leq 0.35$ fm.

For the fiducial region, one obtains finally [199]:

$$\left.\begin{array}{ll} \rho \leq \rho_{max} & \approx 0.35 \text{ fm} \\ \frac{R}{\rho} \geq \left(\frac{R}{\rho}\right)_{min} & \approx 1.05 \end{array}\right\} \Longrightarrow \left\{\begin{array}{ll} Q'^2 \geq Q'^2_{min} = \left(30.8\,\Lambda_{\overline{\text{MS}}}^{(n_f=3)}\right)^2 & \approx 113 \text{ GeV}^2 \\ x' \geq x'_{min} & \approx 0.35 \end{array}\right. \tag{E.25}$$

The scale parameter Λ_{QCD} depends on the number of involved flavours n_f and is the result of the mean value of the coupling constant of the strong interaction [2]:

$$\alpha_s(M_Z) = 0.1184 \pm 0.0007 \Longrightarrow \Lambda \frac{(n_f = 3)}{\mathrm{MS}} = 0.346 \;^{+0.031}_{-0.029} \; \mathrm{GeV}.$$
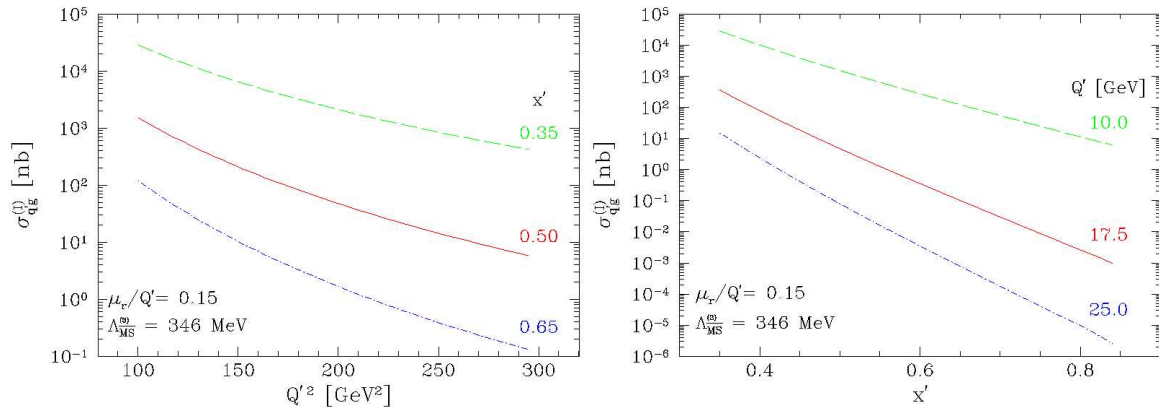
Figure E.6: Cross section of the instanton subprocess as function of Q'^2 and x' [178]

Fig. E.6 shows the cross section of instanton-induced events as a function of x' and Q'^2. In the fiducial region and with additional cuts $x > 10^{-3}$ and $0.1 < y < 0.9$, which corresponds to a photon virtuality of $Q^2_{min} \geq 9\ \mathrm{GeV}^2$, one obtains for the instanton cross section for the three light flavours at HERA [178, 205]:

$$\sigma^{(I)}_{\mathrm{HERA}} \approx 89 \;^{+18}_{-15} \; \mathrm{pb} \tag{E.26}$$

with uncertainties only referring to the one of Λ_{QCD}. Further theoretical uncertainties, especially by non-planar Feynman diagrams, can be suppressed by applying an additional cut on the photon virtuality Q^2:

$$Q^2 \geq Q^2_{min} = Q'^2_{min} \approx 113\ \mathrm{GeV}^2, \tag{E.27}$$

yielding for the cross section of instanton-induced events at HERA in the kinematical range $x' \geq 0.35$, $Q^2 \geq Q'^2 \approx 113\ \mathrm{GeV}^2$, $x > 10^{-3}$ and $0.1 < y < 0.9$ of:

$$\sigma^{(I)}_{\mathrm{HERA}} \approx 29 \;^{+10}_{-8} \; \mathrm{pb}. \tag{E.28}$$

This is about 1% of the total D.I.S. cross section at HERA.

Instanton-induced events in photoproduction can also be predicted, but the calculation of the cross section for those events in instanton-perturbation theory is more challenging [206]. Results so far imply that the cross section for those events does not diverge for low values of x', but increases approximately by one order of magnitude [178]. The cross section $\sigma^{(I)}_{HERA}$ for instanton-induced events with heavy flavours is not explicitly calculable, because it is suppressed by an unknown factor, which has to be determined experimentally and depends exponentially on the large masses of the charm and beauty quark [207]. Nevertheless, it was found out in [15], that the suppression factor should not be greater than about two orders of magnitude for a verification of heavy flavour instantons at HERA.

Appendix F

Bin meaning of μ finder key

		Bin	Finder	Comment
4	**=**	quality 4		
		4.2	BREMAT	inner chambers
		4.4	BAC	
		4.5	BAC/BREMAT + MV	low quality or not vertex associated
		4.6	MPMATCH or MUFO	low probability, with track match
		4.7	MUFO	no track
5	**=**	quality 5		
		5.1	BREMAT + MV	outer chambers low probability (BREMAT)
		5.2	BREMAT + MV	inner chambers (BREMAT), $|\eta^\mu| > 0.6$ (MV)
		5.4	BAC + MV	$|\eta^\mu| > 0.6$
		5.5	BREMAT + BAC + MV	inner chambers (BREMAT), $|\eta^\mu| < 0.6$ (MV)
		5.6	MPMATCH/MUFO	lower quality forward muon
6	**=**	quality 6		
		6.1	BREMAT	outer chambers
		6.6	MPMATCH or MUFO	with tracks
		6.8	MPMATCH/MUFO + MV	lower probability (MPMATCH/MUFO)
7	**=**	all dimuons		
		7.2	quality 4 & 4	
		7.3	quality 5 & 4	
		7.4	quality 6 & 4 or	
			quality 5 & 5	
		7.5	quality 6 & 5	
		7.6	quality 6 & 6	
		7.8	muon chambers only	MPMATCH, MUFO or BREMAT
				(inner or outer)
		7.9	BAC only	

Table F.1: Definition of the bin contents of Fig. 5.17

Appendix G

Control plots for multi-heavy-flavour events

In the following, control distributions for the invariant dimuon mass for like- and unlike-sign as well as isolated and non-isolated muon pairs are shown. The contributions from $b\bar{b}b\bar{b}$, $b\bar{b}c\bar{c}$ and $c\bar{c}c\bar{c}$ processes are illustrated in blue while the sum of the contributions from $b\bar{b}-, c\bar{c}-$, heavy quarkonia-, Bethe-Heitler and light flavour events are depicted by a green-shaded area.
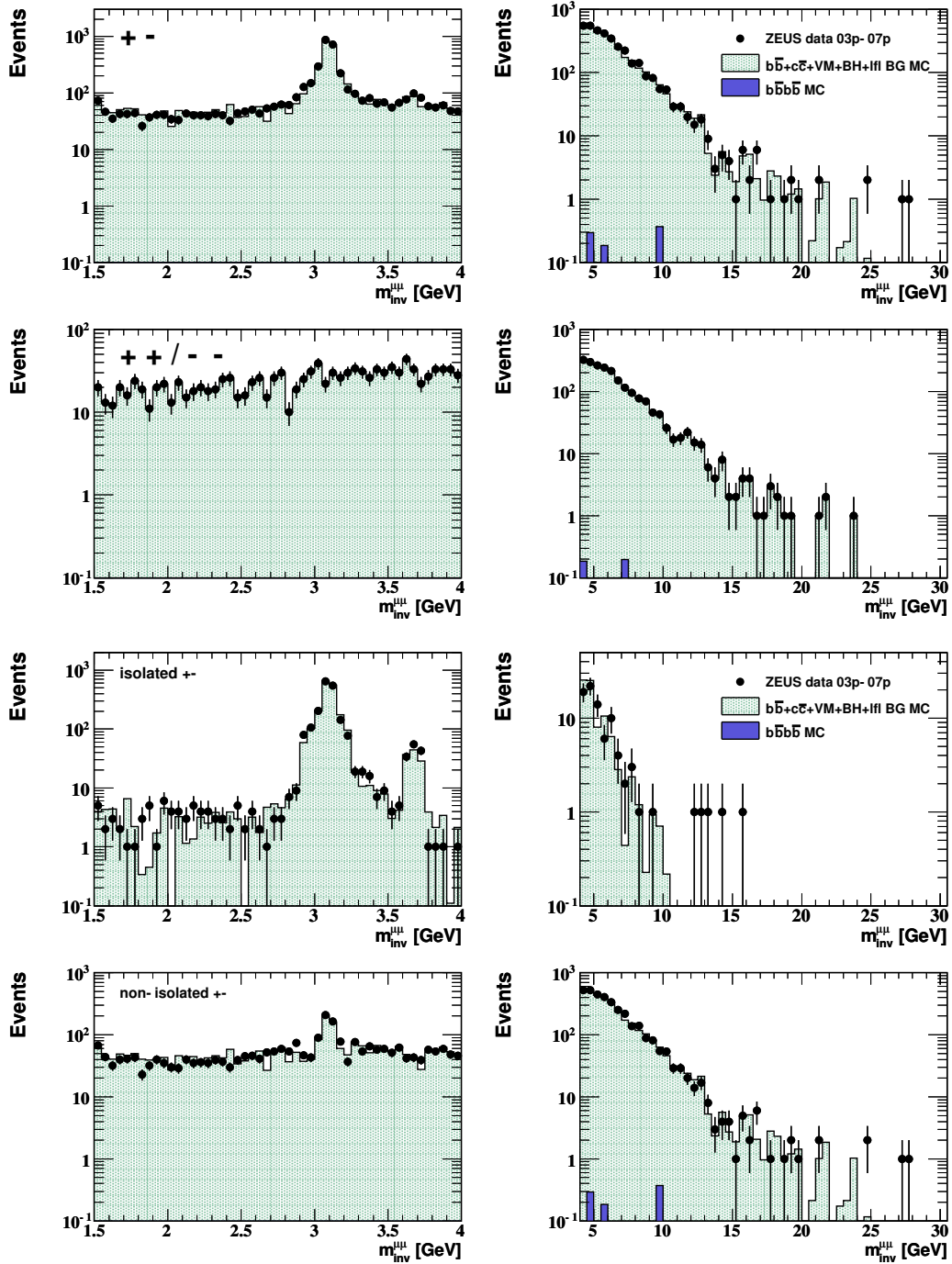
Figure G.1: Invariant dimuon mass for like- and unlike-sign as well as isolated and non-isolated muon pairs for $b\bar{b}b\bar{b}$ production (blue) and the sum of all MC dimuon sources (green-shaded area).
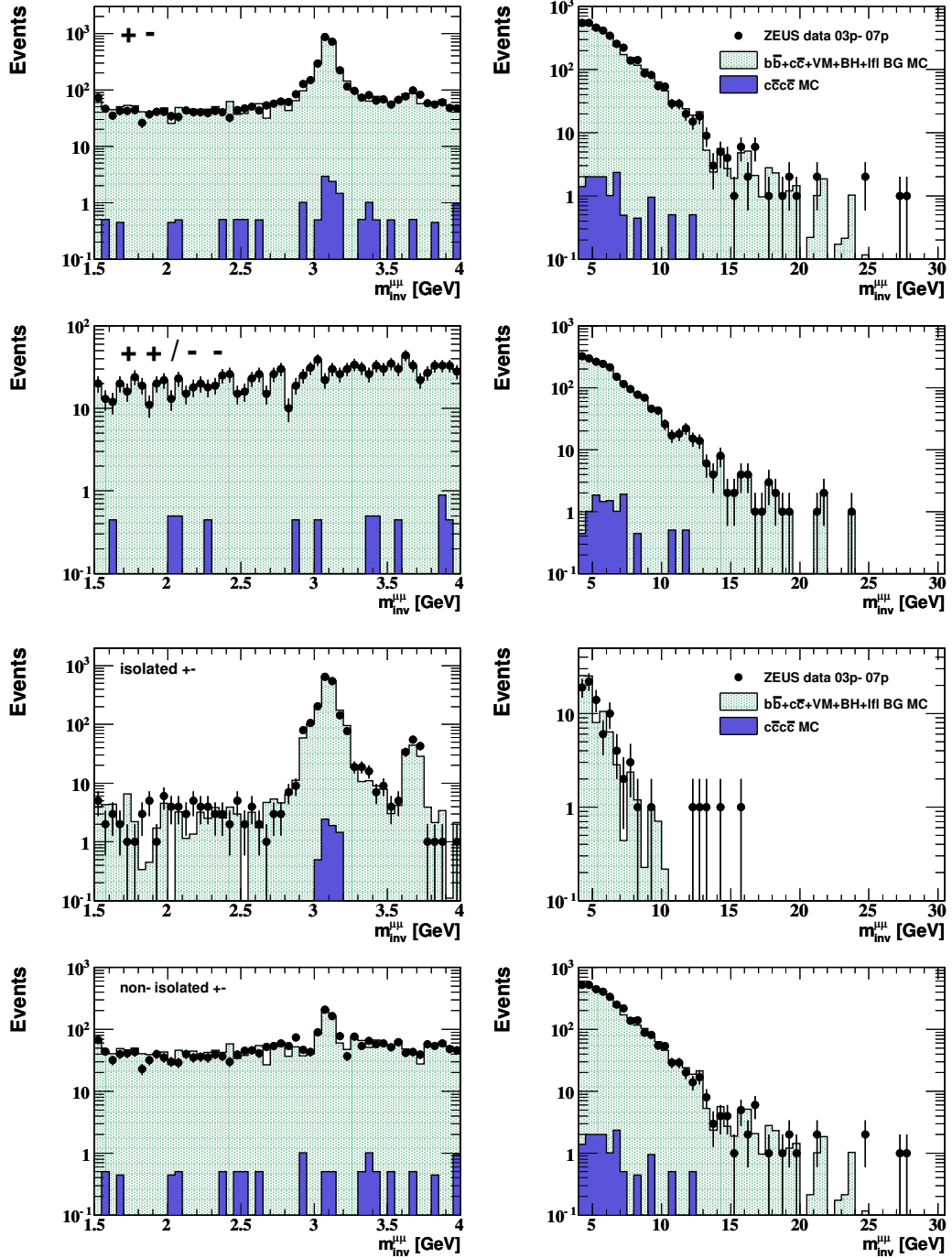
Figure G.2: Invariant dimuon mass for like- and unlike-sign as well as isolated and non-isolated muon pairs for $c\bar{c}c\bar{c}$ production (blue) and the sum of all MC dimuon sources (green-shaded area).
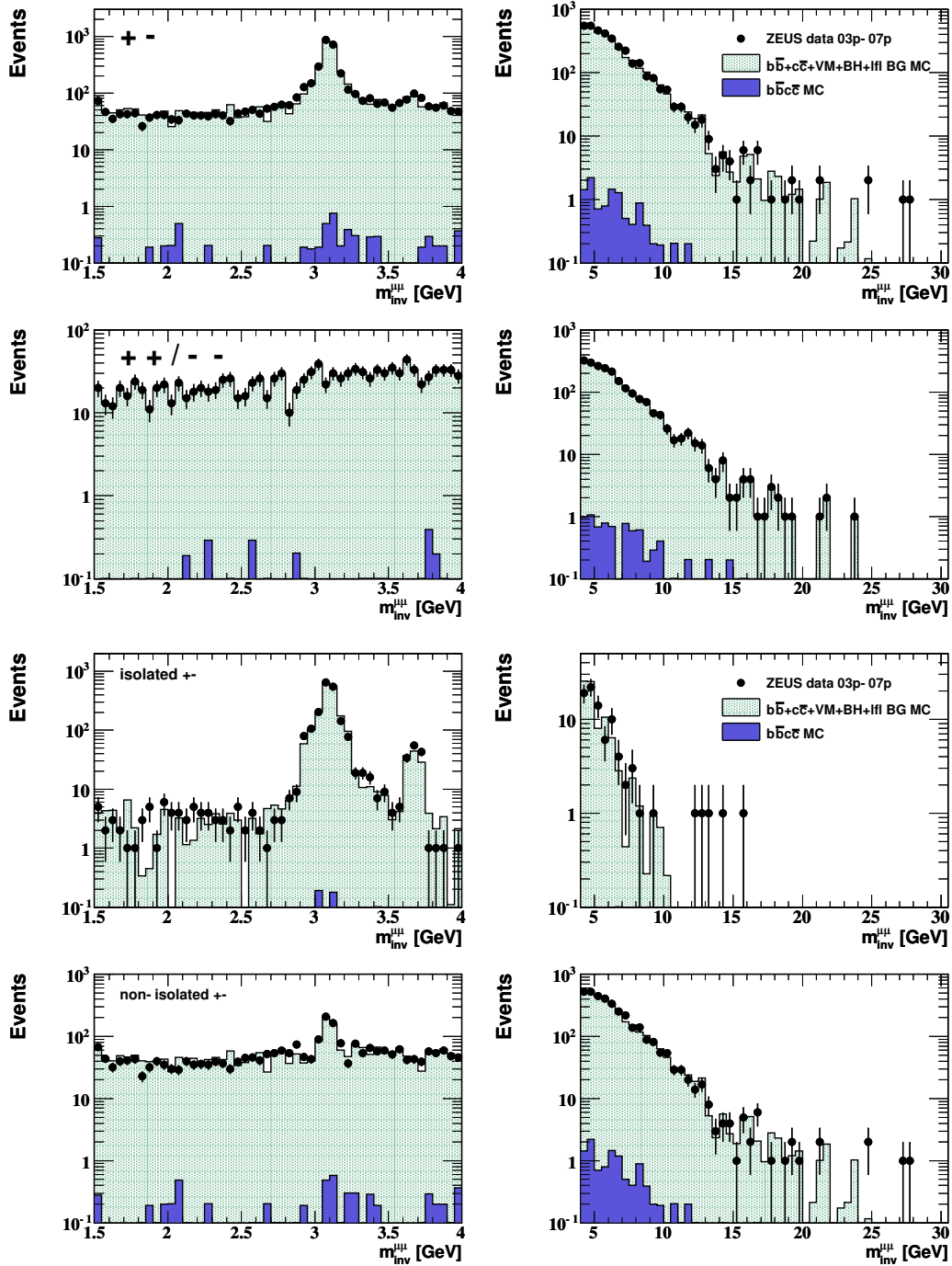
Figure G.3: Invariant dimuon mass for like- and unlike-sign as well as isolated and non-isolated muon pairs for $b\bar{b}c\bar{c}$ production (blue) and the sum of all MC dimuon sources (green-shaded area).

List of Figures

List of Tables

Bibliography

[1] F. Halzen, A. D. Martin, *"Quarks and Leptons: Introductory Course in Modern Particle Physics"*, John Wiley & Sons, N.Y. (1984).
C. Berger, *"Elementarteilchenphysik"*, Springer, Berlin (2006).

[2] K. Nakamura et al. (Particle Data Group), *"The Review of Particle Physics"*, J. Phys. **G 37**, (2010) 075021.

[3] S. L. Glashow, Nucl. Phys. **22**, (1961) 579.
S. Weinberg, Phys. Rev. Lett. **19**, (1967) 1264.
A. Salam, Proc of the 8th Nobel Symposium on 'Elementary Particle Theory, Relativistc Groups and Analycity', Stockholm, ed. by N. Svartholm, (1969) 367-377.

[4] I. Bloch, *"Measurement of Beauty Production from Dimuon events at HERA/ZEUS"*, Ph.D. Thesis, Hamburg University (2005), DESY-THESIS-05-034.

[5] G. 't Hooft, Phys. Rev. Lett. **37**, (1976) 8.
G. 't Hooft, Phys. Rev. **D 14**, (1976) 3432.
G. 't Hooft, Phys. Rev. **D 18**, (1978) 2199 (Erratum).
G. 't Hooft, Phys. Rep. **142**, (1986) 357.

[6] A. Belavin et al., Phys. Lett. **B 59**, (1975) 85.

[7] Johannes Gerigk, *"QCD - Instanton induzierte Prozesse in tiefinelatischer $e^{\pm}p$ - Streuung bei HERA"*, Diploma Thesis (German), Hamburg University (1998).

[8] Sonja Hillert, *"A search for QCD-instantons in deep inelastic ep scattering with the ZEUS detector at HERA"*, Ph.D. Thesis, Hamburg University (2002), DESY-THESIS-2002-052.

[9] Michael Sievers, *"Search for QCD - Instanton-induced Processes in Deep inelastic Scattering at HERA"*, Ph.D. Thesis, Hamburg University (2000), DESY-THESIS-2000-027.

[10] Birger Koblitz, *"Search for Instanton-Induced Processes with the H1 Detector in Deep Inelastic Electron-Proton Collisions at HERA"*, Ph.D. Thesis, Hamburg University (2002), DESY-THESIS-2002-015.

[11] Frank Winklmeier, *"Analysis of Instanton-Induced Processes with the H1OO Framework in Deep-Inelastic Scattering at the H1 Detector"*, DESY Summer Student Program 2002, Ulm University, (2002).

[12] T. Carli, J. Gerigk, A.Ringwald, F. Schrempp, *"QCD Instanton-induced Processes in Deep-inelastic Scattering - Search Strategies and Model Dependencies"*, (1999), DESY-PROC-1999-02, 329.

[13] C. Adloff et al., H1 Collaboration, *"Search for QCD Instanton induced Events in Deep-Inelastic Scattering at HERA"*, Eur. Phys. J. **C 25**, (2002) 495.

[14] ZEUS Collaboration, S. Chekanov et al., *"Search for QCD-instanton induced events in deep-inelastic ep scattering at HERA"*, Eur. Phys. J. **C 34**, (2004) 255.

[15] D. Bot, *Untersuchung der Nachweisbarkeit von QCD-Instanton mit schweren Quarks in $e^{\pm}p$-Kollisionen bei HERA*, Diploma Thesis (German), Hamburg University (2008), DESY-THESIS-2008-014.

[16] F. R. Klinkhamer, N. S. Manton, *A saddle-point solution in the Weinberg-Salam theory"*, Phys. Rev. **D 30**, (1984) 10.

[17] A. D. Sakharov, *"Violation of CP invariance, C-assymetry and baryon asymmetry of the Universe"*, J. Exp. Theor. Phys. **5**, (1967) 24.

[18] R. P. Feynman, *"Photon Hadron interactions"*, W. A. Benjamin, New York (1972).

[19] M. Gell-Mann, *"A schematic model of baryons and mesons"*, Phys. Lett. **8**, (1964) 241.
G. Zweig, *"An SU(3) model for strong interactions symmetry and its breaking"*, (1964) CERN-TH-401.

[20] A. M. Cooper-Sarkar, R. Devenish, A. De Roeck, *"Structure functions of the nucleon and their interpretation"*, Int. J. Mod. Phys. **A 20**, (1998) 3385.

[21] J.D. Bjorken, *"Asymptotic sum rules at infinite momentum"*, Phys. Rev. **179**, (1969) 1547.

[22] C. G. Callan, D. J. Gross, *"High energy electroproduction and the constitution of the electric current"*, Phys. Rev. Lett. **B 22**, (1969) 156.

[23] M. Breidenbach et al., *"Observed behaviour of highly inelastic electron-proton scattering"*, Phys. Rev. Lett. **23**, (1969) 935.

[24] F. Carvalho et al., Phys. Rev. **C 79**, (2009) 035211.
V. P. Goncalves, M. V. T. Machado, Eur. Phys. J. **C 37**, (2004) 299.
M. V. T. Machado, Eur. Phys. J. **C 47**, (2006) 365.
B. Foster, *"Lectures on HERA physics"*, Eur. Phys. J. DIRECTA1, (2002) 1, hep-ex/0206011.

[25] J. C. Collins, *"The problem of scales: Renormalization and all that"*, (1995) hep-ph/9510276.

[26] S. Bethke, *"The 2009 world average of α_s"*, Eur. Phys. J. **C 64**, (2009) 689.

[27] J. C. Collins, D. E. Soper *"The Theorems Of Perturbative QCD"*, Ann. Rev. Nucl. Part. Sci. **37**, (1987) 383.

[28] A. Gabareen Mokhtar, *"Study of neutral and charged current cross sections at high Q^2 at HERA"*, Ph.D. Thesis, Tel Aviv University (2006), DESY-THESIS-2006-005.
R. Ciesielski, H1 and ZEUS Collaboration, *"Charged and neutral current cross sections from HERA"*, published in J. Phys. Conf. Ser. **110:042007** (2008).
H1 and ZEUS Collaboration, *"Compiled H1+ZEUS NC and CC plots for conferences"*, ZEUS-prel-09-001, H1prelim-09-043 (2009).

[29] R. Brock et al., *"Handbook of perturbative QCD"*, Rev. Mod. Phys. **67**, (1995) 157.
R. K. Ellis, W. J. Stirling, B. R. Webber, *"QCD and collider physics"*, Cambride Monographs on Particle Physics, Nuclear Physics and Cosmology **8** (1996).
G. Dissertori and G.P. Salam, *"Quantum chromodynamics"*, in K. Nakamura et al., J. Phys. **G 37**, (2010) 075021.

[30] G. Altarelli, G. Parisi, Nucl. Phys. B **126**, (1977) 298.
V. N. Gribov, L. N. Lipatov, Sov. J. Nucl. Phys **15**, (1972) 438.
Y. L. Dokshitzer, Sov. Phys. JETP **46**, (1977) 641.

[31] H1 and ZEUS Collaboration, *"Combined Measurement and QCD Analysis of the inclusive $e^{\pm}p$ Scattering Cross Sections at HERA"*, JHEP **01**, (2010) 109.

[32] E. Fermi, Z. Phys. **29**, (1924) 315.
V. M. Budnev et al., Phys. Rep. **C 15**, (1975) 181.

[33] C. F. Weizsäcker, Z. Phys. **88** ,(1934) 612.
E.J. Williams, Phys. Rev. **45**, (1934) 729.

[34] L. Jones, H. Wyld, *"Charmed-particle production by photon-gluon-fusion"*, Phys. Rev. **D 17**, (1978) 759.

[35] B. Anderson et al., *"Parton fragmentation and string dynamics"*, Physics Reports **97**, (1983) 31.
T. Sjöstrand, *"Jet fragmentation of multiparton configurations in a string framework"*, Nucl. Phys. **B 248**, (1984) 469.

[36] C. Peterson et al., *"Scaling violation in inclusive e^+e^- annihilation spectra"*, Phys. Rev. **D 27**, (1983) 105.

[37] P. Nason, C. Oleari, *" A phenomenological study of heavy quark fragmentation functions in e^+e^- annihilation"*, Nucl. Phys. **B 565**, (2000) 245.

[38] *"ROOT - A Data Analysis Framework"*, available on http://root.cern.ch (11.07.2011)

[39] K. Abe et al., BELLE Collaboration, Phys. Rev. Lett. **89**, (2002) 142001, arXiv: hep-ex/0412041.
K. Abe et al., BELLE Collaboration, Phys. Rev. Lett. **88**, (2002) 052001.

[40] B. Aubert et al., BABAR Collaboration, Phys. Rev. Lett. **87**, (2001) 162002.
B. Aubert et al., BABAR Collaboration, Phys. Rev. **D 72**, (2005) 031101.

[41] Xin-Heng Guo et al., "*Double heavy-quarkonium production from electron-positron anni-hilation in the Bethe-Salpeter formalism*" (unpublished), (2008) [arXiv:0804.0949v1[hep-ph]].

[42] R. Li et al., "*Pair production of Heavy Quarkonium and $B_c(^*)$ Mesons at Hadron Collid-ers*", Phys. Rev. **D 80**, (2009) [arXiv:0903.2250 [hep-ph]].
T. Binoth et al. Phys. Lett. **B 685**, (2010) 293 [arXiv:0910.4379 [hep-ph]].

[43] T. Stelzer, W. F. Long, Comput. Phys. Commun. **81**, (1994) 357 [hep-ph/hep-ph/9401258].

[44] T. Sjöstrand, Comp. Phys. Commun. **135**, (2001) 238.

[45] H. Jung, Comp. Phys. Commun **86**, (1995) 147.
H. Jung, "*The RAPGAP Monte Carlo for Deep Inelastic Scattering v3.10*, Lund Univerity (2005).

[46] S. Frixione et al. "*Heavy quark correlations in photon-hadron collisions*", Nucl. Phys. **B 412**, (1994) 225.

[47] A. Geiser, A. E. Nuncio Quiroz, "*The FMNR⊗PYTHIA interface for Heavy Quark Pro-duction at HERA*", ZEUS-NOTE 06-012 (2006) [arXiv:0707.1632v1 [hep-ph]].

[48] S. W. Herb et al., Phys. Rev. Lett. **39**, (1977) 252.

[49] C. Albajar et al., UA1 Collaboration, Phys. Lett. **B 186**, (1987) 237.
C. Albajar et al., UA1 Collaboration, Phys. Lett. **B 213**, (1988) 405.
C. Albajar et al., UA1 Collaboration, Phys. Lett. **B 256**, (1991) 121,
Erratum-ibid., Phys. Lett. **B 262**, (1991) 497.

[50] C. Albajar et al., UA1 Collaboration, Z. Phys. **C 61**, (1994) 41.

[51] P. Nason, S. Dawson and R. K. Ellis, Nucl. Phys. **B 303**, (1988) 607.
P. Nason, S. Dawson and R. K. Ellis, Nucl. Phys. **B 327**, (1989) 49.

[52] C. Albajar et al. Phys. Lett. **B 256**, (1991) 121.

[53] M. L. Mangano, P. Nason, G. Ridolfi, Nucl. Phys. **B 373**, (1992) 295.

[54] F. Abe et al., CDF Collaboration, Phys. Rev. Lett. **68**, (1992) 3403.
F. Abe et al., CDF Collaboration, Phys. Rev. Lett. **69**, (1992) 3704.
F. Abe et al., CDF Collaboration, Phys. Rev. Lett. **71**, (1993) 500.
F. Abe et al., CDF Collaboration, Phys. Rev. Lett. **71**, (1993) 2396.
F. Abe et al., CDF Collaboration, Phys. Rev. Lett. **71**, (1993) 2537.
F. Abe et al., CDF Collaboration, Phys. Rev. Lett. **D 50**, (1994) 4252.
F. Abe et al., CDF Collaboration, Phys. Rev. Lett. **75**, (1995) 1451.

F. Abe et al., CDF Collaboration, Phys. Rev. Lett. **D 53**, (1996) 1051.
F. Abe et al., CDF Collaboration, Phys. Rev. Lett. **D 55**, (1997) 2546.
D. Acosta et al., CDF Collaboration, Phys. Rev. Lett. **D 65**, (2002) 052005.
D. Acosta et al., CDF Collaboration, Phys. Rev. Lett. **D 66**, (2002) 032002.
D. Acosta et al., CDF Collaboration, Phys. Rev. Lett. **D 71**, (2005) 032001.
D. Acosta et al., CDF Collaboration, Phys. Rev. Lett. **D 71**, (2005) 092001.
T. Aaltonen et al., CDF Collaboration, Phys. Rev. Lett. **D 77**, (2008) 072004.

[55] S. Abachi et al., DØ Collaboration, Phys. Rev. Lett. **74**, (1995) 3548.
S. Abachi et al., DØ Collaboration, Phys. Rev. Lett. **B 370**, (1996) 239.
B. Abbott et al., DØ Collaboration, Phys. Lett. **B 487**, (2000) 264.
B. Abbott et al., DØ Collaboration, Phys. Rev. Lett. **84**, (2000) 5478.
B. Abbott et al., DØ Collaboration, Phys. Rev. Lett. **85**, (2000) 5068.

[56] S. Frixione et al., *"Heavy quark production"*, hep-ph/9702287.

[57] M. Cacciari et al., J. High Energy Phys. 0407, (2004) 033.

[58] M. Bishai, CDF II Collaboration, *"Beauty and Charm physics at CDF Run II"*, Eur. Phys. J. **C 34**, (2004) 347.
http://www-cdf.fnal.gov/physics/new/bottom/030904.blessed-bxsec-jpsi

[59] S. Frixione et al. J. High Energy Phys. 0308, (2003) 007.

[60] ZEUS Collaboration, H. Abramowicz et al., *"Measurement of beauty production in deep inelastic scattering at HERA using decays into electrons"*, Eur. Phys. J. **C 71**, (2011) 1573.

[61] ZEUS Collaboration, H. Abramowicz et al., *"Measurement of beauty production in DIS and F_2^{bb} extraction at ZEUS"*, Eur. Phys. J. **C 96**, (2010) 347.

[62] ZEUS Collaboration, S. Chekanov et al. *"Measurement of charm and beauty production in deep inelastic ep scattering from decays into muons at HERA"*, Eur. Phys. J. **C 65**, (2010) 65.

[63] ZEUS Collaboration, S. Chekanov et al., *"Measurement of beauty photoproduction using decays into muons in dijet events at HERA"* JHEP **04**, (2009) 133.

[64] ZEUS Collaboration, S. Chekanov et al., *"Measurement of beauty production from dimuon events at HERA"*, JHEP **02**, (2009) 32.

[65] ZEUS Collaboration, S. Chekanov et al., *"Beauty photoproduction using decays into electrons at HERA"*, Phys. Rev. **D 78**, (2008) 072001.

[66] ZEUS Collaboration, S. Chekanov et al., *"Measurement of open beauty production at HERA in the $D^*\mu$ final state"*, Eur. Phys. J. **C 50**, (2007) 299.

[67] ZEUS Collaboration, S. Chekanov et al., *"Measurement of beauty production in deep inelastic scattering at HERA"*, Phys. Lett. **B 599**, (2004) 173.

[68] H1 Collaboration, F.D. Aaron et al., *"Measurement of Charm and Beauty Jets in Deep Inelastic Scattering at HERA"*, Eur. Phys. J. **C 71**, (2011) 1509

[69] H1 Collaboration, A. Aktas et al., *"Measurement of Beauty Production at HERA using Events with Muons and Jets"*, Eur. Phys. J. **C 41**, (2005) 453.
H1 Collaboration, A. Aktas et al., *"Measurement of Charm and Beauty Photoproduction at HERA using $D^*\mu$ Correlations"*, Phys. Lett. **B 621**, (2005) 56.
H1 Collaboration, C. Adloff et al., *"Measurement of Open Beauty Production at HERA"*, Phys. Lett. **B 467**, (1999) 156.

[70] ZEUS Collaboration, H. Abramowicz et al., *"Measurement of Heavy-Quark Jet Photoproduction at HERA"*, DESY 11-067, to be published in EPJC, (2011) [arXiv:1104.5444 [hep-ph]]

[71] A. Yagües Molina, *"Study of Beauty Phodoproduction with the ZEUS Experiment at the Electron-Proton Collider HERA"*, Ph.D. Thesis, Humbold University of Berlin (2008), DESY:6561.

[72] V. E. Schönberg, *" Measurement of beauty and charm photoproduction using inclusive secondary vertexing with the ZEUS detector at HERA*, Ph.D. Thesis, Bonn University (2010), Bonn-IR-2010-05.

[73] P. Roloff, *"Measurement of charm and beauty production in deep inelastic scattering at HERA"*, Ph.D. Thesis, Hamburg University, (2011).

[74] ATLAS Collaboration, G. Aad et al., *"The ATLAS Experiment at the CERN Large Hadron Collider"*, JINST **3**, (2008) S08003.

[75] CMS Collaboration, S Chatrchyan et al., *"The CMS experiment at the CERN LHC"*, JINST **3**, (2008) S08004.

[76] LHCb Collaboration, A. A. Alves et al., *"The LHCb Detector at LHC"*, JINST **3**, (2008) S08005.

[77] LHCb Collaboration, A. A. Alves et al., *"Measurement of $\sigma(pp \to b\bar{b}X)$ at $\sqrt{s} = 7\ TeV$ in the forward region"*, Phys. Lett. **B 694**, (2010) 209.

[78] See J. M. Campbell, K. Ellis, *"MFCM, A Monte Carlo for FeMtobarn processes at Hadron Colliders - Users Guide"*, available on http://mcfm.fnal.gov/ (30.08.2011).

[79] CMS Collaboration, *"Measurement of $B\bar{B}$ Angular Correlations based on Secondary Vertex Reconstruction at $\sqrt{s} = 7\ TeV$"*, submitted to JHEP, (2011) available on arXiv:1102.3194v2 [hep-ex]

[80] CMS Collaboration, *"Inclusive b hadron Production Cross Section with Muons in pp Collision at $\sqrt{s} = 7\ TeV$"*, submitted to JHEP, (2011) available on arXiv:1101.3512 [hep-ex]

[81] CMS Collaboration, *"Measurement of $\sigma(pp \to b\bar{b}X \to \mu\mu Y)$ in pp collisions at $\sqrt{s} = 7\ TeV$"* CMS-Note, (2011) CMS PAS BPH-10-015.

[82] ATLAS Collaboration, *"Measurement of the b-jet production cross section using muons in jets with ATLAS in pp Collisions at $\sqrt{s} = 7$ TeV"*, (2011) ATLAS-CONF-2011-057.

[83] S. Aliolo et al, *"Jet pair production in POWHEG"*, JHEP **4**, (2011) 81, arXiv:1012.3380v1 [hep-ph].

[84] ATLAS Collaboration, *"Measurement of the inclusive and dijet cross section of b-jets in pp Collisions at $\sqrt{s} = 7$ TeV with the ATLAS detector"*, (2011) ATLAS-CONF-2011-056.

[85] CMS COllaboration, *"Search for $B_s^0 \to \mu^+\mu^-$ and $B^0 \to \mu^+\mu^-$ decays in pp collisions at $\sqrt{s} = 7$ TeV"*, submitted to PRL, (2011) CERN-PH-EP-2011-120, arXiv:1107.5834v1 [hep-ex].

[86] LHCb Collaboration, R. Aaij et al., *"Search for the rare decays $B_s^0 \to \mu^+\mu^-$ and $B^0 \to \mu^+\mu^-$"*, Phys. Lett. **B 699**, (2011) 330.

[87] CMS Collaboration, S. Chatrchyan et al., *"Measurement of the B^0 Production Cross Section in pp Collisions at $\sqrt{s} = 7$ TeV"*, Phys. Rev. Lett. **106**, (2011) 252001

[88] CMS Collaboration, S. Chatrchyan et al., *"Measurement of the B_s^0 Production Cross Section in pp Collisions at $\sqrt{s} = 7$ TeV"*, submitted to the PRD-DC, (2011) CERN-PH-EP-2011-063, arXiv:1106.4048v1.

[89] CMS Collaboration, V. Khachatryan et al., *"Measurement of the B^+ Production Cross Section in pp Collisions at $\sqrt{s} = 7$ TeV"*, Phys. Rev. Lett. **106**, (2011) 112001.

[90] ATLAS Collaboration, *"Observation of the B_d^0 and B_s^0 mesons in the decays $B_d^0 \to J/\psi K^{*0}$ and $B_s^0 \to J/\psi\phi$ in ATLAS"*, (2011) ATLAS-CONF-2011-050.

[91] ATLAS Collaboration, *"Observation of the decay $B_d^0 \to J/\psi(\mu^+\mu^-)K_s^0(\pi^+\pi^-)$ with the ATLAS experiment at the LHC"*, (2011) ATLAS-CONF-2011-105.

[92] https://twiki.cern.ch/twiki/bin/view/CMSPublic/PhysicsResultsBPH (30.08.2011).

[93] https://wof-cluster.desy.de/sites/site_hasylab/content/e81/e5400/e41243/ e5399/e83/index_ger.html (11.07.2011)

[94] I. Abt et al., H1 Collaboration, *"The H1 Detector at HERA"*, Nucl. Instr. and Meth., **A 386**, (1997) 310.

[95] U. Holm et al., ZEUS Collaboration, *"The ZEUS Detector"* (unpublished), Status Report (1993).
http://www-zeus.desy.de/bluebook/bluebook.html (11.07.2011)

[96] K. Ackerstaff et al., *"The HERMES Spectrometer"*, Nucl. Instr. and Meth., **A 417**, (1998) 230.

[97] E. Hartouni et al., HERA-B Collaboration, *"HERA-B Design Report"*, DESY-PRC-95-01 (1995).
HERA-B Collaboration, *"HERA-B Status Report"*, DESY-PRC-00-04 (2000).

[98] J. L. Augneres et al., *"HERA - A Proposal for a Large Electron Proton Colliding Beam Facility at DESY"*, DESY-HERA-81-10 (81, REC. AUG.), 292p.

[99] M. Seidel, *"The Upgraded Interaction Regions of HERA"* DESY HERA-00-01 (2000).

[100] H1 Coll., F. D. Aaron et al., *"Measurement of the Proton Structure Function $F_L(x, Q^2)$ at Low x"*, Phys. Lett. **B 665**, (2008) 139.
ZEUS Coll., S. Chekanov et al. *"Measurement of the Longitudinal Proton Structure Function at HERA"*, Phys. Lett. **B 682**, (2009), 8.
J. Gebrenyuk, ZEUS and H1 Collaboration, *"Combined measurement of the inclusive $e^{\pm}p$ scattering cross section at HERA for reduced proton beam energy runs and determination of the structure function F_L"*, 18th International Workshop on Deep Inelastic Scattering and related subjects (DIS 2010), Florence (Italy), April 2010.

[101] http://www-zeus.desy.de/pictures.php3 (11.07.2011)

[102] N. Harnew et al., *"Vertex Triggering using time difference measurements in the ZEUS Central Tracking Detector"*, Nucl. Instr. Meth. **A 279**, (1989) 290.
B. Foster et al., *"The performance of the ZEUS central tracking detector z-by-timing electronics in a transputer based data acquisition system"* Nucl. Phys. Proc. Suppl. **B 32**, (1993) 181.
B. Foster et al., *"The design and construction of the ZEUS central tracking detector"* Nucl. Instr. Meth. **A 336**, (1994) 254.

[103] R. Hall-Wilton et al., *"The CTD Tracking Resolution"* (unpublished), ZEUS-NOTE 99-024.

[104] E. Maddox, *"Study of heavy quark production at HERA using the ZEUS microvertex detector*, PhD Thesis (2004).
A. Spiridonov, *"Tracking Status"*, Talk at the ZEUS Collaboration Meeting, DESY Hamburg, Germany (2011).

[105] ZEUS Collaboration, A. Polini et al., *" The design an performance of the ZEUS Micro Vertex detector*, Nucl. Instr. Meth., **A 581**, (2007) 656-686, 0708.3011.

[106] V. Chiochia, Nucl. Instr. Meth. **A 501**, (2003) 60.
E. Koffemann, Nucl. Instr. Meth. **A 473**, (2001) 26.
M. Petrucci, Int. J. MOd. Phys. **A 16S1C**, (2001) 1078.
U. Koetz, Nucl. Instr. Meth. **A 461**, (2001) 210.
E. Koffemann, Nucl. Instr. Meth. **A 453**, (2000) 89.
C. Coldewey, Nucl. Instr. Meth. **A 453**, (2000) 149.
C. Coldewey, Nucl. Instr. Meth. **A 447**, (2000) 44.

[107] M. Derrick et al., Nucl. Instr. Meth. **A 309**, (1991) 101.
A. Caldwell et al., Nucl. Instr. Meth. **A 321**, (1992) 356.

[108] G. Wolf et al., *"The ZEUS Detector: Technical Proposal"*, (1986) DESY-HERA-ZEUS-1.

[109] Battistoni, G. et al., *"Electrodeless plastic streamer tubes"*, Nucl. Instr. Meth. **217**, (1983) 429.

[110] Abbiendi, G. et al., *"The ZEUS barrel and rear muon detector"*, Nucl. Instr. Meth. **A 333**, (1993) 342.

[111] Tomash Jezynksi et al., Proc. SPIE **5484**, (2004) 180.
Krzystof T. Pozniak et al., Proc. SPIE **5484**, (2004) 186.

[112] http://www-zeus.desy.de/physics/lumi (11.07.2011)

[113] K. J. Gaemers, M. van der Horst, Nucl. Phys **B 316**, 269 (1989).

[114] J. Andruszkow et al., Acta Phys. Polon. **B 32**, 2025 (2001).

[115] H1 Collab., *Luminosity measurement in the H1 expreiment at HERA*, submitted to the 28th International Conference on the High-Energy Physics, ICHEP1996, Warsaw, Poland.

[116] H. Bethe, W. Heitler, *"On the stopping of fast particles and on the creation of positive electrons"*, Proc. Roy. Soc. Lond. **A 146**, (1934) 83-112.

[117] J. Chwastowski, J. Figiel, A. Kotarba, K. Olkiewicz, L. Suszycki, *"Aerogel Cherenkov detectors for the luminosity measurement at HERA"*, Nucl. Instr. Meth. **A 504**, (2003) 222-227.

[118] M. Helbich et al., *"The spectrometer system for measuring ZEUS luminosity at HERA"*, Nucl. Instr. Meth. **A 565**, (2006) 572-588, physics/0512153.

[119] W. H. Smith, K. Tokushuku, L. W. Wiggers, *"The ZEUS Trigger System"*, contributed to 10th International Conference on Computing in High Energy Physics (CHEP 92), Annecy (France), (1992).

[120] S. Silverstein et al. *"The ZEUS Calorimeter First Level Trigger"*, Nucl. Instr. Meth. **A 360**, (1995) 322-324.

[121] H. Uijterwaal, *"The Global Second Level Trigger for ZEUS"*, Ph.D Thesis, University of Amsterdam (1992).

[122] P. Allfrey et al., *"The Design and Performance of the ZEUS Global Tracking Trigger"*, ZEUS-NOTE-07-001 (2007), published in Nucl. Instr. Meth. **A 580**, (2007) 1257.
D. Gladkov, *"Charm quark pair correlations with D^*-muon tag at HERA"*, Ph.D. Thesis, Hamburg University (2007), DESY-THESIS-07-025.

[123] S. M. Fisher, P. Palazzi, *"ADAMO Reference Manual for Version 3.3"*, CERN ECP http://adamo.web.cern.ch/adamo/refmanual/Document.html (11.07.2011)

[124] ZEUS TLT Group Collaboration, D. C. Bailey et al., *"The ZEUS Third Level Trigger Hardware Architecture"*, presented at International Conference on Open Bus Systems 92, Zurich, Switzerland (1992).

[125] S. M. Fisher, A. Palazzi, "The ADAMO Data System Programmers' Manual - Version 3.2", CERN ECP and RAL, available on http://adamo.web.cern.ch/adamo/refmanual/Document.html (11.07.2011)

[126] T. Haas, "Generating Monte Carlo Events with MOZART" (unpublished), ZEUS-NOTE 92-021 (1992).

[127] E. de Wolf (editor) et al., "ZGANA - ZEUS Trigger Simulation Library", available on http://www-zeus.desy.de/components/offline/offline.html (11.07.2011)

[128] R. Brun, "GEANT3", Technical Report, CERN-DD/EE/84-1, CERN (1987).

[129] S. Dusini, A. Fox-Murphy, I. Grabowska-Bold, C. Gwenlan, J. Sztuk et al., ZEUS Collaboration, "ORANGE User Manual", available on http://www-zeus.desy.de/ZEUS_ONLY/analysis/orange/index.html (11.07.2011)

[130] L. Wai, R. Yoshida, "Running MOZART-ZGANA-ZEPHYR chain using FUNNEL and Monte-Carlo Environment (FMCE) for ZOW cluster" (unpublished), ZEUS-NOTE 93-065 (1993).

[131] G. F. Hartner et al., "VCTRAK (3.07/04): Offline Output Information" (unpublished), ZEUS-NOTE 97-064 (1997).
G. F. Hartner "VCTRAK Briefing: Program and Math(unpublished), ZEUS-NOTE 98-058 (1998).

[132] E. Maddox, "A Kalman filter track fit for the ZEUS microvertex detector" (unpublished), ZEUS-NOTE 03-008 (2003).
R. Früwirth, "Application of Kalman filtering to track and vertex fitting", Nucl. Instr. Meth. **A 262**, (1987) 444.

[133] A. Spiridonov, "Mathematical framework for fast and rigorous track fit for the ZEUS detector", DESY 08-182 (2008).

[134] R. Früwirth, A. Strandli, "Track fitting with ambiguities and noise: a study of elastic tracking and nonlinear filters", Comp. Phys. Comm. **120**, 197 (1999).

[135] J. Repond, "Jet Energy Corrections", ZEUS-NOTE 96-113 (1996).

[136] A. Caldwell, W. Liu, B. Mellado, B. Straub "BCAL Electron Studies Part II: Energy Scale Calibration", ZEUS-NOTE 98-018 (1998).

[137] K. Nagano, "Hadronic Energy Scale checht with NC events" (unpublished), Talk at the ZEUS Collaboration Week, Amsterdam (2005).

[138] B. Reisert, "Cal Energy Scale Calibration" (unpublished), Talk at the ZEUS F_L Monthly Meeting, DESY, January 2008.

[139] J. Ferrando, "Energy Scale and EM showers in 06-07 e^+p data" (unpublished), Talk at the ZEUS Physics Coordinator Meeting, DESY, July 2008.

[140] N. Tuning *"ZUFOs: Hadronic Final State Reconstruction with Calorimeter, Tracking and Backsplash Correcion"*, ZEUS-01-021, 2001.

[141] A. Longhin, *"Measurement of beauty production at HERA with a $D^* + \mu$ tag"*, Ph.D. Thesis, Padova University (2003), DESY-THESIS-2004-050.
M. Turcato, *"Measurement of beauty photoproduction at HERA"*, Ph.D. Thesis, University of Padova (2002), DESY-THESIS-2003-039.
V. Chiochia, *"Measurement of beauty quark production in deep inelastic scattering at HERA"*, Ph.D. Thesis, Hamburg University (2003), DESY-THESIS-2003-031.

[142] V. Sola, priv. communication.

[143] A. Geiser, *"GMUON - a general ZEUS muon finder"*, ZEUS-NOTE 06-016 (2006).

[144] S. Eidelman et al., Particle Data Group, *"Review of particle physics"*, Phys. Lett. **B 592**, (2004) 1.

[145] V. Kuzmin, *"The Muon Finder for FCAL"*, ZEUS-NOTE 96-134 (1996).
V. Kuzmin, Nucl. Instr. Meth. **A 453**, (2000) 336.

[146] G. Abbiendi et al., *"Observation of the $J/\psi \to \mu^+\mu^-$ in the first 273 nb^{-1} of 1993 run"*, ZEUS-NOTE 99-063 (1999).

[147] G. Abbiendi, *"BREMAT: Global Tracking of muons in the Barrel and Rear region"*, ZEUS-NOTE 99-063 (1999).

[148] V. Innocente, M. Maire and E. Nagy, *"GEANE: Average Tracking and Error Propagation Package"*, CERN Program Library, W5013-E (1991).

[149] L. Bellagamba, *"MVMATCH: A package to match FMUON tracks with Central Detectors"*, ZEUS-NOTE 96-051 (1996).
M. Corradi, MPMATCH algorithm, available on
http://www-zeus.desy.de/~corradi/ZEUS_ONLY/mpmatch/mpmatch2.html
(11.07.2011)

[150] R. E. Kalman, *" A new approach to linear filtering and prediction problems"*, Transactions of the ASME-Journal of Basic Engineering **D 82**, (1960) 35.

[151] G. Bruni, MUFO algorithm, available on
http://www-zeus.desy.de/~bruni/ZEUS_ONLY/muons.html (11.07.2011)

[152] R. Ciesielski, MUBAC algorithm, available on
http://www-zeus.desy.de/~robertc/ZEUS_ONLY/mubac.html (11.07.2011

[153] I. Bloch, A. Geiser, O. Gutsche, I. Rubinsky, J. Ziemann, *"Muon efficiency corrections for GMUON"*, ZEUS-NOTE 07-006 (2007).

[154] I. Rubinskiy, *"Measurement of the Υ meson production cross section in ep scattering at HERA"*, Ph.D. Thesis, Hamburg University (2009), DESY-THESIS-09-014.

[155] K. Most, Diploma Thesis - in preparation, (2011).

[156] J. E. Huth et al., *"Research Directions for the Decade"*, Proceedings of Summer Study on High Energy Physics (1990), edited by E. L. Berger, World Scientific (1992), 134.

[157] S. Cantani, Y. L. Dokshitzer and B. R. Webber, Phys. Lett. **B 285**, (1992) 291.
S. Cantani, Y. L. Dokshitzer, M. H. Seymour and B. R. Webber, Nucl. Phys. **B 406**, (1993) 187.

[158] W. B. Kilgore and W. T. Giele, Phys. Rev. **D 48**, (1993) 3160.

[159] H. Abramowicz, A. Caldwell and R. Sunkus, *"Neural network based electron identification in the ZEUS calorimeter"*, Nucl. Instr. Meth. **A 365**, (1995) 508.
R. Sinkus and T. Voss, *"Particle identification with neural networks using a rotational invariant moment representation"*, Nucl. Instr. Meth. **A 391**, (1997) 360.

[160] M. Klein, *"Physics at HERA"*, edited by W. Buchmüller and G. Ingelmann, vol. **1**, (1991) 71, DESY (Hamburg).

[161] S. Bentvelsen, J. Engelen, P. Kooijman, *" Reconstruction of (x, Q^2) and extraction of structure functions in neutral current scattering at HERA"*, Proceedings of the Workshop on Physics at HERA, edited by W. Buchmüller and G. Ingelmann, vol. **1**, (1991) 23, DESY (Hamburg).

[162] F. Jacquet, A. Blondel, *"Proceedings of the Study of an ep facility for Europe"*, Ed. U. Amaldi, DESY 79/48, 391.

[163] R. Brandelik et al., TASSO Collaboration, *"Properties of hadron final staes in e^+e^- annihilation at 13 GeV and 17 GeV center-of-mass energies"*, Phys. Lett. **B 83**, (1979) 261.
C. Berger et al., PLUTO Collaboration, *"Energy-Energy correlations in e^+e^- annihilation into hadrons"*, Phys. Lett. **B 99**, (1981) 292.
A. Petersen et al., *"Multi-hadron events at $E_{cm} = 29$ GeV and predictions of QCD models from $E_{cm} = 29$ GeV to $E_{cm} = 93$ GeV"*, Phys. Rev. **D 37**, (1988) 1,

[164] J. Bjorken, S. Brodsky, Physical Review **D 1**, (1970) 1416.

[165] G. Hanson, *"Proceeding of the 18th Int. Conf. on High Energy Physics"*, **B 1**, Tbilisi (1976).

[166] M. Gibbs et al., *"Future Physics at HERA"*, edited by G. Ingelman, A. de Roeck and R. Klanner, vol **1**, (1996) 509.

[167] E. Farhi, Phys. Rev. Lett. **39**, (1977) 1587.
A. de Rujula et al., Nucl. Phys. **B 138**, (1978) 387.

[168] P. Roloff, priv. communication.

[169] J. Hofestädt, *"Study of different reference axes for secondary vertexing in DIS at ZEUS"*, Summer Student report, DESY (2010).

[170] H. L. Lai et al., CTEQ Collaboration, *"Global QCD analysis of parton structure of the nucleon: CTEQ5 parton distributions"*, Eur. Phys. J. **C 12**, (2000) 375.

[171] M. Glück, E. Reya, A. Vogt, *"Photonic parton distributions"*, Phys. Rev. **D 46**, (1992) 1973.

[172] H1 and ZEUS Collaboration, R. Brugnera, *"Inelastic J/ψ production at HERA"*, Eur. Phys. J. **C 33**, (2004) 494.

[173] ZEUS Collaboration, S. Chekanov et al., *"Measuremants of inelastic J/ψ and ψ' photo-production at HERA"*, Eur. Phys. J **C 27**, (2003) 173.

[174] ZEUS Collaboration, H. Abramowicz et al., *"Measurement of J/ψ helicity distributions in inelastic photoproduction at HERA"*, JHEP **12**, (2009) 007.

[175] G. Marchesini et al., Comp. Phys. Commun., **67**, (1992) 465.

[176] B. List, A. Mastroberardino, *"DIFFVM - A Monte Carlo Generator for Diffractive Processes in ep Scattering"*, (1998), available on
http://www.desy.de/~blist/diffvm.html (11.07.2011)

[177] A. Tetsuo, *"GRAPE - Dilepton v1.1, A Generator for Dilepton Production in ep Collisions"*, Comput.Phys.Commun. 136 (2001), available on
http://arxiv.org/abs/hep-ph/0012029v2

[178] A. Ringwald, F. Schrempp, *"QCDINS 2.0 - A Monte Carlo generator for instanton - induced processes in deep inelastic scattering"*, Comput. Phys. Commun. **132**, (2000) 267.

[179] T. Sjöstrand, Comp. Phys. Commun. **82**, (1994) 74.

[180] F. Schrempp, priv. communication.

[181] J. Franck, *"MG2ZEUS - Documentation and manual"* (2010), available on
http://www.desy.de/~franckj/documents/MG2ZEUS_doc.pdf (11.07.2011)

[182] J. Franck, *"Experimentelle Untersuchung der Higgs-b/c-Kopplungen in Photon-Proton-Kollisionen"*, Diploma Thesis (German), Hamburg University (2010), DESY-THESIS-2011-018.

[183] Y. Golubkov, *"FORMOZA"*, available on
http://www.desy.de/~golubkov/Formoza/formoza/doc/index.html (11.07.2011)

[184] U. Samson, *"Beauty Photoproduction Using Decays into Muons at HERA"*, Ph.D. Thesis, Bonn University (2006), BONN-IR-2008-06.

[185] S. Boutle, *"Beauty in Photoproduction at HERA II with the ZEUS Detector"*, Ph.D. Thesis, University College London (2009), DESY-THESIS-2010-005.

[186] E. Lohrmann, priv. communication.

[187] A. N. Barakbaev, E. G. Boos, *"A new method to improve instanton selection in DIS"* (unpublished), ZEUS-NOTE 05-008 (2005).

[188] H1 Collaboration, F.D. Aaron et al., *"Measurement of the photoproduction of b-quarks at threshold at HERA"*, H1-prelim-11-071, published on DIS2011 in JLAB/USA (2011).
M. Sauter, *"Measurement of Beauty Photoproduction as Threshold using Di-Electron Events with the H1 Detector at HERA"*, Ph.D Thesis, Swiss Federal Institute of Technology in Zurich (2009), DESY-THESIS-2009-047.

[189] M. Göttlich, *"Study of Charm and Beauty Production at HERA/H1 using Dilepton Events"*, Ph.D Thesis, Hamburg University (2007), DESY-THESIS-2007-012.

[190] A. I. Vainshtein, V. I. Zakharov, V. A. Novikov, M. A. Shifman, *"ABC of Instantons"*, Sov. Phys. Usp. **25**, (1982) 195.
M. A. Shifman, *"Instantons in Gauge Theorioes"*, World Scientific (1994).
T. Schäfer, E. V. Shuryak, *"Instantons in QCD"*, Rev. Mod. Phys **70**, (1998) 323.

[191] R. P. Feynman, *"The Principle of least Action in Quantum Mechanics"*, Ph.D. Thesis, Princeton University (1942).
R. P. Feynman, *"Space-Time Approach to non-relativistic Quantum Mechanics"*, Rev. Mod. Phys. **20**, (1948) 367.
R. P. Feynman, A. R. Hibbs, *"Quantum Mechanics and Path Integrals"*, New York: McGraw Hill (1965).

[192] A. M. Polyakow, *"Compact Gauge Fields and the infrared Catastrophe"*, Phys. Lett. **B 59**, (1975) 82.

[193] A. Utermann, *"QCD-Instantonen und Saturation bei kleinem Bjorken-x"*, Ph.D. Thesis (german), Hamburg University (2003), DESY-THESIS-2003-029.

[194] A. Ringwald, F. Schrempp, *"Towards the Phenemenology of QCD-instanton induced Particle Production at HERA"*, hep-ph/9411217, in: *Quarks '94*, Proc 8th Int. Seminar, Vladimir, Russia (1994), ed. by. D. Grigoriev et al. (World Scientifi, Singapore 1995), 170.

[195] R. Jackiw, C. Rebbi, Phys. Rev. Lett. **37**, (1976) 172.

[196] F. Schrempp, *"Phenomenology of QCD-Instanton Induced Events"*, DESY Theory Workshop, Hamburg, (1995).

[197] A. Ringwald, F. Schrempp, *"Auf der Spur von Instantonen - grundlegenden Tunnelprozessen in der Teilchenphysik"*, Colloquium in Würzburg, Germany (1999).

[198] F. Schrempp, *"Tracking QCD-Instantons"* DESY-01-012, Talk presented at the Ringberg Workshop on *New Trends in HERA Physics 2001*, Ringberg Castle, Tegernsee, hep-ph/0109032 (2001).

[199] A. Ringwald, F. Schrempp, Phys. Lett. **B 438**, (1998) 217.

[200] V. V. Khoze, A. Ringwald, Phys. Lett. **B 259**, (1991) 106.
J. Verbaarschot, Nucl. Phys. **B 362**, (1991) 33.

[201] C. Bernard, Phys. Rev. **D 19**, (1979) 3013.

[202] T. Morris, D. Ross, D. Sachradja, Nucl. Phys. **B 255**, (1985) 115.

[203] S. Moch et al., Nucl. Phys. **B 507**, (1997) 134.

[204] D. A. Smith, M. J. Teper, UKQCD Collaboration, Phys. Rev. **D 85**, (1998) 014505.
A. Ringwald. F. Schrempp, *"Confronting Instanton Perturbation Theory with QCD Lattice Results"*, DESY 98-201, hep-lat/9903039, Phys. Lett. **B 459**, (1999) 219.

[205] A. Ringwald, F. Schrempp, in the proceedings of the *"8th Int. Workshop on Deep-inelastic scattering, DIS 2000"*, Liverpool, England, (2000), J. Dainton, J. A. Gracey, T. Greenshaw, Eds., pp. 318, hep-ph/00063215.

[206] F. Schrempp, *"Instanton-Events in Hard Photoproduction - Can they be predicted?"*, 3rd UK Phenomenology Workshop on HERA Physics, Durham (GB) (1998).

[207] F. Schrempp, priv. communication.

Acknowledgements

Danksagung